Visible light driven photocatalytic hydrogen evolution via water splitting using novel approaches in semiconductor catalysts

By
Priyanka S Walko
(10CC17A26011)

A thesis submitted to the
Academy of Scientific & Innovative Research
for the award of the degree of

DOCTOR OF PHILOSOPHY
in
Science

Under the supervision of
Dr. R. Nandini Devi
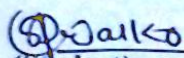

CSIR-National Chemical Laboratory, Pune

Academy of Scientific and Innovative Research
AcSIR Headquarters, CSIR-HRDC campus
Sector 19, Kamla Nehru Nagar,
Ghaziabad, U.P.–201 002, India

July-2023

Certificate

This is to certify that the work incorporated in this Ph.D. thesis entitled, *"Visible light driven photocatalytic hydrogen evolution via watersplitting using novel approaches in semiconductor catalysts,"* submitted *by Ms. Priyanka S Walko (10CC17A26011)*, to the Academy of Scientific and Innovative Research (AcSIR) in fulfillment of the requirements for the award of the Degree of *Doctor of Philosophy in Science*, embodies original research work carried out by the student. We certify that this work has not been submitted to any other University or Institution in part or full for any degree or diploma award. Research material(s) obtained from another source (s) and used in this research work has/have been duly acknowledged in the thesis. Image(s), illustration(s), figure(s), table(s), etc., used in the thesis from another source (s) have also been duly cited and acknowledged.

(Student)
Priyanka S Walko
Catalysis Division,
CSIR-NCL, Pune

(Supervisor)
Dr. R. Nandini Devi,
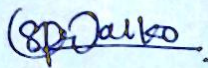Principal Scientist,
Catalysis Division,
CSIR-NCL, Pune

(Co-supervisor)
-

Date: 14/07/2023
Place: CSIR-NCL, Pune

STATEMENTS OF ACADEMIC INTEGRITY

I, Priyanka S Walko, a Ph.D. student of the Academy of Scientific and Innovative Research (AcSIR) with Registration No. 10CC17A26011 hereby undertake that the thesis entitled **"Visible light driven photocatalytic hydrogen evolution via water splitting using novel approaches in semiconductor catalysts"** has been prepared by me and that the document reports original work carried out by me and is free of any plagiarism in compliance with the UGC Regulations on *"Promotion of Academic Integrity and Prevention of Plagiarism in Higher Educational Institutions (2018)"* and the CSIR Guidelines for *"Ethics in Research and in Governance (2020)"*.

Signature of the Student:

Date: 14/07/2023

Place: Pune

It is hereby certified that the work done by the student, under my/our supervision, is plagiarism-free by the UGC Regulations on *"Promotion of Academic Integrity and Prevention of Plagiarism in Higher Educational Institutions (2018)"* and the CSIR Guidelines for *"Ethics in Research and in Governance (2020)"*.

Signature of the Co-supervisor (if any)
Name :-
Date :-
Place :-

Signature of the Supervisor
Name : Dr.R.Nandini Devi
Date : 14/07/2023
Place: Pune

…...Dedicated to

My parents and Family……

A special connection is there in Lab-918 because the first time I joined NCL, I went to that lab, and I got Dr.Anurag Chahande, with whom I fight like anything till date it's been 5 years, and our bond is the same. I would like to thank him for taking out time and motivating me during the bad days and good days of my life till today; thank you, bhaiya….I also got Chinnu the person with whom I share everything till today. Thank you ladaki for listening to all the nonsense I tell you….Love you…

"Nothing goes perfect if you do not have good company" This is true because my labmates are so good …I would like to thank all of them, starting from Neetha trainee who joined me as a Project trainee, Amrutha, Meghana, Athira, Neetha, Jishnu, etc and special thank to Mohsin (Happy person on the planet), Shubham, Rushikesh, Wasi, Vipul dada, Seema, Jyoti, Deepali, Shunottata and everyone who has I have missed in the list sorry……

You need guidance during your research and I got it from my DAC members. First, I would like to thank Dr. C.S. Gopinath the person I liked the most in the NCL; he has guided me regarding my work and motivated me during my bad days. I would like to thank Dr.Santoshbabu Sukumaran and Dr. A.K. Bhattacharya for their constant guidance related to organic parts and etc.

When you have good friends around to cheer, everything seems to be perfect…I am very lucky to have Garba girls(Ishani, Donring, Kathakali, and Dimpi) in my life from thick and thin situations in life they have been there for that I really like to thank them from the bottom of my heart. We have been together from 2014 till today…

At NCL, I got a group of friends with whom I can spend my free time for that, I would like to thank them from the bottom of my heart…If I start naming it will be partiality to one person or the other, so it's better I will not name one person instead I will say THANK YOU ALL For the love I got during my stay in NCL for the past many years. I would like to thank the MARATHI@NCL team for the opportunity I got because of you guys and got exposure to many activities and social work. Finally would like to thank my husband Prakash Kumare with whom I got married last year, and I really appreciate his thoughfullnes and helping nature. I am lucky to have him in my life, as whenever I was staying late in the lab, he used to cook food for me..THANK YOU, HUSBAND….And finally, I would like to thank my family for always having faith in me and believing in me, and allowing me to follow my passion for research….

Thank you to everyone…..

Though many have not been mentioned, none is forgotten.

Yours

Priyanka Walko

Table of Contents

3. Chapter: One-pot hydrothermal synthesis of Zinc oxide-Perylene for the photocatalytic hydrogen evolution via methanol oxidation   **46-76**

4. Chapter: Supramolecular self-assemble structure of ZnO nanoparticles modified with perylene tetracarboxylic acid dianhydride.   77-94

5. Chapter: Synthesis of $[M(II)_{(1-x)}M(III)_x(OH)_2](A_{x/n}).mH_2O$/PDI layered double hydroxides and their applications in the photocatalytic hydrogen evolution (M=Co & A= Cl) 95-116

7.Chapter: Summary and Conclusion **147-151**

List of Figures

Abstract

Earth receives an incredible amount of sunlight. motivated by continuously growing global energy demands and the depletion of readily accessible fossil fuels, the search for alternative energy sources, particularly renewable solar energy, has become vital. Different types of innovative ideas have been explored. The earth absorbs a large amount of energy, and only a few of it is used by humankind annually. Hydrogen will be the greenest fuel for the planet in the future source since its combustion product is water. The discovery of photolytic cleavage of water into hydrogen and oxygen is attributed to Honda and Fujishima in 1972 using titania and a Pt electrode. Afterward, many attempts have been carried out to develop semiconductors to produce hydrogen from water. The suitable materials should possess a small band gap to absorb visible light in the solar spectrum. On irradiation with light, electrons, and holes are created, which travel to the materials' surface and help reduce and oxidize water. While these processes are occurring, there will be chances of recombination, i.e., holes and electrons can combine, leading to a waste of energy. Another one is that many semiconductors absorb UV light, thus wasting the abundance of visible light irradiance in sunlight falling on the earth's surface. Hence, the two most important problems to address are identifying visible light-absorbing semiconductors and minimizing recombination by appropriate strategies. We synthesized different materials with different morphologies to get the photocatalytic hydrogen evolution activity. It includes layered double hydroxides and zinc oxides modified with organic dyes.

Scattering is one of the main challenges in scaling up photocatalytic water splitting using the most prevalent powder catalysts. Materials development has not translated into many large-scale photocatalytic H_2 production facilities yet. One of the main drawbacks is the necessity for huge light installations in the medium which would render

them uneconomical. In addition, limitations of the catalyst forms which can be used for efficient utilization of light from an external source also contributed to the difficulty in scaling up. The most common form of the catalysts used is powder dispersion in the reactant medium, which immediately brings in the disadvantage of scattering and is even more severe in large-scale systems. An alternative reported in an allied process, i.e., photocatalytic wastewater treatment, is to immobilize photocatalysts on substrates like thin films and employ them in a fixed bed configuration for continuous flow models. However, these models also demand multiple high-energy lamps immersed in the reaction medium, ruling out utilizing sunlight directly. To fully use the solar spectrum, increase the system's efficiency, and make the system sustainable and economically favourable, bridging the gap between reactor design and modifying the semiconductor-based systems with band gap engineering is significant.This thesis comprises six chapters, and a summary is given below:

Chapter 1: This chapter gives details of the introduction of how the work on the thesis has started. This chapter explains the principle behind photocatalytic water splitting and why it is necessary to look for alternative renewable energy sources for the future of humankind. It details the literature survey on the different types of steps involved in photocatalytic water splitting and various necessary components. This chapter deals with the literature survey on the different kinds of semiconductor materials used for applying photocatalytic water splitting. It also details the multiple strategies for increasing the utilization of the visible spectrum of the sun's energy. Finally, the chapter gives the thesis's scope and objective.

Chapter 2: Describes the synthesis of different morphologies of ZnO and its characterizations by using different techniques and applications in photocatalytic H_2 production via water splitting.

Chapter 3: ZnO has disadvantages of recombination and photo corrosion which have been overcome by modifying the ZnO nanorods morphology by using the perylene tetracarboxylic acid dianhydride (PTCDA) (named as ZnO-P) with the hydrothermal synthesis method. Its structural and photophysical characterizations have been carried out followed by the photocatalytic hydrogen evolution via methanol oxidation to value-added products (formaldehyde). It was found that the material was active for hydrogen evolution without adding a co-catalyst.

Chapter 4: Describes the synthesis and characterizations of the s supramolecular structure of TC-PTCDA-ZnO photocatalysts are synthesized by moderate conditions and used as a successful photocatalyst for photocatalytic H_2 evolution via water splitting. This photocatalyst showed an activity of about 2050µmol/h. Once the terminal end of the anhydride group changed from the tetra carboxylate group to the monocarboxylate group (MC-PTCDA-ZnO), the drastic change in the structural features observed which led to a decrease in the activity to 1000µmol/h. During the MC-PTCDA-ZnO, the structures form simple composite rather than supramolecular structures. The reason is that the supramolecular system leads to π-π stacking, leading to intermolecular charge transfer. Thus, it facilitates electron transfer more efficiently, increasing activity in TC-PTCDA-ZnO. This photocatalyst works without any co-catalyst, reducing the synthesis cost; therefore, this can form a future generation of organic-based photocatalysts.

Chapter 5: describes the synthesis and structural characterizations of α-Co(OH)$_2$ modified with perylene diimide (PDI=N, N'- bis(p-carboxyl-phenylene) perylene-3,4: 9,10-perylene bisimide) and its application in photocatalytic hydrogen evolution via water splitting. The changes in absorption and emission properties of modified material have been well observed and studied. The absorption properties of both the α-Co(OH)$_2$

and PDI have been seen and this has enhanced the electron transfer phenomenon thus photocatalytic hydrogen evolution activity via water splitting has been increased in this type of system. The emission intensity of α-Co(OH)$_2$-PDI has decreased compared to PDI's. This confirms the decrease in the rate of recombination and transfer of electrons and helps enhance activity. Electrochemical studies have also confirmed the electron transfer properties. The formation of layered double hydroxide system of α-Co(OH)$_2$-PDI for photocatalytic hydrogen evolution.

Chapter 6: Scattering is one of the main challenges in scaling up photocatalytic water splitting using the most prevalent powder catalysts. This can be overcome by decoupling the reaction medium from light transmission, as in the case of optical fibers. Here we explore utilizing optical fibers coated with 5wt% CuO supported on TiO$_2$ for water splitting. CuO/TiO$_2$ is a well-studied photo catalyst in which photo-reduced Cu species are known to act as sensitizers for inducing visible light activity. The scalability of such optical fiber-based systems and potential in non-potable turbid water media is demonstrated.

Chapter 7: summarizes the results and conclusions based on the work reported in the thesis. This thesis reports the detailed structural characterizations and photocatalytic hydrogen activities of ZnO modified with different morphologies. The construction of ZnO-P using perylene-based organic-based material has been explored along with the formation of self-assemblies of ZnO. The construction of layered double hydroxide structure α-Co(OH)$_2$-PDI is also given for photocatalytic H$_2$ evolution. Finally, the scattering issue in reactor design and scalability issues of powdered and this film-based systems have been addressed by using optical fibers coated with semiconductor materials given in the thesis.

List of Abbreviations

BET: Brunauer-Emmett-Teller

FT-IR: Fourier Transform Infrared

GC: Gas Chromatography

JCPDS Joint Committee on Powder Diffraction Standards

LDH: Layered Double Hydroxide

NMR: Nuclear Magnetic Resonance

PXRD: Powder X-ray Diffraction

SEM: Scanning Electron Microscopy

EDS: Energy Dispersive X-ray Spectroscopy

XPS X-Ray Photoelectron Spectroscopy

TEM: Transmission Electron Microscopy

UV-vis: Ultraviolet-visible

PL: Photoluminescence

Chapter 1

Introduction and Literature Survey

1.1. Introduction

Fossil fuels are currently the primary energy source for humanity and are used to provide electricity, heat for cooking, and power vehicles [2-4]. Because fossil fuels are considered non-renewable energy sources, their supply is finite and may run out at any time soon. The environmental issues associated with excessive fossil fuel consumption are more severe, resulting in considerable CO2 emissions-related air pollution. Due to their ability to transport heat, these gases mostly contribute to environmental problems, including the greenhouse effect and global warming, by raising global temperatures. Additionally, these contaminated gases cause additional harmful side effects like acid rain. Additionally, inefficient burning of fossil fuels results in the emission of CO, which is more hazardous than CO_2 since it has the ability to irreversibly bond with blood hemoglobin, lowering its affinity for O_2 and having harmful consequences on the human body. Given all these detrimental effects on the ecosystem, fossil fuels are a serious problem. [5-7].

If we examine several forms of innovative concepts. Since the 1800s, hydrogen has been utilized as a source of energy. It is considered a green fuel since it can be created from renewable resources. It has fewer emissions, and because H_2 reacts with oxygen to produce water, it possesses tremendous energy. Under typical atmospheric circumstances, hydrogen exists as an odorless, colorless gas. It coexists permanently and safely with oxygen until the energy inputs trigger an external reaction that results in water formation. [11-14]. Hydrogen can be produced in several ways, including heating methods that take heat from organic sources like fossil fuel and biomass. These procedures include the steam reforming of natural gases, the release of which results in greenhouse gas emissions [15–18]. Microorganisms like bacteria and algae can be used by biological processes to release hydrogen. This has drawbacks

regarding sustainability and scalability over the long term for the future [19–21]. In this case, producing hydrogen economically from cheap and plentiful raw resources like water on Earth's surface and solar energy would be the most environmentally beneficial and sustainable way to build a hydrogen economy. Humanity has struggled for years to fully utilize the abundant light that Earth receives. 51% of the total energy entering the atmosphere is absorbed by the Earth as solar radiation. The amount of energy humans use on Earth represents just 0.01% of the total energy the sun supplies to the globe yearly. At the planet's surface, the sun's spectrum is primarily distributed in the visible range (46%). In comparison, the remaining near-infrared ranges are felt as heat with a negligible portion in the near-ultraviolet (5%). Therefore, effective solar radiation utilization, particularly in the visible light spectrum, will be the main focus of sustainable energy solutions. [22].

Plants produce their food by using the phenomenon called photosynthesis. With the help of chlorophyll which is present in plant leaves and sunlight as a source of energy, they produce carbohydrates and oxygen from water and carbon dioxide. The process of mimicking the photosynthesis phenomenon is called 'Artificial Photosynthesis' by using materials synthesized in the laboratory that will show absorption in the solar spectrum. No carbon fixation is involved in directly producing hydrogen and oxygen from water splitting. One of the most promising technologies is the water-splitting method which uses a semiconductor catalyst to convert solar energy into hydrogen, which can be produced in vast amounts cleanly and sustainably [23-36].

Photocatalytic water splitting has three significant categories shown in Fig.1.1. The photovoltaic-based system has higher efficiency than photoelectrochemical and photocatalytic water splitting systems. The manufacturing cost is very high for PV-based water-splitting systems, so it is challenging to rely on. Developing a powder-based photocatalytic system will

be cheaper due to its scalability and reproducibility. The generated hydrogen cost will be less than that of a PV-based electrolysis system [38,39].

.
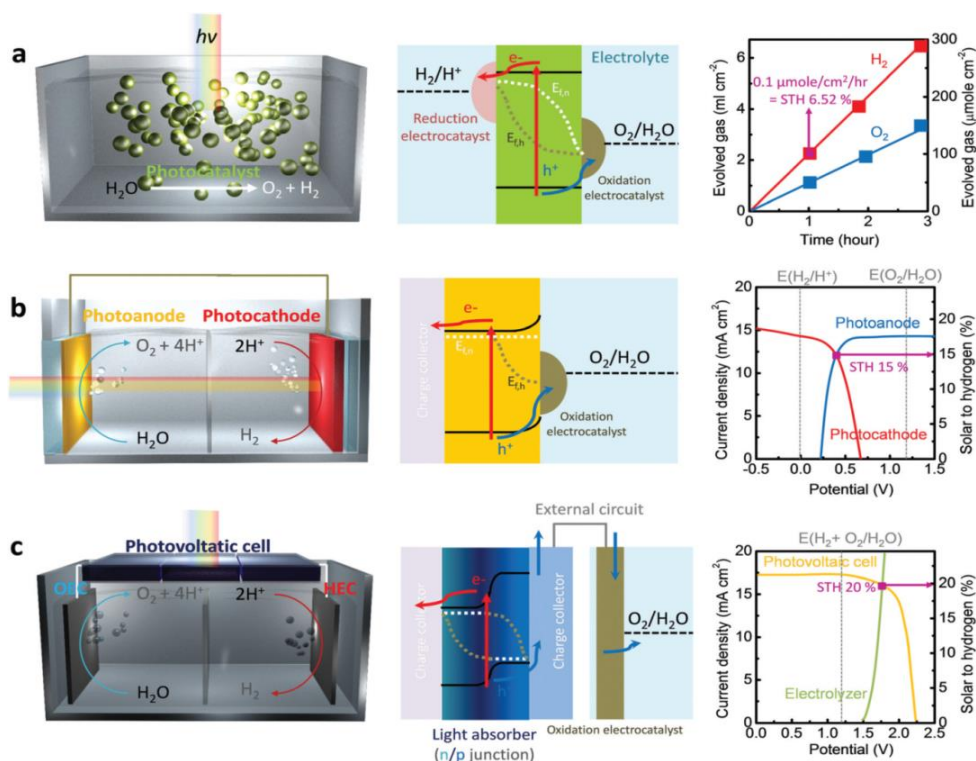
Fig.1.1. Schematics of various solar-driven water splitting systems (Adapted from Ref.38)

1.2 The Solar to hydrogen efficiency

Measurement of the efficiency of photocatalysts about light illumination is a critical concept for splitting water by photocatalysis. Because of the scattering of transient light in particulate suspension, it is hard to establish actual quantum yields. There are no methods for measuring the absorption of photons with precision. Thus, it is estimated as apparent or external quantum yield (AQY). Here, all the photons of incident light are believed to have been captured by a photocatalyst. STH (solar to hydrogen efficiency) and AQY (apparent quantum yield) are essential in analyzing the photocatalyst. The PV-based electrolysis shows a high efficiency of 10-40%, although the cost is very high, so it's not affordable. On the other hand, PECs and powder-based systems have low STH (~1%) but are highly cost-effective and easily scalable.

$$AQY\ (\%) = \frac{A\ X\ R}{I}\ X\ 100$$

A = Amount of Number of moles of H_2 or O_2

R = Rate of reaction

I = Incident photons

$$STH = \frac{\text{the production of chemical energy}}{\text{Incident solar light}} = \frac{r\ X\ \Delta G_r}{P_{sun}\ X\ S}$$

r= Rate

G_r = Gibbs free energy

P_{sun} = Energy flux of the sunlight

S = Area of reactor

1.3. Typical photocatalytic water splitting mechanism

When utilizing a photocatalyst to split water, the main procedures are as follows:

(I) Semiconductors absorb light to produce electron-hole pairs

(II) Charge migration and separation to the semiconductor's surface

(III) Surface oxidation or reduction processes involving water
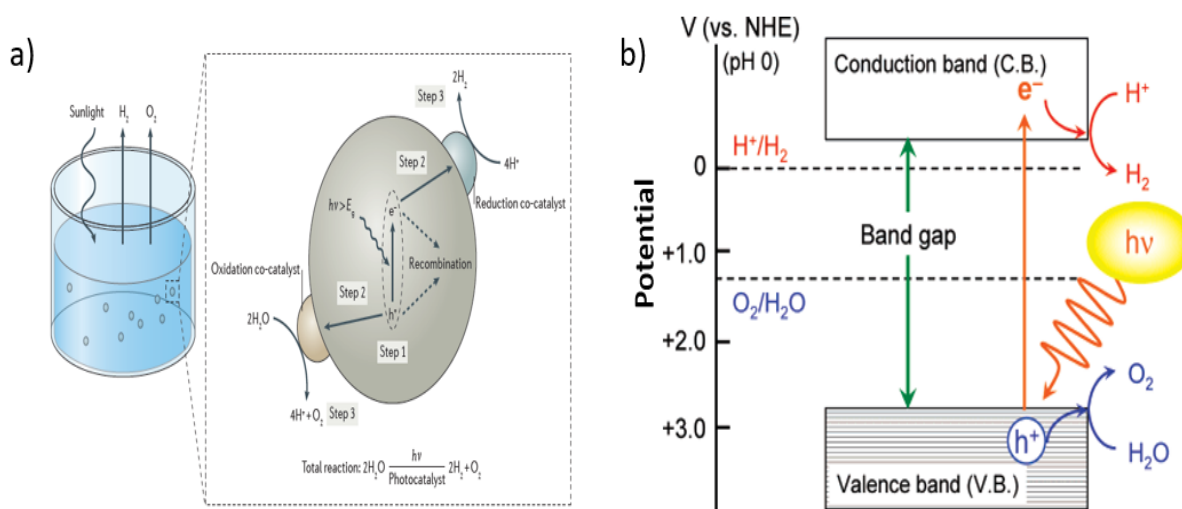
Fig.1.2. The general steps involved for the photocatalytic water splitting adapted from Ref-40
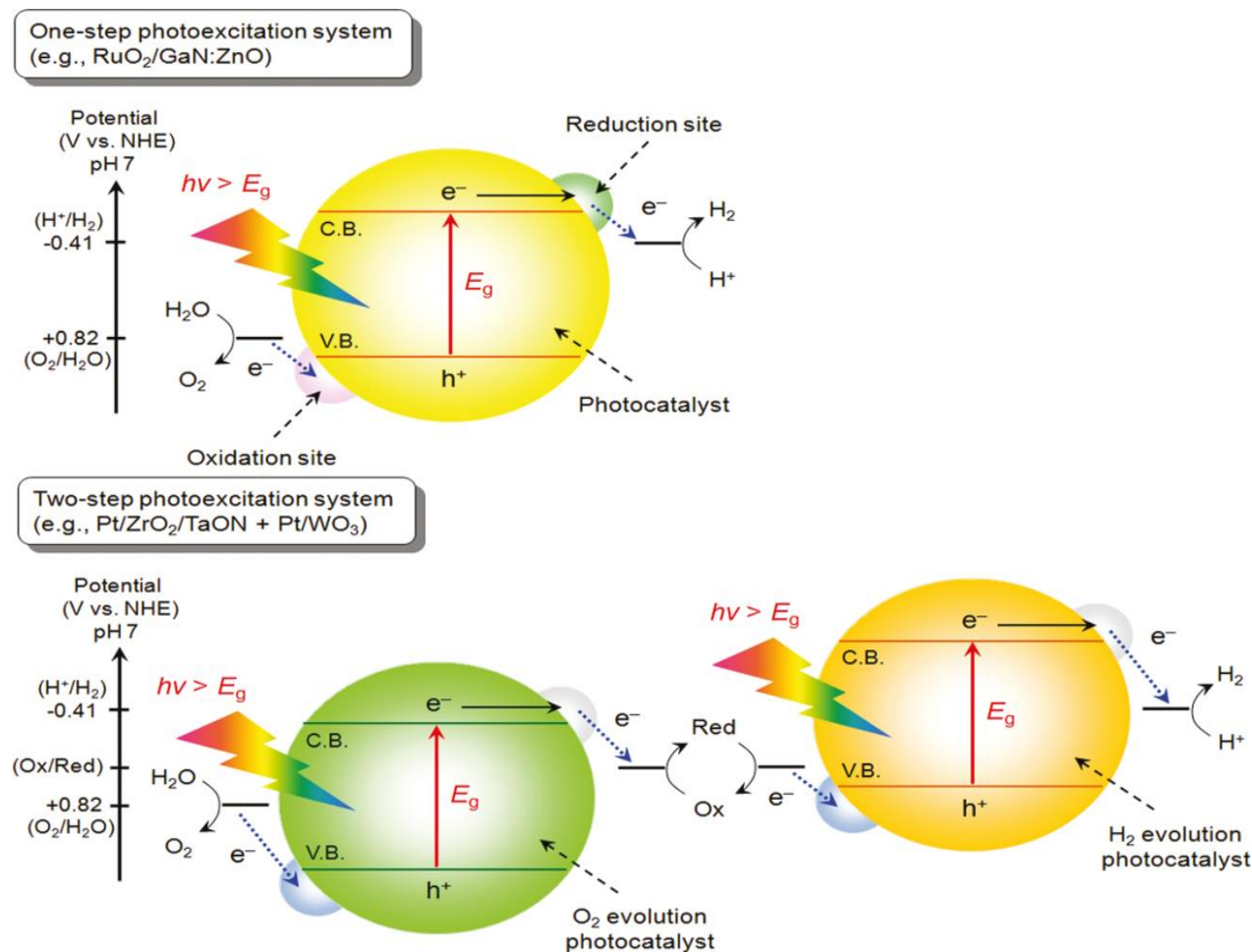
Fig.1.3 Representation of types of photocatalytic water splitting system (Adapted from Ref 40)

The first step is to light the sunlight with greater or equal energy than the band gap, followed by electron flow from the valence band into the conduction band. It'll form holes in the valence band and electrons within the conduction band.

$$\textbf{Photocatalyst} \xrightarrow{\textbf{hv}} \textbf{e}_{CB^-} + \textbf{\textit{h}}_{VB^+}$$

A mechanical band structure should be present in the photocatalysts. First, semiconductors must have a conduction band that is at least smaller than the reduction potential of H^+/H_2. The electrons from the semiconductor's band conduction minimum are reduced to H_2 and

transported to H^+ in this manner. Second, the O_2/H_2O reduction potential must be greater than the semiconductor's valence band maximum. The water will then be moved into the hole left in the valence band, oxidizing and forming O_2. The lower region of the conduction band should have a stronger negative potential than that from converting H^+ to H_2 (0 V at pH 0) or higher to increase overall water splitting. In contrast, the oxidation potential of H_2O to O_2 (1.23 V) must be placed higher than the top of the valence band. 1.23eV is the absolute lowest photon energy [40, 41].

1.4. Key parameters in water splitting

In general, charge transfer, active surface sites, and the phenomenon of light absorption are the foundations of photocatalytic hydrogen production. Dopants, dye sensitizers, and defect-related colour centres are all used to increase absorption [42–51]. For instance, Mo-doped BiVO4 and La- and Rh-co-doped SrTiO3 achieve an AQY of 30% (419 nm) [52]. The architecture of the photocatalyst also affects its capacity to absorb light; for example, when photonic crystals have periodic dielectric structures, a higher H2-evolution rate is attained when the absorption edge is shifted to a higher wavelength [53], as the decline in the band-gap is frequently accompanied by a reduction or loss of redox ability. For the development of photocatalytic H2, the properties of the surface-reaction relationships are also essential. The surface H_2 evolution and oxygen evolution overpotentials are linked to the surface charge transfer, surface reaction sites, and surface HER and OER, which can be accelerated by using cocatalysts like Pt. Ti_3C_2 is used as a cocatalyst on CdS to provide a stable H_2-evolution rate of 14342 µmol g-1 h-1 [55]. There have been reports of higher H_2-evolution rates when using a dispersed CoP nanoparticulate cocatalyst than when using noble-metal cocatalysts[54].

1.5. Photocatalytic water splitting catalyst

Honda and Fujishima effectively separated water into H_2 and O_2 in 1972 using TiO_2 as an anode and a platinum as cathode in the presence of ultraviolet irradiations and some external bias[56]. Following this groundbreaking breakthrough, research in this field has been

advancing daily, and many catalysts are being developed to split water in the presence of sunshine to produce H_2 and O_2. Table 1.1 depicts the timeline of several methods for photocatalyst development for water splitting. Oxides, nitrides, oxynitrides, sulfides, selenides, carbides, phosphides, perovskite-type materials, inorganic complexes, layered compounds, etc., are candidates for hydrogen evolution by water splitting. Because of their high band gaps, ZnO, TiO_2, and other materials are said to be active in hydrogen evolution when exposed to UV light.

Table 1. The developments in photocatalyst materials:

Year	Developments using particulate photocatalyst	Strategies to be done
1972	Discovery of photoelectrochemical water splitting by Honda and Fujishima	✓ The catalyst was UV Active (Solar spectrum contribution is only 4%
1979	Z-Scheme model	
1980	Overall water splitting on particulate photocatalyst	
1998	Valence band structure engineering and synthesis of new oxides	
2001	d ^{10} oxides as new photocatalyst group	✓ Lack of suitable visible-light absorbers (45% Solar spectrum) for OWS was the first problem to be overcome
2002	Oxysulfide's and Oxynitrides came into picture	
2005	Overall water splitting on oxynitrides and sulphides	
2009-2014	Z-scheme OWS via solid-state charge transfer, Natural–artificial hybrid Z-scheme OWS system	
2015-2016-2017	OWS on a metal-free semiconductor of C_3N_4 The concept of Plasmon effect came into picture	✓ The design of suitable electronic band structures is the first requirement for the development of such new catalytic substances Structural Factors
2017-2022	Self-assembly of organic compounds	

1.5. A. Semiconductor- composites and heterojunctions

It is evident from the foregoing talks that semiconductor systems ideal for photocatalytic water splitting have band gaps that are properly aligned to the reduction/oxidation potentials of H2O. The catalyst's chemical makeup and electronic band structure impact the material's activity [57]. The use of semiconductor composite photocatalysts for charge separation and light absorption. Carbon-based materials are well-known; composites made of Co3PO4 and TiO2-C have demonstrated higher activity than pure semiconductors[58, 59]. Effective charge separation and electron transfer mechanisms are well-known characteristics of heterojunctions and the Z-scheme [60]. As new O2-evolution photocatalysts, metal oxy-halides as Bi4NbO8Cl and PbBiO2X (X = Cl, Br) are employed. Z-scheme water-splitting systems can be created by combining this catalyst with photocatalysts for H2 production[61]. The H2- and O2-evolution rates of 38.2 and 19.1 mol h1 g1 were observed with a 2D - Fe2O3/g-C3N4 Z-scheme system in clean water[62,63].

The photocatalytic water splitting system in particulate semiconductor systems has two basic types of photoexcitation systems, as shown in Fig. 3. Catalytically active regions for both the hydrogen and oxygen evolution processes are located over a single photocatalyst in a one-step photoexcitation system. Therefore, maintaining the electron transfer mechanism in such a system is difficult (Table 2). Then the two-step method, which utilizes two distinct catalyst sites for water reduction and oxidation, entered the scene. A redox mediator, an electron transfer/electron mediator, was used to link the two catalysts. Redox mediators come in two main varieties: solid and liquid-state redox mediators. The Z-scheme, similar to the natural photosynthesis system, is another name for the two-step photoexcitation process. One of Z-Scheme's benefits is the ability to use various semiconductor types for total water splitting.

Numerous semiconductors are frequently utilized for photocatalytic hydrogen evolution, as shown in Table.1.2.

Table.1.2 The one and two-step photoexcitation system:

Semiconductor		Cocatalyst	Light source	Efficiency
One step photoexcitation				
UV Light				
SrTiO3:Al(<390nm)		$Rh_{2-y}Cr_yO_3$ (Rh 0.1 wt%, Cr 0.1 wt%)	300 W Xe lamp (>300 nm)	AQY: 30% at 360 nm
$NaTaO_3$:La (<300 nm)		0.2 wt% NiO	400 W Hg lamp	AQY: 56% at 270 nm
Visible Light				
TaON (<495 nm)		3 wt% RuOx/2.5 wt% Cr2O3–4 wt% IrO2	450 W Hg lamp (>400 nm	AQY: <0.1% at 420 nm
C3N4 (<442 nm)		3 wt% Pt–1 wt% CoOx	300 W Xe lamp (>420 nm)	AQY: 0.3% at 405 nm
α-Fe2O3/2D g-C3N4		RuO2/Pt	300-W Xe lamp	NA
Two step photoexcitation				
Aqueous redox mediator				
HEP	**OEP**	**Electron mediator**		
0.5 wt% Pt/TiO2 (anatase)	TiO_2 (rutile)	IO^{3-}/I^-	400 W	NA
0.4wt% Pt/SrTiO3:(Cr,Ta)	1wt% PtO_x/WO$_3$	IO^{3-}/I^-	300 W Xe lamp	AQY: 0.1% at 420 nm
Rh@Cr2O3/ZrO2/TaON	CoOx/BiVO$_4$/Au	$[Fe(CN)_6]^{3-/4-}$	300W Xe lamp	AQY: 10% at 420nm
Solid-state electron mediator				
HEP	**OEP**	**Electron mediator**		
1.0wt% Ru/SrTiO3:Rh	BiVO$_4$	NA	300 W Xe lamp	AQY: 1.7% at 420 nm
Ru/Cr2O3/SrTiO3:La,Rh	BiVO$_4$	Au, Rh or Ni	300 W Xe lamp	AQY: 5.9%

According to the literature review mentioned above, several methods for exploiting solar energy to make hydrogen by water splitting have been proposed. Since most semiconductor-based materials are UV-active, more study has been conducted by using the band gap engineering phenomena to alter the electronic properties of semiconductors including ZnO, TiO2, SrTiO3, CuO, and MoO3, among others.[64-84] . The idea of dye sensitization also entered the picture, and researchers who modified semiconductors conducted studies using various dyes including perylene, curcumin, etc. For photocatalytic hydrogen evolution applications, supramolecular self-assemblies of organic dyes are also anticipated as a successful tactic. In spite of this, there are not many large-scale photocatalytic H2 generation facilities due to the boom in material development. The need for extensive light installations in the medium, which would make them uneconomical, is one of the key limitations. Scaling up was challenging because to restrictions in the catalyst forms that can be used to effectively exploit light from an external source. Powder dispersion in the reactant medium is the most widely employed form of catalyst, which instantly introduces the disadvantage of scattering and is more severe in large-scale systems. An alternative study demonstrates the method photocatalyst, which is used in a fixed bed arrangement and immobilised on substrates such thin films. However, these models also preclude the use of direct sunlight by requiring numerous high-energy bulbs to be submerged in the reaction media.

1.6. Role of cocatalyst

In water-splitting processes, the cocatalyst is important. Water splitting requires photocatalytic oxidation and reduction after the photogenerated electrons have reached the surface. As seen in Fig.1.4, a cocatalyst is required to prevent backward reactions. Noble metals, such as Rh, Pt, Pd, Ag, methanol, etc., as well as other types of catalysts are utilised as water reduction and oxidation catalysts to this day[85]. There are also several non-metals that are well-known, such as metal chalcogenides (such CuS, NiS, etc.) [86]. The most effective examples of the

combination of both reduction and oxidation catalysts that has demonstrated promising activity are Pt/C3N4/CoOx and RuOx/Cr2O3/ZrO2/TaON/IrO2 [87,88]. Fig.1.5 summarises the various cocatalyst varieties.
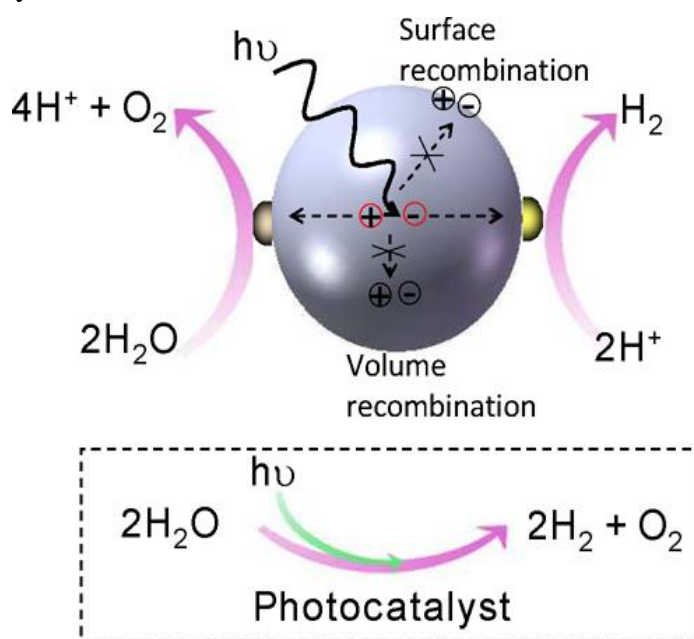
Fig1.4. Schematic description of the functions of cocatalysts adapted from Ref-41
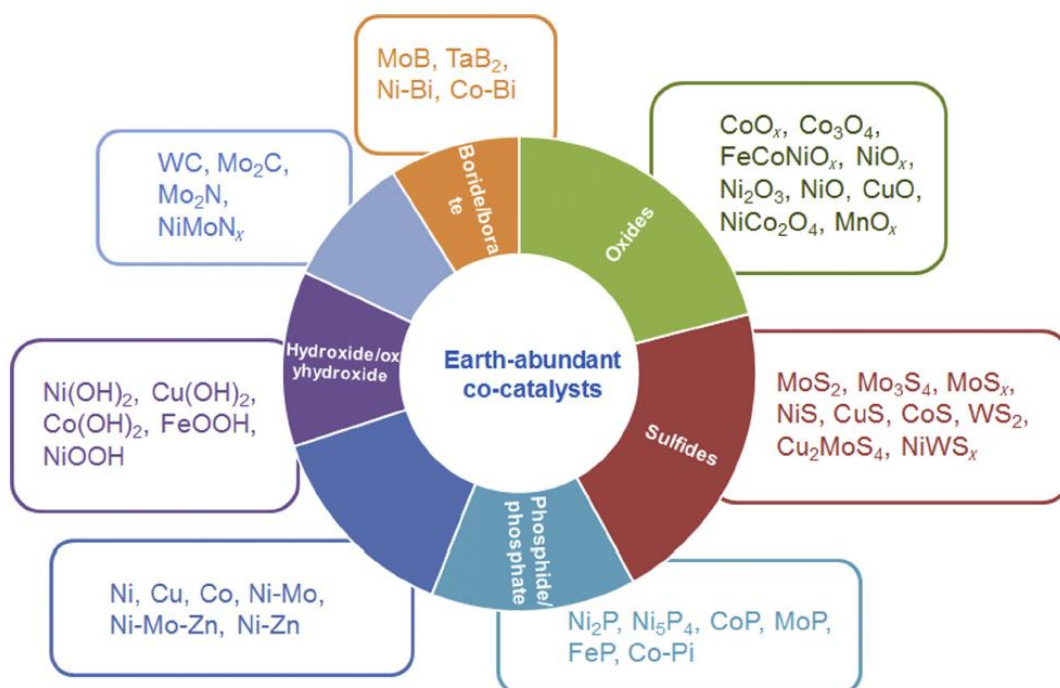
Fig.1.5. Cocatalyst used for photocatalytic water splitting (Adapted from Ref-87)

1.7. Strategies to utilize broader solar spectrum

Under UV light illumination, various metal oxides and other structures have been employed to divide water. However, as the solar spectrum contains more visible and NIR light, more attention should be paid to creating catalysts that absorb in spectral ranges other than UV light. The following techniques should be applied to expand the UV-absorbing photocatalysts' visible light absorption range.

• Band-gap engineering (larger solar energy spectrum)

• Adjusting crystal structure (charge separation and migration), particle size, and other physical characteristics.

• Matching the redox potentials of water oxidation and reduction by band-level engineering

Examples include using elements having oxidation states between d^0 and d^{10} from the d-block of the periodic table and doping it with other elements like metals and non-metals [89,90].
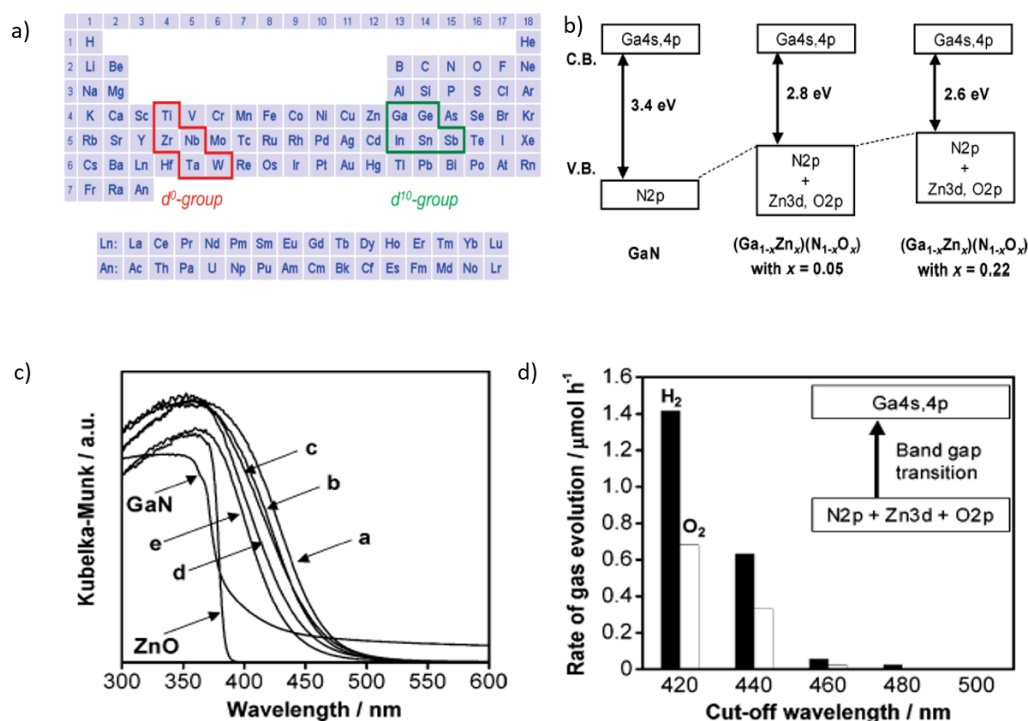
Fig.1.6. a) The Representation of the periodic table b) The example of band gap engineering carried out over GaN and ZnO to make it visible active c) UV-visible diffuse reflectance spectrum for GaN and ZnO d) Photocatalytic H_2 evolution (adapted from Ref.89)

1.7. A. Use of dyes as a sensitizer

Another method is to use dye sensitizers, which have a wider range of absorption than dyes and cause photocatalysts to absorb in the visible spectrum. Wide-bandgap semiconductors may capture visible light using a potent technique called dye sensitization. As photosensitizers, organic pigments have several benefits, including a significant molar extinction coefficient, control over absorption wavelength, ease of design and synthesis, and cheaper cost. There have been reports of effective organic dyes such as coumarin, indoline, phthalocyanine, and conjugated oligoene dyes. This method was first applied in DSSCs, where the dye enters the exited state in the presence of light, causing the creation of excitons at the dye-electrode interfaces and allowing for the transfer of electrons from the dye to semiconductor-based materials. The dye takes on electrons from electrolytes to take on its native form. I3-/I- the system is a commonly utilized electrolyte [91-104]. as shown in Fig.1.7 a. The efficiency of DSSCs depends on how dyes adsorb on semiconductor surfaces. Covalent attachment, electrostatic interactions, donor-acceptor interactions, hydrogen bonds, molecular physisorption, and van der Waals forces are only a few adsorption mechanisms [105-111]. The photocatalytic systems are called dye-sensitized photocatalysts (DSP) because of the analogy with DSSCs. The dye-semiconductor interfaces of the DSP and DSSC are identical. Still, in DSP, photogenerated electrons are moved to the photocatalyst's conduction band to manufacture solar fuel, whereas in DSSCs, they are used for electricity generation. To continue the process in DSP, the oxidized dye molecules must be reduced by an appropriate hole scavenger (Fig.1.7b)[112-116].
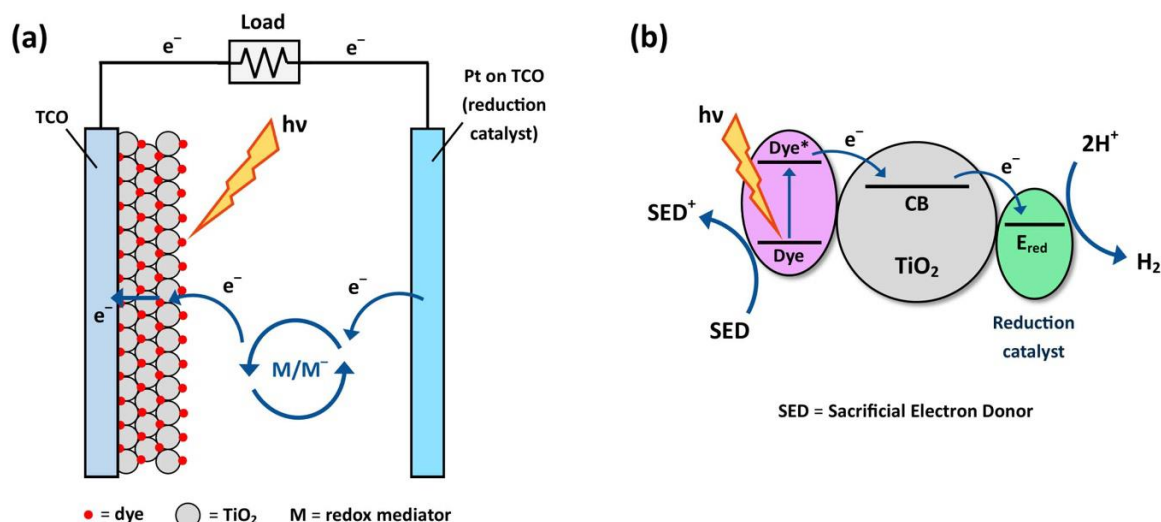
Fig.1.7.Schematic Representation of working mechanism of a) DSSCs and b) DSPs adapted from ref.113

The following qualities must be present in the photosensitizer materials [91]:

I. For charge transfer to the semiconductor to happen more quickly than the decay of electrons from the dye's excited state, the lowest unoccupied molecular orbital (LUMO) of the dye needs to be more negative (higher) than the conduction band (CB) of the semiconductor. Although for the semiconductor to work, it needs to be more negative (higher) than the redox potential of water.

II. It should be stable under thermal, electrochemical, and photocatalytic conditions.

III. The redox potential of the electrolyte should be higher than the dye's highest occupied molecular orbital (HOMO).

IV. It should have anchoring groups that firmly bond to the semiconductor's surface. ((-COOH, $-H_2PO_3$, $-SO_3H$, etc.).

The idea of dye sensitization investigates the various water splitting characteristics of semiconductors. Even yet, there are still a lot of difficulties to be solved, such as their poor scalability, stability, and efficiency. In order to suppress the backward reactions and balance the H2 production activity with dye regeneration, the researcher began to investigate several chemical systems with short conjugation that are simpler to synthesise, broad spectral response, and ultrafast electron transfer.

1.7. B. Supramolecular self-assembly

Self-assembly is the process of creating an ordered structure from previously chaotic parts through localised, specialised interactions without outside guidance. The process is referred to as molecular self-assembly when molecules are the constituent features. Self-assembly has emerged as a key technique for creating a variety of novel organic and inorganic material characteristics. The development of soft materials inspired by biology that can perform light-harvesting, charge-transport, and catalytic tasks to create solar fuels is a notable gap. Self-assembly methodologies for materials, where a bottom-up approach fine-tunes all functional features of a catalytic system, can close this gap [117–121]. By altering the substitution at the imide site, perylene is also reported to be used for visible-light-driven H2-evolution, as seen in Fig.1.8. They were able to achieve a maximum concentration of 11.7 mmol h-1 g-1 with an AQY of 2.96% at 550 nm[122] by using the notion of dipole moment interaction and the electron-withdrawing property of a functional group.

Due to their chemical, thermal, and photochemical stability, strong visible light absorption, fluorescence quantum yields, and low toxicity, the 3, 4, 9, and 10 perylenetetracarboxylic dianhydride (PTCDA) and its derivatives, known as PDIs, have been used in a variety of applications [123,124].

They have been employed in photovoltaics, solar cells, and many other optoelectronic applications due to interactions between the perylene core and the nature of n-type semiconductors[125,126]. To create new electronic materials, PDIs can form organized supramolecular structures that function like semiconductor-organic electronic materials[127]. Numerous studies show how PDIs self-assemble at the imide site and how they are used in diverse applications[128–130].

It has been demonstrated that perylene bisimides can self-assemble to regulate photoconductivity [131–133]. In recent studies, PBIs have been employed as water oxidation catalysts[135], in addition to their previous uses as biosensors, diagnostic nanoprobes, and targeted drug delivery[134]. According to studies, 1D organic materials with nanostructures can be used more effectively in optoelectronic applications[137]. By enhancing the overlap between the electronic wave functions of nearby molecules, such arrangements promote π-π interactions and increase the materials' charge carrier mobility [138,139]. Additionally, they have the ability to construct nanoparticles of variable size and shape[140–144].
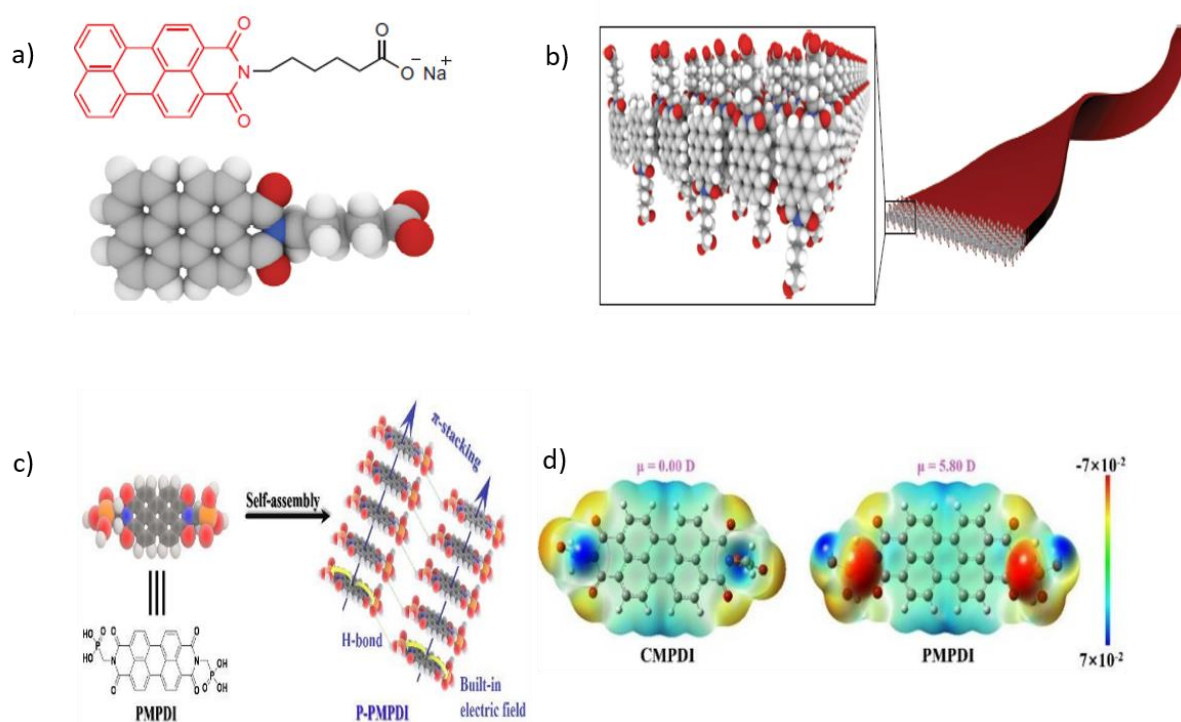
Fig.1.8. a)Molecular structure of perylene moiety, b)schematic representation of perylene moiety to form supramolecular self-assembly (a&b adapted from Ref.121), c) schematic representation of the synthesis of perylene moiety forming self-assembly, and d) diagram of molecular dipoles and electron distribution in PDI derivatives(c &d adapted from Ref.122)

These self-assembled structures of dyes also have certain disadvantages related to photostability and low efficiency towards the photocatalytic hydrogen evolution. These organic structures need to have the presence of a cocatalyst, such as platinum, for the successful

electron transfer process to the water redox potential. Thus, systems become less efficient compared to semiconductor-based systems. Thus these led to the search for innovative ideas to explore this concept of self-assembly by incorporating metal oxide-based semiconductors is needed.

1.8. Subject matter and goal of the thesis

Considering the aforementioned information, the effort attempts to identify several methods for effectively utilizing the solar energy spectrum and improving photon harvesting. The crucial variables include reactor design, ambient conditions, and the stability and scalability of the catalyst and the process. Metal oxides have been chosen to research the broad solar spectrum because ZnO has been used in various applications, including photodetectors, solar cells, gas sensors, and photocatalysis due to its unique optoelectronic characteristics and thermal and chemical stability. The small band gap (3.37eV), which limits the usefulness of the visible spectrum of solar energy, which accounts for around 45% of the solar energy's electromagnetic spectrum, even though it has been used in numerous applications, is one of its limitations. Another is that ZnO has a higher rate of electron-hole recombination, which lowers its effectiveness as a photocatalyst. As a result, to overcome this drawback of ZnO, other structural morphologies and changes through dye sensitization are needed. It is important to learn more about catalytic site separation and how it might be used to photocatalyst layered compounds other than metal oxides, including double hydroxides. The electrochemical evolution of hydrogen has previously been investigated using layered double hydroxides (LDHs). However, there is still a need for greater investigation into photocatalytic hydrogen evolution. Anions in the hydrated interlayer galleries can counteract the positive charges in the host layer. Due to the host layer's broad tunability and the ion-exchangeable properties of the interlayer guest ions, LDHs are a diverse family of materials. Due to multiple efforts to enhance the composition and usefulness of LDHs and LDH-based products, LDH usage has also

expanded. Assume that the LDHs modified with organic sensitizers can improve the optical characteristics and aid in the creation of hydrogen. One can consider using optical fibers to overcome the drawbacks of light scattering, which demonstrates the phenomena of complete internal reflection. Optical fibers offer a continuous flow immobilized model several advantages.

On the basis of these, the further works in the current thesis have been completed.

1. The synthesis of various ZnO morphologies and their characterization in this section focus on applying ZnO nanostructures in photocatalytic H2 evolution.

2. Synthesis and characterizations of ZnO-Perylene (ZnO-P) heterostructures and its application in photocatalytic H_2 evolution, here more emphasis is given to understanding the optical and morphological changes in the structure of ZnO-P and its application in H_2 evolution

3. Synthesis and characterizations α-Co(OH)$_2$-PDI and its application in photocatalytic H_2 evolution, this part focuses on the synthesis of cobalt layered double hydroxides and its sensitization by using perylene dye

4. Study of total internal reflection phenomenon in optical fiber coated with semiconductor-based materials, mainly xCuO/TiO$_2$, for the complete utilization of visible light for the application in photocatalytic H_2 evolution

1.9. Reference

1. Lewis, N. S et al., *Natl. Acad. Sci, U. S. A*. **2006**, *103*, 15729.

2. "Fossil fuel". *ScienceDaily*. Retrieved 29 October 2021.

3. Joseph E. Fleckenstein., Three-phase electrical power, CRC Press, Boca Raton, **2016**, OCLC 958799795, P.58.Bockris, et al., *Int. J. Hydrogen Energ,* **2002**, *27*, 731.

4. Bard, A. J.et al., *Acc. Chem. Res,* **1995**, *28*, 141.

5. Muradov N.,*Int.J.Hydrog.Energy*,**2017**;42:14058–88.

6. Chu S, Majumdar A., *Nature* ,**2012**;488:294–303.

7. Wang M.,J.Power Sources ,**2002**;112:307–21.

8. Yun Zhao et al., *Langmuir* **2022**, 38, 8719−8732

9. https://www.goodenergy.co.uk/how-do-solar-panels-work/

10. Jin Hyun Kim et al.,*Nat. Commun* **2016**, 7, 13380

11. Chu, S.et al, *nature,* **2012**, *488*, 295.

12. Florin, N.et al, *Environmentalist,* **2007**, *27*, 207.

13. A review: Solar cell current scenario and future trends by Recent Research in Science and Technology, **2012**.,4(8): 99-101, ISSN: 2076-5061.

14. S.Dunn et al., *Int. J. Hydrog. Energy,* **2002**, 27, 235–264

15. K. Chouhan et al., Int. J. Hydrog. Energy,**2021**, 46, 26809-26824.

16. M. Balat et al., Int. J. Hydrog. Energy,**2009,**34**,** 3589–3603

17. N. Sanchez et al., Int. J. Hydrog. Energy,**2020,** 45, 11923-11942

18. NZ. Muradov et al., Int. J. Hydrog. Energy,**2005**,30,225-237.

19. R. Rozendal et al., Environ. Sci. Technol. **2008**, 42, 629–634

20. N. Savla et al., Microorganisms for Sustainable Environment and Health, **2020**,343-365

21. A.Stephen et al., Microb. Biotechnol. **2017**,19,1120-1127.

22. Rajeshwar, K.,et al., *Springer Science*, **2008**.

23. Fujishima A, Honda K. *Nature* **1972**;238:37–8.

24. Chen S et al., *Nat. Rev. Mater.* **2017**;2:1–17.

25. Liu R et al .,Int. J.Hydrog. Energy **2021**;46:28462–73.

26. Ahmad H et al., *Renew. Sust. Energ. Rev.* **2015**;43:599–610.

27. Fajrina N et al., *Int. J.Hydrog. Energy* **2018**;44:540-577.

28. Zhu J et al *Curr Opin Colloid Interface Sci* **2009**;14:260–9.

29. Abouelela MM et al., *J. Clean. Prod.* **2021**;294:126200.

30. Chauhan DK et al., *J. Clean. Prod.***2021**;307:127162.

31. Almomani F et al., *Int. J.Hydrog. Energy* **2022**;47:3294–305.

32. Li Q et al., *Energy Fuels* **2022**;36:4541-4548.

33. Gupta NM.*Int.J.Hydrog.Energy.***2017**;71:585–601.

34. Idriss H. *Energy Technol.* **2021**;9:2000843.

35. Anta JA et al., *Chem Soc Rev.* **2022**:3794–818.

36. Narendranath SB et al., ACS *Appl. Mater. Interfaces.* **2014**;6:12321–7.

37. Qian Wang et al,*Faraday Discuss* **2017**, 198, 11–35

38. Jin Hyun Kim et al., *Chem. Soc. Rev*., **2019**;48, 1908-1971.

39. Hao Lyu et al., *Chem. Sci*., **2019**, 10, 3196–3201

40. Kazuhiko Maeda and Kazunari Domen., *J. Phys. Chem. C* **2007**, 111, 7851-7861

41. Yang et al., *Acc. Chem. Res.***2013,** 46, 1900–1909.

42. H. Zhang et al. *J. Catal*. **2018**, 359, 112–121.

43. V. Kumaravel et al. *Appl. Catal. B.,2019, 244, 1021–1064*

44. D. Kim and K. Yong, *Appl. Catal. B.***2021**,282, 119538

45. A. Mukherji et al., *J. Phys. Chem. C* **2011**, 115, 15674–15678

46. P.Gomathisankar et al., *ACS Sustainable Chem. Eng.* **2013**, 1, 982−988

47. M. Watanabe et al., *ACS Appl. Energy Mater*. **2018**, 1, 6072−6081

48. H.Lai et al .,*ACS Omega* **2020**, 5, 2027−2033

49. P. Chowdhury et al., *Inorganics* **2017**, 5, 34

50. L. Zani et al., *J. Phys. Energy* **2021**,3, 031001

51. Hu.W. et al,. *J. Am. Chem. Soc*, **2017**,139, 15429–15436

52. Wang. Q. et al. *Nat. Mater*, **2016**,15, 611–615

53. Kshirodra K. Patra et al., *ChemCatChem*, **2016**, 8, 3294 – 3301

54. Cao. S. et al ,*Joule* ,**2018**,2, 549–557

55. J. Ran et al., *Nat. Commun.* **2017***,* 8**,** 13907

56. Fujishima, A.; Honda, K., *Nature* ,**1972**, *238,* 37.

57. Chen, S.S. et al. *Nat. Rev. Mater***, 2017,** 2, 17050

58. Si, Y. et al. *Nano Energy*, **2017**. 41, 488–493

59. Yang, Y. et al. *Nano Energy* , **2017,**33, 29–36

60. Zhu, M. et al,. *J. Colloid Interface Sci*, **2018 ,** 530, 256–263

61. Xiao, M. et al. *Adv. Mater,* **2018**, 30, 1705193-1705202

62. Suzuki, H. et al.*Chem. Mater,***2018,** 30, 5862–5869

63. Takashi Hisatomi et al., *Catal Lett*, **2015**, 145,95–108

64. N. Alhokbany et al., *Catalysts* **2022**, 12, 530

65. S. Kumar et al., *Catalysis Reviews*, **2019**,62, 346-405

66. Y.R. Girish et **al.**, *J. Hazard. Mater.*2023,9,100230

67. T. N. Quynh et al., *ACS Appl. Mater. Interfaces.* **2020**, 12, 12195−12206

68. Aiping Wu et al., *Sci. Rep.* **2015**, 5, 8858

69. C. Belabed et al., Int. J. Hydrog. Energy,**2021**, 4 6 ,17106 -17115

70. R. Khokhra et al., Sci. Rep., 2017. 1-14

71. Anta, J.A et al., *J. Phys. Chem. C* **2012**, *116*, 11413–44425

72. J. Chang *Sensors* **2013**, *13*, 8445-8460

73. Ouyang, G et al., *ACS Appl. Mater. Interfaces* **2012**, *4*, 210–213

74. Li-Ting Chen et al., *Langmuir* **2018**, 34, 5030−5039

75. Height, M. J et al., *Appl. Catal. B* **2006**, 63, 305−312

76. Guo, M. Y et al., *J. Alloys Compd*. **2011**, 509, 1328−1332

77. Wang, Z et al.*, Langmuir* **2017**,33, 12276−12284

78. Wang, X et al., *ACS Appl. Mater. Interfaces* **2012**, *4*, 817–825

79. Xiao, Y et al., *ACS Appl. Mater. Interfaces* **2012**, *4*, 3797–3804

80. Yuanhui Zheng et al., *Inorganic Chemistry*,**2007**, 46,17

81. K. Byrappa, J Mater Sci ,**2008**, 43,2348–2355

82. T. Yoshida et al., *Chem. Mater.* **1999,** *11,* 2657-2667

83. T. Yoshida et al., *Chemistry letters* 1998

84. V.B. Kumar et al.,*J. Mater. Chem. B,* **2014**, 2, 3956–3964

85. Cao. S. et al. *ChemSusChem,* **2017**, 10, 4306–4323

86. Li. X. et al., *J. Mater. Chem. A,* **2015,**3, 2485–2534

87. Chen.S.S. et al., *Nat. Rev. Mater,***2017** , 2, 17050

88. Shuang Cao et al.,*Trends in Chemistry*, **2019**, 1-14

89. Kazuhiko Maeda et al.,J. Phys. Chem. B., **2005**, 109, 20504-20510

90. K. Qanugo et al., *E3S Web of Conferences* **2021**,309, 01032

91. K. Hara et al., *J. Phys. Chem. B*.**2005**, 109, 15476

92. K. Hara et al., *J. Phys. Chem. B*. **2003**, 107, 597

93. D. P. Hagberg et al., *Chem. Commun*. **2006**, 2245-2247

94. W. Zhang et al., *J. Am. Chem.Soc*. **2011**, 133, 20680−20683

95. T. Funaki et al., *Angew. Chem. Int. Ed.***2012**,51, 7528 –7531

96. J. Zhanga et al., *Phys. Chem. Chem. Phys.* **2014**, 16, 8655--8660

97. B. O'Regan and Michael Grtazel., *Nature*.**1991**,404,737

98. A. Hagfeldt et al., *Chem. Rev.* **2010**, 110, 11, 6595–6663

99. Takeo Shimidzu et al., *J. Am. Chem. Soc*.**1985**, 107, 1-4

100. Ryu Abe et al., *J. Am. Chem. Soc.* **2013**, 135, 45, 16872–16884

101. P. Roy et al., *Nanoscale*, **2010**, 2, 45–59

102. K. G. Reddy et al., *Phys. Chem. Chem. Phys*. **2014**, 16, 6838—6858

103. X. Yang et al., *Energy Environ. Sci*., **2013**, 6, 54–66

104. X. Wang et al., *Nano Research* **2016**, 9, 2862–2874

105. T. Suresh et al., *RSC Adv*. **2016**, 6, 26559–26567

106. P. Pechy et al., *J. Chem.Soc. Chem.Commun.* **1995**, 65-66

107. Md. K. Nazeeruddin et al*., J. Phys. Chem. B*, **2003**, 107, 34, 8981–8987

108. K. Kalyanasundaram and M. Gra¨tzel., *Coord. Chem. Rev*. **1998**,177,347-414

109. Leena George,et al., *J. Phys. Chem. C* ,**2015**, 119, 3060−3067

110. Lei Zhang and Jacqueline M. Cole., *ACS Appl. Mater. Interfaces* **2015**, 7, 3427−3455

111. Yuan, Y.J. et al.. *Chem. Soc. Rev*, **2017**., 46, 603–631

112. X. Zhang et al *J. Mater. Chem. A*. **2016**,4, 2365

113. L. Zani et al *J. Phys. Energy*. **2021,** 3,031001

114. S. Min and G. Lu, *J. Phys. Chem. C* **2011**, 115, 13938–13945

115. H. Bao et al., *RSC Adv*., **2021**, 11, 32671–32679

116. K. L.V. Joseph et al., *J. Mater. Chem. A*, **2015**, 3, 232–239

117.   C. Li and H. Wonneberger, *Adv. Mater*, **2012**, 24, 613–636.23

118. T. Abe, Y. Tanno, N. Taira and K. Nagai, *RSC Adv*, **2015,** 5,46325–46329.

119. J. Raeburn, A. Zamith Cardoso and D. J. Adams, *Chem. Soc.Rev*, **2013**, 42, 5143–5156.

120. Stupp, S. I. et al.,*Science,* **2012**,335, 813–817 .

121. Würthner, F.et al., *Chem. Commun,* **2004**, 1564−1579.

122. Kangyi Kongetal.,et al., *Chem. Commun,* **2019,**55, 8090-8093

123. Demmig, S.; et al.,. *Chem. Ber,* **1988**, 121, 225−230.

124. Liu X F et al ., *J. Phys. Chem. B* , **2008** ,112 10778

125. Yan Sun et al., *RSC Ad,* **2017,** 7, 24215–24220

126. Zhao. Y.et al., *Mater,* **2007**, 19, 3554–3558

127. A. S. Weingarten et al., *Nature Chemistry*, **2016,** 6, 964-970,

128. Roman V. Kazantsev et al., *J. Am. Chem. Soc*, **2017**, 139, 6120−6127

129. Soichiro Ogi et al., *J. Am. Chem. Soc,* **2015**, 137, 3300−3307

130. Chen. K. et al ., *Tetrahedron Lett,* 2010, 51, 5959–5963

131. Zhou. J. *et al*. *Langmuir,***2012** ,28, 14386–14394 2012.

132. Draper et al., C*ellpress,* **2017**, 716–731

133. Mei Li et al., *Dyes and Pigments,* **2017,** 139 , 79-86

134. Partha Bairi et al., *RSC Advances*, **2012**, 2, 264–272

135. L. Schmidt-Mende et al*., Science,* **2001**, 293, 1119–1122.

136. M. D. Curtis et al., *J. Am. Chem. Soc*, **2004**,126, 4318–4328.

137. A. N. Aleshin et al ., *Adv. Mater***, 2006,** 18, 17–27.

138. Wei Zhang et al ., *RSC Adv,* **2015,** 5, 2207–2212

139. Jia-Xin Li et al., *Catal. Sci. Technol*,**2016**,6, 672

140. Liu X F et al., Langmuir, **2008**, 24, 11967

141. Maye M M et al., *J. Am. Chem. Soc*, **2003**, 125 9906

142. Srivastava S et al., *Chem. Mater*, **2005,**17 487

143. Huang H Y et al., *J. Phys. Chem. B*, **2005**,109, 24288

144. Lin S et al., *Adv. Mater*, 17, 2553

Chapter 2

Synthesis and characterizations of ZnO nanostructures and their application in photocatalytic hydrogen evolution

2.1. Introduction

Due to their unique optical and transport characteristics, semiconductor compounds have drawn a lot of attention in recent years. Due to its numerous optoelectronic features, thermal stability, and chemical resistance, ZnO is one of the best type-II-IV semiconductor materials. It has been employed in numerous applications, including photodetectors [1,2], solar cells [3,], gas sensors [4,], LED [5,], and photocatalysis [6-9]. Its direct band gap, 3.37 eV, demonstrates the solar spectrum's UV absorption. Since ZnO has greater electron mobility and is more affordable than TiO2, it can exhibit equivalent to or more activity than TiO2[10–13].

Depending on the synthesis technique, ZnO can be nanorods, nanoflowers, nanotubes, nanocubes, nanoparticles, etc. For various applications, ZnO porous structures can be 0D, 1D, 2D, or 3D, with a greater surface area and more active sites [14–20]. A high specific surface area is crucial to the function of a catalyst. Greater surface area ZnO hollow spheres than commercial ZnO exhibited stronger photocatalytic activity. However, improved surface areas of the catalysts did not improve catalytic performance in subsequent investigations. According to the literature, differences in photocatalytic activity depend on the kind and quantity of oxygen vacancies on the surface and surface adsorption capacity [21–27]. Understanding the connection between a material's structure and function concerning different applications.[28]. With alternate tetrahedrally coordinated O2- and Zn2+ ion planes along the c-axis, ZnO is a polar crystal. A ZnO is made up of negatively charged (000 1) oxygen planes, (0 1̅10) nonpolar planes, and (000̅1) positively charged Zn terminated planes [29]. Because of its simplicity, hydrothermal synthesis is one of many techniques investigated for the synthesis of ZnO. Applying the hydrothermal method, ZnO tends to build various structures with varied morphologies [30–33]. Different surfactants can be used to modify the crystal growth behavior

on the polar crystals' planes. Different morphologies of ZnO have been synthesized using surfactants such as CTAB, polyacrylamide, citrate ions, HMT, and polymers[34–40].

Here we have explored the synthesis of different morphologies of ZnO by using different methods and their characterizations by using different techniques and applications in photocatalytic H_2 production via water splitting.

2.2. Experimental Section

2.2.1. Synthesis

2.2.1. Synthesis of ZnO

2.2.1.1. Synthesis of ZnO Nanoparticles(15-35nm)

Sol-gel Method

Sol-gel synthesis was used to create ZnO NPs. At 60 °C, ethanol (144 mL) was used to dissolve zinc acetate dihydrate ($Zn(OAc)_2.2H_2O$) (0.02389 mol), which took around 30 min. At 50 °C, ethanol (98 mL) was dissolved in oxalic acid dihydrate (0.04878 mol). The heated ethanolic zinc acetate solution was stirred as the oxalic acid solution was gradually added. A thick, white gel developed and was allowed to dry for 20 hours at 80 °C. ZnO NPs with a 20–30 nm size range were produced by calcining the gel at 400 °C for two hours.

2.2.1.2. Synthesis of ZnO Nanoparticles (5-11nm)

Precipitation Method

The precipitation method was applied to smaller nanoparticles (5–11 nm). Refluxing KOH (56 mM, 75 mL) in methanol for 30 min at 60 °C was a typical procedure. In a different reaction mixture, methanol was stirred at room temperature to produce $Zn(OAc)_2.2H_2O$ (56 mM, 25

mL). The dissolved zinc acetate solution was then added dropwise through an addition funnel while the refluxing KOH solution was being aggressively agitated. The answer was evident as soon as ZnO NPs started to form.

2.2.1.3. Synthesis of ZnO Nanorods (20-30nm)

Hydrothermal Method

The diverse morphologies of ZnO were created using the hydrothermal technique. Typically, the solvent was used to dissolve the zinc precursor, the mixture was agitated for varied lengths of time, then put into a 100ml Teflon-lined autoclave and heated to 150°C for 24 h. The autoclave was left to cool when the reaction was finished. After that, the reaction was cleaned with a centrifuge at 14,000 rpm, washed numerous times with water and ethanol, and dried for 24 h at 80 °C. In Table 2.1, the specifics of the synthesis conditions are listed. For instance. For HTZNR1, 50 ml of ethanol was used to dissolve 14 g of sodium hydroxide (NaOH) and 7.435 g of zinc nitrate (Zn $(NO_3)2.6H_2O$). After stirring for 30 min, 10ml of each solution was combined with 20ml of ethanol. Zinc acetate (Zn $(OAc)_2.2H_2O$) was also utilised as a starting material to examine the impact of the zinc source on the finished product, and the influence of the solvent was examined using water and ethanol.

Table. 2.1. Hydrothermal reaction conditions with sample notation

Sr.No.	Sample Name	Reaction Conditions
1	HTZNR1	Zinc nitrate +Ethanol +NaOH (30min Stirring)
2	HTZNR2	Zinc nitrate +Ethanol +NaOH (4h Stirring)
3	HTZNR3	Zinc acetate +Water (0.05M)
4	HTZNR4	Zinc acetate +Water (0.5M)
5	HTZNR5	Zinc acetate +Ethanol + Water (2h stirring)

2.3. Material characterizations

FEI Nova Nano SEM 450 FE-SEM instrument characterized the structure and morphology of as-synthesized material. EDS elemental mapping was done on Quanta 200 3D FEI with the help of TEM EDS analysis system analysis was carried out on FEI, TECNAI G2 F20 transmission electron microscopy (TEM) instrument (conditions: accelerated voltage = S-5 200 kV, and resolution = 0.17 nm). Samples were prepared by sonication. The material thus collected was dispersed in ethanol and drop cast on 200 mesh carbon grids for TEM analysis. Powder x-ray diffraction (XRD) of all the samples was carried out in a PANalytical X'pert Pro dual goniometer diffractometer working under 40kV and 30mA. The radiation used was Cu Kα (1.5418Å) with a Ni filter, and the data collection was carried out using a flat holder in Bragg−Brentano geometry with a 1° slit at the source and receiving sides. The diffuse reflectance and absorbance UV−visible spectra were recorded on a Cary series UV−vis−NIR spectrometer in the 200−800nm wavelength range with $BaSO_4$ as a reference sample. Photoluminescence measurements were done using a Photon Technology International fluorescence QM-40 spectrophotometer at 325nm excitation wavelength. Time-resolved fluorescence lifetime measurements were performed using a HORIBA Jobin Yvon Fluorolog 3 fluorescence spectrophotometer. For lifetime measurements, decay curves were obtained by the time-correlated single-photon counting (TCSPC) technique using a HORIBA Jobin Yvon Nano-LED source with wavelengths 320 and 450 nm. Decay measurements were carried out at an excitonic emission of 380 nm and a defect emission of 520 nm. All experiments were performed under identical conditions. Fluorescence lifetime values were determined by deconvoluting the data with exponential decay using DAS6 decay analysis software. The fit quality was judged by fitting parameters such as χ^2 and the visual inspection of the residuals. The surface states of the samples were analyzed by X-ray photoelectron spectroscopy (XPS) in a K-Apha+ Thermo Fischer Scientific (UK) instrument with an Al Kα source. XPS peaks of the compounds were fitted with Shirley type background subtraction method using XPS PEAK41 software. The data were corrected with the standardized peak for carbon at 284.8 eV. The HPLC used is the Agilent HPLC Column H^+ monosaccharides column which has a mobile phase 5mM H_2SO_4 column, the temperature at 30°C, and refractive index detector (RID). In Appendix 2a, all the characterisation approaches employed throughout the paper are briefly reviewed together with their underlying ideas and instruments.

2.4. Electrochemical measurements

The electrochemical characterizations were completed using the CH Instrument CHI660D electrochemical workstation, which features three electrode configurations. This thesis work's chapters are all run in the same environment. The substance of interest is coated on the working electrode, a glassy carbon electrode with a surface area of 0.0706 cm^2. After making the paste using 1 mg of the sample, 500 µl of methanol, and 10 µl of 5% Naffion, it was processed using ultrasonography for 30 minutes to completely disperse the catalyst and create the slurry, which was then suitable for coating the electrode. The 10 µl slurry sample was then dropped over the glassy carbon electrode, dried under an infrared lamp, and then electrochemically analyzed. A reference electrode of Ag/AgCl and a counter electrode of Pt wire were used in the electrochemical testing at a scan rate of 50 mV s-1. Acetonitrile has LiClO$_4$ as the supporting electrolyte. The 450W Hg lamp was positioned in front of the three-electrode setup during the light-induced CV testing. (Fig.2.1)
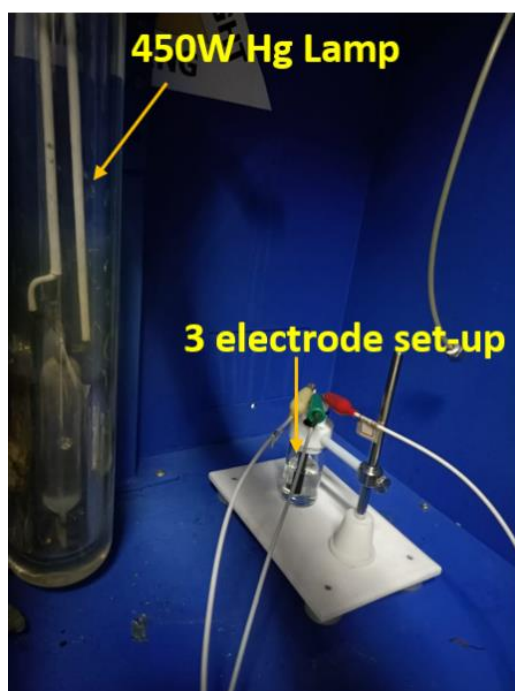
Fig.2.1.Experimental setup for the light-induced CV experiments

2.5. Photocatalytic activity

The photocatalytic process was conducted at room temperature in a 70 ml airtight quartz cell with a silicone rubber septum on top. The catalyst was first sonicated for 15 minutes with various sacrificial reagents and water concertations. For visible light irradiation, a high-pressure 450W Hg lamp with water-circulating Pyrex jackets (supplied by Lelesil Innovative Systems, Maharashtra) was employed as the light source (Emission spectrum shown in Fig. 2.2).
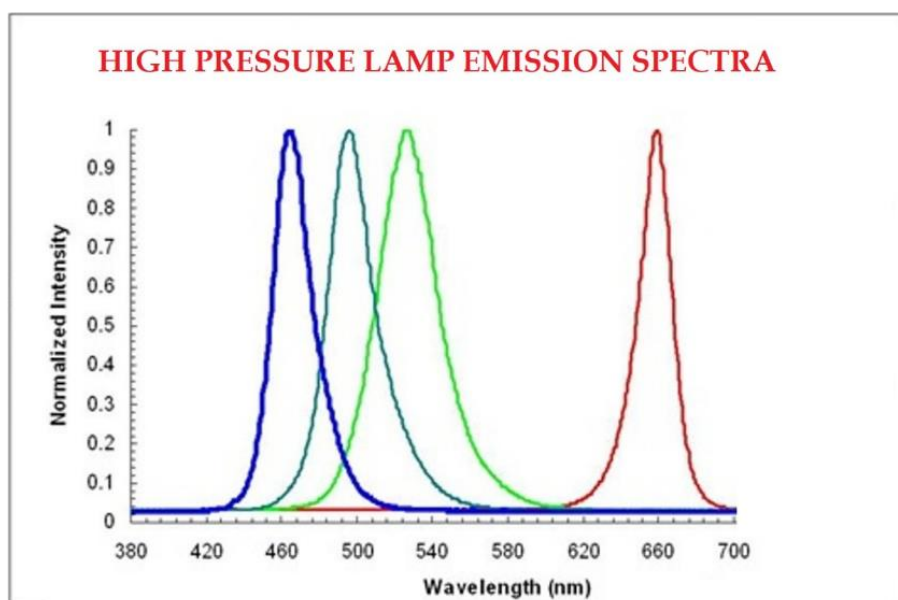
Fig.2.2. Emission spectrum of the used lamp as provided by the vendor, Lelesil Innovative Systems.

The direct sunlight tests were also conducted there on the terrace with full midday exposure, using the identical gas-tight irradiation cell. The amount of H2 evolved was determined using gas chromatography (5700 Nucon gas chromatograph with Carbosphere column and Ar as carrier gas) and a thermal conductivity detector. At the moment of injection, the GC program employed an oven temperature of 50°C and a detector temperature of 100 °C for all analyses.

A 500 µL gas phase syringe was used to inject samples into the reactor's headspace on a regular basis. A variety of times were used to conduct the experiment (Figs. 2.3 and 4)..
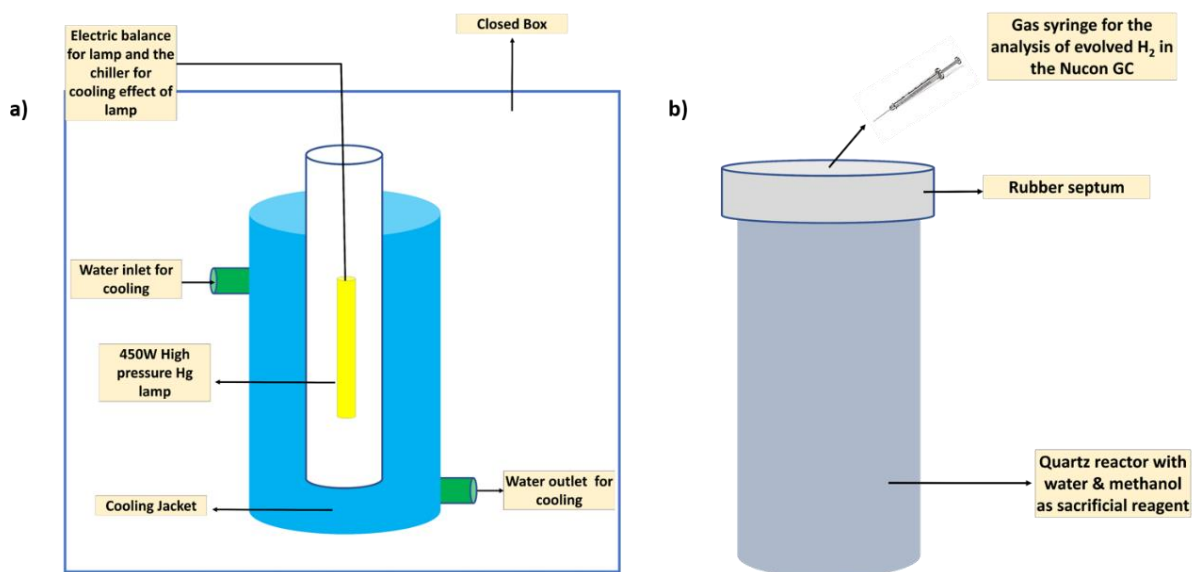
Fig.2.3. Reactor Design for the photocatalytic H_2 evolution a) Photochemical reactor with 450W Hg lamp and cooling jacket b) Quartz reactor with rubber septum with a syringe

Fig.2.4. The photographic image of the photochemical reactor

2.6. Results and Discussion

P-XRD analysis of the samples' crystal structures revealed that ZnO formed into a hexagonal wurtzite structure, matching JCPDS No.01-079-0206 without any impurity phases in the case of HTZNR 1-4 (Fig. 2.5. a). The peaks with relative intensities of (100), (002), and (101) are discovered to differ in each of the four samples. HTZNR5, which was made using an acetate precursor, exhibited an intense diffraction peak at a low diffraction angle of 11.69 °, which is a typical feature of a layered compound with wide interlayer spacing, which corresponds to JCPDS No.01-071-2215 (Fig. 2.5 b), demonstrates the production of orthogonal zinc hydroxide. The samples made using zinc nitrate precursor (HTZNR1-4) under the same circumstances did not yield a comparable layered phase. This finding demonstrates how varied zinc acetate and zinc nitrate behaviors during the synthesis process result in ZnO nanostructures with various shapes.
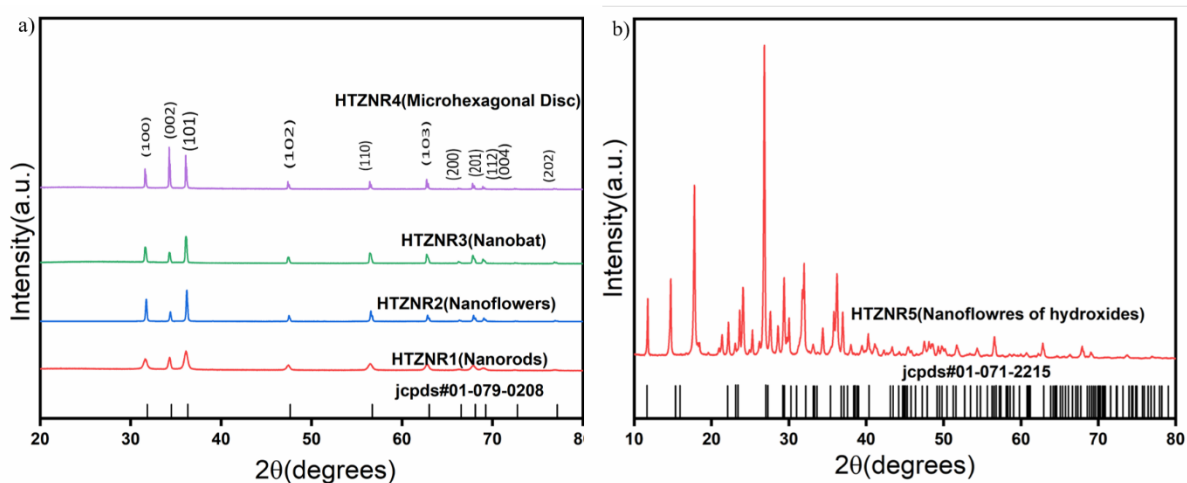
Fig.2.5. P-XRD pattern of a) HTZNR1, HTZNR2, HTZNR3 and HTZNR4 b) HTZNR5
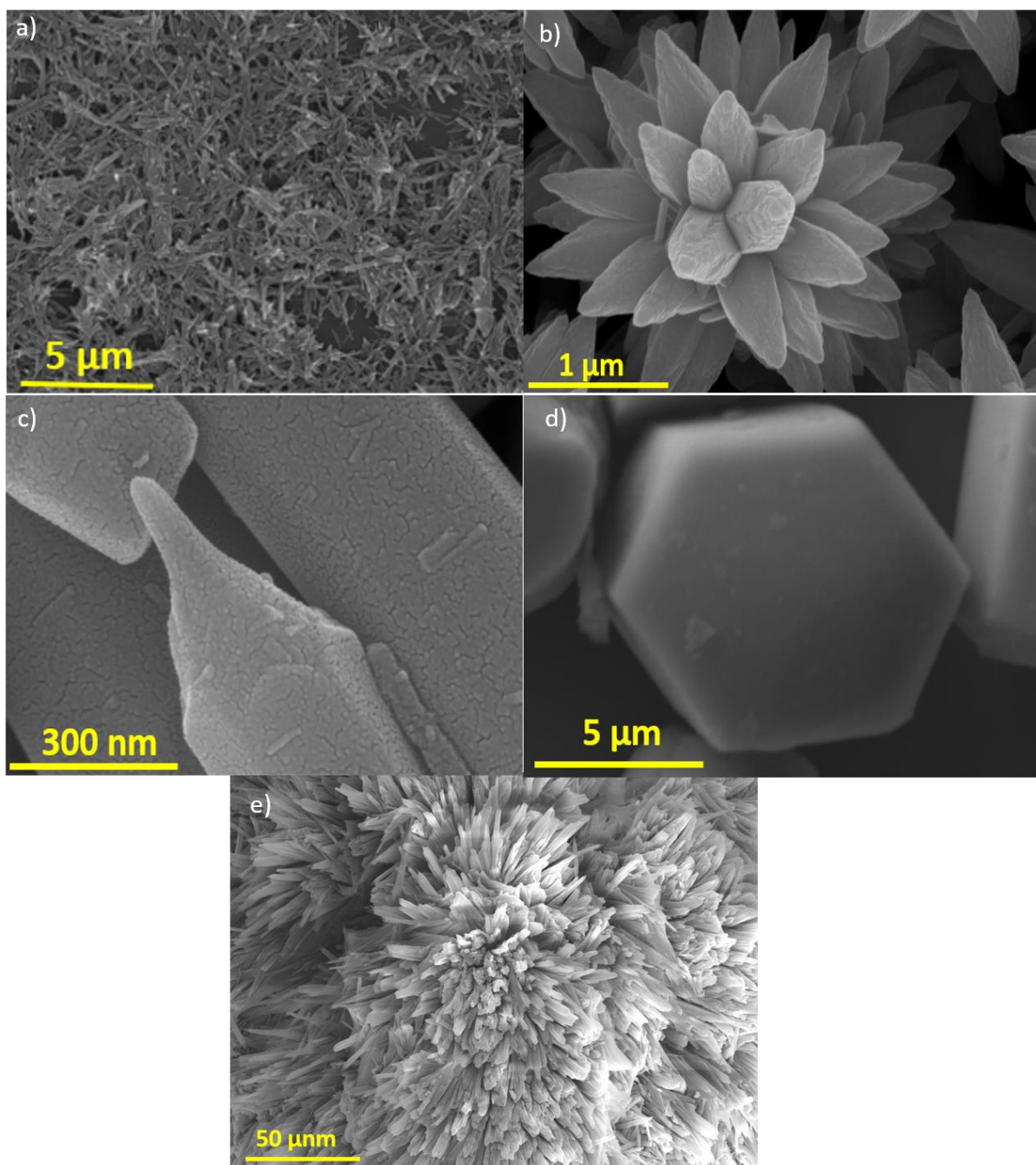
Fig.2.6. FE-SEM images of a) HTZNR1b) HTZNR2 c) HTZNR3 d) HTZNR4 and e) HTZNR5

Figure 2.6 displays FE-SEM images of each ZnO nanostructure.Their morphologies are clearly very different from one another. ZnO nanorods are uniformly dispersed in the HTZNR1, where

the reaction mixture was agitated for 30 minutes before being transferred to the Teflon autoclave (Fig. 2.6a). In the instance of HTZNR2, longer stirring time was given to HTZNR1 for 4h instead of 30min, causing the nanorods to clump together and form bouquets of ZnO nanorods (Fig. 2.6b) without altering the ZnO crystal structure. The zinc nitrate precursor has been employed in HTZNR1 and HTZNR2. When the precursor transforms into zinc acetate, distinct ZnO morphologies are produced for HTZNR3, where only water and zinc acetate (0.05M) are employed to produce the nanobat morphology for ZnO (Fig. 2.6c). The creation of the micro hexagonal disc of ZnO with the uniformly dispersed hexagonal-shaped structure for ZnO occurs with a concentration increase to 0.5M. The P-XRD pattern showed an increase in intensity along the (002) plane, indicating that the Zinc acetated favored the growth along the 001 direction and that this preference increased development along the (002) plane (Fig. 2.6d and Fig. 2.5b). In HTZNR5(Fig. 2.6e), which used zinc acetate precursor, ethanol, and water, nanoflowers of ZnO hydroxides developed. This morphology [41-43] is produced in this instance by the interaction of ethanol and water, which produces extra hydroxyl groups. The ZnO NRs are structurally homogeneous and free of flaws such as dislocations or stacking, as seen by the HRTEM picture and selective area electron diffraction (SAED) pattern (Fig.2.7).
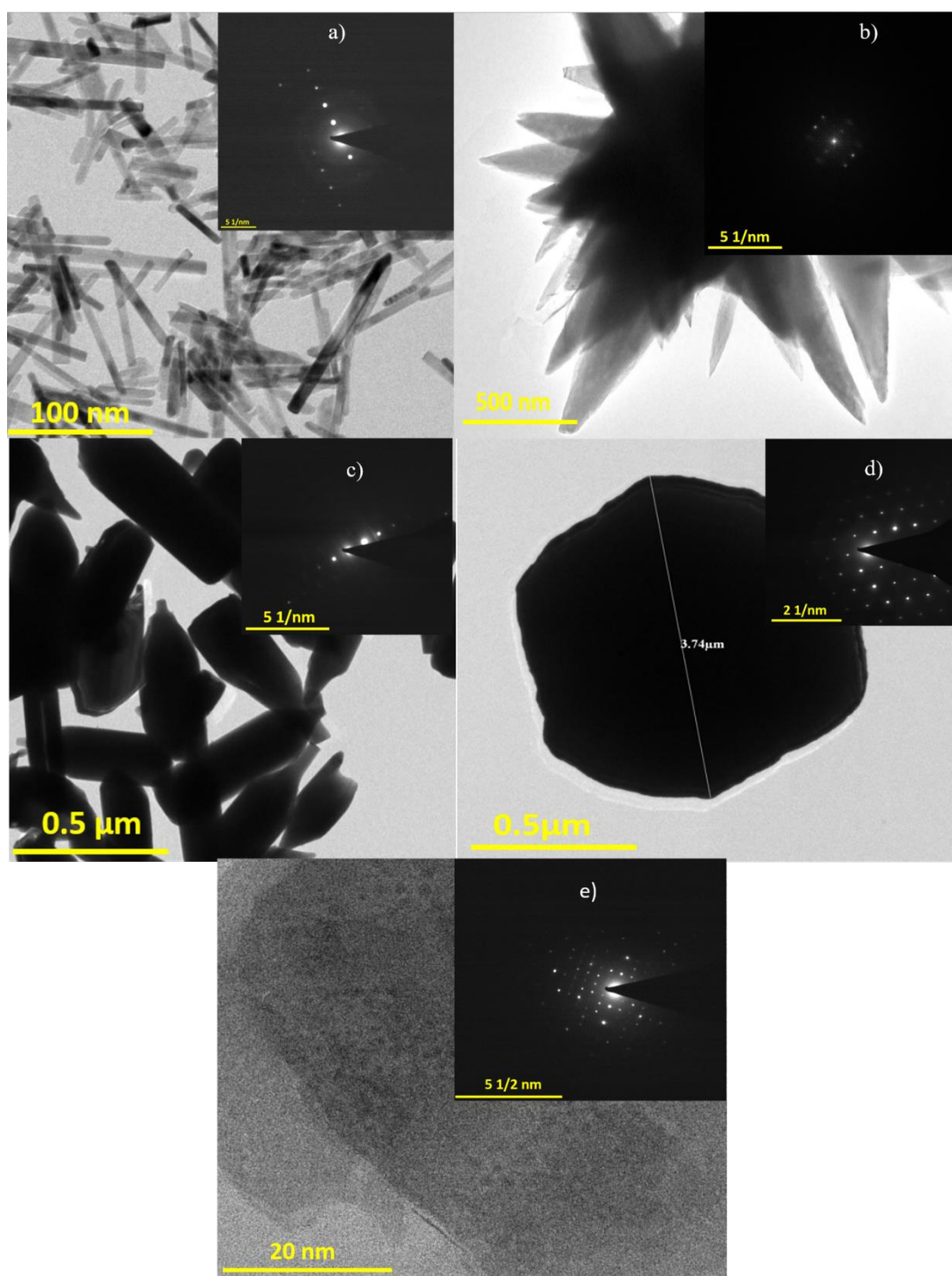
Fig.2.7. TEM images (an inset shows SAED pattern) of a) HTZNR1, b) HTZNR2, c)

HTZNR3, d) HTZNR4, and e) HTZNR5

Once the structural characterization is done, the photocatalytic hydrogen evolution is carried

out using the photocatalytic reactor setup explained in section 2.5. Fig.2.8. Shows the

photocatalytic H_2 evolution activity. Activity is 290µmol/h and 250 µmol/h for HTZNR1 and

HTZNR5, respectively. Other morphologies show lesser activities compared to these two. As mentioned earlier, the HTZNR5 is the form of hydroxide. Under illumination, it completely degrades after 4h of irradiation and thus cannot be used for further studies of H_2 evolution activity.
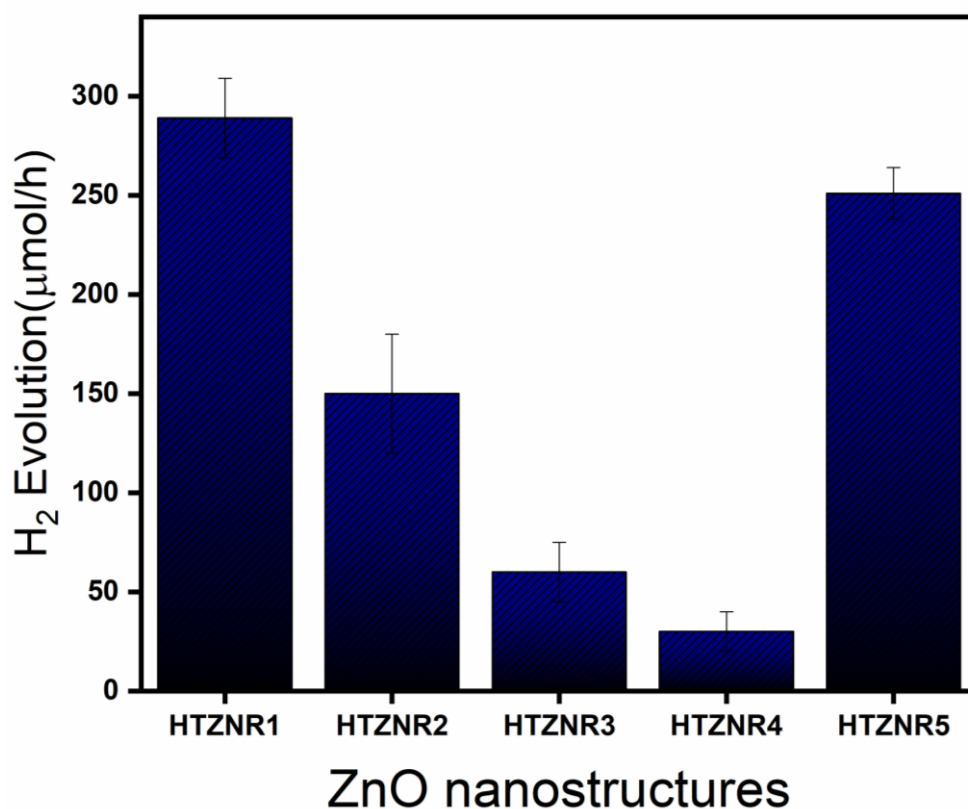
Fig.2.8. H_2 evolution activity of HTZNR1, HTZNR2, HTZNR3, HTZNR4, and HTZNR5 under the irradiation of high-pressure mercury lamp with 450W with Water: Methanol Mixture for 4h time irradiation.

To further elaborate this, the comparative synthesis of ZnO nanoparticles with two different methods, that is, sol-gel (ZnO-SG) and precipitation (ZnO-PPT) method, has been carried out, which is explained in the experimental section (2.2.1.1 and 2.2.1.2) respectively. These synthesized ZnO materials are then compared with ZnO nanorods that are HTZNR1. The powder X-ray diffraction of as-synthesized HTZNR1 (Fig.2.5.a), ZnO-PPT (red) & ZnO-SG

(blue) has been compared (Fig.2.9). It shows the formation of Wurtzite structure for ZnO which is matching well with the JCPDS No.01-079-0206.For HTZNR1, ZnO-SG, and ZnO-PPT, the planes (100) and (101) are more intense than that (002). This shows the directional growth axis is along the c-axis and [0001] direction (Fig.2.9). In the case of ZnO-PPT, the peaks are broader due to smaller particles size. however, the (100), (101), and (002) planes are more visible from P-XRD data (Fig.2.9).
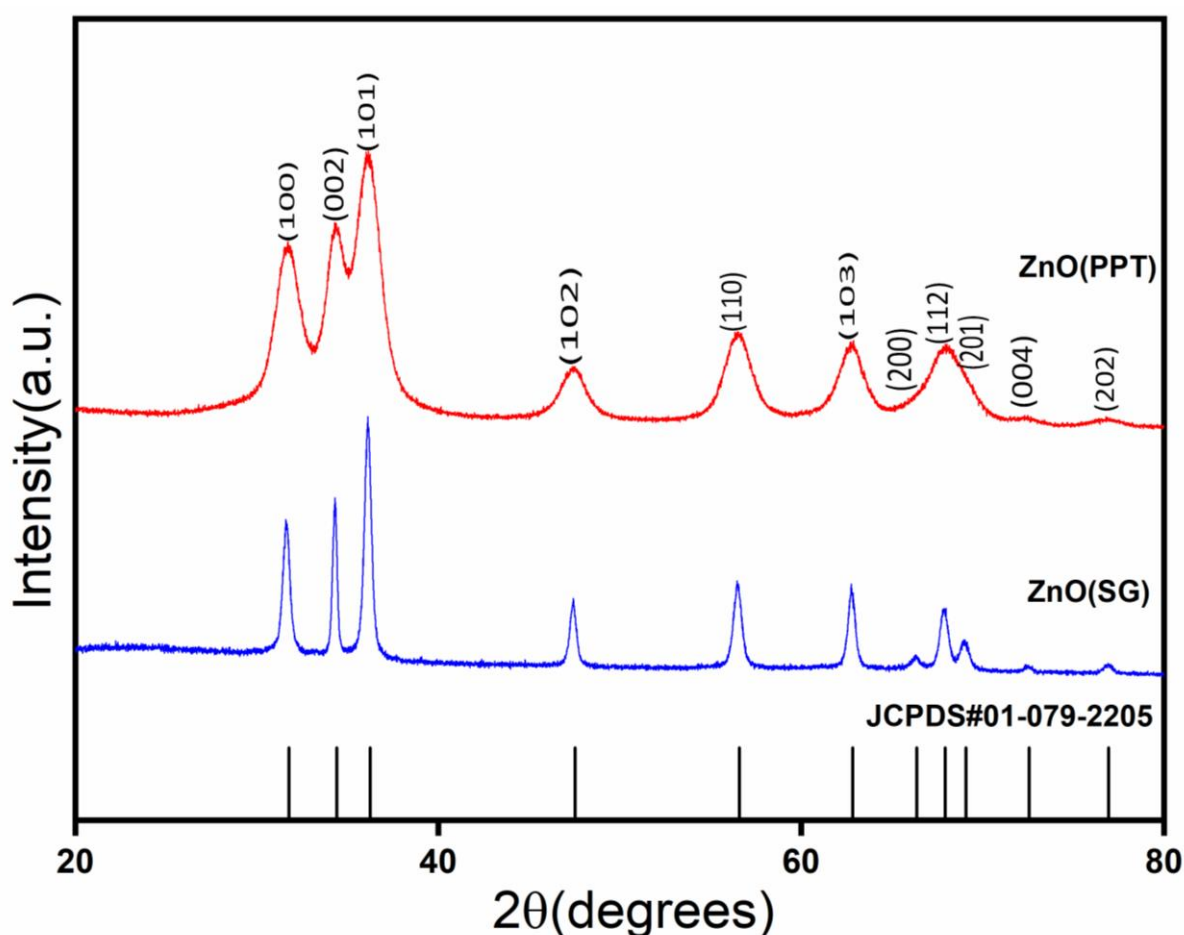
Fig.2.9. P-XRD pattern ZnO-HT (black), ZnO-PPT (red) & ZnO-SG (blue), which is exactly matching with the JCPDS 01-079-0206.
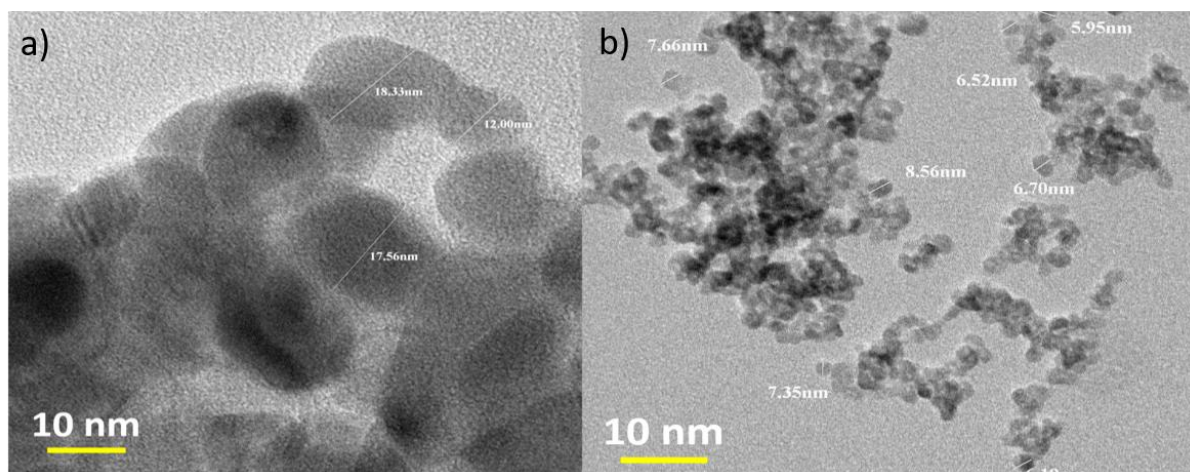
Fig.2.10.TEM analysis of a) ZnO-SG & b) ZnO-PPT

According to the parameters of the reaction, the TEM images demonstrate the creation of three distinct ZnO morphologies. ZnO nanoparticles with a size of 20–30 nm are produced using the sol–gel process (Fig. 2.10. a). ZnO nanorods with suitable hexagonal shapes and diameters ranging from 50 to 100 nm are formed using the hydrothermal technique (Fig. 2.7 a). Smaller particles with a size between 5 and 11 nm are produced by the precipitation process (Fig. 2.10.b). Reaction conditions are, therefore, important for the various synthesized forms of ZnO. The diversity in the absorption of ZnO nanostructures produced by diverse techniques is obvious in their UV-visible spectra, as predicted by their particle size dispersion. The absorption start for ZnO-PPT, ZnO-SG, and ZnO-HT, respectively, changed from 350 nm to 375 nm to 385 nm according to calculations using the band gap generated from the absorption spectra as the particle size grows from the precipitation method to the hydrothermal approach (Fig.2.11a). ZnO nanostructures often show a broad defect emission band from 500 to 650 nm and an exciton emission band in the UV region of their photoluminescence spectra. ZnO heterostructures' size quantization can shift the placements of spectral bands. ZnO's surface flaws have a significant impact on its physical characteristics. The ZnO nanostructures used in this investigation exhibit wider ZnO-SG emission at 530 nm (Fig. 2.11b, blue), consistent with the trap level on the ZnO surface. The emission of ZnO-PPT (Fig.2.11b, red) shows that surface trap emission has decreased as the size of ZnO particles has decreased. ZnO-HT is an example (Fig.2.11b, black). The emission peak has once more become more diffuse, and the emission intensity has decreased, indicating that the recombination factor for nanorods has decreased.
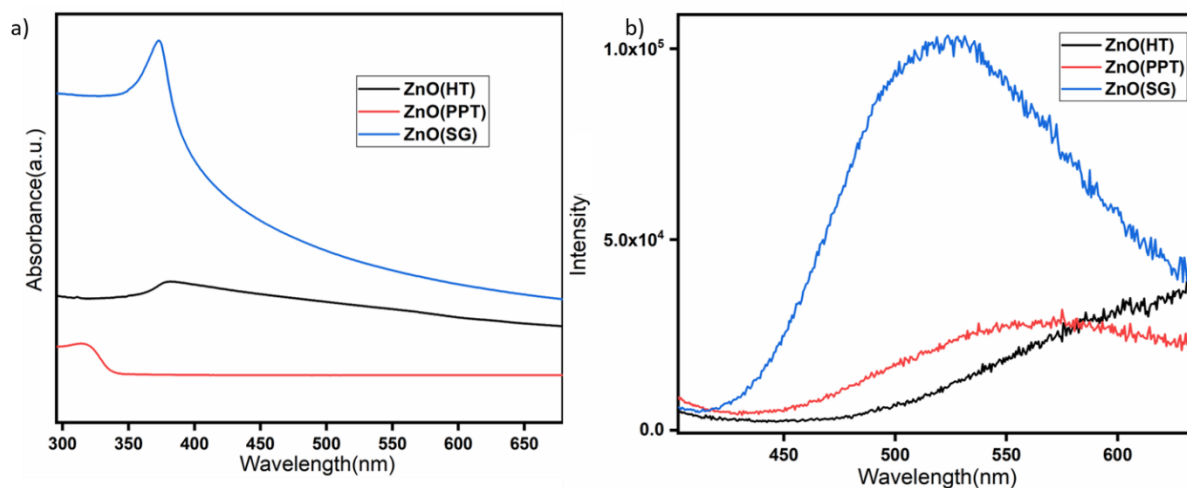
Fig.2.11. a) UV-Vis absorption spectrum b) Photoluminescence spectrum at λexc= 325 nm of ZnO-SG (blue) ZnO-HT (black) & c) ZnO-PPT (red)

Photocatalytic hydrogen evolution activity increased in ZnO nanostructures synthesized by the hydrothermal method by about 289μmol/g compared to the ZnO-PPT and ZnO-SG. This indicates that ZnO with a nanorod shape has more influence on the H_2 activity than other morphologies (Fig.2.12).
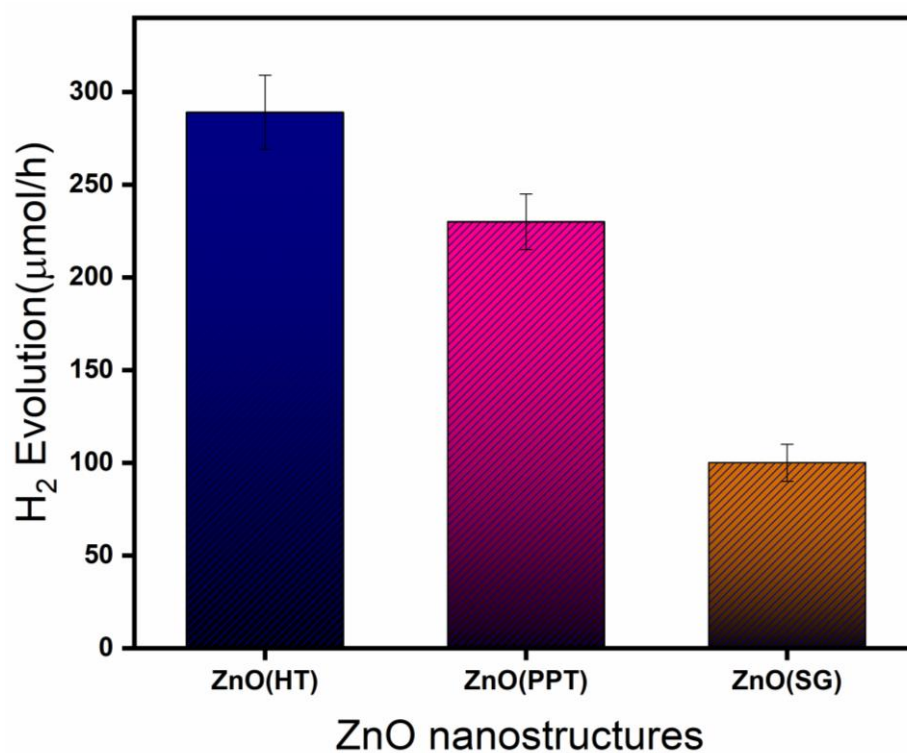
Fig.2.12. H_2 evolution activity of ZnO-HT (Navy blue), ZnO-PPT (Pink) & ZnO-SG(Yellow) the under the irradiation of high-pressure mercury lamp with 450W with Water: Methanol Mixture for 4h time irradiation.

2.7.Conclusion

Sol-gel, precipitation, and hydrothermal methods were used in this chapter to create ZnO nanoparticles with various morphologies under various reaction conditions. These methods produced nanoparticles with wurtzite-structure ZnO that were 20–30 nm, 5–11 nm, and 50–100 nm in size, respectively. By altering the reaction conditions, the hydrothermal method further investigates, which resulted in the production of various ZnO morphologies. Micro hexagonal discs, hydroxides, nanoflowers, and nanobats were all visible in FE-SEM pictures. The photocatalytic H2 evolution has been examined following the completion of the characterisation phase. Pure ZnO samples encouraged the production of H2. Hydrothermal ZnO nanorod synthesis is the most effective H2 generating process. This might be because of its complex architecture, which could scatter incoming light and increase light absorption and photoefficiency. It is vital to consider many alternative modification techniques because ZnO causes photo-corrosion and has the drawback of a smaller band gap, which restricts its use of visible light.

2.8. References

1. Srivastava S et al., *Chem. Mater*, **2005**,17, 487

2. Huang H Y et al., *J. Phys. Chem. B*, **2005**,109, 24288

3. Lin S et al., *Adv. Mater*. **2012**,17, 2553

4. S P Ghosh et al., Materials Science and Engineering, **2016**, 115,012035

5. Richa Khokhra et al., *Scientific Reports*, **2017.** 1-14

6. Anta, J.A et al., *J. Phys. Chem. C* **2012**, *116*, 11413–44425

7. Leena George et al., *J. Phys. Chem. C*,**2015**, 119, 3060−3067

8. Jin Chang., Sensors*, **2013**, *13*, 8445-8460

9. Bulut H. et al., *Int. J. Hydrog. Energy*,**2018,**43,7381-7387

10. Ouyang, G et al., *ACS Appl. Mater. Interfaces* **2012**, *4*, 210–213

11. Li-Ting Chen *Langmuir* **2018**, 34, 5030−5039

12. Height, M. J et al., *Appl. Catal., B* **2006**, 63, 305−312.

13. Guo, M. Y et al., J. *Alloys Compd*. **2011**, 509, 1328−1332.

14. Wang, Z et al., *Langmuir* **2017**,33, 12276−12284.

15. Wang, X et al., *ACS Appl. Mater. Interfaces* **2012**, *4*, 817–825

16. Yuanhui Zheng et al., *Inorganic Chemistry*,**2007**, 46,17

17. K. Byrappa*, J Mater Sci ,***2008**, 43,2348–2355

18. T. Yoshida et al., *Chem. Mater.* **1999,** *11,* 2657-2667

19. T. Yoshida et al., *Chemistry letters* 1998

20. V.B. Kumar et al.*,J. Mater. Chem. B,* **2014**, 2, 3956–3964

21. C. Q. Zhu et al., *Nanoscale*, **2012**, 4,3060–3064.

22. Fang Lu et al., Adv. Funct. Mater. **2008**, 18, 1047–1056

23. W Chen et al., *Applied Surface Science ,***2019**,470,807–816

24. R. Al-Gaashani et al., *Ceram. Int.* **2013**, 39,2283–2292.

25. Y. Wang et al. *Mater. Lett.***2008**, 62,2359–2362.

26. H. Wang et al. *Powder Technol.***2013**,239,266–271

27. G. R. Li. *et al.,J J. Phys. Chem. C* **2008,** *112,* 11859–11864

28. Kotov, N. A. *Nanoparticle assemblies and superstructures*; Taylor & Francis Group: Boca Raton, FL, 2006; Chapters 1 and 2.

29. Wang, Z. L. *J. Phys.: Condens. Matter,* **2004**, *16*, R829.

30. Wang, J. M. et al., *J. Cryst.Growth* **2004**, *262*, 290-294.

31. Jiechao Ge et al., *Nanotechnology,2006,* 17 1316

32. Yuzhen Lv. et al., *Appl. Phys. Lett.2005,* 87, 163103

33. Yueping F.et al.,*J Solgel Sci Technol*, **2005**,36,227–234.

34. Liang, J. B. et al.,*J. Phys. Chem. B* **2005**, *109*, 9463-9467

35. Ni, Y. H. et al., *Cryst. Growth,***2005**, *283*, 48-56.

36. Zhang, H. et al., *Phys. Chem. B,* **2004**, *108*, 3955-3958

37. Mina z. et al., *J Mater Sci Technol.***2018**,34,1035-1043.

38. Sikai Z. et al., *Sens. Actuators B: Chem,***2019**,286,501-511.

39. Ruixia S. et al., CrystEngComm, **2012**, 14, 5996-6003

40. Kuo C. H. et al., *Integr. Ferroelectr,***2013**,143,97-106

41. Zhang, J et al., *Chem. Mater*. **2009**, 21, 2875–2885

42. W.J. Li et al., *J. Cryst. Growth*, **1999**,203,186-196

43. Alisa G. et al., *ACS Omega ,***2020**, 5, 17617−17627

Chapter 3

One pot hydrothermal synthesis of Zinc oxide-Perylene for the photocatalytic hydrogen evolution via methanol oxidation

3.1. Introduction

The small band gap of ZnO, which has been used in many applications, has some drawbacks that reduce the usefulness of the visible spectrum of solar energy, which accounts for about 45% of the overall electromagnetic spectrum of solar energy. Additionally, ZnO has a higher rate of electron-hole recombination, which lowers ZnO's effectiveness as a photocatalyst. Equation 1 states that photo-corrosion occurs when ZnO is exposed to light[1,2].

$$ZnO \xrightarrow{\text{Light}} Zn + 1/2 O_2 \qquad\qquad (1)$$
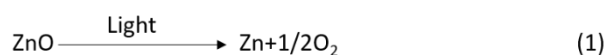
Therefore, using unaltered ZnO for photocatalytic H2 evolution is not desirable. Appropriate surface alterations can be used to mitigate these drawbacks. Attaching conducting organic molecules to the semiconductor surfaces is one technique [3]. This will cause quick electron transfer to the conducting channel rather than recombination. Dye sensitization is covered in Chapter 1, Section 1.7.A, as a method for charge transfer control and visible spectrum utilization. The highly stable and simple-to-make PDIs are functional visible-light absorption chromophores. They are derivatives of perylene tetracarboxylic acid dianhydride (PTCDA). They have been used in photovoltaics, solar cells, and other optoelectronic applications[4–9]. Due to π-π interactions between the perylene core and n-type semiconducting nature. The creation of ZnO-Perylene tetracarboxylic acid dianhydride, its characterization, and photocatalytic hydrogen evolution without the use of a co-catalyst are all covered in this chapter. Understanding the heterojunction between perylene and semiconductor materials and the structure creation mechanism has been attempted.

3.2. Experimental Section

3.2.1. Synthesis of ZnO

7.435g of Zinc nitrate (Zn $(NO_3)_2.6H_2O$) was dissolved in 50 ml of water, and 14g of sodium hydroxide (NaOH) was dissolved in 50 ml of water. Then, 10ml of each solution was mixed with 20ml of distilled water and stirred for 30 min. Then, it is transferred into a 100ml Teflon lined autoclave and kept at 150°C for 24h. After the completion of the reaction, the autoclave was held for cooling. After that, the reaction was washed several times using water and ethanol using a centrifuge machine at 14,000 rpm and then kept for drying at 80°C in an oven for 24h.

3.2.2. Synthesis of ZnO-P

0.04M of Zinc Nitrate (Zn $(NO_3)_2.6H_2O$) (0.30297g) in 40mL of water in a beaker stirred at room temperature and 0.4M Sodium Hydroxide (0.96g) in 60mL water in a beaker. The Zinc Nitrate solution was added dropwise into the alkaline solution, and 0.001M perylene tetracarboxylic acid dianhydride (PTCDA) was added to this mixture immediately. It is stirred for 30 min, transferred into a 150mL Teflon lined autoclave, and kept at 150°C for 24h. After that, the reaction mixture was washed with water several times and finally with methanol, then held for drying at 60°C inside an oven. The final material is denoted as ZnO-P (ZnONR-PTCDA). The reaction scheme is given in Fig.3.1.

To understand the effect of hydrothermal treatment on PTCDA, it was subjected to the same treatment without adding Zn precursor.
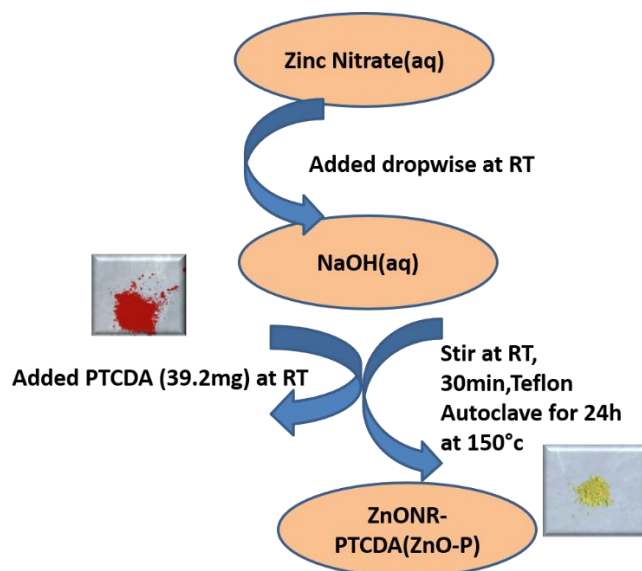
Fig.3.1. Reaction scheme for the synthesis of ZnO-P (ZnO NR-PTCDA)

3.3. Material characterizations

The methodologies utilized for PXRD, FE-SEM, TEM, IR, UV-vis, photoluminescence, NMR, electrochemical tests, and elemental analysis are identical to those outlined in Chapter 2's Section 3. In Appendix 2a, all the characterization approaches employed throughout the thesis are briefly reviewed together with their underlying ideas and instruments.

3.4. Results and Discussion

3.4.1. Structural characterization

The powder x-ray diffraction of as-synthesized ZnO-P, PTCDA@HT, and ZnO has been compared (Fig.3.2a-b). It shows the formation of the wurtzite structure for ZnO, which matches the JCPDS No.01-079-0208. For ZnO, the planes (100) and (101) are more intense than that of (002), indicating that the directional growth axis is along the c-axis and [0001] direction

(Fig.3.2a). In the case of PTCDA@HT, four peaks appear at d-spacing values of 0.93,0.73,0.36 and 0. 32nm. It was reported that the π-π stacking is the characteristic feature of perylene which is present at 2Θ 25-27° with 0.312-0.365nm of d-spacing [10-15]. Since in the case of PTCDA@HT, the peaks are observed at 2Θ 25-27° with a d-spacing of 0.36-0.32nm, this is assigned to the distance between single layers of two stacked perylene.[16-21]. Thus, in PTCDA@HT the highly crystalline structure is formed with stacked perylene layers compared to PTCDA powderAfter introducing PTCDA, the characteristic peaks of ZnO are still present in the ZnO-P; however, the peaks corresponding to the PTCDA are visible in the XRD pattern. After introducing PTCDA, the characteristic peaks of ZnO are still present in the ZnO-P; however, the peaks corresponding to the PTCDA are visible in the XRD pattern. The series of peaks at a low diffraction angle (d-spacing of 0.334nm) is assigned to the π-π stacking distance of PTCDA in ZnO-P.The peaks corresponding to PTCDA@HT are not present in the ZnO-P this means that while interacting with ZnO the PTCDA retains its powder characteristics.
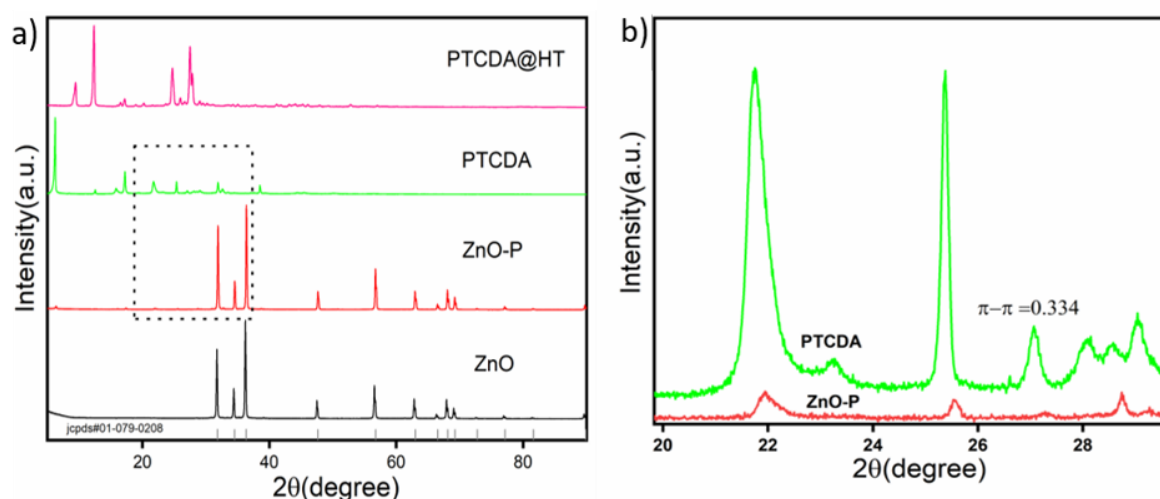
Fig.3.2. P-XRD pattern a) ZnO (black), ZnO-P(red), PTCDA (green) & PTCDA@HT (pink) which is exactly matching with the JCPDS 01-079-0208 b) Zoomed P-XRD pattern of ZnO-P with PTCDA (2Θ-20-28) showing the π-π interaction

The morphological characterizations have been carried out by FE-SEM and TEM analysis. It can be seen from Fig.3.3 a) the morphology of well-aligned ZnO nanorods is formed. The ZnO shape doesn't change by the anchoring of PTCDA during synthesis(Fig.3.3 c).The perylene alone shows the sheet morphology, and ZnO shows the proper nanorods (Fig.3.3 b).
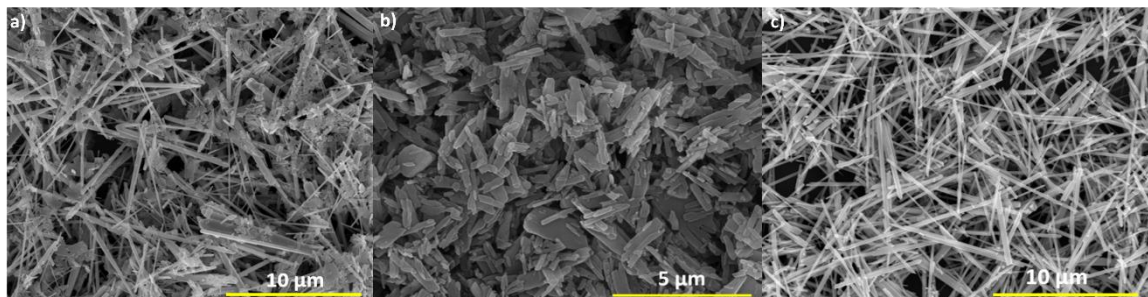
Fig.3.3.FE-SEM analysis of a) ZnO-P b) PTCDA@HT and c) ZnO

The TEM images show that the thin sheet-like morphology of PTCDA is visible and interacts with the ZnO nanorods through the surface and faces, which can be seen in Fig.3.4a). From the P-XRD pattern, the highly exposed face of ZnO is (100) and (101). The ZnO(100) plane shows the interaction with PTCDA through this face (Fig.3.4b). SAED pattern suggests the crystalline nature of ZnO and the amorphous nature of PTCDA (Fig.3.4c). The further SAED study reveals the interaction between the PTCDA, which has the (102) plane at a d-spacing of 0.334nm, which is the value for the π-π stacking of perylene [22,23]. This observation is also corroborated by the powder x-ray diffraction for ZnO-P(Fig.3.2 b). To know about elemental content and formation uniformity, elemental mapping has been carried out, which shows the presence of Zn, O, and C in the ZnO-P material (Fig.3.4d-i). The perylene part only shows the presence of C and O, which confirms the presence of perylene in the form of sheets in the

system, and the ZnO part shows the presence of Zn and C, indicating an interaction between

ZnO and dye.
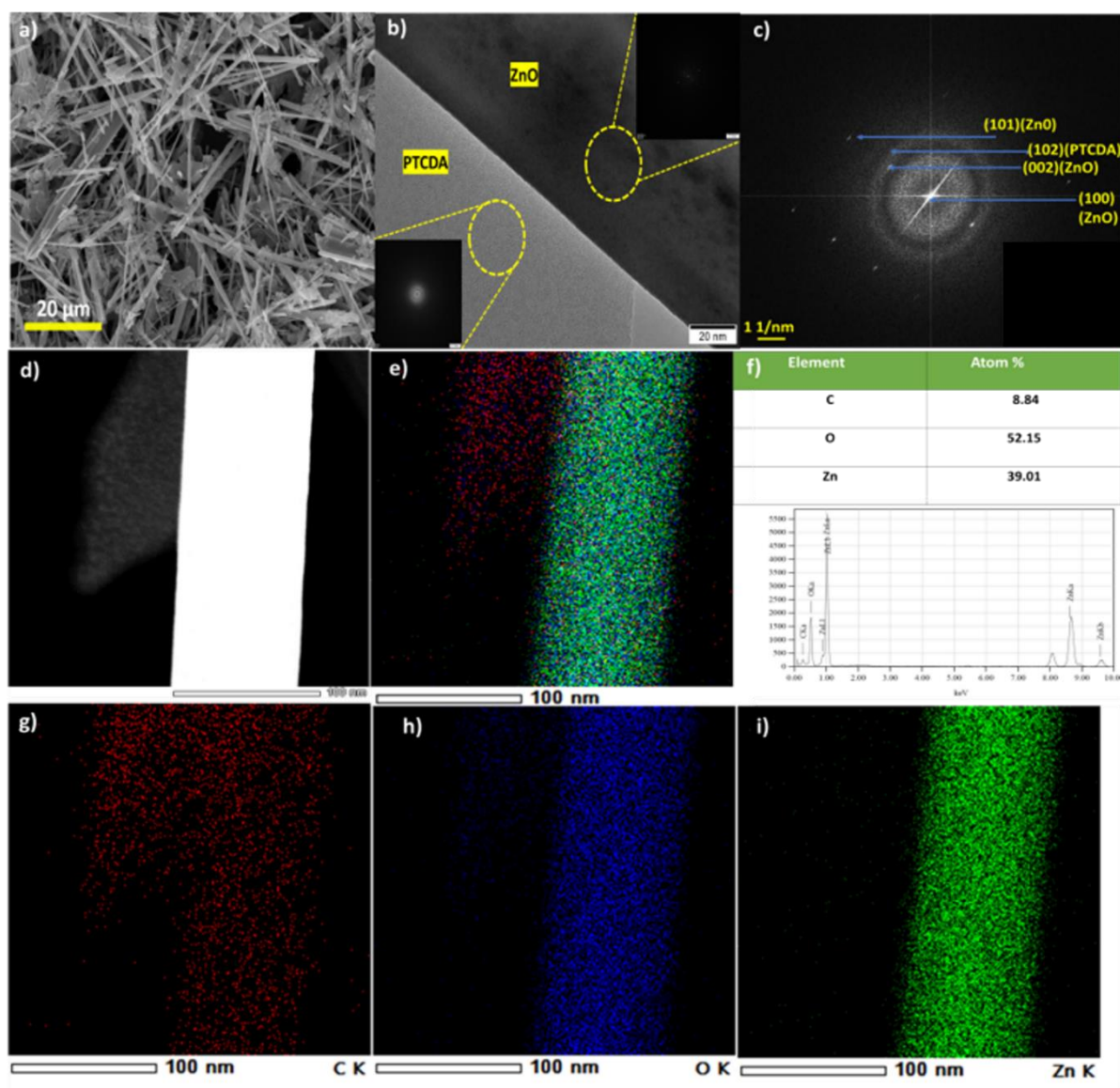
Fig.3.4. FESEM & TEM analysis a) FE-SEM of ZnO-P b) TEM of ZnO-P c) saed pattern for

ZnO-P d-i) Elemental mapping for the ZnO-P showing elements Zn, O, and C

To know further in detail about the ZnO-P interaction, Fourier transform infrared (FT-IR) spectroscopy for ZnO, ZnO-P, PTCDA, and PTCDA@HT was performed. The FT-IR spectra (Fig.3.5) clearly show the sharp peaks for carbonyl stretching frequency (-C=O) at 1770cm-1 for PTCDA, which splits into asymmetric stretching vibrations at 1605cm-1 and symmetric stretching vibrations at 1334cm-1 for PTCDA@HT. This indicates the ring opening at PTCDA structure at anhydride group and the formation of -COO$^-$ with coordination ability. After forming the bond with the Zn atom in the ZnO lattices, the vibrations shifted to 1554cm-1 and 1437cm-1. The ZnO shows the characteristics of vibrations at 540cm-1 for Zn-O, which is moved to 577cm-1 in the ZnO-P, confirming the interaction between ZnO and PTCDA[24-26].
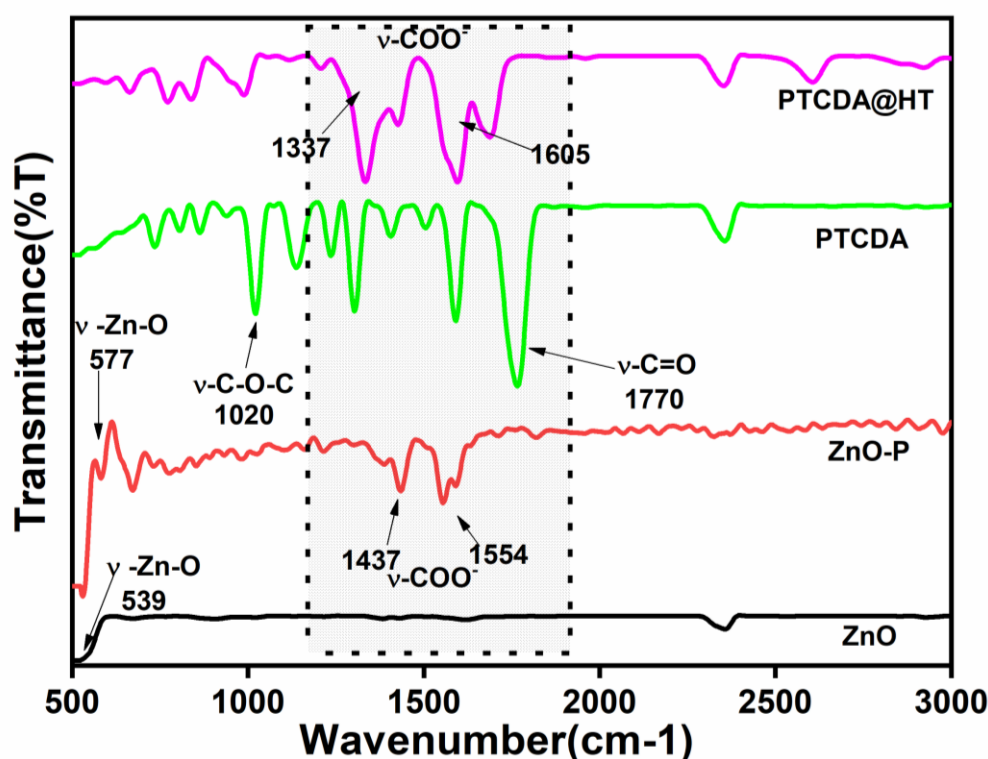
Fig.3.5.FTIR spectra of ZnO, ZnO-P, PTCDA and PTCDA@HT

The red color of PTCDA changes to yellow on the formation of ZnO-P, as seen in the photographic images in Fig.3.6a. The same shift in color is observed on hydrothermal treatment of PTCDA (sample PTCDA@HT). The absorption spectra for ZnO, PTCDA, PTCDA@HT, and ZnO-P have been studied to understand these changes (Fig.3.6b). ZnO shows absorption at around 380nm, and in the case of PTCDA, it ranges from 400-700nm(27-29). The blue shift in PTCDA@HT could be ascribed to the strong confinement effect caused by the nature of molecules. This phenomenon also reveals the strong π-πinteraction between the neighboring perylene molecules, promoting the lower energy intermolecular charge transfer[30-33]. The ZnO-P shows the combination of both absorption bands for PTCDA and ZnO. The band gap of ZnO nanorods is estimated to be 3.20eV (Fig.3.7). In ZnO-P, the band gap reduces to 2.98eV, which is red-shifted, and ZnO-P has both the characteristics peaks for ZnO and PTCDA indicating enhanced light absorption in the visible region. In the case of PTCDA@HT, the band gap position changes to 1.96eV.
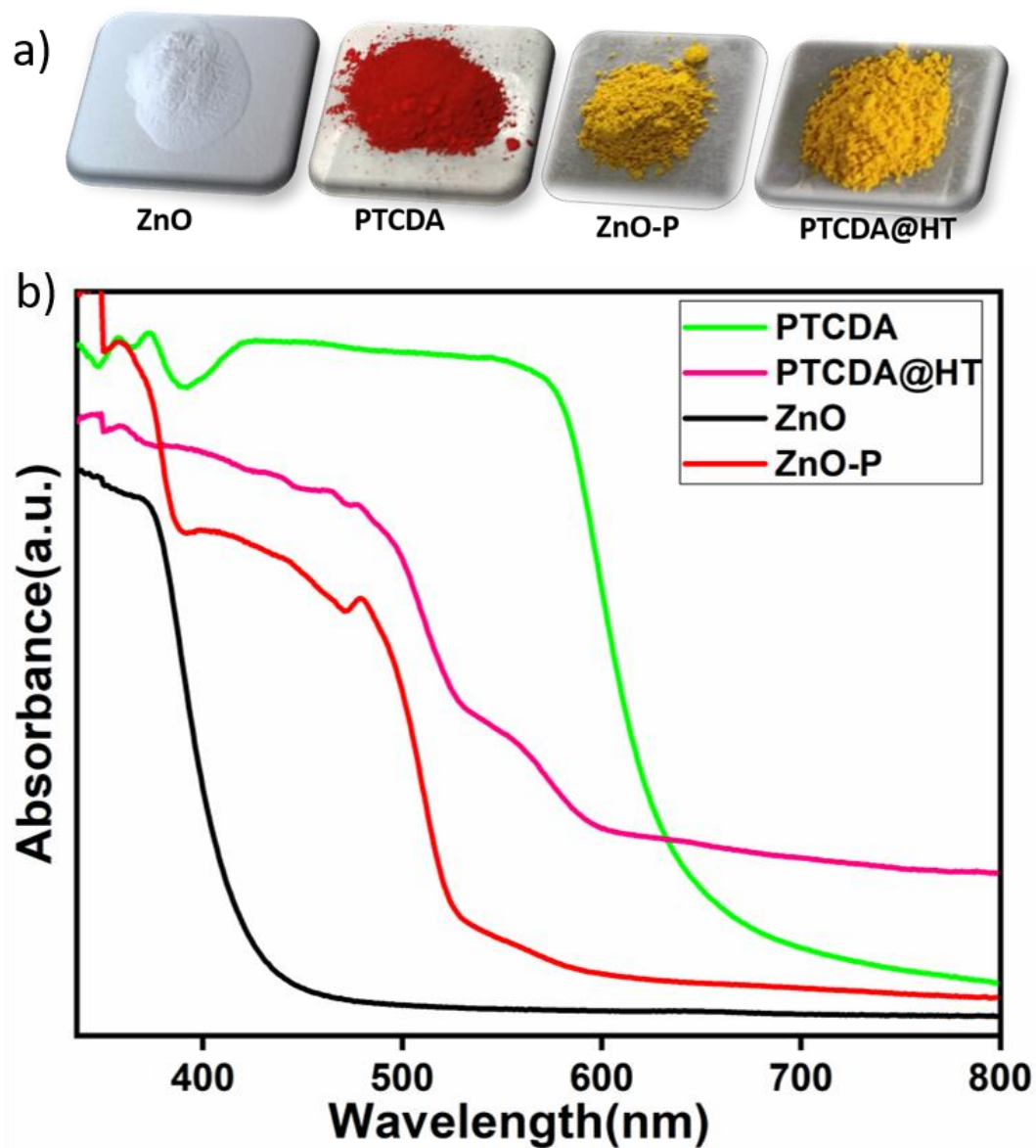
Fig.3.6. (a) Photographic images of ZnO, PTCDA, ZnO-P, and PTCDA@HT

(b)UV-Visible absorption spectra of ZnO, ZnO-P &PTCDA@HT
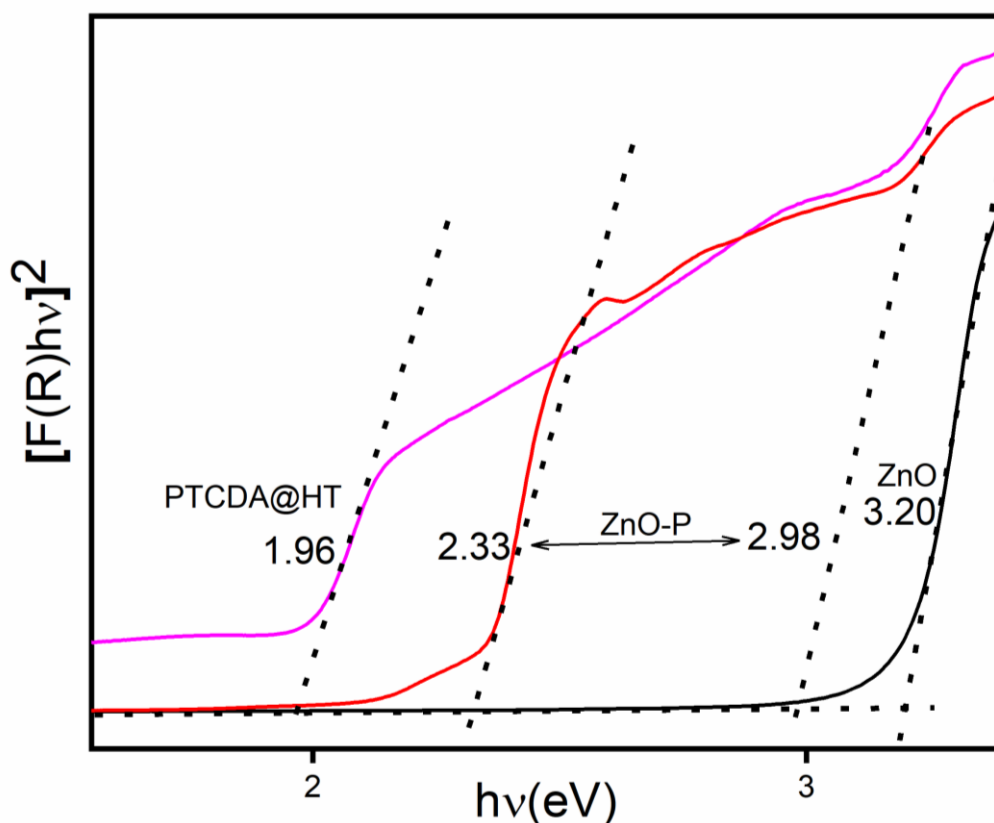
Fig.3.7.(Tauc Plots)Band gap measurements for ZnO, ZnO-P and PTCDA@HT

Photoluminescence studies have been carried out to learn more about the electron transfer and to understand the structural features of ZnO-P and PTCDA@HT. The solution of the same concentration($1x10^{-5}M$) has been prepared using methanol as the solvent. The ZnO-P and PTCDA@HT have been compared to see the differences between the ZnO and Perylene characteristics. The absorption edge for ZnO lies at 390nm, which is red-shifted after adding PTCDA(Fig.3.8a). The absorption spectra of perylene structures show the typical features at 410,440,470 and small shoulder at 520nm. This peak is characteristic of the perylene core (Fig.3.8a). In the case of PTCDA@HTthe absorption bands become broader than that of ZnO-

P, which means that in the case of PTCDA@HT, more aggregation and stacking is happening as compared to that of ZnO-P. The ZnO shows the characteristic green emission at 520nm, which generally occurs due to the oxygen vacancies and due to interstitial species. This green emission is called the defect emission, which leads to the recombination of electrons and holes, and due to this, the activity in the ZnO is minimal. The emission characteristics for PTCDA are generally the peaks at 520nm and 580nm for the emission in the visible region. This emission is also visible in the photoluminescence spectra of ZnO-P, where peak intensities are suppressed compared to parent PTCDA. It means the extent of recombination in ZnO has been reduced by the electron transfer mechanism from PTCDA to ZnO, which is very understandable from the photoluminescence spectra for ZnO-P (Fig.3.8b).
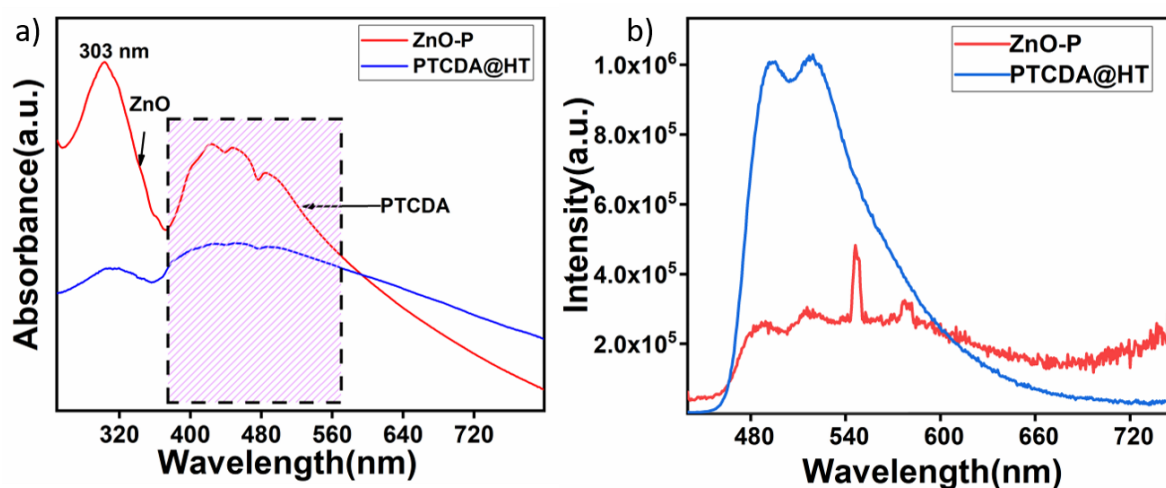
Fig.3. 8. a) UV-Visible spectra (b)Photoluminescence spectra of ZnO-P &PTCDA@HT(The spike in Fig.3.8.b is due to the 2λpeak of the instrument)

3.4.2. Formation mechanism of ZnO-P

The scheme of synthesis is given in Fig.3.1.The synthesis mechanism of ZnO-P can be explained in the following assumptions as the absorption spectra and photoluminescence spectra reveal the changes in the absorption properties as well as emission properties of ZnO and PTCDA when they are coming together. The ZnO is known to form different morphologies depending on the synthesis procedure. Here, well-dispersed ZnO nanorods show the interaction with the sheet-like structure of PTCDA. The TEM data reveals the morphologies and their interaction with each other. During the reaction, Zinc nitrate dihydrates react with water and form the Zn^{2+} and $2(NO_3)^-$ (eq.1), and then simultaneously, the sodium hydroxide forms Na^+ and OH^- (eq.2). After the addition of Zinc nitrate solution to alkaline solution it forms Zinc hydroxide (eq.3). PTCDA was added after this step. The whole solution turns yellow due to the formation of of Na_4(PTCDA) (eq.6). Thus, during synthesis itself, , Zinc hydroxide and Na_4(PTCDA) come together to form a heterojunction structure which can be visible from TEM-SEM data as well as a powder diffraction pattern. Thus ZnO-P formation takes place by creating a strong bond between the exposed Zn atom of the (100) plane of ZnO and the carboxylate group of perylene ($-COO^-$) (Fig.3.9a). During the ZnO synthesis, solvent, pH as well as zinc source play the critical role. Here, the most exposed plane is (100) and PTCDA is showing interaction with (100) plane[34]. Thus, the reaction mechanism of formation in the schematic format can be explained in Fig.3.9a-c.

$$\bullet \quad Zn(NO_3)_2 \xrightarrow{\text{aq.}} Zn^{2+} + 2(NO_3)^- \qquad\qquad 1$$

$$\bullet \quad NaOH \xrightarrow{\text{aq.}} Na^+ + OH^- \qquad\qquad 2$$

$$\bullet \quad Zn^{2+} + 2OH^- \longrightarrow [Zn(OH)_4]^{2-} \qquad\qquad 3$$

- $[Zn(OH)_4]^{2-} \longrightarrow ZnO_2^{2-} + 2H_2O$ 4

- $ZnO_2^{2-} + 2H_2O \longrightarrow ZnO + 2OH^-$ 5

- $PTCDA \longrightarrow Na_4(PTCDA)$ 6

Final reaction

- $[Zn(OH)_4]^{2-} \xrightarrow{Na_4(PTCDA)} ZnO\text{-}P$
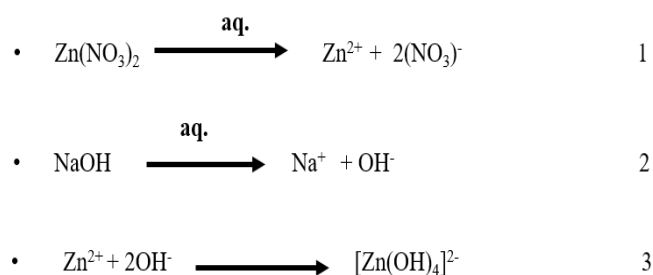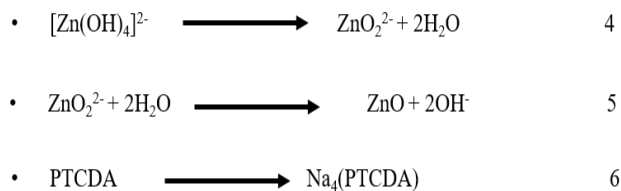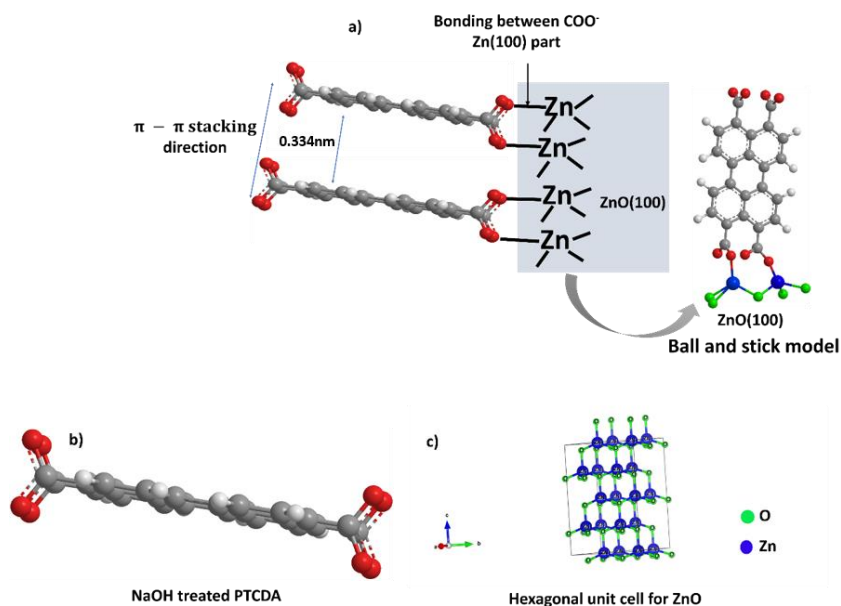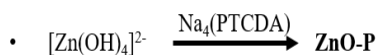
Fig.3.9. a) The reaction mechanism for the formation of ZnO-P b) the structure of PTCDA in the alkaline solution c) the Hexagonal unit cell of ZnO in the ZnO-P structure.

3.4.3. Hydrogen evolution activity

The ZnO, ZnO-P, and PTCDA@HT activity performance has been studied. The hydrogen evolution activity has been checked with 25% methanol in water without adding any co-catalyst. The activity comparison between pure ZnO, ZnO-P, and PTCDA@HT shows quite a drastic variation in the activity (Fig.3.10 a). The activity for the pure ZnO is 297μmolh^{-1} and for PTCDA@HT is 329 μmolh^{-1}. For ZnO-P, the activity increased substantially to 49650

μ molh^{-1} (Fig.3.10 a). This increase in activity can be concluded as due to a synergetic effect of ZnO and PTCDA interaction in the composite, with PTCDA acting as a sensitizer in the ZnO-P.

3.4.3.1.Role of sacrificial reagent

By preventing electron-hole recombination, sacrificial reagents are crucial for improving the photocatalytic activity of hydrogen synthesis. Therefore, the activity in aqueous solution with various sacrificial reagents, such as methanol, isopropanol, and triethanolamine, was studied in order to have a better knowledge of the influence of sacrificial reagent against the photocatalytic hydrogen production in the ZnO-P system. The photocatalytic hydrogen generation of ZnO-P photocatalyst in additional sacrificial reagents is depicted in Fig. 3.10b. The hydrogen generation rates were 6240,1330, and 8044 μmol/h for methanol, isopropanol, and triethanolamine, respectively. The best sacrificial reagent for ZnO-P to produce hydrogen at the best rate is triethanolamine. Since methanol breakdown results in the formation of value-added compounds, including formaldehyde, formic acid, and CO, methanol was utilized as the sacrificial reagent. H$_2$ evolution activity of ZnO-P was examined with and without methanol (Fig. 3..10 c) to determine the effect of components on the system's activity; in the absence of methanol, activity decreased to 20 μmol/h, which is significantly less.
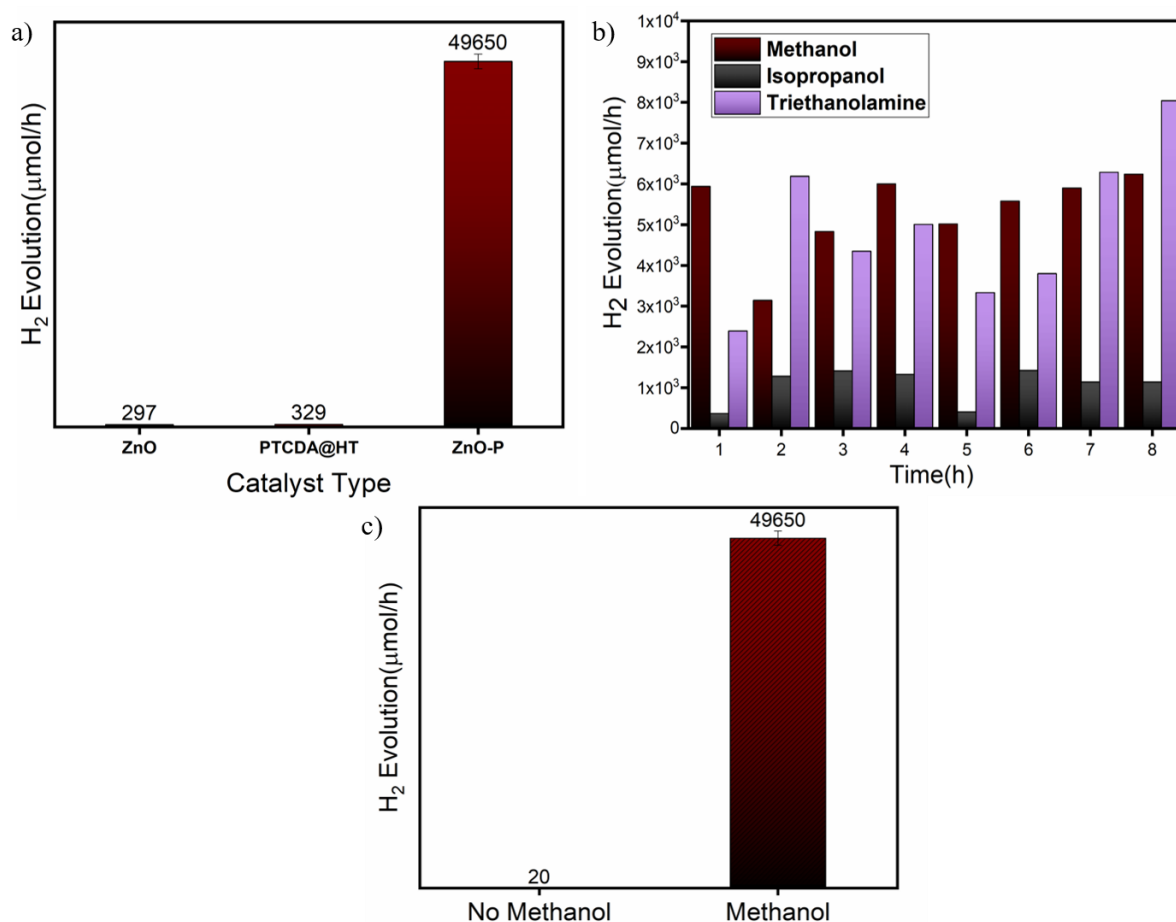
Fig.3.10. a) H$_2$ evolution activity of ZnO, PTCDA@HT &ZnO-P in 25% (v/v)MeOH/Water system under illumination with visible light (λ >450 nm)(5mg catalyst)b) H$_2$ evolution activity of ZnO-P in 25% (v/v)MeOH, Triethanolamine & isopropanol/Water system under illumination with visible light (λ >450 nm c) H$_2$ evolution activity of ZnO-P in 25% (v/v)MeOH/Water &without MeOH(30mg catalyst)

To check the stability of the catalyst ZnO-P after reaction, PXRD and FT-IR analysis were carried out. The crystallinity of ZnO-P after the reaction is decreased, which can be visible from the comparative diffraction pattern of ZnO-P after and before reactions (Fig.3.11). The

FT-IR spectra, also shows reduction in intensities of peaks in IR spectrum in ZnO-P(Fig.3.12).

Thus, from all these observations, it can be concluded that although ZnO-P shows some changes related to the structural features its activity remains intact and it shows high activity for the H_2 evolution.
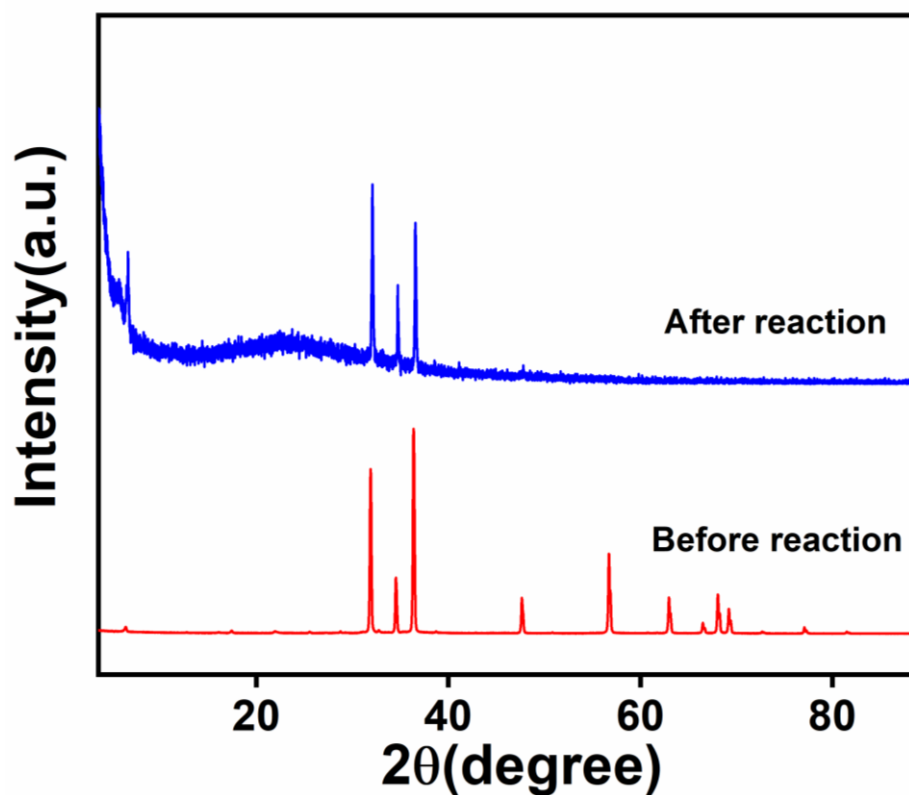
Fig.3.11. P-XRD pattern of ZnO-P after and before irradiation
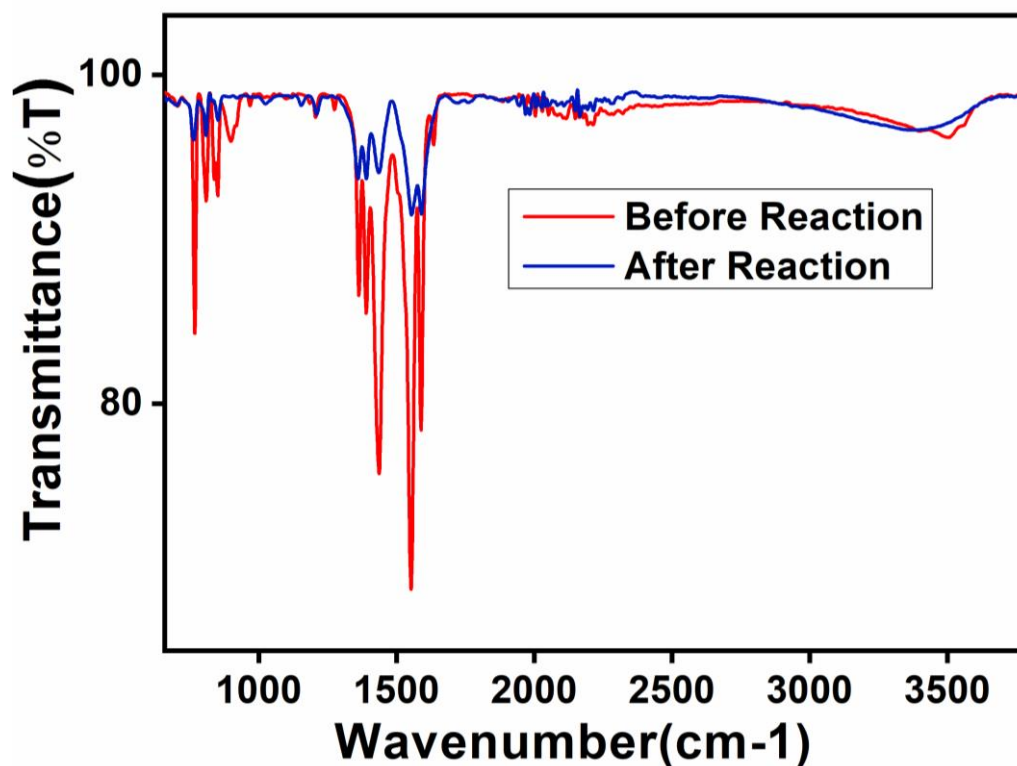
Fig.3.12. FTIR spectra of ZnO-P after and before irradiation

Similarly, to know the efficiency, apparent quantum yield measurement (AQY%) has been recorded using a solar simulator with a cut-off filter of λ>400nm. The efficiency of ZnO-P is 3.126% which is comparable to many perylene-based systems. It is higher than other reported perylene-semiconductor-based systems (Table .3.1).

Table. 3.1. Comparison of the apparent quantum efficiency of different materials

Sr.No.	Catalyst Type	Reaction condition	Irradiation type	H$_2$ evolution(μmol)	Apparent quantum yield(%)	Reference
1	ZnO-P	5mg ZnO-P +20ml water +5ml methanol	300W Xenon lamp(λ>455nm cutoff filter)	12.05 μmolg-1h-1	3.126	This work
2	PTCDI/Pt/TiO$_2$	25mg catalyst +90ml water +10ml triethanolamine	300W Xenon lamp(λ> 420 nm cutoff filter	0.075 μmolg-1h-1	0.047	1
3	P-PMPDI	50mg catalyst +5mg ascorbic acid +45ml water	300W Xenon lamp(λ> 420 nm cutoff filter	11.7μmolg-1h-1	2.06	2

3.4.4. Production of value-added products (formaldehyde from methanol oxidation)

The reduction and oxidation reactions (0 V vs. NHE) are photocatalytic processes that generate hydrogen and oxygen. Regarding thermodynamics, the photocatalytic water-splitting reaction requires a minimum photon energy of 1.23 eV. When the photocatalytic reaction is carried out in an aqueous solution along with a reducing agent like methanol, photogenerated holes in the valence band irreversibly oxidize the reducing agent instead of H$_2$O if the bottom of the photocatalyst's conduction band is situated at a more negative potential than the water reduction potential. Conduction band electrons can decrease water more readily as a result of this. By enhancing the number of photogenerated electrons in the conduction band of a photocatalyst, excitation speeds up the H$_2$ evolution reaction. It is well known that during oxidation, hydroxyl radicals interact with methanol predominantly by removing a hydrogen atom from the C-H bond to form hydroxymethyl (E$_0$ ($\cdot$CH$_2$OH/ CH$_2$O) =- 0.95 v NHE)[35–37]. The resultant radical then adds a fresh electron to the conduction band of the photocatalyst. The following reaction happens when methanol is oxidized:

$$CH_3OH \xrightarrow{h^+} HCHO \longrightarrow CO + 2H^+$$

As a result, methanol can be used as a sacrificial reagent and still provide valuable byproducts like formaldehyde or formic acid. CO, the final product, is useful for numerous purposes, including precise chemical synthesis. The end product of the reaction, formaldehyde reacting with CO, is reported in Table.3.2 along with the evolution of hydrogen that occurs during the reaction.By doing an HPLC examination on the samples, it was possible to confirm the generation of formaldehyde (Fig. 3.13).
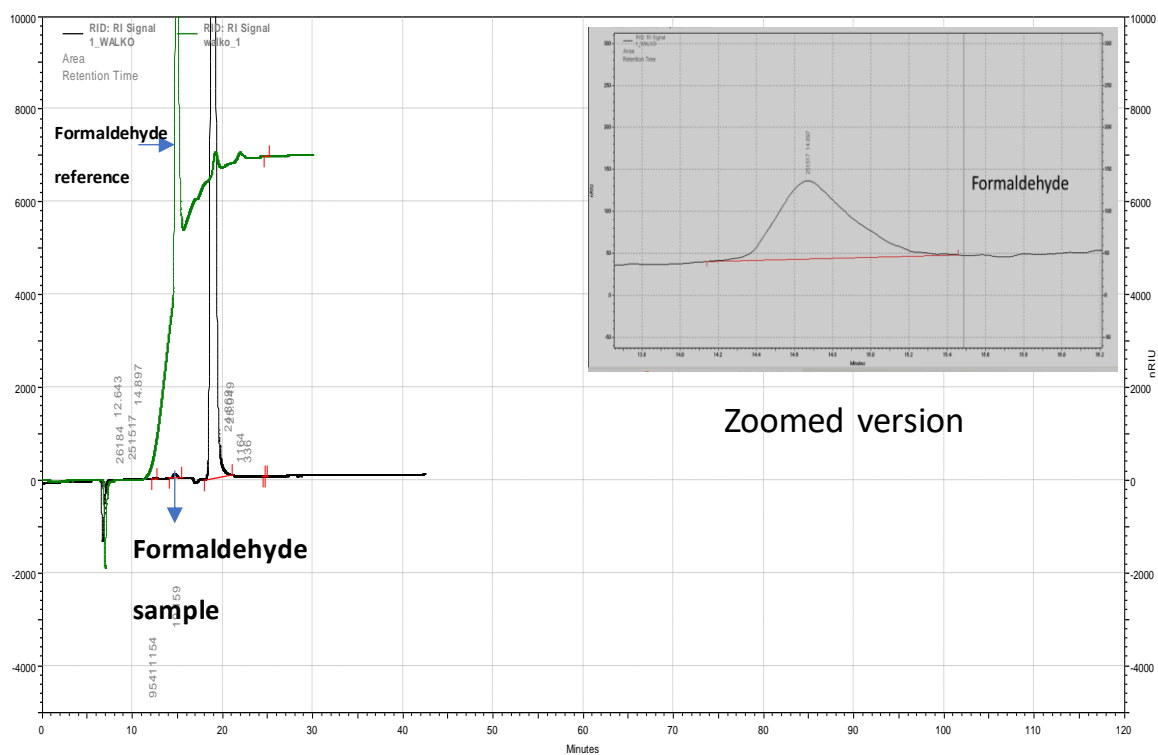
Fig.3.13. HPLC data showing the standard formaldehyde (1%) with sample ZnO-P showing the formation of formaldehyde from the methanol oxidation

The amount of conversion of methanol to formaldehyde has been calculated and plotted in the data (Fig.3.14). The 20% methanol showed the conversion of $2.80 \mu molh^{-1}$ of formaldehyde from the reaction mixture. Experiments with other methanol concentrations did not show any formaldehyde formation; thus, 20% was optimized for the reaction studies (Table.3.2.).
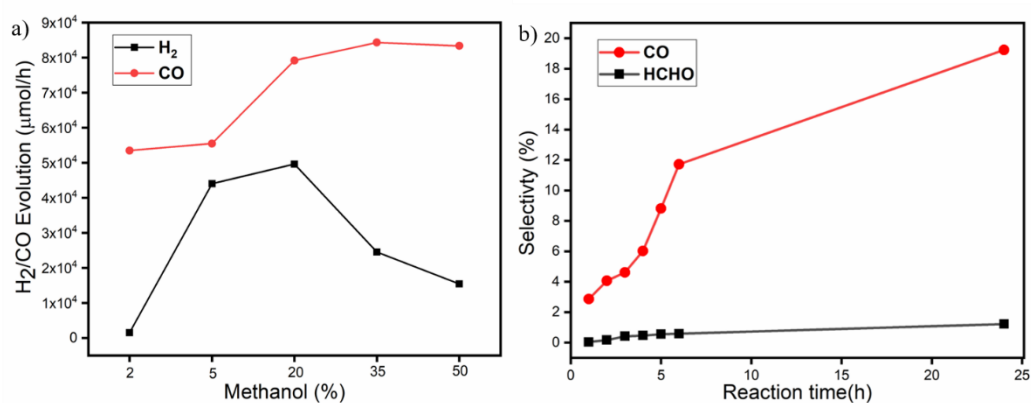
Fig.3.14. (a) Amount of H_2 and CO evolved in ZnO-P at various % of Methanol: Water (b) The selectivity of CO and HCHO concerning the time of conversion of methanol in ZnO-P

Table.3.2. Products Yield

Methanol (%)	Product yield of H_2 (μmol/h)	The product yield of CO (μmol/h)	The product yield of HCHO (μmol/h)
2	1530	0	-
5	44021	1981	-
20	49650	25685	2.80473
35	24511	30836	-
50	15445	29865	-

3.4.5. Photocatalytic H₂ evolution mechanism via methanol oxidation

The photoinduced electrons need to be transported easily in order to lengthen the separation of charge carriers, which will improve the photocatalytic performance of the composites. Electrochemical characterizations have been performed under the influence of a light source in order to better understand the mechanism of photocatalytic activity (details are provided in Chapter 2-Section 2.5). In contrast to ZnO, ZnO-P exhibits a higher current density in the presence of light (Fig. 3.15 a). It refers to the movement of electrons, or charge, from the ZnO side to the PTCDA side. These findings have been verified using the EIS Nyquist plot analysis. EIS Nyquist graphs with larger arc radii typically indicate more interfacial charge transfer resistance during the photocatalytic activity. Better conductivity and charge transfer ability are correlated with a smaller arc radius. The ZnO-P exhibits a smaller arc radius (Fig. 3.15 b) and a superior capacity for hydrogen evolution; consequently, these findings are supported by the ZnO-P's lower PL emission intensity. Fig. 3.16 shows a comparison of ZnO-P's ON and OFF modes.
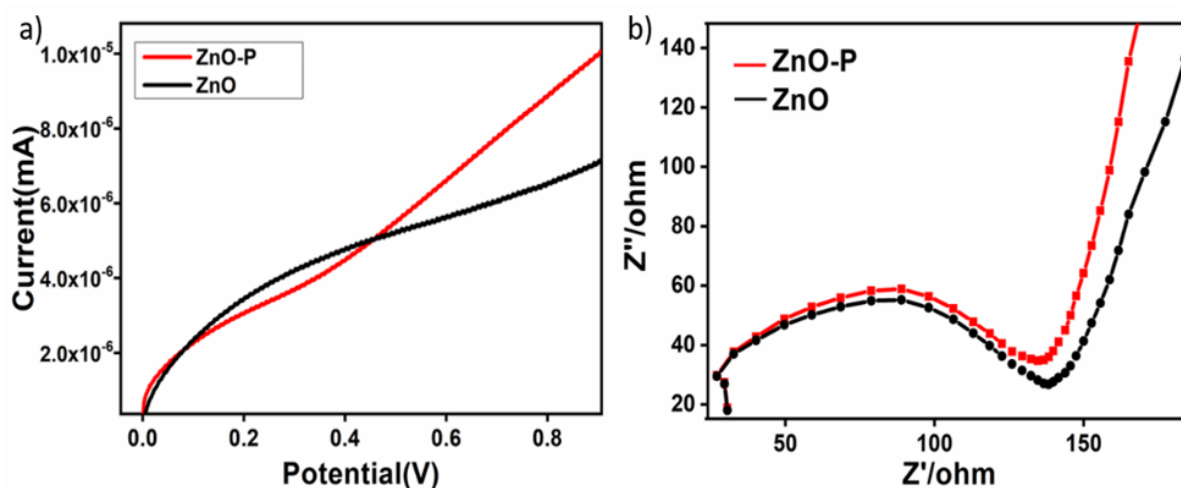
Fig.3.15.a) LSV profile for photoelectrochemical cells employing ZnO-P and ZnO (10mV/s) upon light ON mode (450W Hg lamp) by cyclic voltammetry, b) Electrochemical Impedance employing ZnO-P and ZnO upon light ON mode (450W Hg lamp).
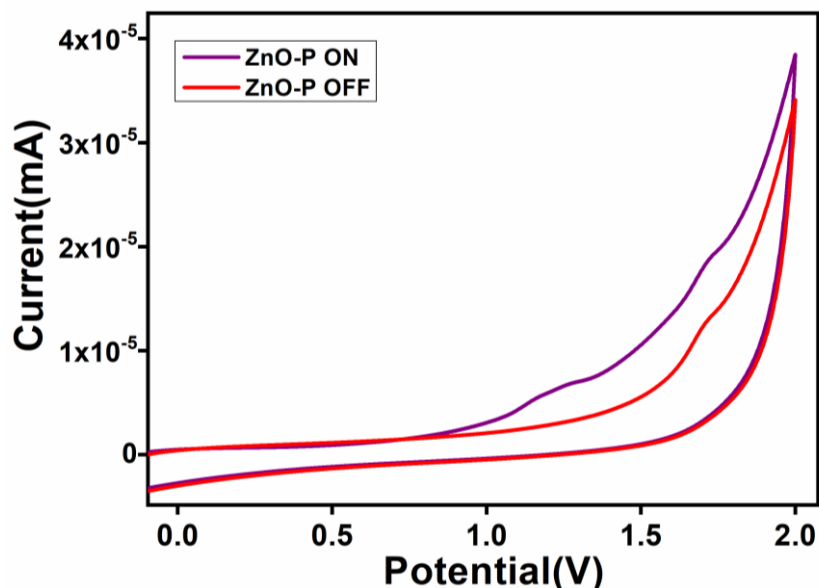
Fig.3.16. Cyclic voltammogram for ZnO-P ON-OFF mode (10mV/s) in 450W Hg Lamp by using three electrode setups (Platinum wire counter electrode, glassy carbon working electrode, Ag/AgCl working electrode in 0.2MClO$_4$ in acetonitrile as supporting electrolyte.

SiO$_2$-P was synthesized utilizing TEOS (tetra ethyl orthosilicate) as a source for Si to better comprehend this. ZnO-P synthesis conditions were used in the process. The electron transfer is predicted to fail since SiO$_2$ lacks a facile electron acceptor. Due to that, the activity is significantly less than ZnO-P (Fig.3.17). In addition, ZnO nanorods were taken, and the salt of PTCDA was mixed well with grinding for 30min, dried at 80°C, and kept for irradiation. This leads to the complete degradation of the sample(Fig.3.18). These two control experiments indicate strongly the interface between ZnO and PTCDA facilitating charge transfer and enhanced photocatalytic activity.
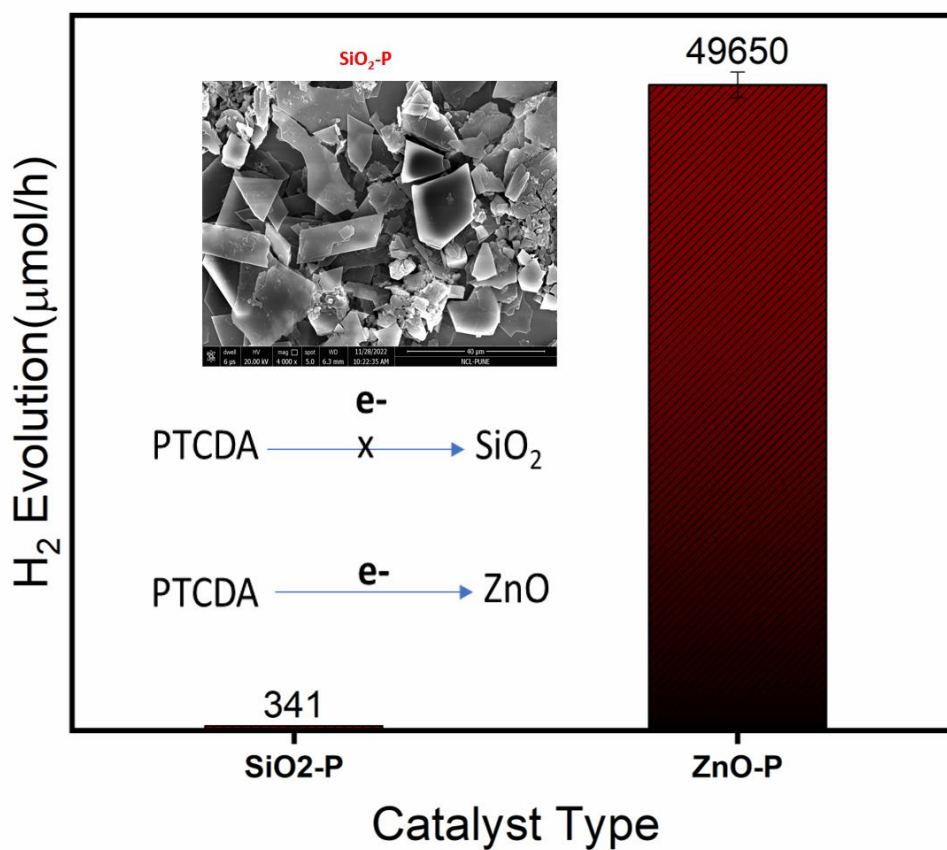
Fig.3.17. Comparison of H_2 evolution activity of SiO_2-P&ZnO-P in 25% (v/v)MeOH/Water system under illumination with visible light (λ >450 nm) with inset showing the FE-SEM image of SiO_2-P along with electron transfer in PTCDA, ZnO, and SiO_2.

a)

b)
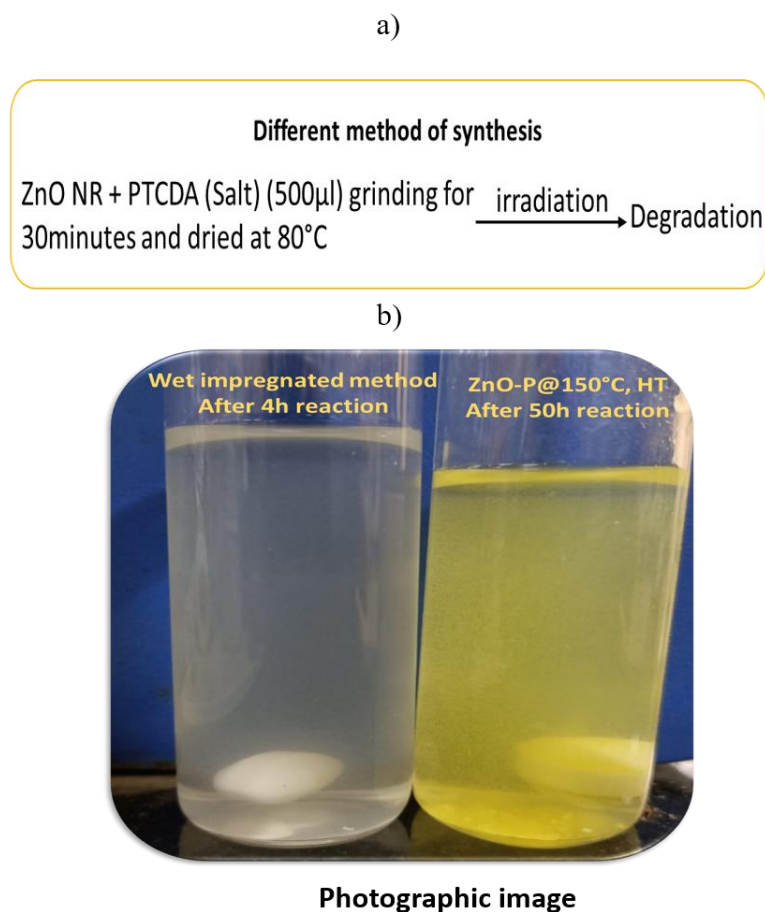
Fig.3.18.a) Wet impregnation method of synthesis to understand the interaction in ZnO-P b) Photographic image of samples under illumination with visible light (λ >450 nm)

To better understand the mechanical aspects of the photocatalytic hydrogen evolution and the crucial roles of PTCDA and ZnO in the reaction, the fluorescence lifetime study of the system was conducted by TCSPC (time-correlated single photon counting) in powdered samples of ZnO and ZnO-P at room temperature. The deterioration profile is shown in Fig. 3.19a–d. In Table.3.3, the tabular format is displayed. The numerical convolution technique, which assumes that the delta pulse response is tri-exponential and bi-exponential, deconvolutes the decay curves. Bi-exponential fits have been used to fit the response at emission wavelengths

of 380 nm and 480 nm, while tri-exponential fits have been used to fit the emission (defect emission) response at 520 nm. According to reports, the defect emission lifetime has slower components than exciton emission and is detected at roughly 79.35% components. In the case of ZnO-P, the 380nm emission from the component with a lifetime of 0.01302(94.18%) and 7.25(5.85%) indicates a two-component system, whereas the 520nm emission is the defect emission, which indicates the presence of three components with a significant contribution from the PTCDA side with 2.47(1.66%), 26.33(3.24%), and 0.018(95.09%). With a contribution of 95.09%, 0.018ns had the biggest contribution. This explains why the ZnO-P is more stable and active. The cyclic voltammetry analysis of ZnO-P in light ON-OFF mode (Fig. 3.20) further supports the development of three species in ZnO-P. Here, the emergence of three species is seen. In addition, Fig. 3.21 provides a schematic illustration of the mechanism for H2 evolution across the ZnO-P surface via methanol oxidation.
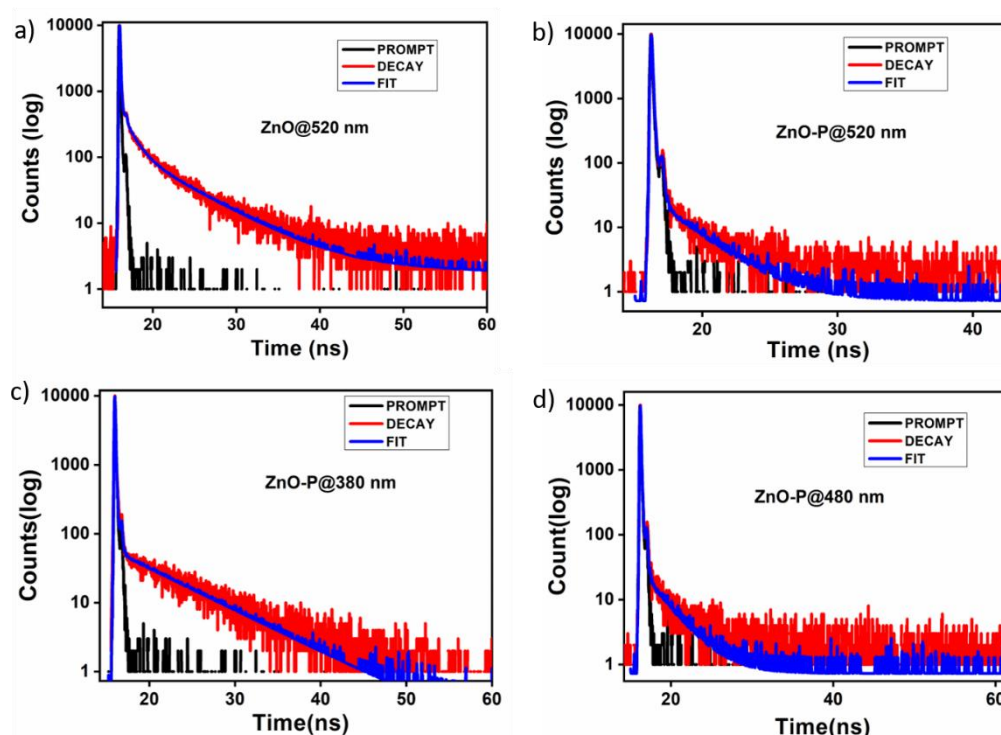
Fig.3.19. The emission decay profiles upon excitation at 374 nm for (a) ZnO @520nm emission, (b) ZnO-P@520nm emission, (c) ZnO-P@380nm emission, (d) ZnO-P@480nm emission, Instrument response function in black, decay profile in red and experimental fit in blue

Table.3.3. Lifetime parameters for pure ZnO and ZnO-P

Photocatalyst	Emission Wavelength (nm)	Lifetime(ns)		
		τ_1 (a1)	τ_2(a2)	τ_3(a3)
ZnO NR(Without PTCDA)	520 nm	0.03796 (79.35%)	4.1300 (20.65%)	-
ZnO-P(With PTCDA)	380nm	0.01302 (94.18%)	7.25 (5.82%)	-
	480nm	2.7482 (1.64%)	0.093 (98.36%)	-
	520nm	2.47 (1.66%)	26.33 (3.24%)	0.018 (95.09%)
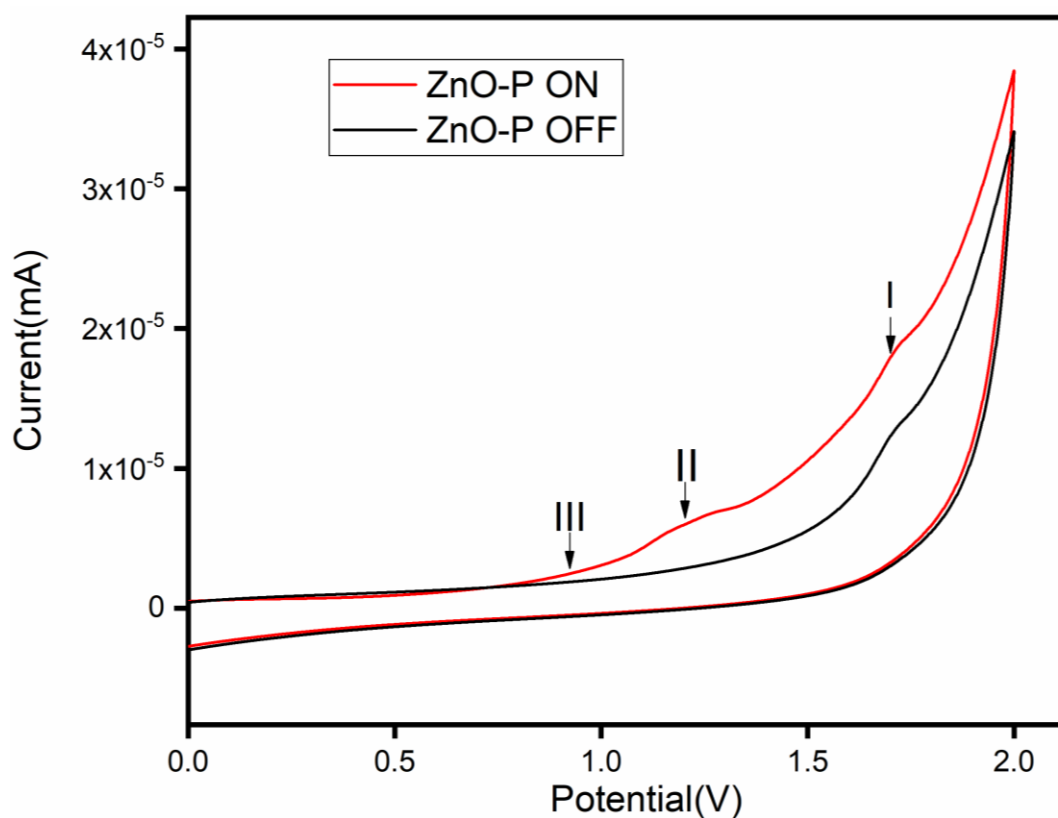
Fig.3.20. Cyclic voltammogram for ZnO-P ON -OFF mode (10mV/s) in 450W Hg Lamp by using three-electrode setup (Platinum wire counter electrode, glassy carbon working electrode, Ag/AgCl working electrode in 0.2M LiClO4 in acetonitrile as supporting electrolyte.
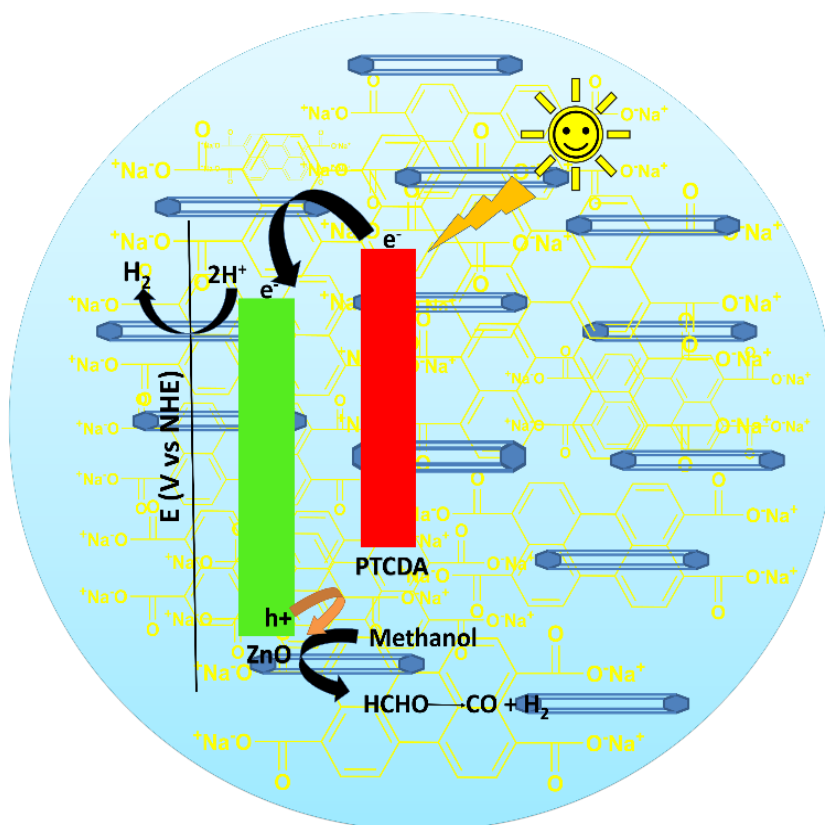
Fig.3.21. Schematic representation of the mechanism of H_2 evolution on ZnO-P photocatalyst

3.5. Conclusion

In conclusion, the synthesis of the ZnO-P heterostructure has been completed effectively. Excellent visible-range absorption is displayed by ZnO-P. After testing the photocatalytic activity, it was discovered that ZnO-P exhibits higher activity than bare ZnO and PTCDA. The creation of π-π stacking in the PTCDA and the covalent link between the two O atoms of the perylene (-COO-) group and the Zn atoms of the ZnO lattices are what cause the activity to be increased. It causes heterojunction formation, which lowers ZnO's capacity for photoreduction and reduces the recombination of electrons and holes, resulting in increased activity. Absorption experiments that combine the absorption bands for ZnO and PTCDA in ZnO-P have been done to help us comprehend this. ZnO nanorods are thought to have a band gap of 3.20 eV. The band gap shrinks in ZnO-P to 2.98eV, which is red-shifted, and ZnO-P has both the ZnO and PTCDA characteristic peaks, indicating increased light absorption in the visible spectrum. The oxygen vacancies and interstitial species are typically to blame for the characteristic green fluorescence of ZnO at 520 nm. The activity in ZnO is very low due to this green emission, also known as the defect emission, which causes the recombination of electrons and holes. To comprehend the emission characteristics of ZnO-P, fluorescence properties are used. PTCDA displays the visible emission peak at 520 nm and the peak at 580 nm. This emission is also discernible in the photoluminescence spectra of ZnO-P, where peak intensities are reduced compared to parent PTCDA. It indicates that the electron transfer mechanism from PTCDA to ZnO has lowered the amount of recombination in ZnO. This information is further connected with cyclic voltammetry data, demonstrating that ZnO-P current density rises in light compared to ZnO. It refers to the movement of electrons, or charge, from the ZnO to the PTCDA side.

3.6.References

1. Walter M. G. et al., *Chem. Rev.* **2010**, *110*, 6446-6473.

2. Ni M. et al., *Renew. Sust. Energ. Reviews* **2007**, *11*,401-405

3. C. Belabed et al., *Int. J. Hydrog. Energy,***2021**,46,17106-17115

4. Demmig, S.; et al.,. *Chem. Ber,* **1988**, 121, 225−230.

5. Liu X F et al ., *J. Phys. Chem. B* , **2008** ,112 10778

6. Yan Sun et al., *RSC Ad,* **2017,** 7, 24215–24220

7. Zhao. Y.et al., *Mater,* **2007**, 19, 3554–3558

8. A. S. Weingarten et al., *Nature Chemistry*, **2016,** 6, 964-970,

9. Roman V. Kazantsev et al., *J. Am. Chem. Soc*, **2017**, 139, 6120−6127

10. Liu, D. et al.,.*Adv Mater* **2016**, *28* (33), 7284–7290.

11. Van der Boom, et al.,. *J.Am.Chem.Soc***2002**, *124* (32), 9582–9590

12. Ji, H. F et al., *J.Am.Chem.Soc* ,**2008**, *130* (31), 10056–10057.

13. Kong,Ketal.,*Chem Commun,* **2019**, *55* (56), 8090–8093.

14. Xiaoyong Z. et al.,*ACS Appl. Mater. Interfaces* **2013**, 5, 6, 1943–1947

15. X. Ren et al., *J. Phys. Chem. B*, **2010**, 114, 4802

16. Bo Yang, et al.,*Phys. Chem. Chem. Phys*. **2014**,16, 25251-25254

17. L R. Hart et al., *Polymer* ,**2015**,69,293-300

18. Samuel E.P.*J. Am. Chem. Soc,* **2022**, 144, 27, 12290–12298

19. Qing W. et al., *J Solid State Electrochem*, **2021**,25,659–670

20. Xu D. et al., *Nat Commun,***2014,** 5, 4262

21. Yang J. et al., *Appl. Catal. B . Environ* **2018**,240,225-233

22. Haozhe Z. et al., *Energy Environ. Sci.*, **2020**, 13, 2515--2523

23. Ma, Y et al., *Sci Rep* .,2022,**10**, 22005.

24. Lionel F. et al., *J. Mater. Chem. A*, **2014**, 2, 18225–18228.

25. Xiaoyan H. et al., *J. Electron. Mater.* 2019, 48, 5055–5061

26. Yaojun L et al.,*Chem* ,**2018**, 4, 2463–2478

27. Fei Liu et al.,*J.Chem.Eng*,**2022**,429,132377

28. Giaimo, J. M et al., *J. Phys. Chem. A* **2008**, 112, 2322–2330.

29. Emilie M.G. et al*., J. Am. Chem. Soc.* **2009**, 131, 10, 3700–3712

30. Liyun Zhao et al., *Chem Commun*, **2003**, 2442–2443

31. Haijun Z et al., *Phys. Chem. Chem. Phys*., **2015**, 17, 6280—6288

32. Joel T.K. et al.,*ACS Appl. Mater. Interfaces* **2014**, 6, 16, 13367–13377

33. Kangyi K et al.,*Chem.Commun*. **2019**,55,8090-9093

34. Leena George et al., *J. Phys. Chem. C*,**2015**, 119, 3060−3067

35. Zieliñska B. et al., J. *Int. J. of Hydrog. Energy,* **2008**, *33*,1-3.

36. Schneider J. et al., *J. Phys. Chem. Lett.* **2013**, *4*, 3479-3483

37. Teoh W. Y. et al., *J. Phys. Chem. Lett.* **2012**, *3*, 629-639

Chapter 4

Supramolecular self-assemble structure of ZnO nanoparticles modified with perylene tetracarboxylic acid dianhydride.

4.1.Introduction

The process through which particular, local interactions between members without external direction form an ordered structure from previously existent chaotic components. If the constituent molecules are molecules, the process is known as molecular self-assembly. Until now, substituted perylene has been the main focus of all writing.It is well known that perylene helps Au nanoparticles self-assemble[1]. There are reports on the synthesis of self-assembled ZnO that has been modified with tetra sulfonated metal phthalocyanines on the template and its application to DSSC[2–3]. Here, we discuss a method for assembling supramolecular self-assembled structures of perylene tetracarboxylic acid dianhydride and their interactions with ZnO nanoparticles to produce a material for light-driven hydrogen (H2) production that combines light-absorbing chromophores and catalysts. ZnO nanoparticle synthesis was done in this location. Then, use perylene tetracarboxylic acid dianhydride (PTCDA), a readily available starting ingredient. The anhydride connection was then broken using KOH. The self-assembled ZnO-PTCDA structure was then created after that. PTCDA of the two varieties has been applied. The first has MC-PTCDA, whereas the second contains TC-PTCDA. It has been done to carry out structural and photophysical characterizations.

4.2. Experimental Section

4.2.1. Materials

Zinc acetate dihydrate 98% (extra pure) is brought from Sigma-Aldrich. The PTCDA (Perylene 3, 4, 9, 10-tetracarboxylic dianhydride) 97% pure is obtained from Sigma, Potassium hydroxide is brought from Merck chemicals, and absolute ethanol was purchased from analytical reagent for laboratory purposes

4.2.2. Synthesis

4.2.2.1. Synthesis of ZnO nanoparticles

Following the procedure from the research that our group previously published, ZnO nanoparticles have been created. Sol-gel synthesis was used to create ZnO NPs. At 60 °C, ethanol (144 mL) was used to dissolve zinc acetate dihydrate (0.02389 mol), which took around 30 min. At 50 °C, ethanol (98 mL) was dissolved in oxalic acid dihydrate (0.04878 mol). The heated ethanolic solution of zinc acetate dihydrate was stirred as the oxalic acid solution was gradually added. A thick, white gel developed and was allowed to dry for 20 h at 80 °C. ZnO NPs with a 20–30 nm size range were produced by calcining the gel at 400 °C for 2h.

4.2.2.2. Hydrolysis of perylene tetracarboxylic acid dianhydride (TC-PTCDA&MC-PTCDA)

Here, we have used 39.2 mg of PTCDA (4 mM mmol), first dissolved in 20 mL of aqueous potassium hydroxide solution (30 mM) at a high temperature of 50°C. The anhydride group was hydrolyzed to produce the potassium salt (TC-PTCDA). TC-PTCDA was then made by simply treating PTCDA with the aqueous potassium hydroxide. The PTCDK solution was cooled to room temperature once PTCDA had entirely disintegrated. For purposes of further characterization, the aforementioned solutions are left in place.

MC-PTCDA, prepared by dissolving PTCDA (1.96g/5mmol) in water containing Potassium hydroxide (1.12g) in 25ml of Distilled water at 90°C, with a pH value of 10. Its value is maintained up to 4 to 5 by adding 4ml of 30% HCl over 2h. The mixture was further stirred for 2 h at the same temperature. The mixture was then cooled to RT, and the precipitate was filtered and washed with hot water to get the final product in red color. 1H-NMR(Appendix 4b) is used to characterize the materials.

4.2.2.3. Synthesis of ZnO-Perylene self-assembly

A beaker containing 4mM of ZnO in a 1:1 mixture of Distilled water and methanol was prepared, and the prepared TC-PTCDA or MC-PTCDA were kept as synthesized in section 4.2.2.2.ZnO mixture under stirring conditions. The solution was stirred for 24 h at room temperature (35°C), and collected the samples by centrifugation at 13000 rpm speed for about

10 min. Washed with distilled water several times and then finally with methanol. The sample was collected by drying it at 60°C for 24h. The different sets of reactions were carried out depending on the surface modification, concentration, and size of ZnO nanoparticles used in the study, to see the difference in self-assembly formation. Oleic acid has been used to modify the surface since it is known to form hydrophobic ends over the surface of ZnO. To understand the concentration variation, different concentration of PTCDA has been synthesized in two different particle size of ZnO has been chosen and the results have been discussed in other sections of the results and discussion scheme of reaction given in Table 4.1.

Table 4.1. A different set of reactions under various conditions

Sr.No.	ZnO	PTCDK (mL)	Oleic acid	Methanol(mL)	Water(mL)	Observation
1	250mg (12-15nm)	25(0.4mM)	-	10	10	Self-assemble
2	250mg(20-40nm)	25(0.4mM)	--	10	10	No
3	250mg(20-40nm)	25(0.4mM)		-	20	No
4	-	25(0.4mM)	-	10	10	No precipitate
5	250mg(20-40nm)	25(0.05mM)	-	10	10	No
6	250mg(20-40nm)	-	1mL	-	20mL	Surface modification
7	250mg(20-40nm)	25(0.4mM)	2mL	10	10	No
8	250mg(20-40nm)	-	10µl	-	20mL	Surface modification
9	250mg(20-40nm)	25(0.4mM)	10µl	10	10	No
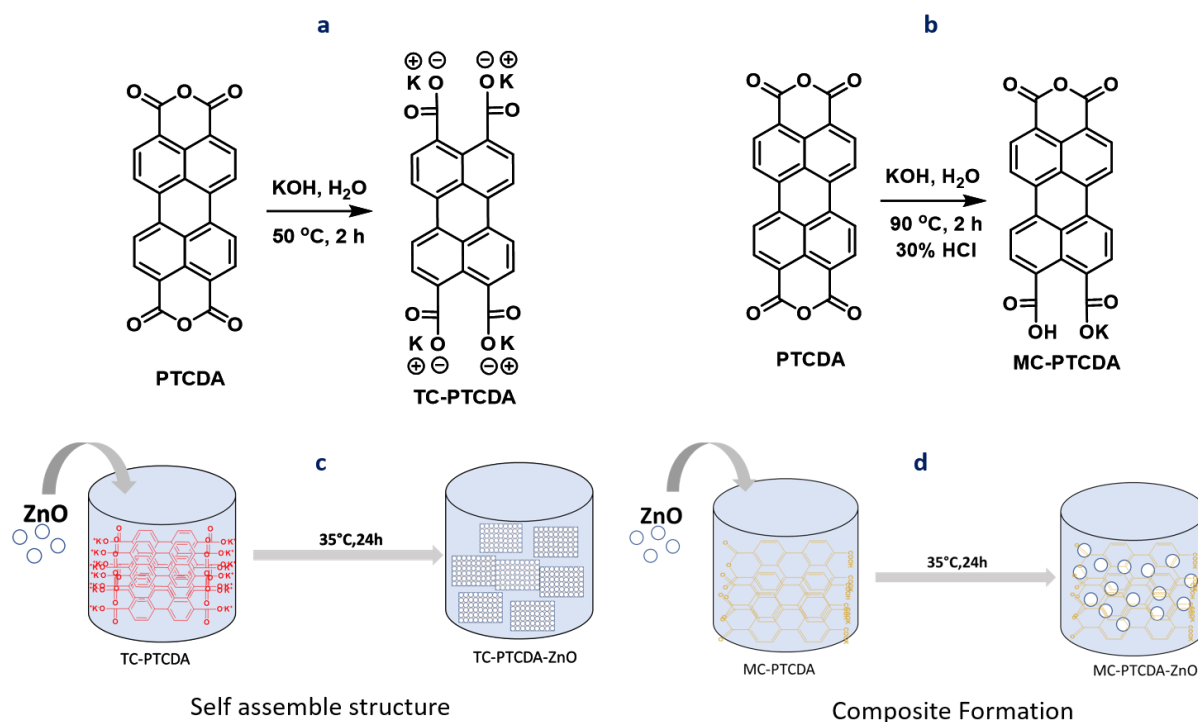
Scheme 4.1.Synthesis of MC-PTCDA and PTCDA, along with the formation of MC-PTCDA-ZnO and TC-PTCDA-ZnO

4.3. Material characterizations

The steps taken for PXRD, FE-SEM, TEM, IR, UV-vis, photoluminescence, NMR, electrochemical tests, and elemental analysis are identical to those given in chapter 2 Part 2A, section 3. In Appendix 2a, all the characterisation approaches employed throughout the paper are briefly reviewed together with their underlying ideas and instruments.

4.4.Results and discussion

The production process and solvent that we use affect the size and form of ZnO nanoparticles.

Since ZnO has a hexagonal crystal structure, it typically forms hexagonal structures such cones

and columns, micro prisms, and microtubes. Figure 4.1 a, created from the FESEM images. With TEM pictures displaying the spherically shaped morphology with a size of 20- 30 nm, ZnO synthesized by the sol-gel technique exhibits aggregated spherical-shaped geometry (Fig.4.1.d). Following treatment with TC-PTCDA, self-assembled Zinc Oxide (ZnO) nanoparticles can be seen to have a particular shape in representative FESEM pictures. ZnO exhibits a self-assembled structure with a well-defined rectangular shape. Around 2.294 um is the length of rectangular ZnO (Fig. 4.1.b). The self-assembled structure of perylene with ZnO is also visible in the TEM pictures (Fig. 4..1.e). ZnO treated with MC-PTCDA exhibits no morphological changes in the FESEM or TEM pictures (Fig. 4.1.c and f). It demonstrates that the presence of a tetra-substituted carboxylic group in perylene is required for the formation of self-assembly with ZnO nanoparticles. As seen in Fig.4.2, X-ray diffraction (XRD) was employed to examine the phase purity of the synthesized ZnO. Most of the peaks' relative intensities are in good accord with the ZnO wurtzite hexagonal structure determined by JCPDS No.01-079-0206. For any of the synthesized samples, there were no peaks associated with impurities.
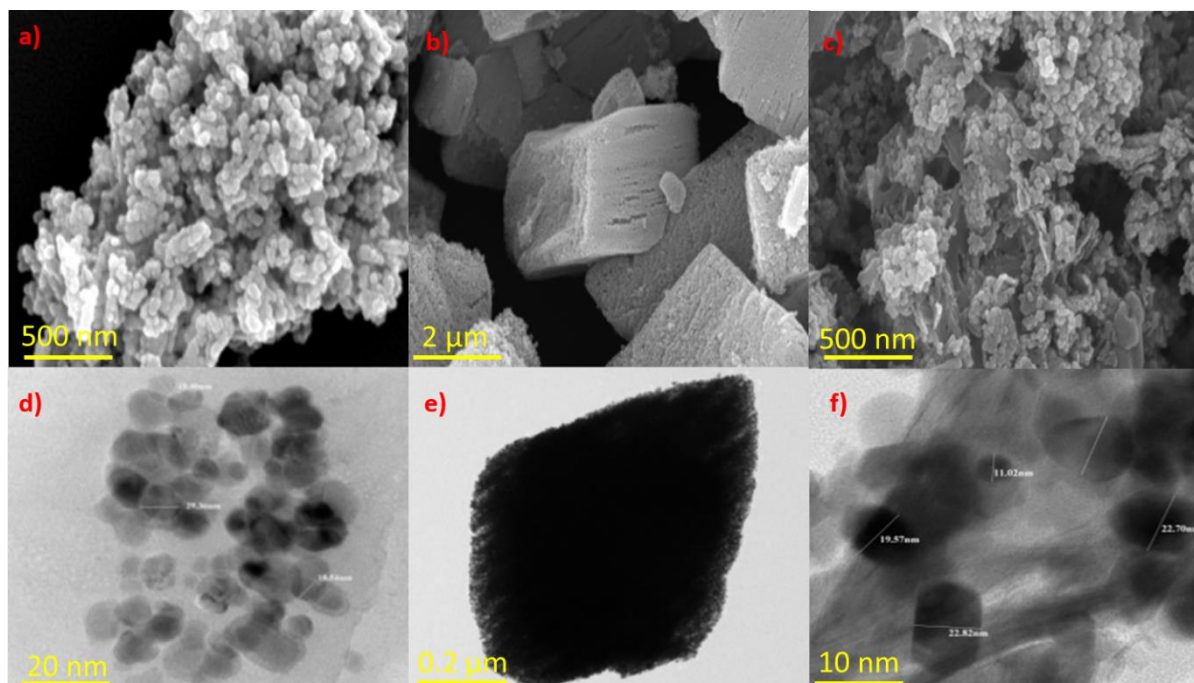
Fig.4.1. FESEM analysis of (a) ZnO (b) TC-PTCDA-ZnO (c) MC-PTCDA-ZnO and

TEM analysis of (d) ZnO (e) TC-PTCDA-ZnO (f) MC-PTCDA-ZnO
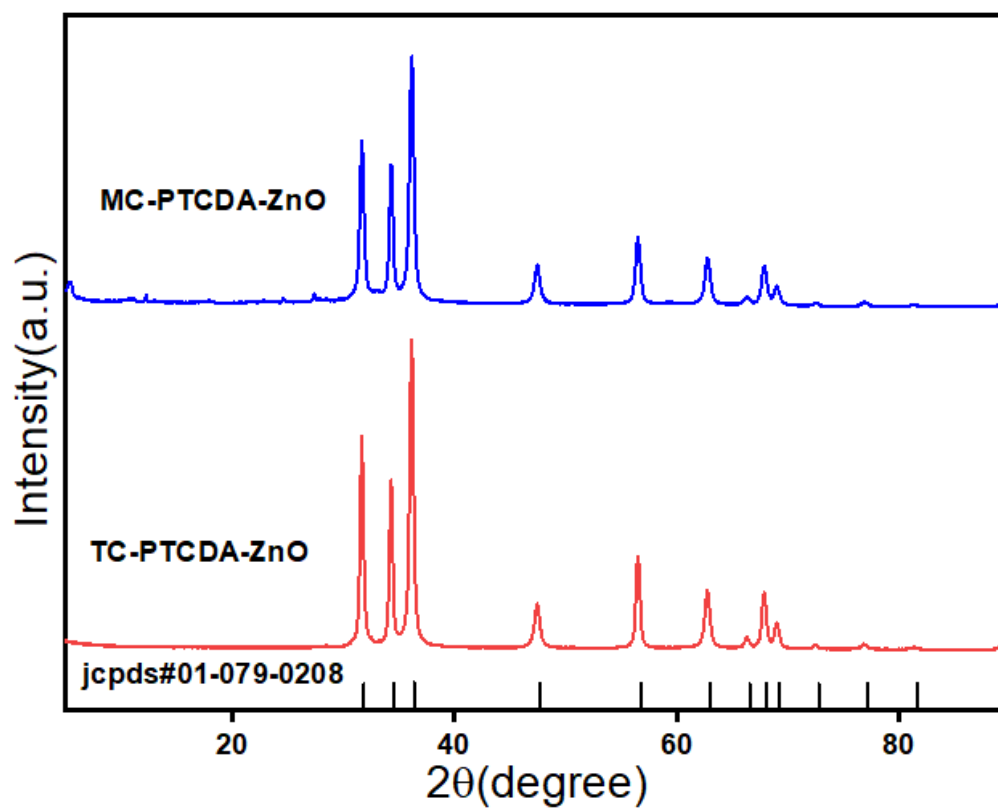
Fig.4.2. P-XRD pattern of TC-PTCDA-ZnO and MC-PTCDA-ZnO

As described in section 4.2.2.4 of the synthesis chapter, numerous synthesis approaches have been used further to comprehend the concept generation of self-assembly in TC-PTCDA-ZnO. The creation of uniform self-assembly is not observed when the particle size grows from 12 to 40 nm, which indicates that the size of the ZnO particles is crucial in determining the shape of the self-assembly of TC-PTCDA-ZnO (Fig. 4.3a-b). When the concentration of TC-PTCDA is decreased from 4mM to 0.05mM to understand the effect of the concentration on the self-assemble structure, it is seen that small agglomerated structures of ZnO are visible but not as such self-assemble structures, indicating that it is also not affecting the structural formation (Fig. 4.3c). The absence of a source of methanol causes the reaction to fail to produce the TC-PTCDA-ZnO self-assembly structure, indicating that methanol is also necessary for self-assembly to occur (Fig. 4.3d). Since many years ago, ZnO has had its surface modified with oleic acid, and this surface modification has been applied to numerous devices[4-6]. Oleic acid makes ZnO's surface more water-repellent by increasing its surface hydrophobicity. This is the first place this idea has been used. Oleic acid is applied to the ZnO surface in two distinct concentrations. ZnO's spherical particle shape completely transforms into sheets when 1 ml of oleic acid is applied, but the crystal structure remains unaltered (Fig. 4.4a). After adding TC-PTCDA solution to the oleic acid-treated ZnO, the shape does not change (Fig. 4.4b). It is evident that the shape of ZnO is kept with spherical particles even after treatment with TC-PTCDA; it remains the same and no formation self-assembly is observed (Fig. 4.4c-d) as the concentration of oleic acid is again reduced to 10 µl. This finding supports the hypothesis that

the surface should be hydrophilic. To achieve a consistent self-assembly structure, consideration must be given to the nanoparticle size and solution concentration.
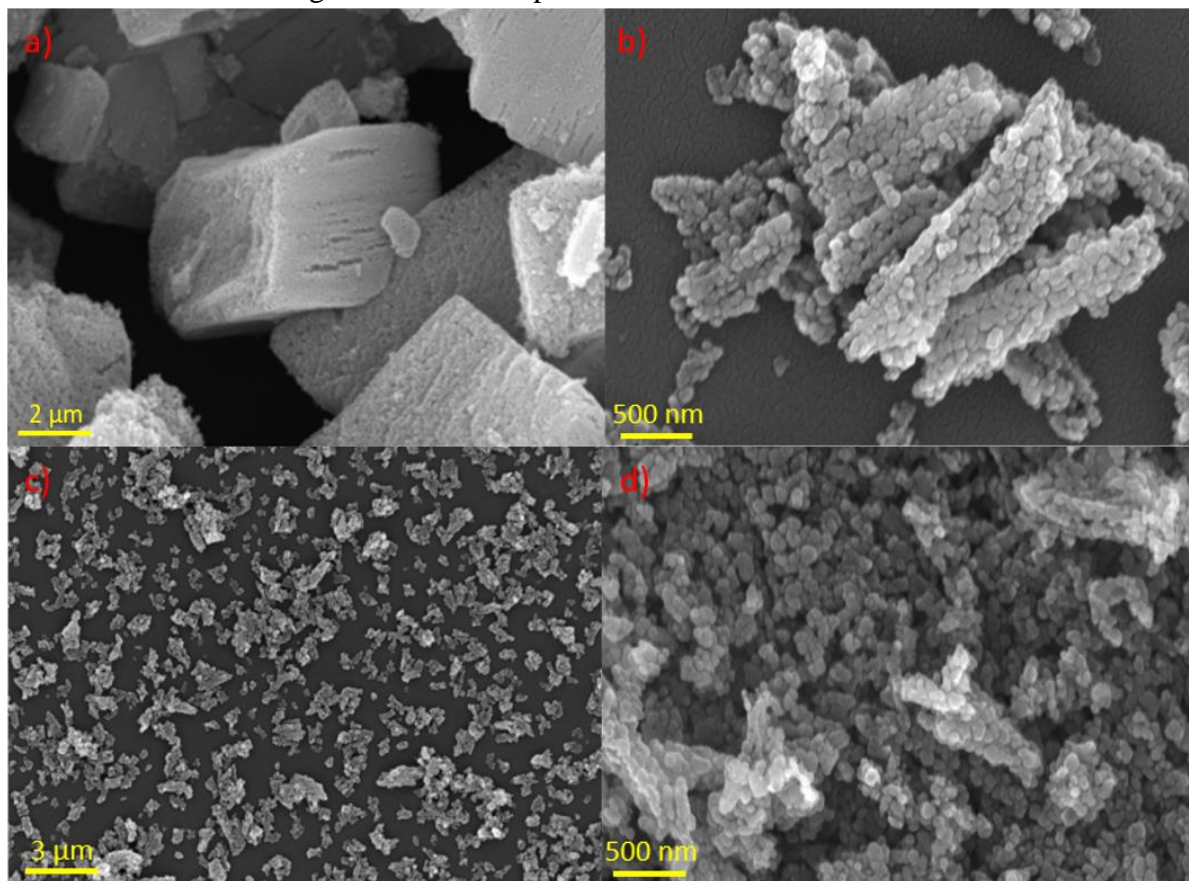
Fig.4.3. FESEM analysis of a) TC-PTCDA-ZnO(12-15nm) b) TC-PTCDA-ZnO(20-40nm) c) TC-PTCDA-ZnO(0.05mM of TC-PTCDA) and d) TC-PTCDA-ZnO (No methanol)
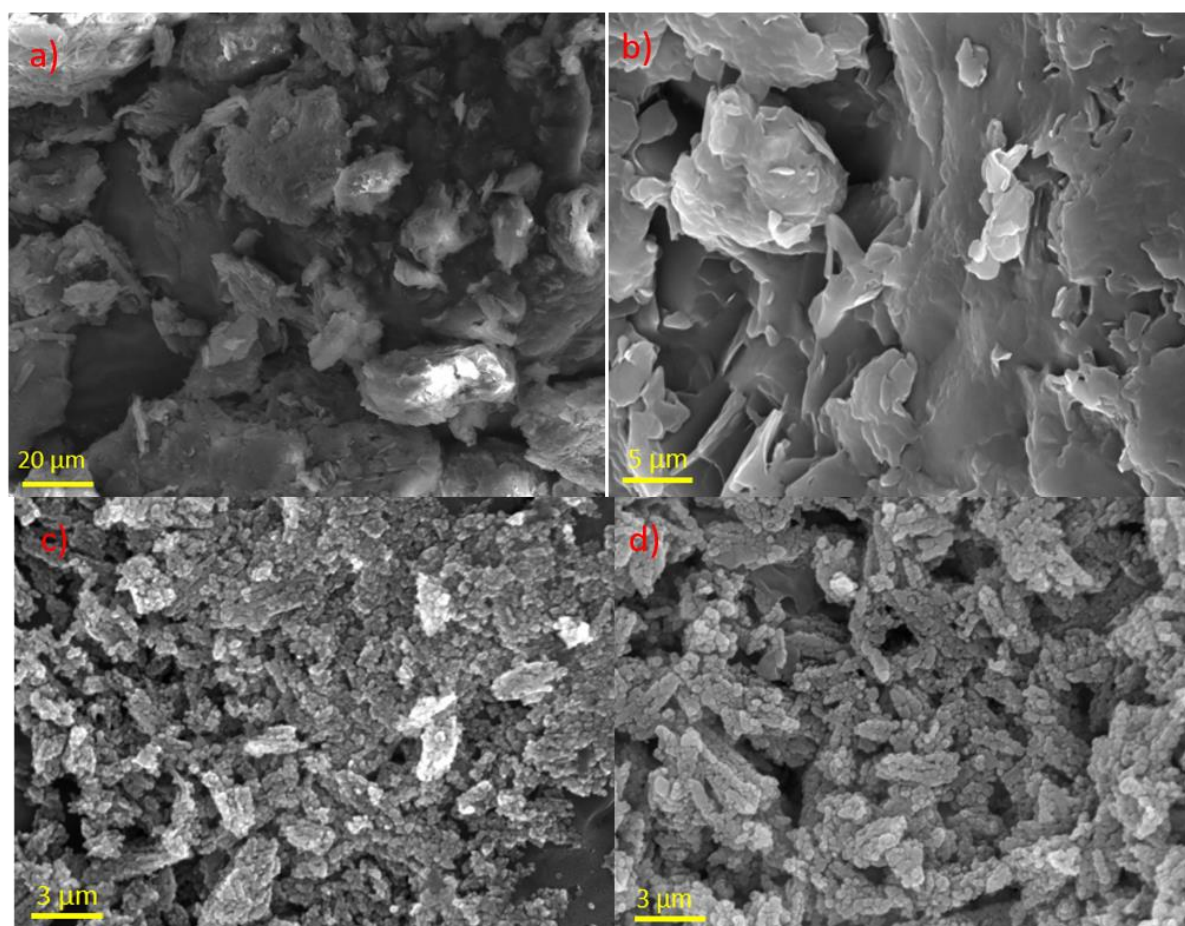
Fig.4.4. FESEM analysis of a)ZnO(oleic acid 1ml) b) TC-PTCDA-ZnO(oleic acid 1ml) c) ZnO(oleic acid 10µl) and d) TC-PTCDA-ZnO(oleic acid 10µl)

The interactions between the nearby molecules in the system directly impact the optical and electrical characteristics of photocatalysts. ZnO, TC-PTCDA-ZnO, and MC-PTCDA-ZnO were all measured for their optical characteristics using the UV-Visible absorbance spectrum. The structures of TC-PTCDA-ZnO and MC-PTCDA-ZnO exhibit wider visible range absorption, as shown in Fig. 4.5, making it possible to use long wavelength visible light for the application in visible light H2 evolution. The significant confinement effect brought on by the neighboring perylene molecules might be attributed to the blue shift of the highest absorption

peak of supramolecular TC-PTCDA-ZnO. The TC-PTCDA's strong π-π interactions between nearby perylene molecules are also revealed by this event.

Additionally, the ZnO particles are arranging themselves properly and producing a self-assembling structure, which would encourage a lower energy intermolecular charge transfer[7-10]. To compute the band gap energies, $F(R) = (1-R)^2/2R$, a relation between reflectance and the Kubelka-Munk factor, was utilized [11]. By creating a Tauc plot, specifically a plot of $(F(R)hv)^{1/2}$ vs hv, the band gap of bulk powder samples is measured using the Kubelka-Munk model as the foundation. Tauc plots (Fig. 4.6) revealed that TC-PTCDA had a band gap of 2.2 eV, higher than that of MC-PTCDA (1.9 eV). Creating H-type π-π stacking in the supramolecular structure of TC-PTCDA-ZnO may be responsible for this phenomenon.
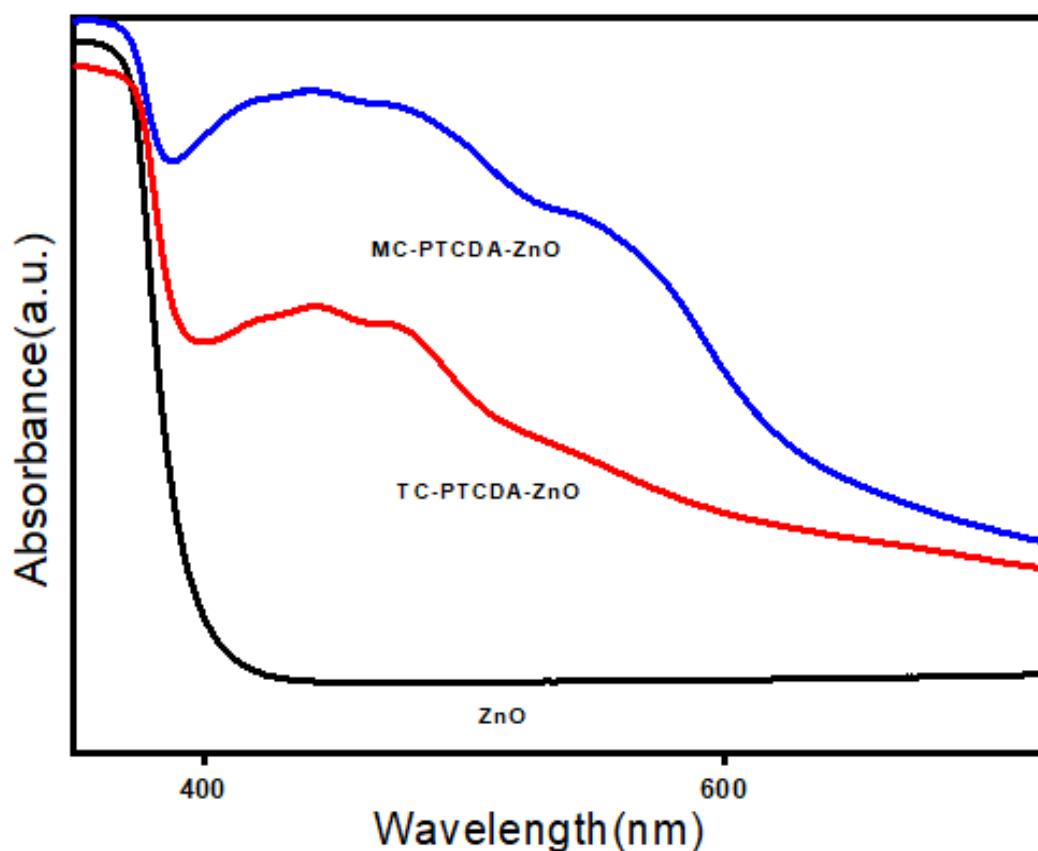
Fig.4.5.UV-Visible absorption spectra of ZnO, TC-PTCDA-ZnO, and MC-PTCDA-ZnO DA-ZnO.
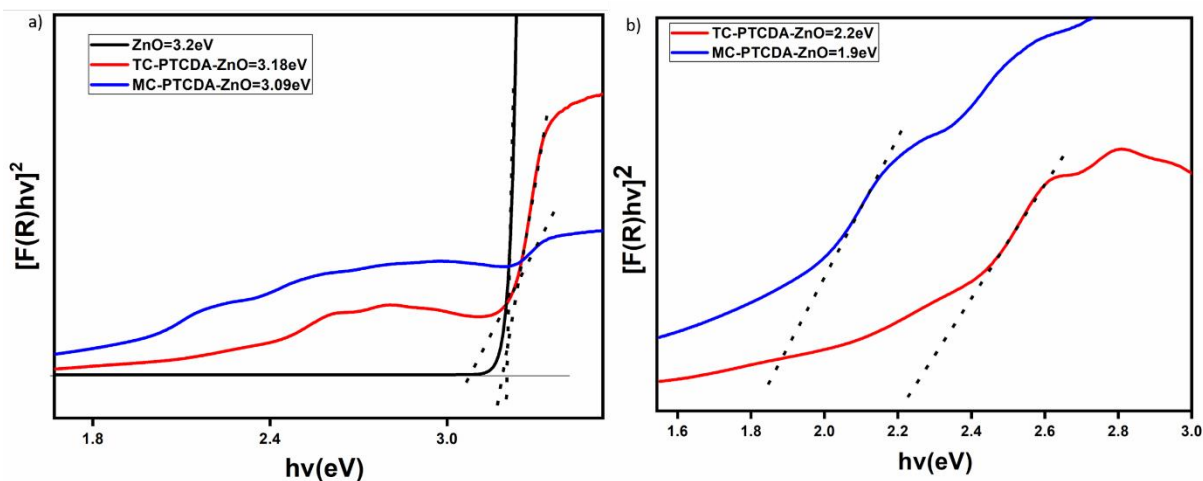
Fig.4.6. Bnad gap calculations (Tauc plots) for a) pure ZnO(black), TC-PTCDA-ZnO(red), and MC-PTCDA-ZnO(blue), b) TC-PTCDA (red) and MC-PTCDA (blue).

An attempt was made to compute flat band potentials based on Mulliken electronegativity using the empirically determined band gap energy [12]. In Appendix 4a, the computations' specifics are described. This technique has been employed frequently to determine the band properties of simple oxides. This approach is recommended to provide thorough knowledge even in complex oxides, even though structural contributions are not considered. The following equation has been used to calculate the band locations of ZnO:

$$E_{vfb} = EA - E_{ref} + (1/2\ E_g) \qquad\qquad (4.1)$$

where EA is each atom's affinity for electrons.

It can be calculated using the geometric mean of each element's electronegativity. Mulliken's calculations served as the basis for the electronegativity. On a hydrogen scale, E_{ref} is the energy of free electrons. In Fig. 4.8, the band locations of ZnO, TC-PTCDA, and MC-PTCDA are depicted about a standard hydrogen electrode.The energy levels of the HOMO of the self-assembled supramolecular were also identified in the cases of TC-PTCDA and MC-PTCDA

by cyclic voltammetry in THF (Fig. 4.7). As an internal reference and as a supporting electrolyte, 0.1 M tetra-n-butylammonium hexafluorophosphate (TBAPF$_6$) was utilised (Appendix 4b). Fig. 4.8 displays the band diagrams. TC-PTCDA and MC-PTCDA had HOMO levels of 1.53V and 0.89V vs. NHE, respectively. Appendix 4b contains the computations' specifics.

The relationship between

$$-E_{V \ vs. \ vacuum} = E^{onset} - E_{V \ vs. \ Fc/Fc+} + 4.8 \ eV \qquad (4.2)$$

$$E_{V \ vs. \ NHE} = -(E_{V \ vs. \ vacuum} + 4.5 \ eV) \qquad (4.3)$$

The LUMO was calculated by using the equation.

$E_{LUMO} + E_{HOMO} = E_g$ \qquad (4.4)

According to the statistics, the LUMO for TC-PTCDA is -0.88V and for MC-PTCDA, it is -1.01V. These results demonstrate that the respective redox potentials of TC-PTCDA and MC-PTCDA are higher than the redox potential of hydrogen evolution. As a result, this will guarantee sufficient driving power to produce both H$_2$ evolution and water reduction. The band diagram demonstrates that TC-PTCDA's redox potential is closer to the conduction band of ZnO (-0.31V). As a result, compared to MC-PTCDA, the excited electrons from TC-PTCDA's LUMO can move more quickly to the CB of ZnO and cause higher H$_2$ evolution activity. By comparing the H$_2$ activity of pure ZnO, TC-PTCDA-ZnO, and MC-PTCDA-ZnO, the photocatalytic H$_2$ activity has been performed to verify this assumption.
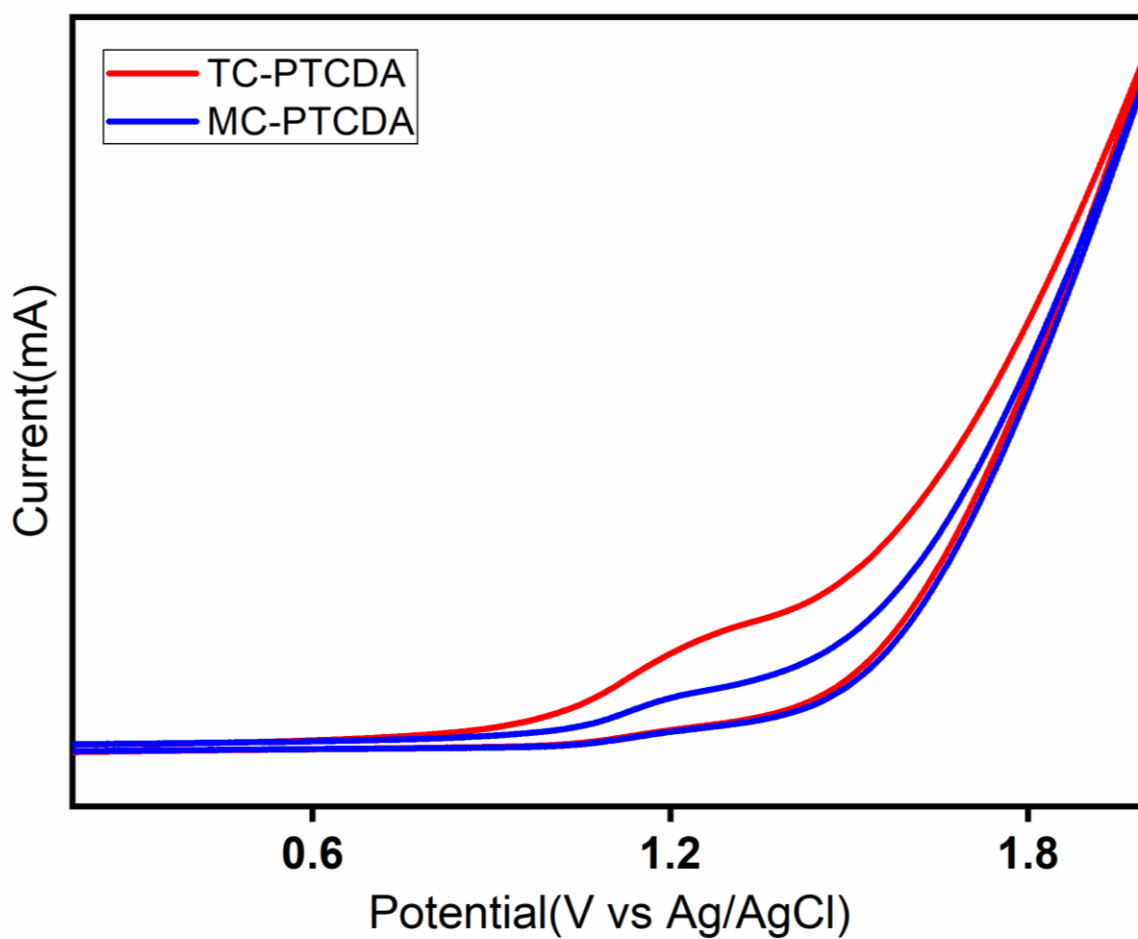
Fig.4.7. Cyclic voltammograms curves of TC-PTCDA and MC-PTCDA
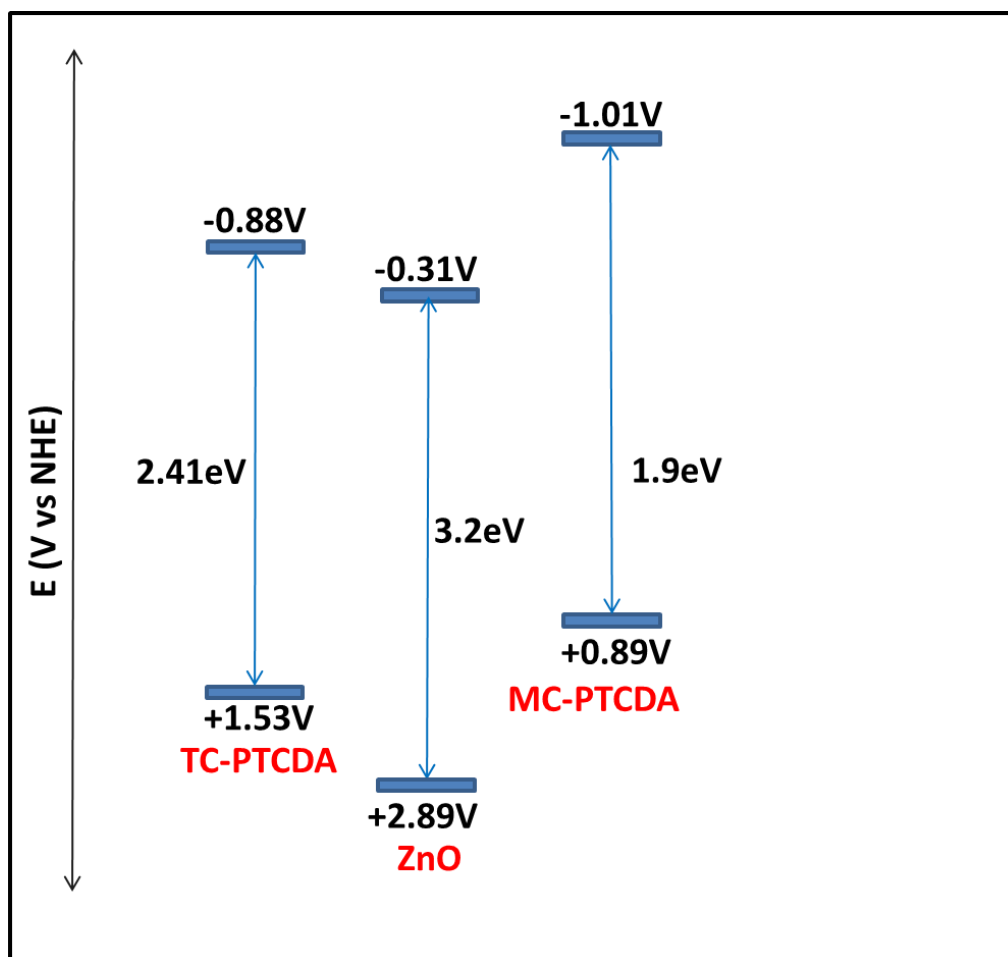
Fig.4.8.The band diagrams of ZnO, TC-PTCDA, and MC-PTCDA

After understanding all the aspects of this study Comparison of the H_2 evolution activity of pure ZnO, TC-PTCDA-ZnO, MC-PTCDA, and MC-PTCDA-ZnO in 25% (v/v)MeOH/Water system under illumination with visible light (λ >450 nm) has been studied. The hydrogen evolution activity has been checked with 25% methanol in water without adding any co-catalyst. The advantage of our system is that we are not using any co-catalyst, and still, the system provides a good amount of hydrogen with stability. Due to the presence of nearer LUMO of TC-PTCDA (-0.88V) to the CB of ZnO(-0.31V), the activity is about 2050μmol/h for TC-PTCDA which is two times highest as that of MC-PTCDA that is 1000 μmol/h(Fig.4.9).The addition of both TC-PTCDA and MC-PTCDA is leading to increasing the

activity of ZnO. This way, one can reduce the recombination in the ZnO as well as the utility

of broader visible absorption spectrum talks place; thus disadvantage of UV light activity of

ZnO has overcome hereafter that the continuous activity of TC-PTCDA-ZnO has been carried

out up to 5h, and it was showing an increase in activity(Fig.4.10).
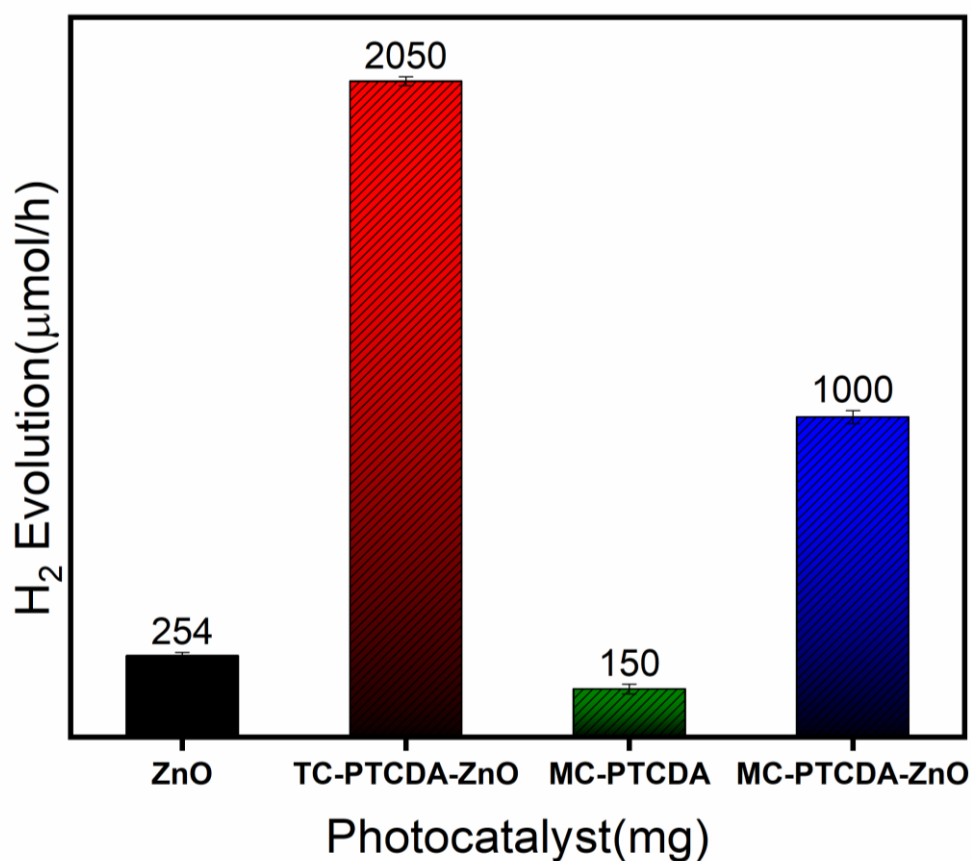
Fig.4.9. Comparison of H_2 evolution activity of pure ZnO, TC-PTCDA-ZnO, MC-PTCDA, and MC-PTCDA-ZnO in 25% (v/v)MeOH/Water system under illumination with visible light (λ >450 nm)
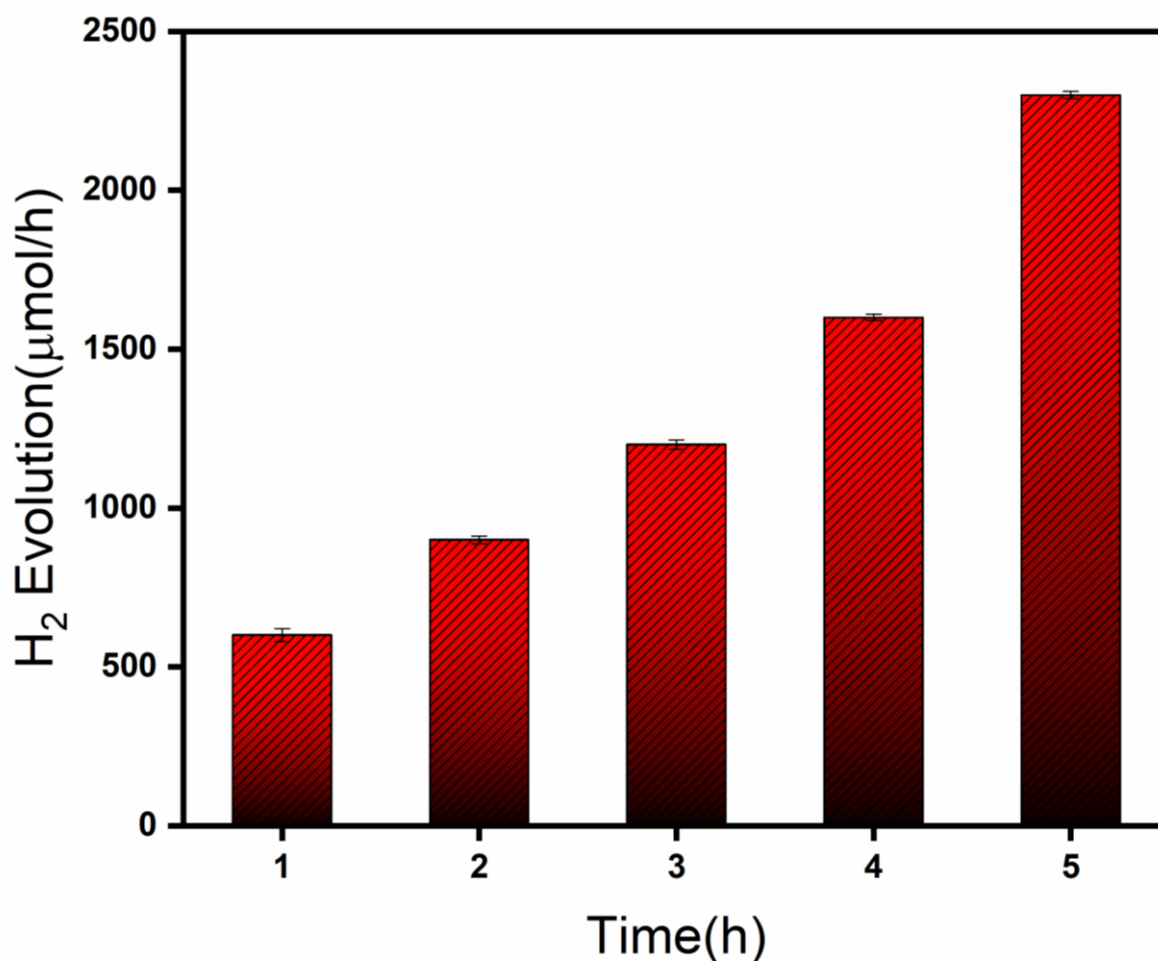
Fig.4.10. H_2 evolution activity of TC-PTCDA-ZnO in 25% (v/v)MeOH/Water system under illumination with visible light ($\lambda >450$ nm)

4.5.Conclusion

The supramolecular TC-PTCDA-ZnO photocatalyst was successfully employed as a photocatalyst for photocatalytic H_2 evolution via water splitting after being synthesized under mild circumstances. This photocatalyst showed an activity of about 2050µmol/h. Once the terminal end of the anhydride group changed from the tetra carboxylate group to the

monocarboxylate group (MC-PTCDA-ZnO), the drastic change in the structural features observed which led to a decrease in the activity to 1000µmol/h. During the MC-PTCDA-ZnO, the structures form simple composite rather than supramolecular structures. The reason is that the supramolecular system leads to π-π stacking, leading to intermolecular charge transfer. Thus, it facilitates electron transfer more efficiently, increasing activity in TC-PTCDA-ZnO. This photocatalyst works without any co-catalyst, reducing the synthesis cost; therefore, this can form a future generation of organic-based photocatalysts.

4.6.References

1. G. Santosh et al., *J. Phys. Chem. B*,**2010**, 114, 14389–14396

2. Tsukasa Yoshida et al., *Chem. Mater.* **1999,** *11,* 2657-2667

3. Tsukasa Yoshida et al., Chemistry letters 1998,27,599-600

4. Hengzhi Chen et al., *Polymers*, **2018**, 10, 362

5. C.P. Leo et al., *Sep. Purif. Technol.***2012**,89, 51–56

6. Lili Wu et al., *RSC Adv*, **2016**,6, 69836-69844

7. Liyun Zhao et al., *Chem Commun*,**2003**,2442-2443

8. Haijun Z et al.*, Phys.Chem.Chem.Phys*,**2015**,17,6280-6288

9. Joel T.K. et al., *ACS Appl.Mater.Interfaces*, **2014**,6,16,13367-13377

10. Kangyi K et al., *Chem.Commun*.**2019**,55,8090-9093

11. Murphy, A. B. *Sol. Energy Mater. Sol. Cells* **2007**, *91,* 1326

12. Kim, Y. F et al., *J. Phys. Chem.* **1993**, *97,* 11802

Chapter 5

Synthesis of $[M(II)_{(1-x)} M(III)_x(OH)_2](A_{x/n}).m H_2O$/PDI layered double hydroxides and their applications in the photocatalytic hydrogen evolution (M=Co & A= Cl)

5.1. Introduction

The vast class of anionic layered materials known as layered double hydroxides (LDHs) is based on the brucite structure with edge-sharing M(OH)6 octahedra [1-2]. The formula for LDHs is $[M^{2+}_{1-x}M^{3+}_{x}(OH)_2] (A^{n-})_{x/n}.mH_2O$, where M^{2+} and M^{3+} are divalent (like Mg^{2+}, Zn^{2+}, Cu^{2+}, or Co^{2+}) and trivalent metal cations (like Al^{3+}, Fe^{3+}, or Cr^{3+}). Anions in the hydrated interlayer galleries can counteract the positive charges in the host layer. Due to the broad tunability of the host layer and the ion-exchangeable properties of the interlayer guest ions, LDHs are a diverse family of materials. Due to multiple efforts to enhance the composition and usefulness of LDHs and LDH-based products, LDH usage has also expanded. The typical procedures for preparing LDH include coprecipitation and heat treatment. LDHs with different particle sizes, morphologies, and crystallization levels can be created by varying the reactant concentration, temperature, and aging time. Other approaches, including in situ growth, electrosynthesis, and calcination-reconstruction, have also been developed to produce LDHs with tunable morphology and properties. Intriguing applications for layered hydroxides include electrodes, catalysis, and other fields [3]. Due to the structural flexibility of layered hydroxides, numerous anionic species can be distributed between their interlayers, creating a variety of hybrid materials with different properties [4–11]. Cobalt hydroxide has a greater separation of catalytic sites than its equivalent because it exhibits more fascinating interlayer chemistry and has a more flexible structure. Therefore, this chemical was selected as the semiconductor support in this study.

Perylene and its derivatives are appropriate as a photocatalyst among all of these and are employed in Chapter 3 as well. Due to the several uses for this dye, the same perylene has been utilised throughout this chapter [12–17]. The activity towards the hydrogen evolution by splitting water and the stability of the organic photocatalyst are yet unclear. The synthesis and characterisation of α-Co(OH)2 and β--Co(OH)2 were the main topics of this chapter. Next, the structure of α-Co(OH)2 was modified with PDI to allow for additional investigation and H2 evolution reactions.

5.2. Experimental Section

5.2.1. Synthesis of α-Co(OH)$_2$

The synthesis was conducted in an ambient atmosphere in a flask with a circular bottom. Typically, 200 mL of a 9:1 mixture of Millipore ultrapure water and ethanol was used to dissolve CoCl2.6H2O (0.4758 g), NaCl (0.5845 g), and Hexamethyl tetraamine (HMT) to yield the final concentrations of 10, 50, and 60 mM, respectively. The reaction solution was then heated at roughly 90 °C and stirred magnetically. Approximately two hours of heating produced a suspension with green particles. The solid result underwent numerous rounds of filtering, washing with deionized water and anhydrous ethanol, and air drying at room temperature. Initially, the solution's color was pink. After about 30 minutes, it changed to a bluish hue, and eventually, a suspension of green particles was formed.

5.2.2. Synthesis of β-Co(OH)$_2$

The procedure was comparable to that of -Co(OH)2. The intercalated anions in the hydroxide layers are what make the difference. The synthesis was conducted in an ambient atmosphere in a flask with a circular bottom. In a typical process, millipore ultrapure and ethanol were dissolved in 200 mL of CoCl2.6H2O (0.4758 g) and hexamethyl tetraamine (HMT) (1.6822 g) to give final concentrations of 10 and 60 mM, respectively. The reaction solution was then heated at roughly 90 °C and stirred magnetically. Approximately two hours of heating produced a suspension with pink particles. The solid result underwent numerous rounds of filtering, washing with deionized water and anhydrous ethanol, and air drying at room temperature. Both the supernatant and residue's color changed to pink and remained pink.

5.2.3. Synthesis of PDI (N, N'-bis(p-carboxyl-phenylene) perylene-3,4: 9,10-perylene bisimide)

At 90°C, 30 g of imidazole, 2 mL of chloroform, and 302 mg (0.77 mmol) of 3, 4, 9, and 10 perylene tetracarboxylic dianhydride were mixed together. Then, 4 aminobenzoic acid, 257 mg (1.87 mmol), was added. 1 mg of Zn(CH$_3$CO$_2$)$_2$·2H$_2$O was added to the reaction to carry it out. The mixture was then refluxed at 130°C with stirring for 24 h, acidified, and filtered through a G4 funnel filter.

The residue was extracted in anhydrous ethanol after being rinsed with additional water. Pure N, N'-bis(p-carboxyl-phenylene) perylene-3,4: 9,10-perylene bisimide (PDI) was 90% of the yield. (Scheme 5.1) contains the reaction scheme.

Scheme 5.1: Synthesis of PDI

PTCDA   4-aminebenzoic acid

N,N'-Bis(P-Carboxyl-Phenylene)
perylene-3,4,9,10-Peryelene bisimide
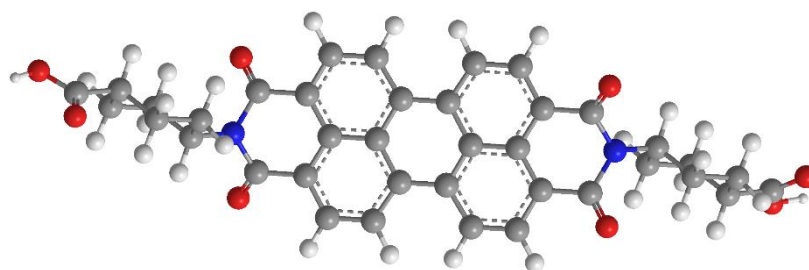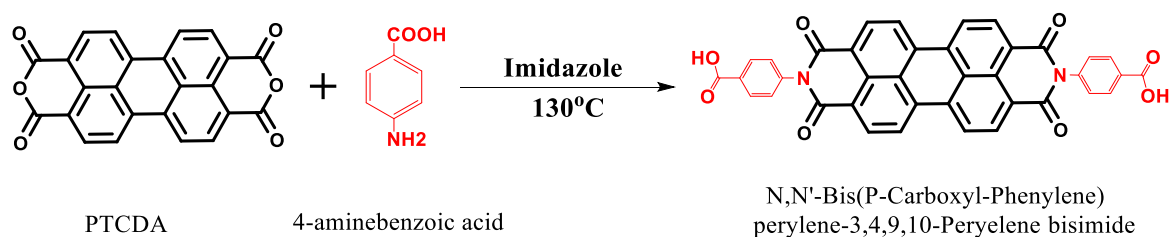
(PDI= N, N'- bis(p-carboxyl-phenylene) perylene-3,4: 9,10-perylene bisimide)

5.2.4. Synthesis of α-Co (OH)$_2$ with PDI [α-Co(OH)$_2$-PDI]

As produced, a solution of (1.6x10-3M) PDI (N, N'- bis(p-carboxyl-phenylene)perylene-3,4:9,10-perylene bisimide) in DMSO (dimethyl sulphoxide) was added to 10 mg of α-Co (OH)2 in 5 ml of Millipore water (0.02152) solution in a 50 ml round bottom flask. The reaction mixture was then maintained for 24 h at 25°C and 400 rpm. The outcome was a suspension with red particle content. The solid product underwent numerous rounds of filtering, deionized water washing, anhydrous ethanol washing, and storage for drying at 60°C.(Scheme.5.2).

Scheme.5.3 provides a photographic representation of the transition from green to a dark red-brown color.

Scheme 5.2. Synthesis of α-Co(OH)$_2$-PDI
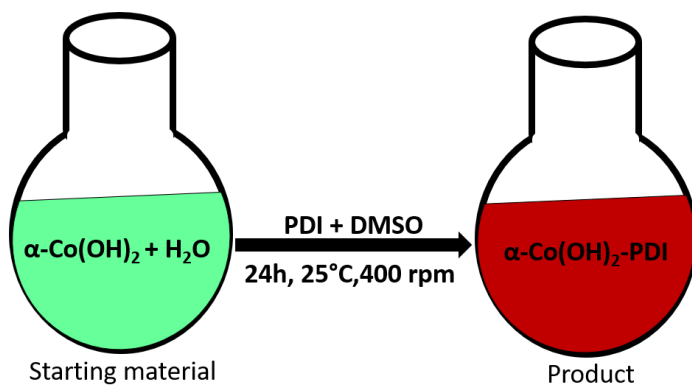
PDI= N,N'- bis(p-carboxyl-phenylene) perylene-3,4 : 9,10-perylene bisimide(1.6x10^{-3}M)
DMSO= dimethyl sulphoxide

Scheme 5.3: Photographic image of the color change of green for α-Co(OH)$_2$ to red-brown of α-Co(OH)$_2$ -PDI
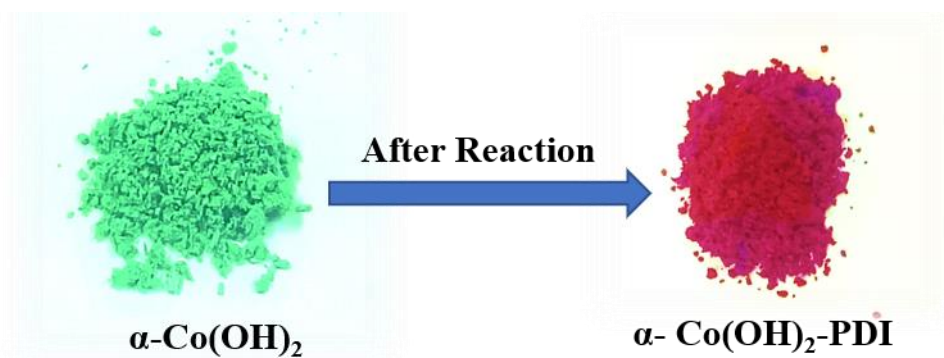
5.3. Characterizations

The steps taken for PXRD, FE-SEM, TEM, IR, UV-vis, photoluminescence, NMR, electrochemical experiments, and elemental analysis are identical to those detailed in Chapter

2's section 3. In Appendix 2a, all the characterization approaches employed throughout the paper are briefly reviewed together with their underlying ideas and instruments.

5.4. Result and Discussion

5.4.1. Characterisation of N, N'- bis(p-carboxyl-phenylene) perylene-3,4: 9,10-perylene bisimide (PDI)

The purity of the PDI was verified using elemental analysis, and the observed and predicted CHN values agree:

Calculated (%): C=70.42%, N=5.00%, H=2.57%, H=2.88; found (%): C=70.42%, N=5.00%. The structure of PDI was verified by using 1H NMR, 13C, and DEPT (spectra shown in Appendix 5a-Fig. 5a.1). The hydroxyl proton linked to the carboxylic moiety of the perylene ring is the wide singlet visible at 10.72 ppm. The doublet at 8.98-8.95 ppm corresponds to the perylene ring's -CH aromatic protons. The -CH aromatic protons bound to the azobenzene ring are represented by the multiplets at 8.24-8.41 ppm and 7.21-7.71 ppm.

The ^{13}C NMR was also recorded in D_2SO_4-D_2O at 500MHz, which shows the values of 177.92, 166.01, 139.01, 134.51, 129.65, 127.47, 126.04, 119.19, 118.99, 117.43.

In the vicinity of 3000 cm-1, the symmetric O-H stretching modes detected a wide, sharp band. Stretching vibrations may be seen in the IR spectrum of the primary amino group's N-H bonds and the aromatic ring's C-H bonds, with maxima at 3236, 3040, and 2931 cm-1, respectively. The C=O bond in the carboxyl group displays a band of vibrations at 1760 and 1698 cm-1. The absorption bands with peaks at 1594 and 1507 cm-1 indicate the valence vibrations of the C=C bonds in the aromatic ring structure. The 1413, 1350, 1280, and 1255 cm-1 peaks are attributed to the aromatic ring structure's strong C=N and N=N stretching vibrations. In Figure 5.1, the bands of the N-H bonds in the deformation vibration of the amino group and the C-H bonds in the deformation vibration of the benzene ring are registered at 1174 and 1119 cm-1, respectively.
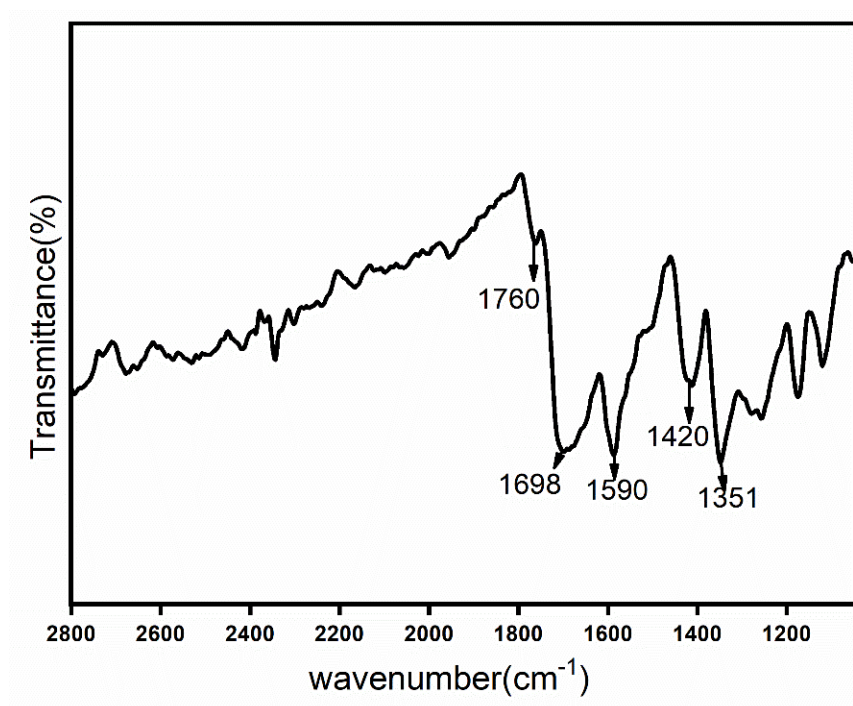
Fig.5.1. FT-IR Spectrum of N, N'- bis(p-carboxyl-phenylene) perylene-3,4: 9,10-perylene bisimide (PDI)

Understanding the variation in optical characteristics is now important. The PDI dye's (1x10-4 M) absorption spectra exhibit two distinct peaks in the visible area, typical of perylenes. The bay substituents at positions 1, 6, and 12 in the perylene core adjust the HOMO and LUMO energies and, consequently, the molecule's absorption and emission properties. The UV-vis absorption spectra of PDI (Fig.5.2 a) show bands at 420, 440, and 470 nm and a little shoulder at 520 nm. The primary components of perylene bisimide are distinguished by this shoulder peak. There were typical 530, 570, and 630 nm emissions for PDI at 420 nm excitation wavelengths (Fig. 5.2. b).
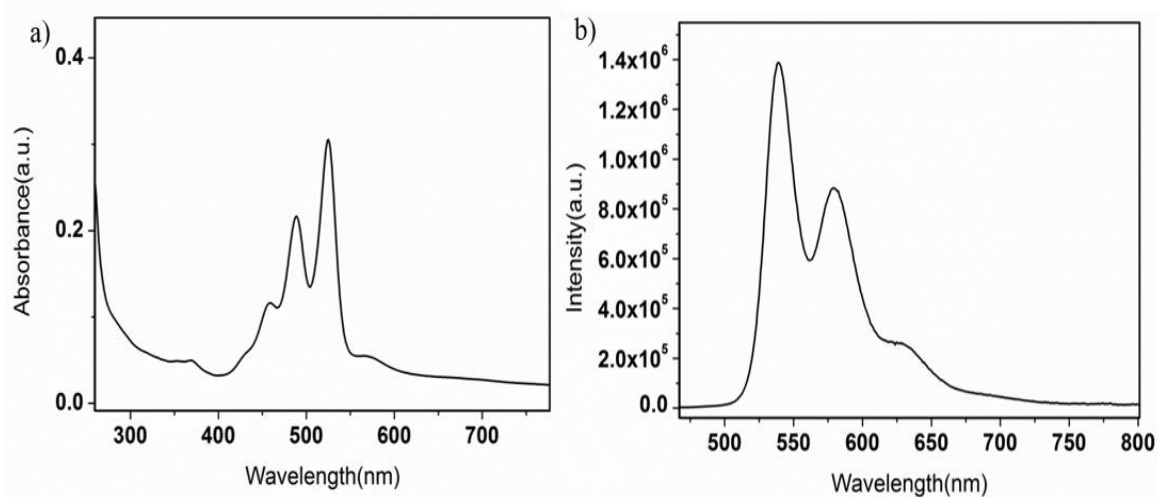
Fig. 5.2. a) UV-Vis and b) Photoluminescence (λexc =420nm) spectrum of PDI

5.4.2. Characterisation of α-Co(OH)$_2$ & β-Co(OH)$_2$

Fig. 5.3 shows the P-XRD patterns of α-Co(OH)$_2$ and β-Co(OH)$_2$. The significant reflections at (001), (100), (011), (012), and (110) are visible in the PXRD pattern. This pattern can be indexed on a hexagonal unit cell (a, b=3.17 and c=4.60) and space group of P-3m1 and matches the assigned pattern of brucite well, which is β-Co(OH)$_2$ (JCPDS No.74-1057).The α-Co(OH)$_2$, on the other hand, exhibits noticeable peaks at (003), (006), and (009). Sharp reflections, the first two can be attributed to (00l) with (l=1,2). In the case of (009), the reflections are wider and their intensity increases dramatically. The 2D structural features are given these phases. To the best of our knowledge, cobalt hydroxides don't have any reports of such phases, but because these characteristics are present in α-Ni(OH)$_2$, the term α-Co(OH)$_2$ and rhombohedral symmetry are given [18–21]. The FE-SEM images in Fig. 5.4, A and B, respectively, corroborate the production of well-separated Co(OH)2 hexagonal sheets. Green in α-Co(OH)$_2$ (Fig. 4.6 d) and pink in β-Co(OH)$_2$ (Fig. 5.4 c) might both have the colour as a distinguishing feature.
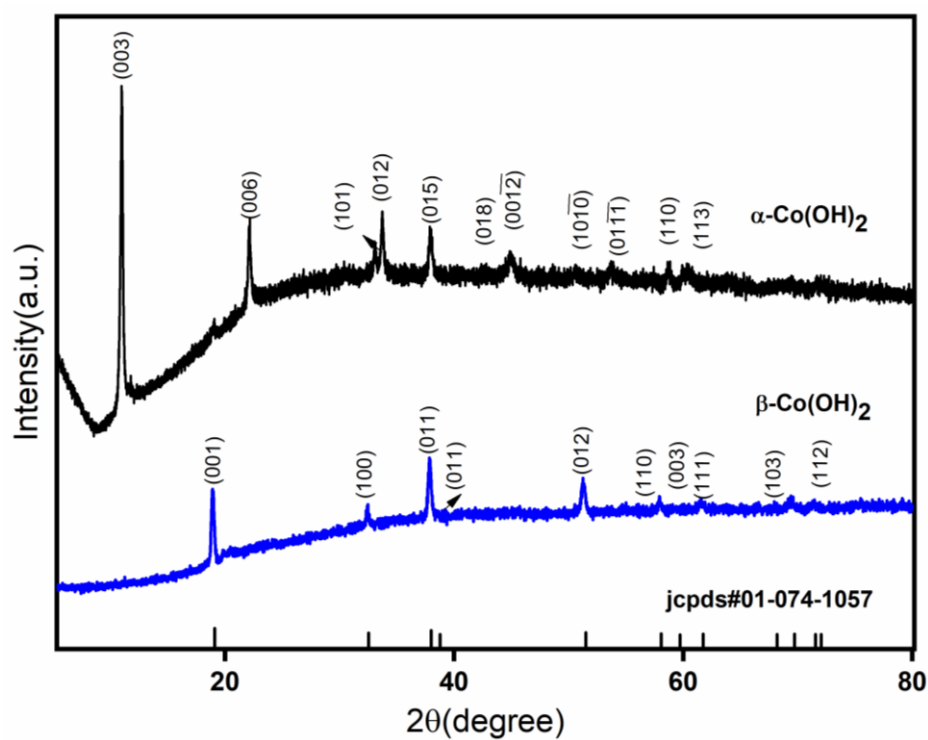
Fig. 5.3. PXRD patterns of (Blue) β-Co(OH)$_2$ and (Black) α-Co(OH)$_2$. hkl planes are indicated against the peak.
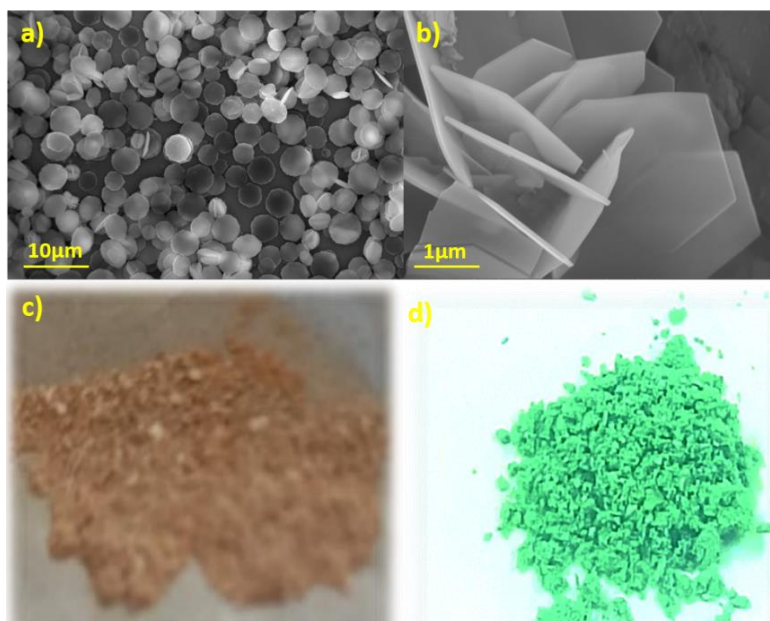
Fig.5.4. FESEM analysis of a) β-Co(OH)$_2$ and b) α-Co(OH)$_2$ & photographic images of c) β-Co(OH)$_2$ b) α-Co(OH)$_2$

5.5.3. Characterisation of α-Co(OH)₂-PDI

The P-XRD pattern of α-Co(OH)₂ and α-Co(OH)₂-PDI is given in Fig.5.5.a-b. The P-XRD pattern for α-Co(OH)₂-PDI agrees with that of α-Co(OH)₂. The intercalation of PDIs into the α-Co(OH)₂ should lead to the change in interplanar distance between the two layers. The calculated d-spacing between the two layers before PDI treatment is around 0.8nm and after treatment, it is just increased by 0.11n,m which means intercalation has not happened and only through the surface adsorption has happened.
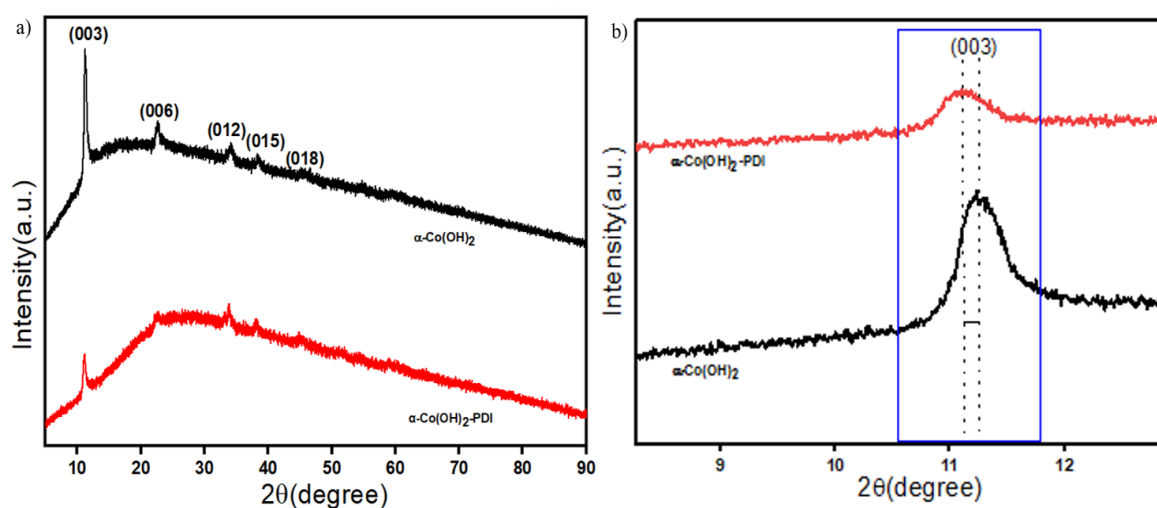
Fig. 5.5. P-XRD of a) α-Co(OH)₂ and α-Co(OH)₂ -PDI b) (003) plane magnified to show the shifting in the peaks of α-Co(OH)₂ and α-Co(OH)₂ -PDI.

The FESEM images (Fig.5.6 a-b) correspond to α-Co(OH)₂ and are well-aligned hexagonal sheets. Once PDI is added, the morphological features are reduced, forming the smaller sheets in a similar fashion to hexagonal sheets (Fig.5.6 c-d). To further illustrate the structure, the TEM analysis has been carried out. The TEM images (Fig.5.7. a) reveal the proper hexagonal sheets for α-Co(OH)₂ and SAED pattern (Fig.5.7.b-c) reveal the well formation of rings of different planes (003) (006) and (009) which are well compared with that of PXRD data (Fig.5.5). whereas in α-Co(OH)₂-PDI(Fig.5.7.d-f), the hexagonal sheets structure has not altered(Fig.5.7.d), but the small particles can be visible from the TEM (Fig.5.7.e). The SAED pattern also shows that the formation planes corresponding to (003), (006), and (009) (Fig.5.7.f) with fewer other impurities. These impurities might have come from organic moiety.
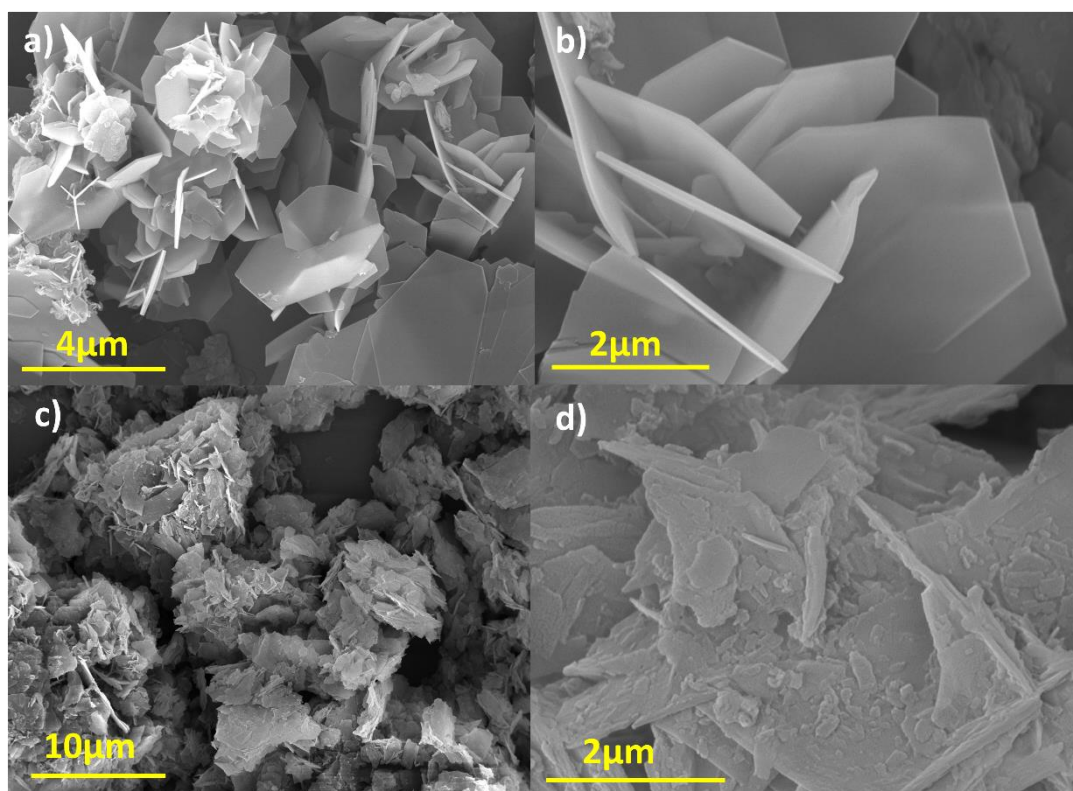
Fig.5.6. FESEM analysis of a-b) α-Co(OH)$_2$ & b-c) α-Co(OH)$_2$-PDI
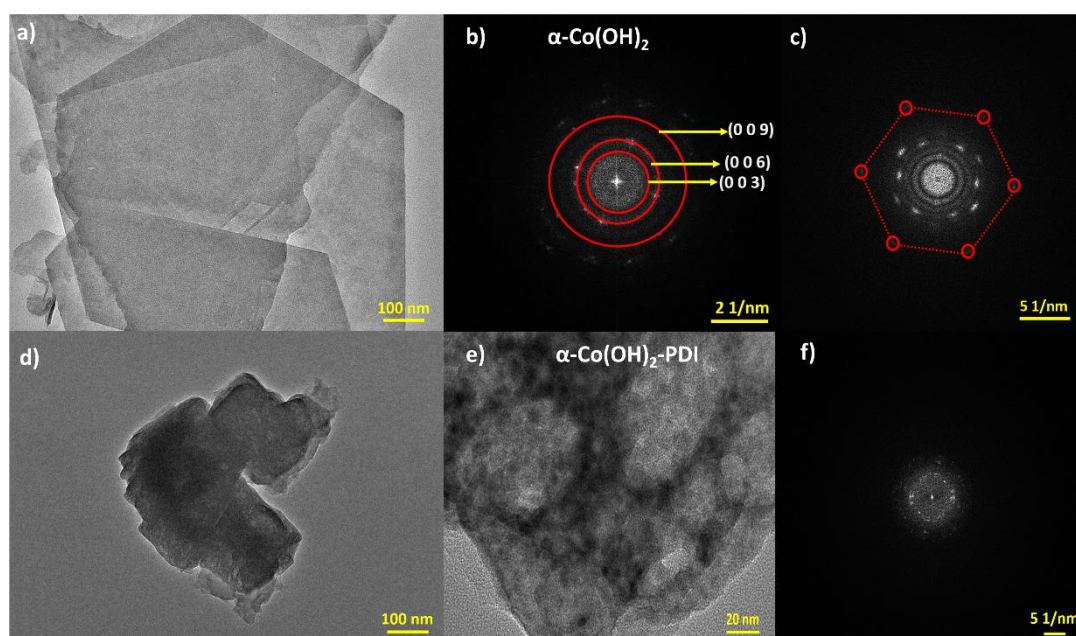
Fig.5.7. TEM analysis of a-c) α-Co(OH)$_2$ & d-f) α-Co(OH)$_2$-PDI

To understand this, the reaction with DMSO alone has been carried out, and no structural changes have been observed in the α-Co(OH)$_2$(Fig.5.8).
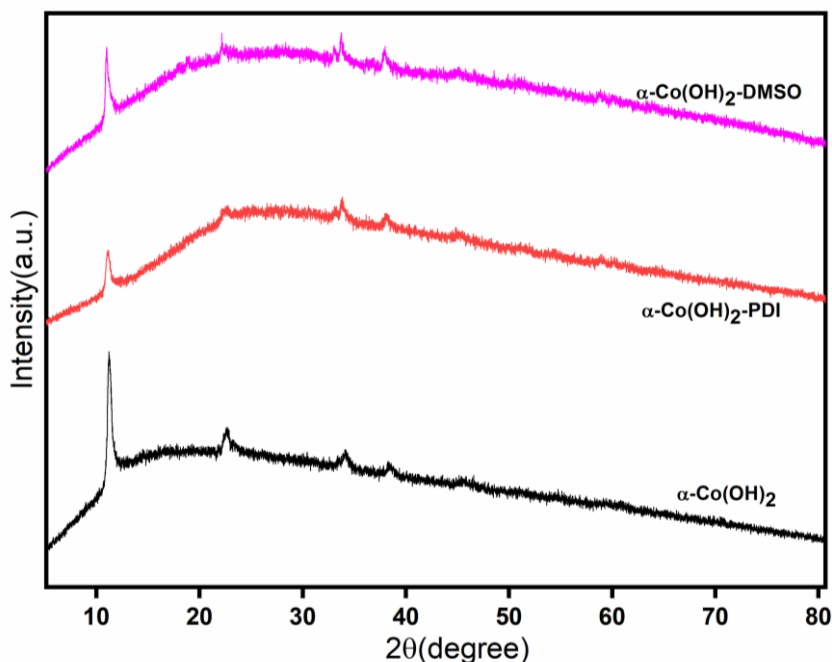
Fig.5.8. P-XRD of a) α-Co(OH)$_2$ (black) and α-Co(OH)$_2$ -PDI(red) and α-Co(OH)$_2$ - DMSO(pink)

Based on the above discussion, the layered double hydroxides have interesting properties of intercalating different ions between the layers. The main purpose of this synthesis route is to understand the interaction of different dyes, such as dyes based on perylene, and then understand the changes in the structural and application properties of formed compounds. Thus, after analysis, the two pathways have been proposed in which the reaction is proceeding: A-pathway and B-pathway. The reaction proceeding via the A-pathway results in the intercalation of foreign moiety between the layers and changes in the interplanar distance (d-values) of the characteristic plane (003) concerning the size of the foreign moiety. In B-pathway, no changes were observed in the interplanar distance. Only the slight shift in the values observed means that the adsorption of moiety over the surface was observed. In this case, the second pathway has been followed as no changes were observed in the d-spacing of interplanar distance. Only

0.11nm shifts have been observed. Thus B-Pathways have been followed, and PDIs is forming a strong bond with the -COOH group of dye with functional groups of α-Co(OH)$_2$ (Fig.5.9).
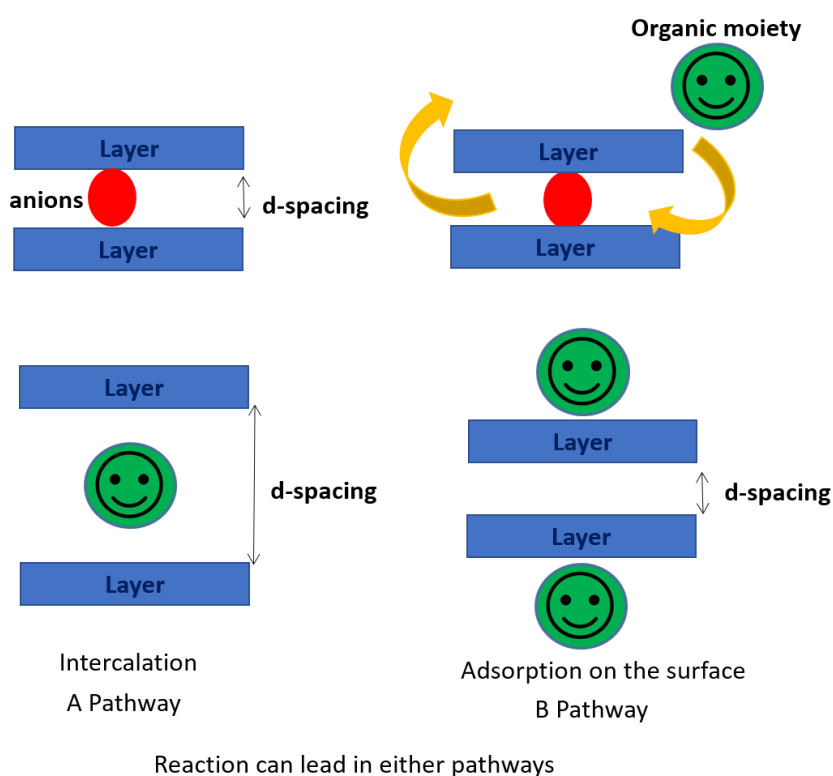
Fig.5.9. The proposal of the synthesis of α-Co(OH)$_2$-PDI

UV-vis absorption spectroscopy was analyzed for the sample dispersed in a TEOA-Water mixture for better solubility. The solid-state diffused reflectance spectra (Fig.5.11) have been done. The results are shown in Fig.5.10a. It is observed that α-Co(OH)$_2$ has strong absorption in the visible region at 675 nm. This can also be visible from the inset in Fig.5.10 a. The characteristics peaks for PDIs are not showing any change, and characteristics features are present for the perylene core from 420 to 520 nm. Thus, both the characteristics of α-Co(OH)$_2$ and PDI are visible, and this can enhance the activity of, as said above, applications of photocatalytic H$_2$ activity via water splitting. The photoluminescence study has been evaluated

by using similar samples with similar concentrations; the emission intensity in the case of α-Co(OH)$_2$-PDI has been reduced compared to that of PDI alone; thus, this feature indicates that the recombination phenomenon has been avoided by incorporating organic dyes with that of layered double hydroxides. This feature will be very helpful for the application in defects engineering and photocatalytic applications. The diffused reflectance spectra show the presence of both the features of LDHs and PDIs in the reflectance mode (Fig.5.11). Similarly, the FT-IR analysis has been carried out to further understand the interaction between the PDIs and α-Co (OH)2 (Fig.5.12). The FT-IR spectra show the broadening of peaks of -C=O from PDI, it means that the interaction is happening through the functional group.
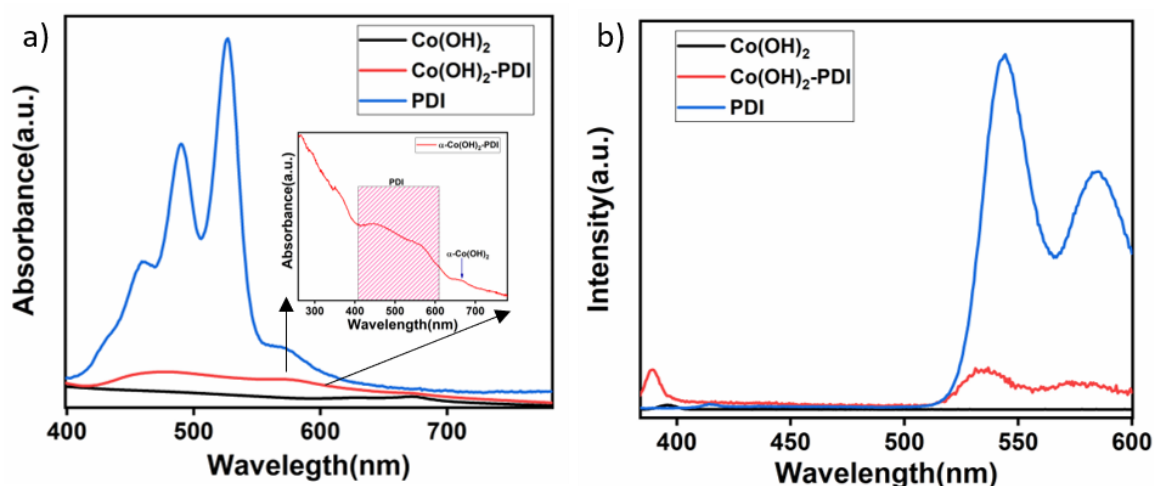
Fig.5.10. UV-Vis (inset shows the absorbance spectrum of α-Co(OH)$_2$-PDI zoomed version) and b) Photoluminescence (λexc =325nm) spectrum of α-Co(OH)$_2$, α-Co(OH)$_2$-PDI and PDI alone.
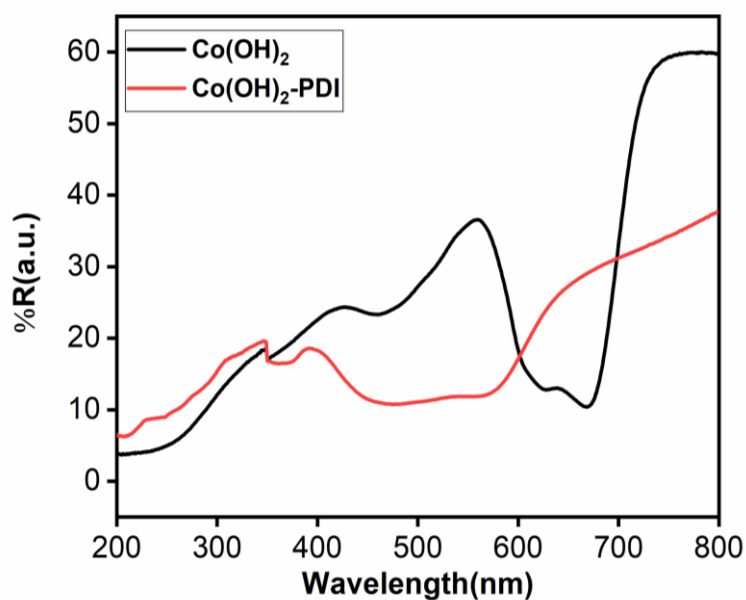
Fig.5.11. UV-Vis Diffused reflectance spectra of α-Co(OH)$_2$ and α-Co(OH)$_2$-PDI
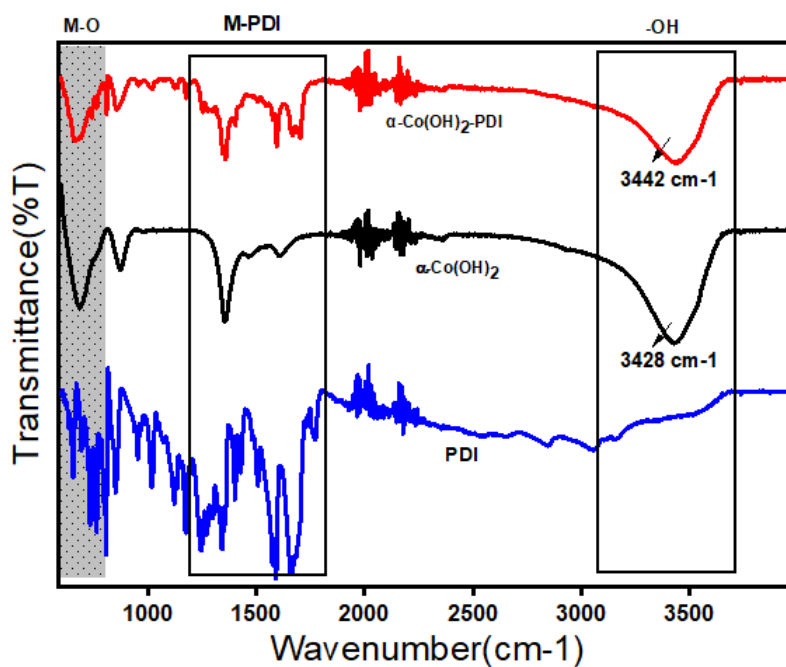
Fig.5.12. FT-IR Spectrum of PDI(Blue), α-Co(OH)$_2$ (black) and α-Co(OH)$_2$-PDI(Red)

5.5. Photocatalytic H$_2$ Evolution study

After understanding the structure. The activity performance for the PDI, α-Co(OH)$_2$ and α-Co (OH)$_2$-PDI has been studied. The hydrogen evolution activity has been checked with 25% methanol in water without adding any co-catalyst. At first, the comparative study of H$_2$ evolution for PDI, α-Co(OH)$_2$ and α-Co (OH)$_2$-PDI has been carried out. The TEOA-Water mixture has been used as a solvent for splitting water since the activity was better in the case of the TEOA: Water mixture than Methanol: Water mixture (Fig.5.13 a). The activity has increased by adding PDI to the α-Co(OH)$_2$ from 2000 µmol/h to 6900 µmol/h increase (Fig5.13 b). The PDI alone was also showing activity but very less compared to that α-Co(OH)$_2$ and α-Co (OH)$_2$-PDI(Fig.5.13 b). Then continuous 4h study has been carried out(Fig.5.13 c), and activity was showing an increase in activity for H$_2$ evolution; thus, this system can be very much advantageous if we consider the facts of UV-Visible activity and stability and activity compared to that of normal semiconductors. To further understand deeper about the activity trends and behavior of dyes in solvents. The pH-based studies have been carried out (Fig.5.13 d). At pH-10, the activity is very high, around 15900 µmol/h thus, this pH value is very active for the application, but as soon as the value increases to 14 the activity suddenly drops. The pH study plays an important role in understanding the organic moieties and their behavior. For that we have studied our system at different pH(1,3,7,8,10 and 14) and plotted the graph (Fig.5.14 a-b) at pH-1 the absent of characteristics of PDIs has been seen, and the intensity has been reduced along with that the emission intensity has been completed it means that the emission is reduced once the pH decreases to below 7 and at pH-14 the emission intensity is very high and it shows that as the pH decreases, the recombination has been reduced which has been seen more at higher Ph[22]. Thus form absorbance and emission correlation shows that at pH-14, the recombination is more, and due to this, activity has been reduced completely because electrons do not have enough time to travel to the surface for splitting the water but in case of pH-10 the recombination has been reduced and due it this activity for splitting of water to H$_2$ is more(Fig.5.13 and Fig.5.14a-b).
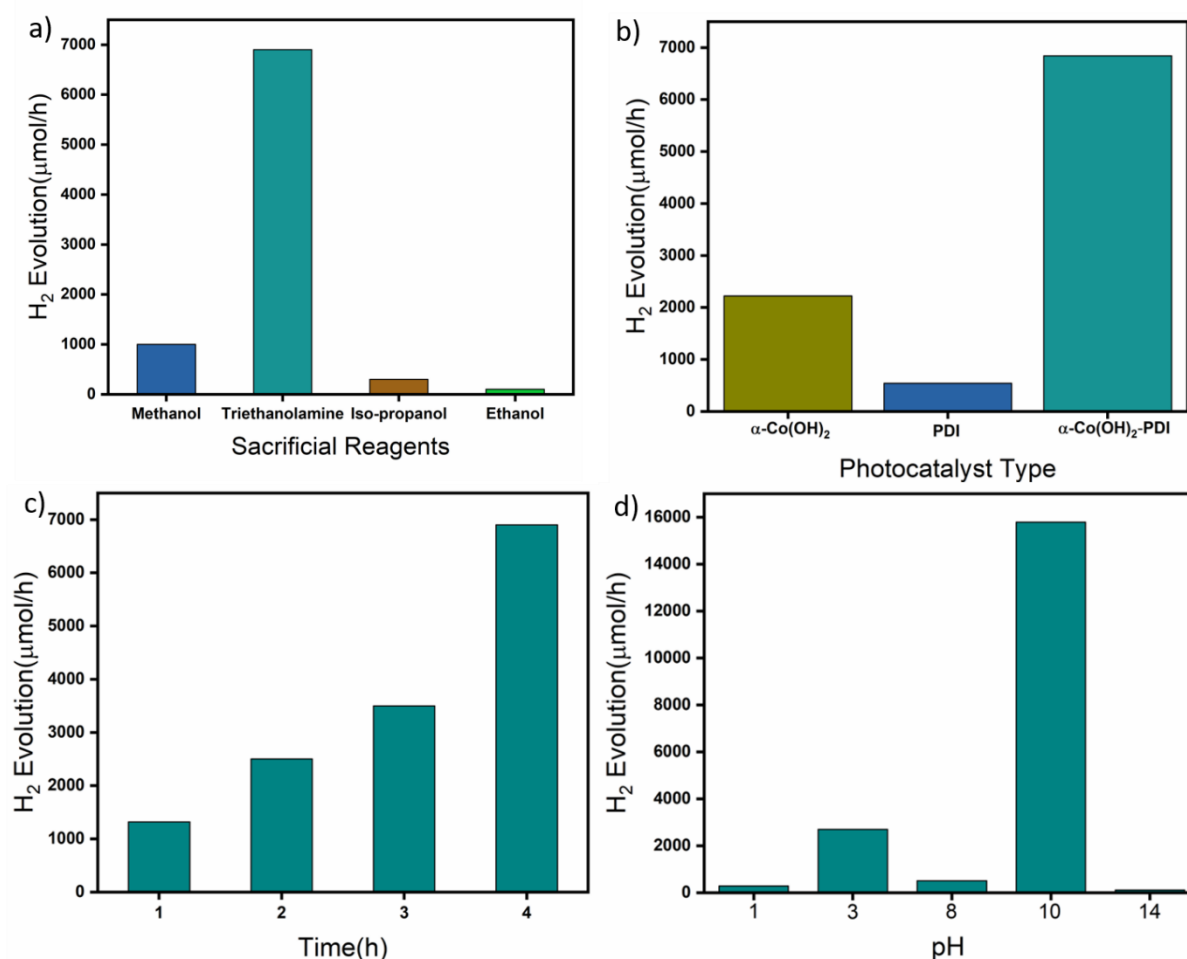
Fig.5.13. The photocatalytic H$_2$ evolution of a) different sacrificial reagents, b) PDI, α-Co(OH)$_2$ and α-Co (OH)$_2$-PDI, c) α-Co (OH)$_2$-PDI under the irradiation of high-pressure mercury lamp with 450W (λ>420nm) with Water: TEOA Mixture for 4h time irradiation, and d) different pH (1-14) (Catalyst amount:10mg).
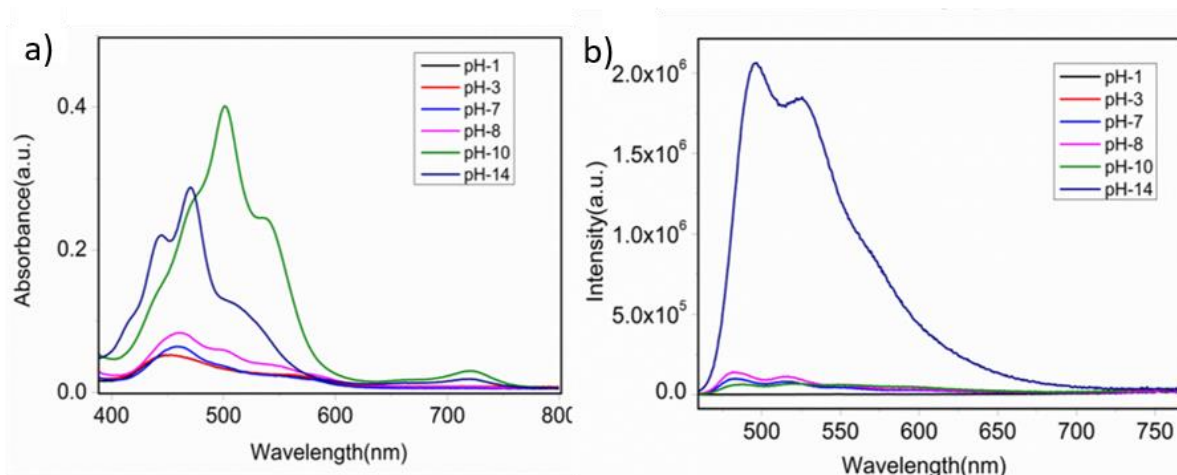
Fig.5.14. a) UV-Vis and b) Photoluminescence (λexc =420nm) at different pH(1,3,7,8,10 & 14) of PDI.

5.6. Mechanism of H$_2$ evolution

The relationship between reflectance and the Kubelka-Munk factor $F(R) = (1 R)^2/2R$[3] is used to compute band gap energy. $(F(R)h\nu)^{1/2}$ against h plots have been drawn, values determined, and band gap energies estimated in relation to the tangent of the plots (Fig. 5.15).The values equate to 1.76eV and 2.30eV, respectively, for Co(OH)2 and Co(OH)2-PDI. The flat band potentials of synthetic materials have been calculated using Mulliken electronegativity [24]. In Appendix 5a, the computations' specifics are described. Even in complex systems, this computation provides a clear grasp of the flat band potentials.

The following equation has been used to determine the band positions:

$V_{fb} = EA - E_{ref} + 1/2 E_g$ (5.1)

EA is the electron affinity of each individual atom, E_{ref} is the energy of free electrons on the hydrogen scale, $E_{ref} = 4.5$ eV, and Eg is the material's band gap. V_{fb} is the flat band potential. The band locations thus obtained are shown in Fig. 5.15 concerning the standard hydrogen

potential. The electron transmission is rising because the conduction bands for PDI are located at higher negative potentials than those for α-Co(OH)$_2$. As a result, the H$_2$ evolution activity (Fig. 5.13 b) demonstrates an increase in α-Co(OH)$_2$-PDI.
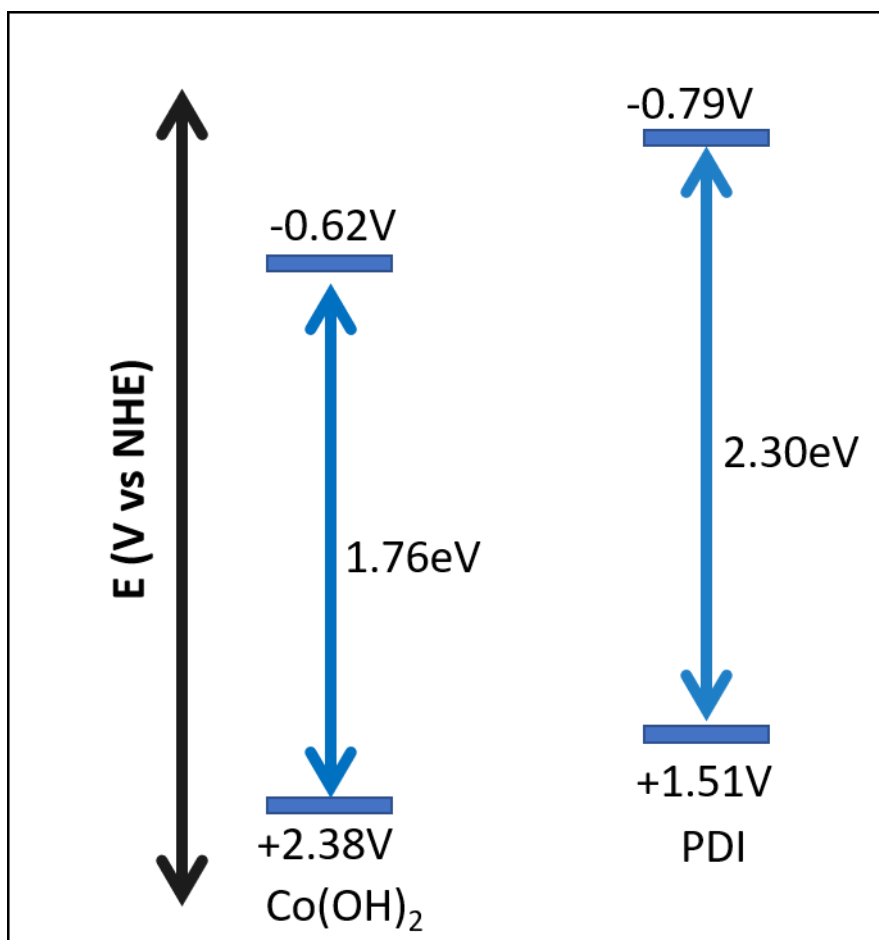
Fig.5.15. valence band and conduction band positions of α-Co(OH)$_2$ and PDI

The photoinduced electrons need to be transported easily in order to lengthen the separation of charge carriers, which will improve the photocatalytic performance of the composites. Electrochemical characterizations under the influence of light sources have been done in order to understand the mechanism of photocatalytic activity (details are provided in Chapter 2, section 4). These findings have been verified using the EIS Nyquist plot analysis. EIS Nyquist graphs with larger arc radii typically indicate more interfacial charge transfer resistance during the photocatalytic activity. Better conductivity and charge transfer ability are correlated with a smaller arc radius. Therefore, our α-Co(OH)$_2$-PDI instance exhibits a smaller arc radius (Fig.

5.16), as well as greater hydrogen evolution capability; these results are supported by the lower α-Co(OH)$_2$-PDI PL emission intensity. With the aforementioned descriptions in mind, the photocatalytic H$_2$ development mechanism can be explained, as shown in Fig. 5.17. Electrochemical experiments have also shown that the electron transfer from PDI to α-Co(OH)$_2$ occurs as the light strikes the photocatalyst's surface. Water splitting into H2 occurs once the electron moves to the redox potential of H$^+$/H$_2$O. To improve the electron feasibility to the conduction bands, hole scavengers have used holes.
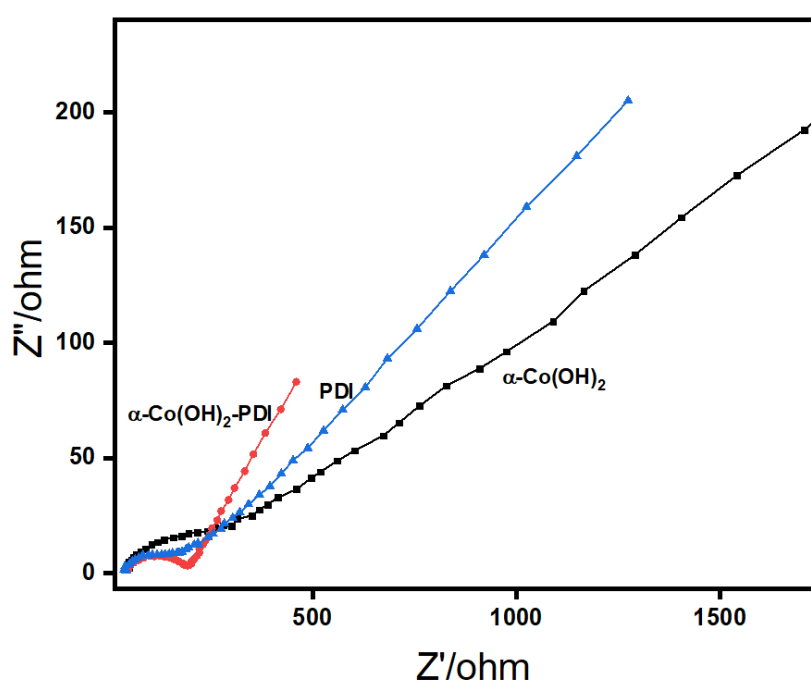
Fig.5.16. Electrochemical Impedance employing α-Co(OH)$_2$(black), PDI (blue) and α-Co(OH)$_2$-PDI (red) upon light ON mode (450W Hg lamp).
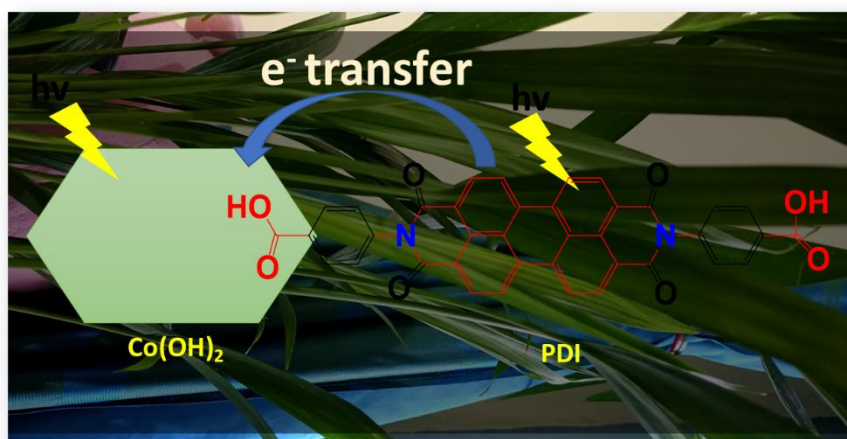
Fig.5.17. The mechanism of H$_2$ evolution from α-Co(OH)$_2$-PDI

5.7. Conclusion

In summary, a thorough study of system α-Co(OH)$_2$ has been studied, and modification has been done by using perylene-based dye (PDI= N, N'- bis(p-carboxyl-phenylene) perylene-3,4: 9,10-perylene bisimide). The changes in absorption and emission properties of modified material have been well observed and studied. The absorption properties of both the α-Co(OH)$_2$ and PDI have been seen, and this has enhanced the electron transfer phenomenon and thus increased photocatalytic hydrogen evolution activity via water splitting in this type of system. The emission intensity of α-Co(OH)$_2$-PDI has been decreased compared to that of PDI, and this confirms the decrease in the rate of recombination and transfer of electrons, which helps enhance activity. The electron transfer properties have also been confirmed by electrochemical studies. Thus all these studies confirm the formation of a layered double hydroxide system of α-Co(OH)$_2$-PDI for photocatalytic hydrogen evolution.

5.8. References

1. X. Sun. et al., *Adv. Funct. Mater.* **2020**, *30*, 1910005

2. Gareth R. et al., *J. Mater. Chem.*, **2006**, 16, 3065–3074

3. Wang Q. et al.,*Chem. Rev.* **2012**, *112*, 4124.

4. Chen H.; Hu, L.; Chen, M.; Wu, Y. Y. *Adv. Func. Mater.* **2014,** *24*, 934.

5. Xu Z. P. et al., *Chem. Mater*. **1999**, *11*, 67.

6. Symes M. et al., *ChemSusChem.* **2013**, *6*, 65.

7. Hutchings G. S. et al., *J. Am. Chem. Soc*. **2015**, *137*, 4223.

8. Mockenhaupt C et al., *J. Mol. Struct.* **1998**, *443*, 191.

9. Ma R. et al., *Inorg. Chem.* **2006**,*45*, 10.

10. Liu Z et al., *J. Am. Chem. Soc*. **2005**, *127,* 13869.

11. Orita M. et al., *Phys.Rev.B*. **2000**,61,1811.

12. Würthner, F. *Chem. Commun*. **2004**, 1564−1579.

13. Demmig, S.; Langhals, H. *Chem. Ber.* **1988**, 121, 225−230.

14. Liu X F ., *J. Phys. Chem. B.***2008**,112 10778.

15. Yan Sun et al., RSC Adv., **2017**, 7, 24215–24220.

16. Zhao, Y., *Mater.***2007***,*19, 3554–3558.

17. Adam S. W. et al., *Nature Chemistry*, **2016**,6, 964-970.

18. R. S. Jayashree et al., *J. Mater. Chem.*, **1999**, 9, 961–963

19. Michael R. P. at al., *J.Power Sources,***1998**, 70,118 – 121

20. P. Jeevanandam, et al., *J. Mater. Chem.*, **2000**, 10, 511±514.

21. Zhaoping Liu, et al., „*J. Am. Chem. Soc*. **2005**, 127, 13869-13874.

22. Yan Guo et al., *Nat Commun 202*2, 13, 2067.

23. Soumya B.N et al., *ACS Appl. Mater. Interfaces*,**2014**, 6, 12321−12327.

24. Kim Y Il. Et al., , *J. Phys. Chem.* **1993**,97:1180 2–10.

Chapter 6

Scalable optical fiber photocatalytic reactor for H$_2$ production from water splitting: Addressing scattering issues

6.1. Introduction

Utilizing the abundant solar energy for fuel production is the holy grail of energy research in the current scenario of alarming pollution levels and impending fossil fuel depletion[1]. Photocatalytic water splitting is considered as the most benign process for producing H_2, the cleanest fuel. Huge strides are made in developing materials for photocatalytic water splitting since 1972, when Honda and Fujishima discovered photolytic cleavage of water into oxygen and hydrogen using titania and Pt electrode [2]. However, such a surge in materials development has not translated into many large scale photocatalytic H_2 production facilities. One of the main drawbacks is the necessity for huge light installations in the medium which would render them uneconomical. In addition, limitations of the catalyst forms which can be used for an efficient utilisation of light from an external source also contributed to difficulty in scaling up. Most common form of the catalysts used is powder dispersion in the reactant mediums[3–8] which immediately brings in the disadvantage of scattering, and is all the more severe in large scale systems. An alternative reported in an allied process i.e., photocatalytic waste water treatment, is to immobilise photocatalysts on substrates like thin films and employ in a fixed bed configuration for continuous flow models[9–11] However, these models also demand multiple high energy lamps immersed in the reaction medium ruling out utilising sunlight directly.

In this context, optical fibres present marked advantages for a continuous flow immobilised model. In the late 70's and early 80's, Marinangeli and Ollis demonstrated photocatalyst immobilisation on optical fibres and their use in waste water treatment [12–14]. This method of photocatalysis is distinctly different from hitherto reported techniques using thin film catalysts, since photons are transmitted to the catalyst from within the light conducting medium in optical fibers. This decouples the reaction medium characteristics from photon transmission

to a large extent. Optical fibres work on the phenomenon of total internal reflection where complete reflection of light takes place within the fiber material due to increase in the angle of incidence more than that of critical angle. The structure of an optical fiber consists of a core which is made up of a polymer or silica (glass) surrounded by appropriate cladding material. To attain total internal reflection, the refractive index of core should be higher than that of the cladding. The absorption at the interface is avoided by coating the fibers with non-absorbing dielectrics. It is possible to deliberately "leak" the photons from the core by various techniques; optimising the refractive indices of core and cladding materials, addition of fluorescent materials to the cladding, creating asymmetries like cavities or air bubbles in the core and cladding geometries are some of them [15]. The leaking can also be affected by chemical, mechanical and laser stripping [16]. Marinangeli and Ollis exploited this phenomenon and used the leaked photons on the interface for pollutant degradation. Further developments in this field have led to demonstration of dye degradation under flow using woven fiber glass cloth as light transmitting medium [17–19]. However, these developments have not been utilised for photocatalytic H_2 generation yet. Very recently, Potter et al. reported the use of microstructure optical fibre canes (MOFCs) as a novel design for the production of hydrogen from water by using the semiconductor material coated onto the surface of fused silica canes [20]. However, here also, internal reflection phenomenon is not exploited for photon impinging to catalyst.

In contrast to this work, we have employed coating of optical fiber bundles with a photocatalyst, to exploit direct delivery of light thereby reducing light losses due to scattering and absorption by reaction medium. Different coating methods of CuO/TiO_2 catalyst on silica optical fibers are adopted to optimize hydrogen production by water splitting under visible light using methanol as a sacrificial reagent. Here, we have demonstrated the potential of such

models for scaling up and utilisation of non-potable water for H_2 generation. TransmissiLight transmissional fibers opens new gates to carry out H_2 evolution at remote environments such as deep sea and in the turbid non-potable water where light reaching capacity is very low.

6.2. Experimental Section
6.2.1. Synthesis of 5wt% CuO/TiO$_2$

500 mg of TiO_2 (Sigma-Aldrich, P25) was taken in a beaker containing 157 mg cupric acetate monohydrate (Cu $(CH_3COO)_2.H_2O$, LOBA Chemie) dissolved in 50 mL of water. The mixture was stirred at 30 °C for 2 h at 400 rpm on magnetic stirrer. The final product was washed with water and finally with ethanol and kept for drying in oven at 80 °C for 24 h. The dried sample was calcined in a muffle furnace at a heating rate of 2 °C/min at 250 °C for 5 h to obtain 5wt% CuO supported on TiO_2.

6.2.2. Coating of catalyst on Optical Fiber Bundle

Optical fibers used in this study (Applied Optical Technologies, Thane, India) consisted of silica core, polymeric cladding and were bundled in an outer jacket made up of rubber which was adjusted according to the length of fibers required for the studies; each such bundle contained 10000 silica fibers. The bundle of optical fibers was washed sequentially with distilled water and acetone and dried in an oven for 30 min at 80 °C. The clean fibers were then treated with 40% HF to remove cladding by dipping in HF solution for 10 s each and finally drying at 80 °C. Catalyst was coated on the etched optical fibers by a simple dip coating method. Slurry solution was prepared by dispersing ~250 mg of 5wt% CuO/TiO_2, CuO or TiO_2 powder in 50 mL distilled water under sonication for 30 min. 7 cm of the HF treated fiber bundle was coated with the slurry by using dip coating method and dried at 80 °C for 24 h. The

extent of coating was checked after weighing the remaining amount of catalyst left after the coating over the optical fibers.

6.3. Characterisation

The structure and morphology of as synthesised material and photocatalyst coated optical fibers were cut into small pieces and mounted on carbon tape for E-SEM analysis. For TEM analysis the coated optical fibers were dispersed into ethanol solution and then drop casted onto the TEM grid. Intensity of light at points for various conditions is measured using a KM-LUX-100K (Kusam Electrical Industries Ltd.) digital luxmeter. The methodologies utilised for PXRD, FE-SEM, TEM, IR, UV-vis, photoluminescence, NMR, electrochemical tests, and elemental analysis are identical to those outlined in Chapter 2's Section 3. In Appendix 2a, all the characterisation approaches employed throughout the paper are briefly reviewed together with their underlying ideas and instruments.

6.4. Photocatalytic experiments

Photocatalytic H_2 evolution experiments were carried out in an in-house developed photoreactor as given in Fig.6.1. It consists of a two necked 100 mL quartz cylindrical vessel, with fiber bundle inserted from the top and evolved gas injected out of the side arm. The fiber bundle is fixed at the neck using gas impermeable epoxy glue. The light source for the optical fibres was a 450 W High Pressure Mercury lamp. In this instance, methanol served as the sacrificial agent. Gas chromatography (5700 Nucon gas chromatograph; carbosphere column; argon as carrier gas; thermal conductivity detector) was used to calculate the amount of H_2 that

was developed. The detector temperature in the GC was set to 100°C, and the oven temperature was set to 50°C at the time of injection.
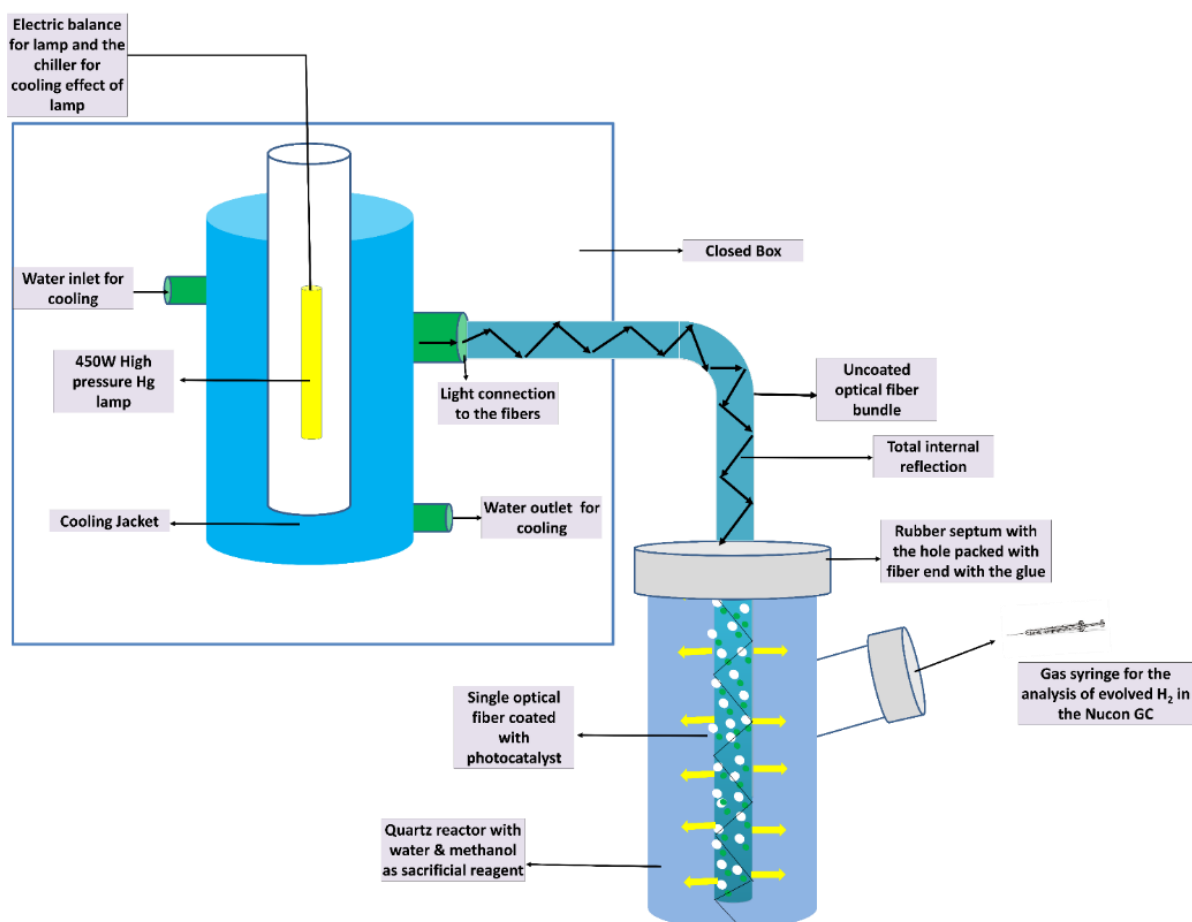
Fig.6.1. Reactor design for the photocatalytic experiment

6.5. Results and Discussion

The strategy adopted for the maximum utilisation of photons is to avoid scattering by the reaction medium and facilitate instantaneous exposure to the reactants at the interface. Employing optical fibres for this would entail appropriate surface modifications, specific design of the photoreactor as well as photocatalyst synthesis methods when compared to conventional powder based photoreactors.

6.5.1. Optical fiber etching

In our experiments, we have used optical fibres made with silica of different refractive indices as core and cladding. To be used in photocatalysis, light has to be leaked in a controlled fashion throughout the length of the fibres. This can be achieved by selectively etching the silica cladding using HF (details given in Fig.6.2).
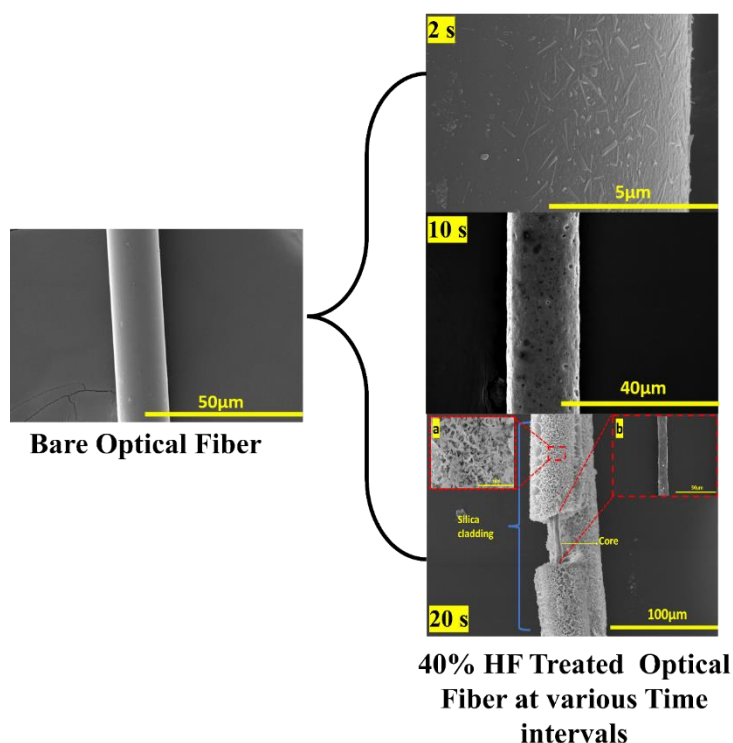
Fig.6.2. Schematics of FE-SEM data showing the effects of 40% HF on the optical fibres at 2s, 10s and 20s and etching of Silica Optical fiber with 40% HF treatment at 20s (inserted a) shows the silica cladding structure changes after 20s 40% HF treatment (inserted b) shows the core of optical fiber after 20s 40% HF treatment

The etching time was optimised to be 10 s, by which time, the surface becomes holey as well as rough along with drastic reduction in diameter from 42.40 µm to 28.66 µm (Fig. 6.3). As expected, emitted light intensity along the side of the fiber walls also increased from 100 lux to 380 lux after HF treatment (inset bar graph in the Fig.6.3). However, increase in etching time to 20 s decreases the transmission possibly due to severe damage to the silica cladding

exposing the core fully. The irradiance spectrum of the optical fiber after etching spans a broad range from ~300 nm up to 700 nm (Fig.6.4).
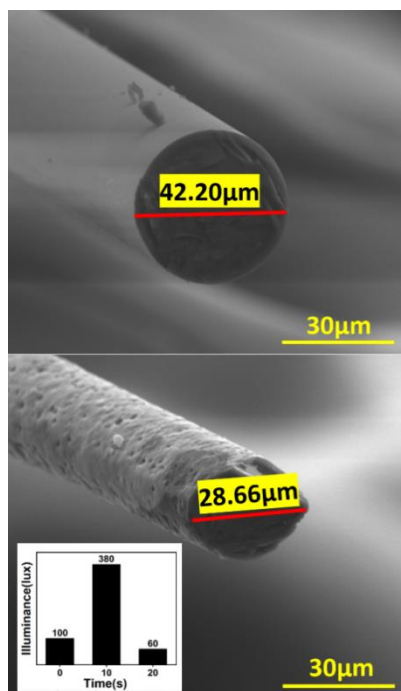
Fig.6.3. Morphology of optical fiber before HF (top) and after HF treatment for 10 s (bottom) Inset shows the extent of light leaking through the defects created by HF treatment
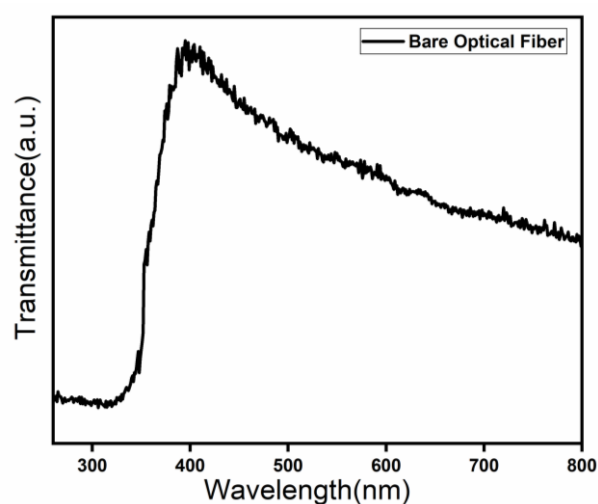
Fig.6.4. UV-Vis Transmittance spectra of bare optical fiber bundle and $5CuO/TiO_2$ coated fiber bundle

6.5.2. Synthesis and characterisation of CuO/TiO$_2$ catalyst

For this study, we selected CuO deposited on TiO$_2$ as the photocatalyst since it is well studied and identified as one of the best H$_2$ evolution photocatalysts [21–29]. Band gap of TiO$_2$ is ~3.2 eV and photoreduced CuOx is known to absorb in the visible region acting as sensitiser as well as catalytic sites for HER [35,48,55–61]. It is suggested that TiO$_2$ acts as the photocatalyst in presence of UV light and CuO gets reduced to CuOx and even further to Cu(0) [27,62]. These reduced CuOx species act as sensitiser and absorb visible light resulting in an electron transfer to TiO$_2$. For further coating, 5 wt% of CuO was deposited on TiO$_2$ (P25) and the as-synthesised powder catalyst (named as 5CuO/TiO$_2$) was characterised to ascertain formation of the desired phase as well as appropriate interface (Fig.6.5). PXRD pattern indicates the presence of rutile and anatase phases of TiO$_2$ as expected; however, no discernible peak characteristic of CuO is seen, indicating its existence in highly dispersed form (Fig.6.5a). TEM studies (Fig.6.5c-h) reveal spherical particles with lattice d-spacing of 0.23 nm corresponding to the (111) plane of CuO (00-001-1117) and 0.34 nm for (101) plane of TiO$_2$ Anatase phase (01-071-1166) and 0.325 nm for (110) plane of rutile phase respectively, indicating intimate surface interaction between TiO$_2$ and CuO particles. SAED pattern also suggests highly crystalline nature of the sample and the planes of CuO (111) and (101) and (110) planes of anatase and rutile phases are visible (Fig.6.5e). FFT diffractogram also indicates intimate interfaces between CuO and TiO$_2$ (Fig.6.5f-h). Surface interaction between CuO and TiO$_2$ may also be indicated by red shifted absorption edge of TiO$_2$ in UV-vis spectroscopy (Fig.6.5b). The EDAX study has been carried out which shows the amount % of Cu is about 4.11 wt% in 5CuO/TiO$_2$ (Fig.6.6).
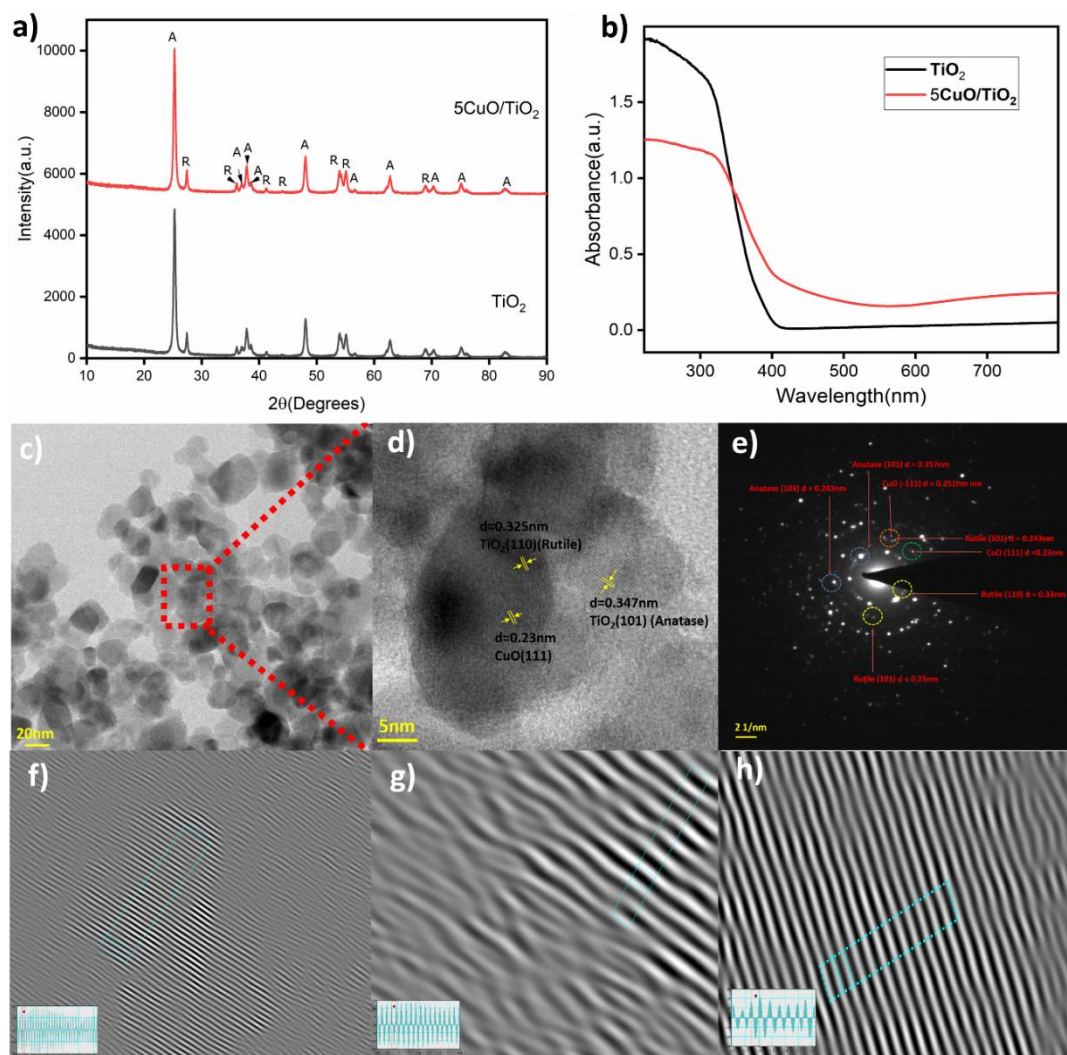
Fig.6.5. Characterization of powder sample of 5wt%CuO/TiO$_2$ a) P-XRD pattern b) UV-Visible absorption spectra c) TEM image showing the uniform distribution of nanoparticles d) high magnification image is taken from the area in red dotted line e) SAED pattern indicating with the dotted blue (anatase phase), orange (CuO phase) and yellow (rutile phase) respectively, (f-h) Inverse Fast Fourier Transform (IFFT) diffractogram along with the d-spacing of different planes of CuO and TiO$_2$

a)			b) Element	Wt%	At%

c:\edax32\genesis\genmaps.spc 07-Oct-2022 16:56:14
LSecs : 20

Element	Wt%	At%
OK	58.37	81.14
CuL	04.11	01.44
TiK	37.52	17.42
Matrix	Correction	ZAF
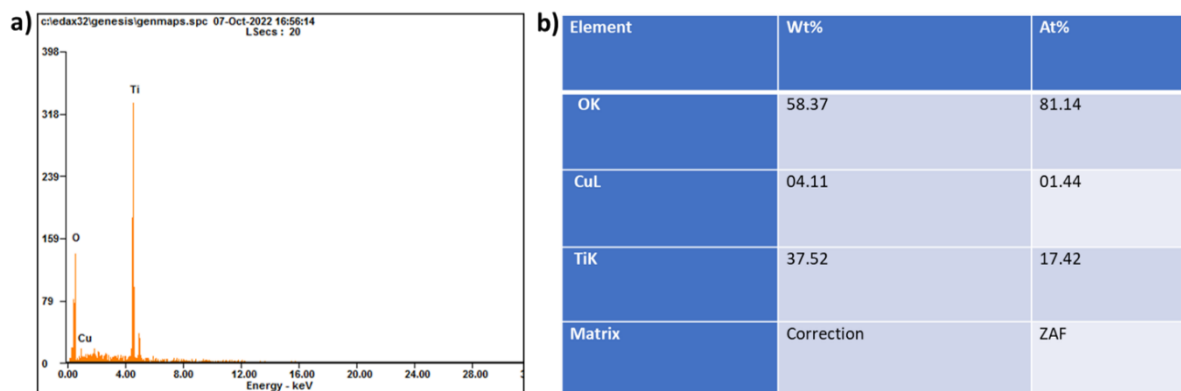
Fig.6.6. EDAX Analysis of powder 5CuO/TiO$_2$

6.5.3. Coating of catalysts over etched optical fibers and their characterisation

Deploying catalyst over the etched optical fibres also is an important step in fine tuning the exposure of catalytic sites to photons. This is mainly due to the change in directionality of light exposure; in a conventional system with dispersed powder catalyst, scattering occurs from the vessel wall, reaction medium and catalyst particles as schematically represented in Fig.6.7. a-b. Whereas, in the optical fibre system, light comes from within the support; hence, designing the right interface with water, sensitizer and semiconductor for interaction with photons is required, but challenging.
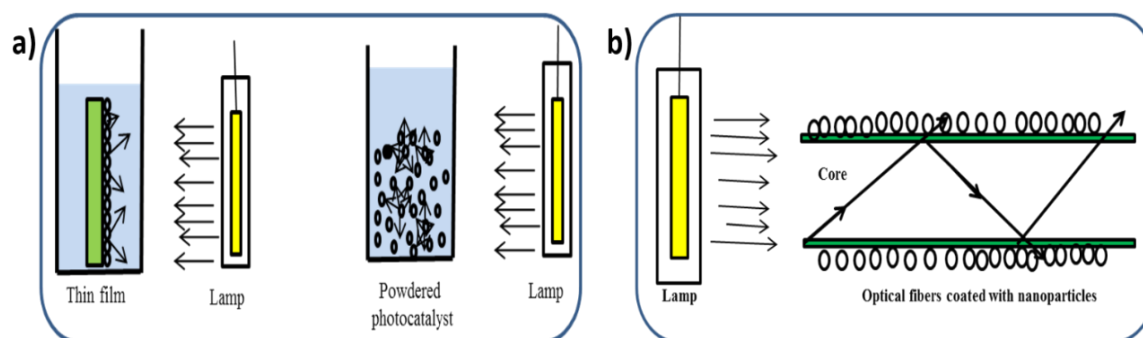
Fig.6.7. Comparison in the activity of photocatalyst coated thin film, powders photocatalyst inside photocatalytic reactor and optical fibre coated with semiconductor under the light irradiation

First, the as synthesised 5wt% CuO/TiO_2 catalyst was coated over the etched optical fiber bundle of diameter 0.5 cm, containing approximately 10,000 fibers(Scheme 6.1)..
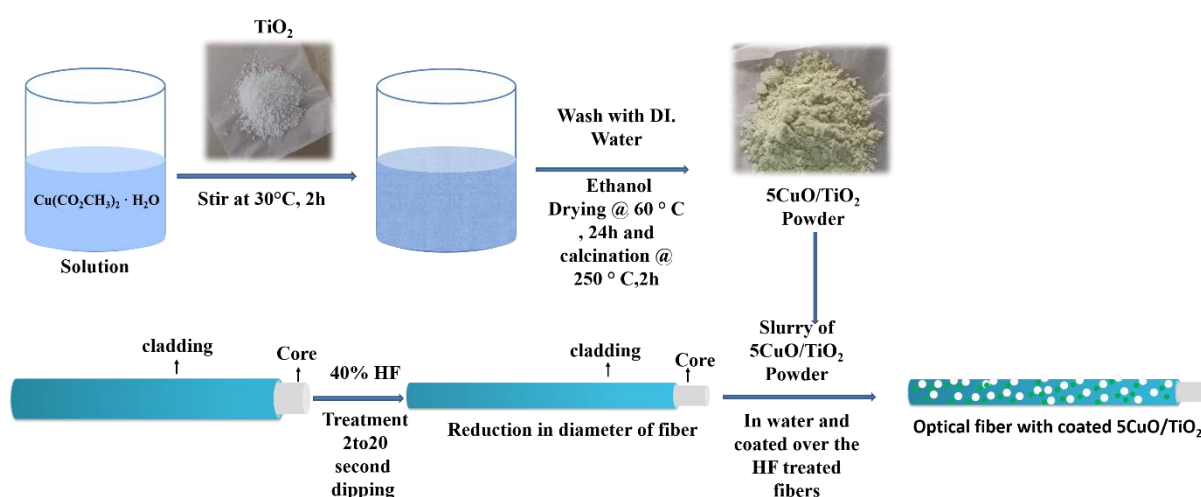
Scheme 6.1. Schematic representation of 5wt%CuO/TiO_2 coating over the surface of HF etched optical fibre

After coating this catalyst, the surface characteristics of the optical fibers was observed by SEM which shows uniform coating over the entire length of the optical fiber as shown in Fig. 6.8 a. The cross section of optical fiber also shows the uniform distribution of the catalyst (Fig. 6.8b). Elemental mapping (Fig.6.8 d-f) indicates the presence of Ti, Cu and O uniformly over the surface of optical fibers revealing the effectiveness of coating. To confirm the retention of the phase of the catalyst upon coating, TEM studies were carried out on the coated material dislodged from the fiber surface, which do not indicate any discernible alterations from the powder catalysts (Fig.6.9)
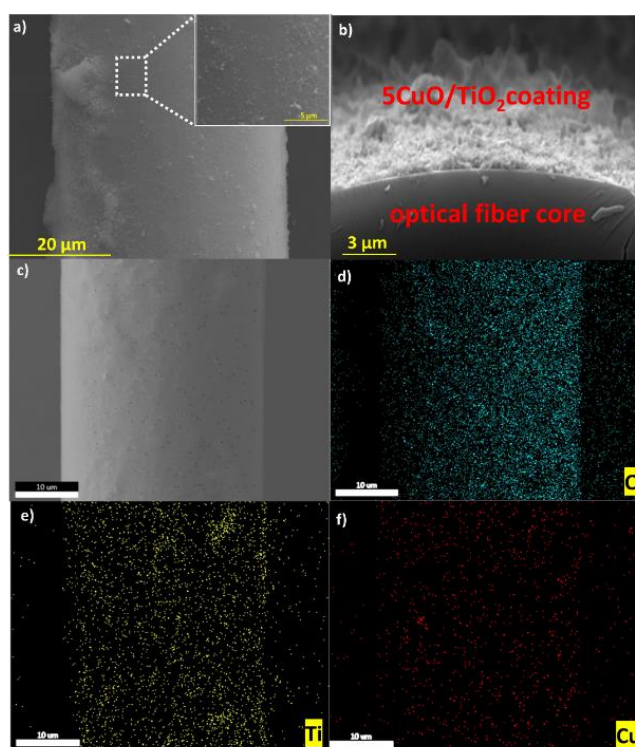
Fig.6.8. SEM images of (a) single optical fiber showing the coating over the length of fiber. Inset shows the uniformity of 5wt%CuO/TiO$_2$ coating in a magnified view (b) Cross-sectional view of optical fiber showing the smooth core and particulate coating (c) SEM image of area selected for the elemental mapping (d-f) Elemental mapping of O, Ti and Cu over the surface of optical fiber
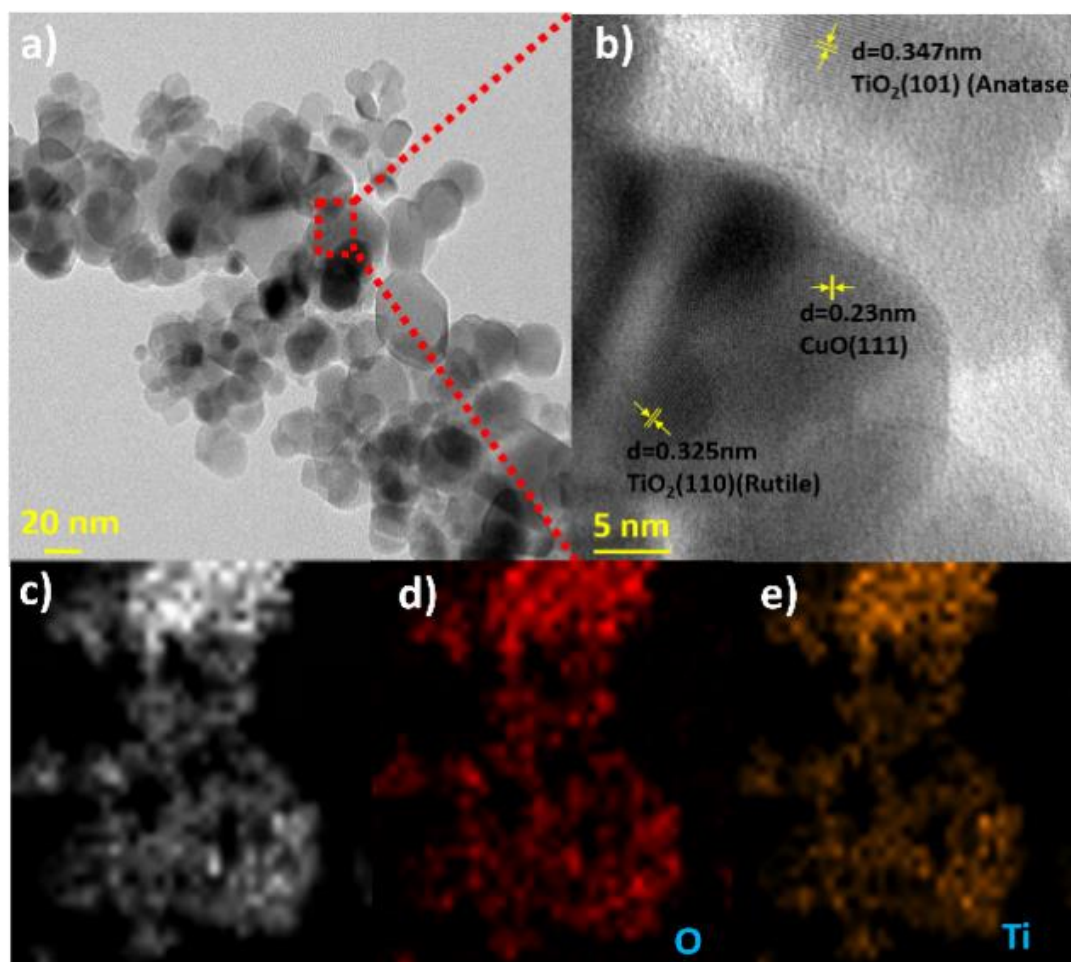
Fig.6.9. TEM study of 5wt%CuO/TiO$_2$ catalyst dislodged from coated optical fibers (a) TEM image showing the uniform distribution of nanoparticles (b) high magnification image is taken from the area denoted in red dotted line (c to e) STM image and elemental mapping of Ti and O respectively (The elemental mapping for Cu is not given due to the use of Copper mesh grid for the TEM analysis, which may lead to inappropriate results)

Our understanding of the mechanism suggests that photons are absorbed by the sensitizer, ie., CuOx and an interfacial electron transfer occurs to the semiconductor, TiO$_2$ [66,67]. To understand the importance of this directionality, two more coating sequences were selected; (i) first CuO slurry deposition and then TiO$_2$ and (ii) first TiO$_2$ was coated over which CuO was

deposited. SEM and elemental mapping reveal the coating of CuO and TiO_2 over the surface of optical fibers (Fig.6.10 & 6.11 respectively for (i) and (ii)) as it is showing the presence of Ti, Cu and O over the surface of optical fibers in the alternate layers. The N_2 adsorption-desorption studies were carried out to understand the surface areas of each sample i.e., CuO, TiO_2 and 5CuO/TiO_2 (Table 6.1). The surface area for TiO_2 was found to be 72.936 m^2/g, CuO (12.000 m^2/g) and for 5CuO/TiO_2 is 55.033m^2/g which lies in between the CuO and TiO_2.
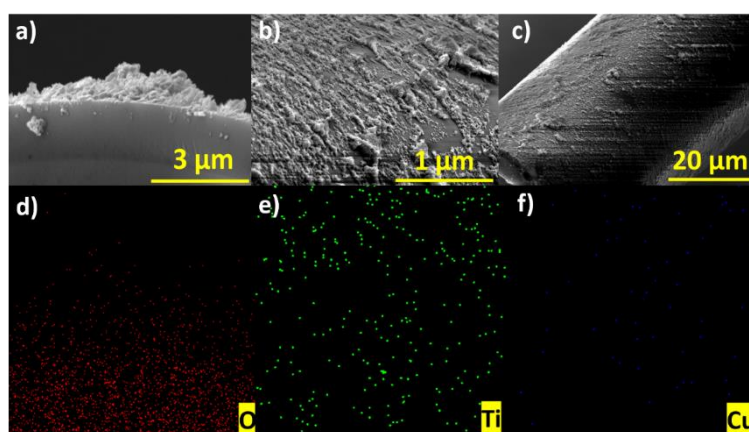
Fig.6.10. The SEM Images and elemental mapping of 1st CuO and 2nd TiO_2 coated optical fiber
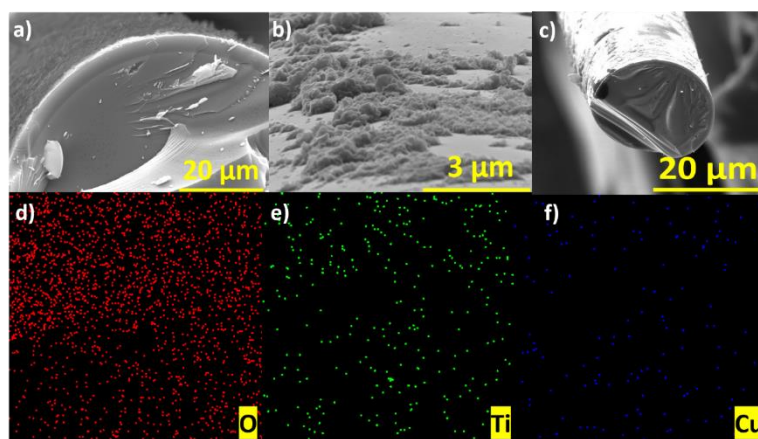
Fig.6.11. The SEM Images and elemental mapping of 1st TiO_2 and 2nd CuO coated optical fiber

TABLE.6.1: BET Surface area analysis

Photocatalyst	BET Surface area (m^2/g)
CuO	12.000
TiO$_2$	72.936
5CuO/TiO$_2$	55.033

6.6. Photocatalytic studies on catalyst coated optical fibers

Photocatalytic activities of the optical fiber bundles coated with catalysts by all the three methods described above, were estimated by measuring evolved H_2 every hour up to 8 h. Amount of catalyst coated on the fiber bundle was quantified by weighing the slurry remaining after dip coating and was found to be ~50 mg. Total H_2 evolved increased with time and a maximum of 22 µmoles of H_2 was produced after 8h in case of 5wt%CuO/TiO$_2$ catalyst coated fibers (Fig. 6.12 a). It also showed stable and repeatable H_2 evolution for 32 h under photocatalytic reaction conditions (Fig.6.12 c). Apparent quantum yield AQY (%) was estimated from the expected wavelength to be 4.72% (details given in Appendix.6a).Comparatively, both the sequentially coated catalysts showed poorer activity; in case (i), ie., optical fiber bundles coated first with CuO and then with TiO$_2$, 12 µmol of H_2 evolution was observed after 8 h, whereas in case (ii), ie., TiO$_2$ coated as the first layer, only 3 µmol H_2 evolved after 8 h (Fig. 6.12 b). On the other hand, CuO or TiO$_2$ individually shows very poor H_2 evolution activity of ~ 2 and 1 µmol respectively (Fig.6.12 b). This indicates a crucial role of the interfaces between CuO and TiO$_2$ conducive for electron transfers dictating the activity.
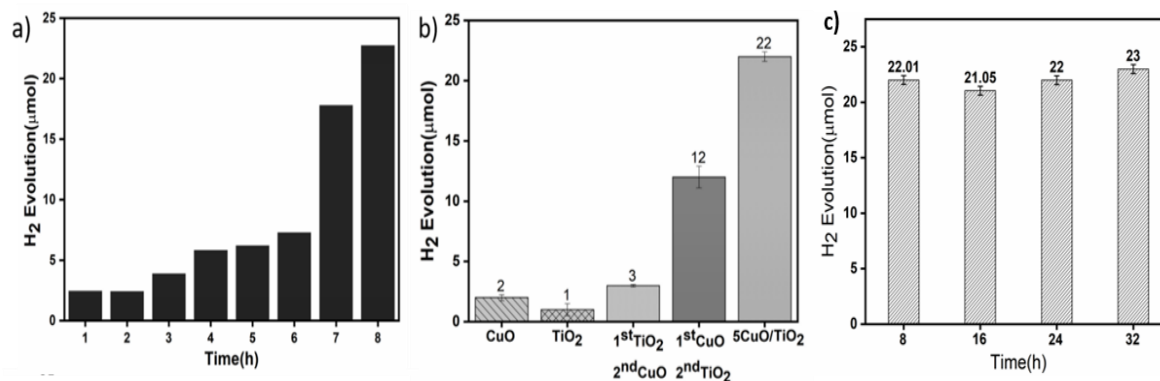
Fig.6.12. (a) H$_2$ evolution activity of 5wt%CuO/TiO$_2$ coated optical fiber bundles in MeOH/Water system under illumination with 450 W High pressure Mercury lamp for 8 h. (b) Comparative H$_2$ evolution activity of 5wt%CuO/TiO$_2$ coated fibers and sequentially coated fibers. All experiments were carried out in MeOH/Water system (35 vol%) under illuminationof 450 W High pressure Mercury lamp for 8 h.

Structural stability of the catalyst after 32 h of reaction was also ascertained by Scanning Electron Microscopy and elemental analysis (SEM), which indicated no discernible variations in composition of interface structure from the fresh coated fibers (Fig.6.13 a-e). After dislodging of sample from optical fibers after 32 h of cyclic study, TEM analysis of samples was carried out which shows no changes in the structural phases in the powdered sample (Fig.6.14 a-b).
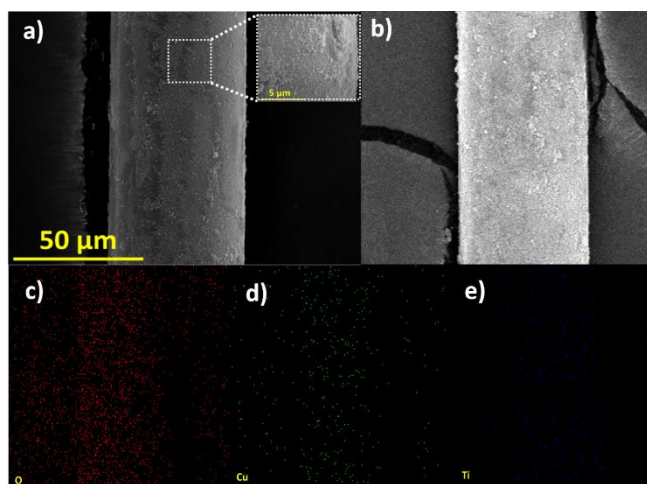
Fig.6.13. SEM images of (a) single optical fiber showing the coating over the length of fiber. Inset shows the uniformity of 5wt%CuO/TiO$_2$ coating in a magnified after 4th cycle of catalytic activity (b-e) elemental mapping of Ti, Cu and O respectively over the surface of optical fiber
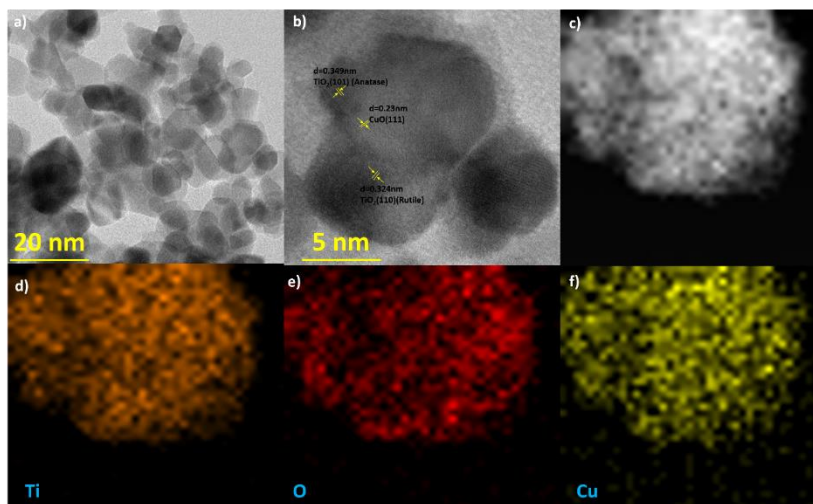
Fig.6.14. (a-b) TEM images (c) STEM-HAADF (d-f) Elemental mapping of Ti, and O respectively of 5CuO/TiO$_2$ Coated Optical fiber dislodged sample after 4th cycle of catalytic activity

6.7. Mechanistic understanding of the activity of catalyst coated optical fibers

Understanding Cu valence states gives an insight into the difference in mechansitic aspects of the three samples. This was done by comparing x-ray photoelectron spectra of the samples before and after irradiation. In case of optical fibers coated with 5CuO/TiO$_2$, the freshly prepared sample (Fig.6.15a) shows the existence of Cu(I) at 932.19 eV and Cu(II) at 933.46 eV with the strong satellite peaks of characteristics of Cu(II) from the range of 940-950 eV [68–70]. During reaction, the reduction of Cu(II) takes place and an increase of Cu(I) concentration is observed in the sample. In addition, intensity of the satellite peaks which are characteristic of Cu(II) also diminished (Fig.6.15b). It is to be noted here that the reduced

species could be Cu(0) which is not possible to be differentiated from XPS due to very close binding energy values [57,60–61].
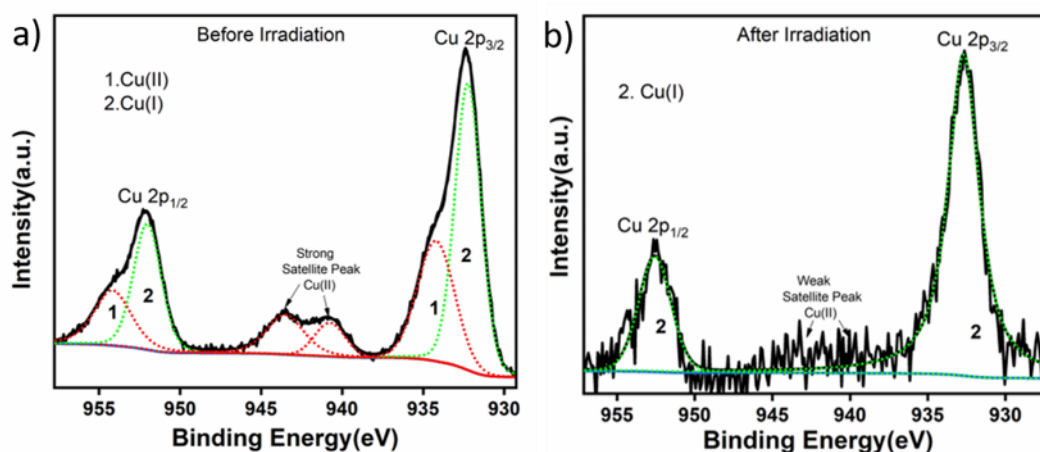
Fig.6.15.(a) Cu 2p spectra of 5CuO/TiO$_2$ coated optical fiber bundles of fresh sample before irradiation(b) Cu 2p spectra of 5CuO/TiO$_2$ coated optical fiber bundles of fresh sample after irradiation

However, such a reduction is commensurate with a notable change in colour from greenish yellow to blackish purple (Fig.6.16 a). In addition, plasmon resonance peak at 570 nm in the absorption spectrum (Fig.6.16 b) of the sample after irradiation may indicate the presence of Cu(0).
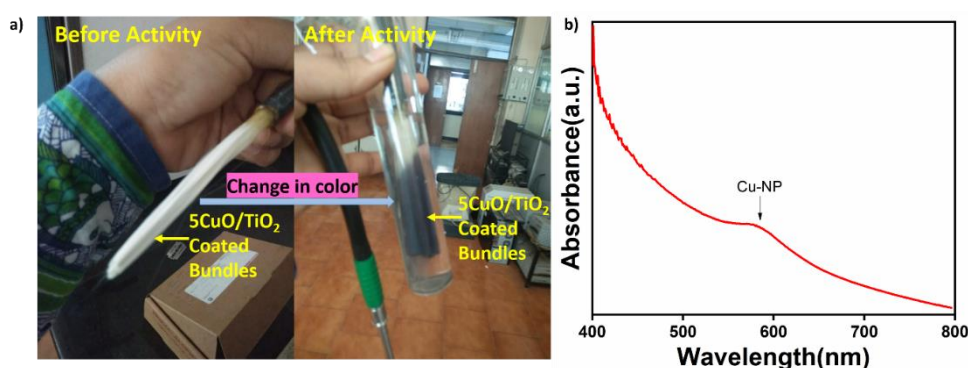
Fig.6.16. After Photocatalytic activty (a)the changes in the color of fiber bundles (b) UV-Vis spectra

However, this interconversion of Cu(II) to Cu(I)/Cu(0) is not observed in the other two samples coated in a sequential manner (Fig.6.17). It is apparent that such redox systems exist only in the as-synthesised catalyst (which is established by HRTEM in the previous section) and not in the sequentially coated fibers. On correlating this observation to the activities of the three samples, it is clear that the inherent interface between CuO and TiO_2 plays major part in imparting the photocatalytic activty.
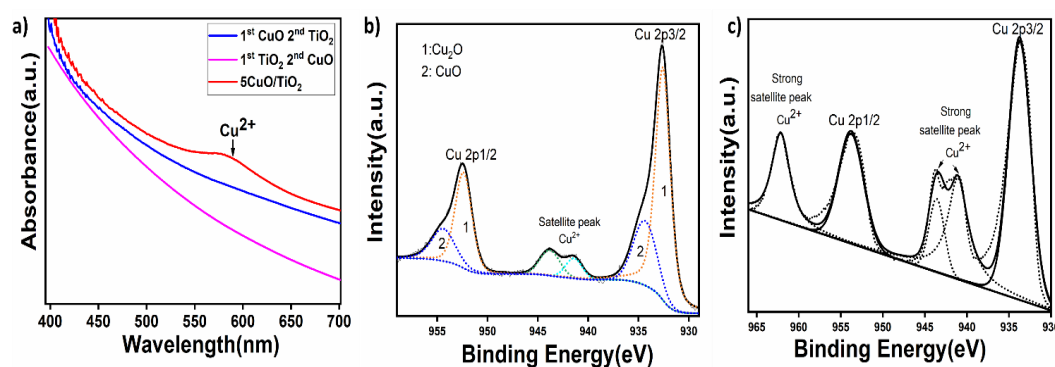
Fig.6.17.After photocatlytic activity the (a)omparative absorbace spectra of $5CuO/TiO_2$, 1st CuO 2nd TiO_2 layers and 1st TiO_2 2nd CuO layers, Cu 2p XPS spectra for (b) 1st CuO 2nd TiO_2 (c) 1st TiO_2 2nd CuO

Utilising Mulliken electronegativity values and band gap analysis, flat band potentials of CuO, Cu2O, and TiO2 are calculated [62]. The computations' specifics are provided in Appendix 6a. And in Fig.6.18a, band locations are shown in relation to the common hydrogen electrode. Although CuO may absorb visible light, TiO2 cannot transfer electrons to it because of the band alignment. It is clear that TiO2 is UV active. However, the UV light present in the light emitted from the optical fiber (as presented in Fig.6.4.) is sufficient for TiO_2 to act as the photocatalyst for CuO to CuOx/Cu reduction, as evident from the increase in reduced Cu species in the irradiated optical fiber as well as from the visual observance of colour change.

These reduced CuOx species now act as visible light sensitisers with right band alignment for feasible electron transfer to TiO_2 which further activates the water splitting (Fig.6.18b).
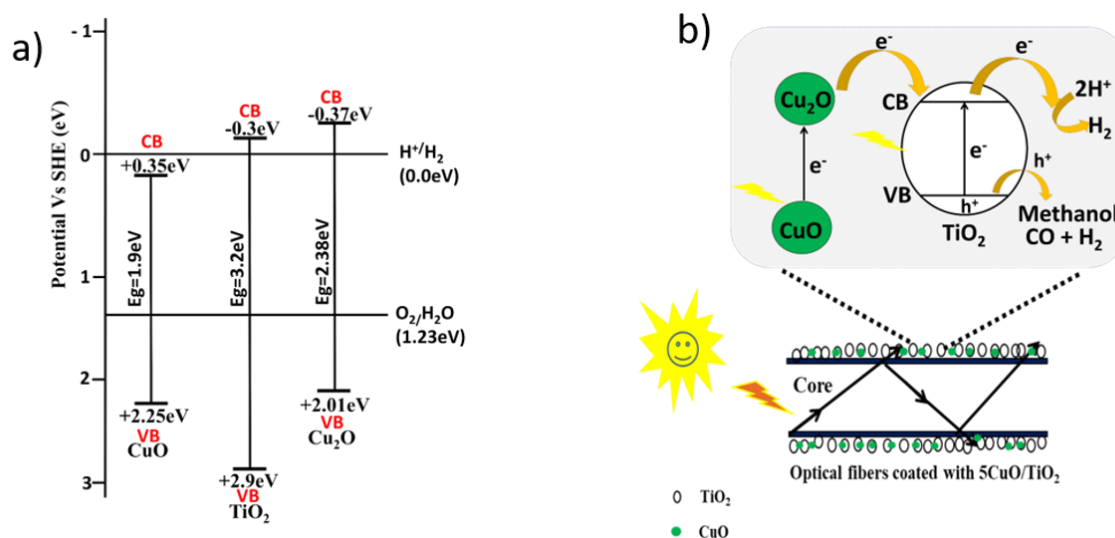
Fig.6.18.a) Valence band and Conduction band positions of CuO, TiO_2 and Cu_2O with respect to water reduction and oxidation potential b) Mechanism of H_2 Evolution from 5CuO/TiO_2 over the surface of optical fibre

6.8. Advantages of catalyst coated optical fibers over dispersed powder catalyst systems

One of the perceived drawbacks of conventional dispersed powder catalysts is the difficulty in scaling up due to increase in turbidity and associated scattering on increasing the catalyst quantity. This is evidenced from Fig. 6.19a, where hydrogen evolution activity is estimated under High pressure 450W Mercury lamp for varying quantities of powder 5CuO/TiO_2 under the same conditions. As the catalyst quantity increases from 50 mg to 1 g, the activity reduces exponentially. Thus, dispersed powder catalyst system is not conducive for scaling up. This disadvantage can be overcome by using optical fiber bundles coated with the catalyst, since scaling up can be achieved by simply increasing the number of coated fibers. This is

demonstrated by increasing the quantity of catalyst by increasing the number of optical fibers (Fig.6.19b). The inset in Fig.6.19b shows the amount of catalyst coated over the optical fiber. As the number of optical fibers increases from 1,000 (1K) to 50,000 (50K), activity also increases accordingly, from ~1 µmole to 120 µmoles, indicating a linear increase in activity with respect to catalyst amount, with a potential to overcome the scattering issue observed in the powder catalyst. Further, the quantity of catalyst coated on 50K fiber bundle was increased from 250 mg to 700 mg. Interestingly, H_2 evolution of 222 µmoles was obtained for this sample, which is more than twice that of the powder sample of same quantity (Fig.6.19c).

Fig.6.19. (a) Effect of 5wt%CuO/TiO_2 catalyst quantity in dispersed powder form (b) H_2 evolution activity of 5wt%CuO/TiO_2 coated optical fiber bundles showing variation in catalyst quantity via number of optical fibers in each bundle (c) Comparitive H_2 evolution activity of

$5CuO/TiO_2$ coated on optical fiber bundles (700mg) and $5CuO/TiO_2$ powderd catalyst (700mg). All experiments were carried out in MeOH/Water system (35 vol%) under illumination of 450 W High pressure Mercury lamp for 8 h.

Same phenomenon holds true for usage of powder catalysts in turbid, non-potable water, whereby scattering from the suspended particles prevents light from reaching the active sites and interfaces. To confirm this phenomenon, hydrogen evolution activities of dispersed powder and catalyst coated optical fibers in water with varying extent of turbidity from 1 to 84 NTU were compared (Fig. 6.20 a). As the turbidity of water sample increases, the activity of both samples decreases (Fig.6.20 b.); however, activity of dispersed powder in turbid water was found to be minimal with a 99.99% reduction in activity compared to clean water. Whereas, even under such severe scattering, ~70% activity was retained in the case of catalyst coated fibres. This reduction in activity in optical fiber is probably due to suspended particles in turbid water blocking the active sites rather than inability of photons to reach the active sites (Fig.6.21).
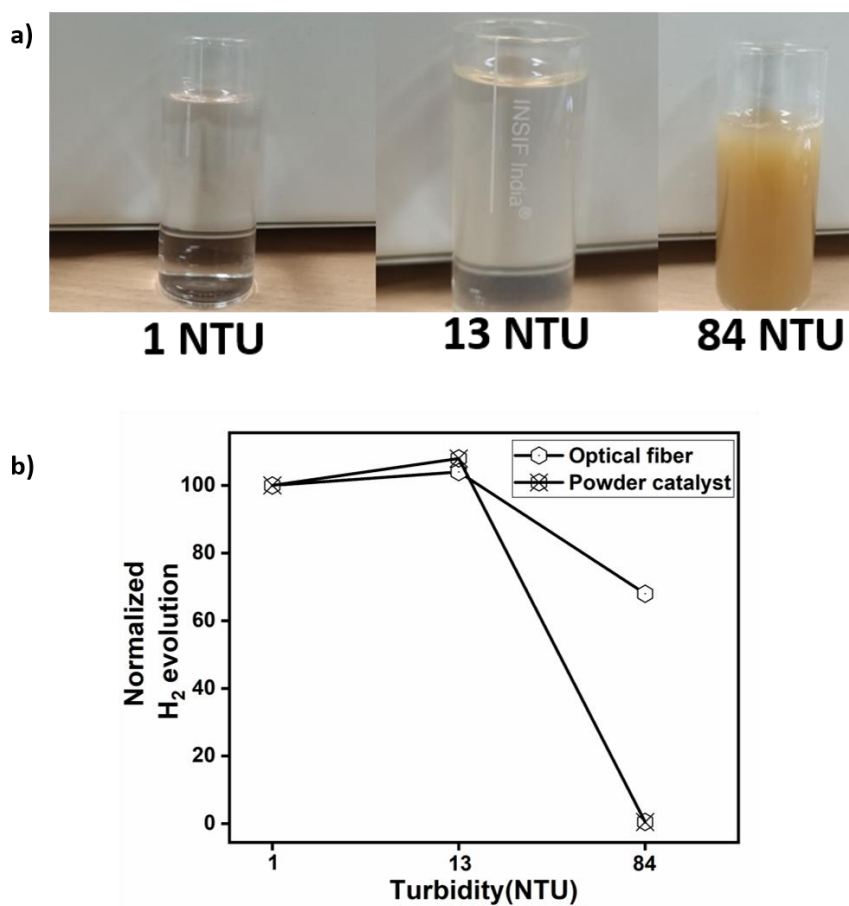
Fig.6.20. a) Extent of Turbidity of water which was measured by using Digital Nephelometer used for photocatalytic H_2 Evolution b)The normalized H_2 evolution activity (against maximum activity) of 5CuO/TiO$_2$ coated optical fiber bundles and powder samples in MeOH/Water system under 8h of illumination of 450 W High pressure Mercury lamp using water samples of different turbidity.
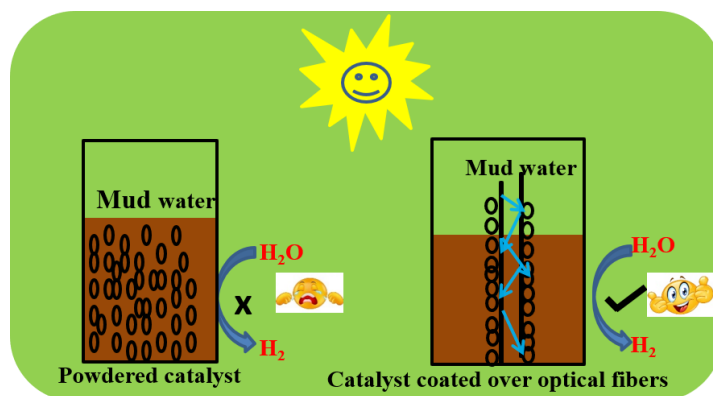
Fig.6.21. Schematic representation of photocatalytic hydrogen evolution in mud water by powder and catalyst coated optical fibers

Similarly, distance of the light source and catalyst/water interface also affects the activity in conventional photoreactors due to loss of intensity by scattering from air. By bringing light directly to the medium of reaction, such losses in intensity and activity can also be addressed (Fig. 6.22).
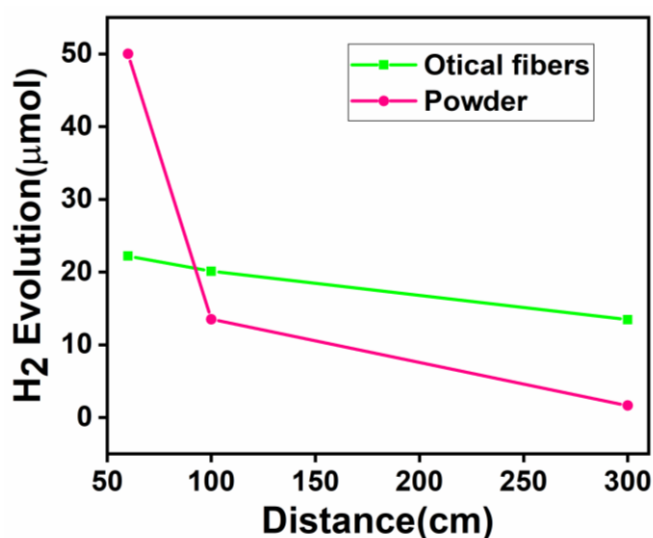
Fig.6.22. Comparison of H_2 evolution activity of 5wt% CuO/TiO_2 coated optical fiber bundles and 5wt% CuO/TiO_2 powdered sample in MeOH/Water system under illumination of 450 W High pressure Mercury lamp at various distance. The activity has been decreased in case of

powdered samples as the distance increases but in case of coated optical fibers the actvity is retained, thus the optical fibers system is more advantageous than that of powderd system

6.9. Conclusion

In summary, a new approach of using optical fibers coated with semiconductor materials for hydrogen evolution is demonstrated. An active catalyst, 5wt%CuO supported on TiO_2, was selected for coating on silica based optical fibers by a simple dip coating method. Characterisation of the loaded catalyst indicates intimate interface between CuO and TiO_2 possibly forming interfaces which are active electron injectors. Photocatalytic H_2 evolution of the catalyst coated optical fibers is compared with dispersed powder catalyst of the same composition. It is found that scattering of light in dispersed powder catalyst systems at higher catalyst quantities has a detrimental effect on activity which prevents scaling up in any meaningful way. However, optical fiber catalyst system can be scaled up easily by increasing the number of fibers without compromising activity due to scattering. We have also shown that powder catalyst is completely deactivated in highly turbid media whereas optical fibers retain activity to a better extent. This is very important since this opens up the type of water sources which can be utilised for H_2 production and helps us to move away from using potable water for fuel production. The lacunae of less illuminance on the surface of the optical fibers need to be addressed by better leaking methods as well as more efficient connections to the light sources. Hence, by combining the abundant and cheap optical fibers to non-potable water usage, we envisage better scaling up opportunities in photocatalytic H_2 production.

6.10. Reference

[1]   Muradov N. *Int.J.Hydrog.Energy.***2017**;42:14058–88.

[2]   Chu S, Majumdar A.*Nature*. **2012**;488:294–303.

[3]   Wang M. *J.Power Sources* **2002** ;112:307–21.

[4]   Song H. et al., *ACS Energy Lett.* **2022**;7:1043–65.

[5]   Sharma S. et al., *Energies* **2021**;14:7389.

[6]   do Sacramento EM. et al.,I*nt. J.Hydrog. Energy* **2008**;33:2132–7.

[7]   Midilli A.et al., *Int. J.Hydrog. Energy* **2008**;33:4209–22.

[8]   Steinberg M.*Int. J.Hydrog. Energy* **1999**;24:771–7.

[9]   VEZIROLU T.*Int.J.Hydrog.Energy* **1997**;22:551–6.

[10]   Fujishima A, Honda K. *Nature* **1972**;238:37–8.

[11]   Chen S.et al., *Nat. Rev. Mater.* **2017**;2:1–17.

[12]   Liu R. et al., *Int. J.Hydrog. Energy* **2021**;46:28462–73.

[13]   Ahmad H.et al., *Renew. Sust. Energ. Rev.* **2015**;43:599–610.

[14]   Fajrina N. et al.,. *Int. J.Hydrog. Energy* **2018**;44:540-577.

[15]   Zhu J.et al., *Curr Opin Colloid Interface Sci* **2009**;14:260–9.

[16]   Abouelela MM. et al., *J. Clean. Prod.* **2021**;294:126200.

[17]   Chauhan DK. et al., *J. Clean. Prod.***2021**;307:127162.

[18]   Almomani F.et al., *Int. J.Hydrog. Energy* **2022**;47:3294–305.

[19] Li Q. et al., *Energy Fuels* **2022**;36:4541

 [20] Gupta NM *Int.J.Hydrog.Energy* **2017**;71:585–601. h

[21] Idriss H. *Energy Technol.* **2021**;9:5-9

[22] Anta JA. et al., *Chem Soc Rev.* **2022**:3794–818.

[23] Narendranath SB.et al., *ACS Appl. Mater. Interfaces*. **2014**;6:12321–7.

[24] Baliarsingh N et al.,. *J. Mater. Chem. A* **2013**;1:4236–43.

[25] Ouyang W. et al.,*Appl.Catal. B: Environ.***2018**;238:434–43.

[26] Hasan MM. et al., *RSC Adv*. **2018**;8:37219–28.

[27] Buraso W. et al., *Mater. Res.Express* **2018**;5:0–10.

[28] Languer MP. et al., *Int. J. Hydrog. Energy* **2013**;38:14440–50.

[29] Darbandi M. et al., *Int. J. Hydrog. Energy* **2019**;44:24162–73.

[30] Pulido Melián E. et al., *Int. J. Hydrog. Energy* **2019**;44:24653–66.

[31] Wang J.et al., *Int. J. Hydrog. Energy* **2018**;43:7388–96.

[32] Li Q. et al., *Energy Fuels* **2022**;36:4541-4548.

[33] Patra KK et al., *J. Mater. Chem. A* **2019**;7:3179–89.

[34] Bajpai H. et al., *ACS Appl. Mater. Interfaces* **2020**;12:30420–30.

[35] de Brito JF. et al., *Appl. Catal. B: Environ.* **2018**;224:136–45.

[36] Gupta A. et al., *Int. J. Hydrog. Energy* **2022**;47:33282–307.

[37]   Nandy S. et al., *Chem. Sci.***2021**; 12:9866–9884.

[38]   Marinangeli RE, Ollls DF, *AlChE Journal* **1977**;23:415–26.

[39]   Marinangeli RE, Ollis DF. *AIChE Journal* **1980**;26:1000–8.

[40]   Du P. et al.,*Appl.Catal. A: Gen*.**2008**;334:119–28.

[41]   Spigulis *J. Opt Photon News* **2005**;16:34-39.

[42]   Lee J. et al., *Opt. Lasers Eng*.**2011**;49:324–30.

[43]   Marinangeli RE. et al., AIChE Journal **1982**;28:945–55.

[44]   Chen Y. et al., *Adv Bio Sci Res* **2017**;3:396–9.

[45]   Chen YL. et al., *Optics Express* **2013**;21:7240.

[46]   Potter ME. et al., *ACS Photonics* **2020**;7:714–22.

[47]   Wang Y. et al., *J. Alloys Compd.* **2020**;813:152184.

[48]   Dieu T. et al., *Adv.Nat. Sci.Nanosci. Nanotechnol*. **2013**; 4:025002.

[49]   Reddy NL. et al., *Ind. Eng. Chem. Res* **2018**;57:568–77.

[50]   Li Y. et al., *Appl. Surf. Sci.* **2015**;324:736–44.

[51]   Kum JM. et al., *Int. J. Hydrog. Energy* **2013**;38:13541–6.

[52]   Manjunath K,. et al., *Mater. Res. Express* **2016**;3:115904.

[53]   Praveen Kumar D. et al.,*Chem Commun* **2013**;49:9443–5.

[54]   Nuo Peh CK. et al., *Procedia Eng.* **2017**;215:171–9.

[55]   Brito JF de. et al., *Chem. Eng. J.* **2017**;318:264–71.

[56]   Echeverria E. *RSC Adv*. **2020**:7839–54.

[57]   Mondal I. et al., *Phys. Chem. Chem. Phys*.**2016**;18:4780–8.

[58]   Xu B. et al.,*J. Chem. Soc. - Faraday Trans.* **1998**;94:1905–9.

[59]   Zainelabdin A. et al., *Appl. Phys. A: Mater. Sci. Process*.**2012**;108:921–8.

[60]   Khan MA. et al., *Nanomaterials* **2020**;10:1–18.

[61]   Bandara J. et al., *Photochem.Photobiol.Sciences* **2005**;4:857–61.

[62]   Wang Z. et al., *Phys. Chem. Chem. Phys.* **2013**;15:14956–60.

Chapter 7

Summary and Conclusion

7.1. Summary

Chapter 1 represents the general introduction to the literature which was done for the thorough research in this thesis. This chapter talks about the importance of renewable energy sources such as hydrogen as fossil fuels are depleting day by day and for the future one need to think about the alternative energy sources. Hydrogen has been used for energy since the 1800s and is considered a green fuel for two reasons: it can be produced from renewable sources and is emission less; H_2, when reacted with O_2, has water as the product with the enormous amount of energy. At normal atmospheric conditions, hydrogen is a colorless and odourless gas. It is stable and coexists harmlessly with oxygen until an energy input drives the exothermic reaction that forms water. Capturing the abundant sunlight falling on Earth has been challenging humankind for decades. The average amount of the sun's radiation penetrating the atmosphere and reaching Earth is 51% of the total incoming energy. This chapter showed the solar spectrum at the earth's surface is mainly spread across the visible range (46%), and the rest near-infrared ranges are experienced as heat with a small part in the near-ultraviolet (5%). Hence, proper exploitation of the solar spectral distribution, especially the visible light spectrum of the solar irradiance, will be the aim of sustainable energy solutions The process of mimicking the photosynthesis phenomenon is called 'Artificial Photosynthesis' by using materials synthesized in the laboratory that will show absorption in the solar spectrum. Water splitting directly yields hydrogen and oxygen; no carbon fixation will occur. This chapter briefly describes the various semiconductor-based materials used for hydrogen evolution via water splitting and dye sensitization as a strategy for fully utilizing solar spectrum. Various strategies have been discussed in this chapter.

Chapter 2 discusses the synthesis and structural characterizations of ZnO as a semiconductor that can be used for the photocatalytic H_2 evolution via water splitting. In this chapter, various

types of morphologies of ZnO have been synthesised by using sol-gel, precipitation, and hydrothermal method. It was found that the hydrothermal method was very advantageous due its simplicity. The hydrothermal method has been further explored and different ZnO starting from nanorods, nanoflowers, nonobat, hydroxides and micro discs has been synthesised just by varying the zinc precursors and reaction medium and keeping the other conditions similar-XRD, FE-SEM, TEM has been used for their characterization. It was found that ZnO nanorods synthesised by hydrothermal method was showing the higher activity in H2 evolution via water splitting.

Chapter 3 further explores the disadvantage of ZnO that is its visible light inactivity since its band gap is 3. 2eV.The concept of utilizing organic dyes with semiconductor for sensitization has been used here. The PTCDA (perylene tetracarboxylic acid dianhydride) is known to have various optoelectronic properties and due to that it has been used widely. So here the ZnO-P (ZnO-Perylene) heterojunction has been formed by hydrothermal method and its characterizations has been carried out. It was found that the ZnO-P shows the very high activity for of an about 49650µmol/h H_2 evolution with stability compare to ZnO (297 µmol/h) and PTCDA (329µmol/h). The higher stability and activity are due to the electron transfer from PTCDA to ZnO and forming the stronger bond during the hydrothermal synthesis.

Chapter 4 explores the concept for forming self-assembly by using the ZnO and PTCDA. These PTCDA are known to form self-assembly via π-π stacking or hydrogen bonding within the molecules. In this chapter this property of PTCDA has been explored. Here the synthesis of ZnO nanoparticles was carried out. After that, the commercially available perylene tetracarboxylic acid dianhydride (PTCDA) as a starting material. Then KOH was used to break the anhydride linkage. After that, the self-assembled structure of ZnO-PTCDA was synthesized. The two different types of PTCDA have been used. One has MC-PTCDA, and the

other one is TC-PTCDA. The structural and photophysical characterizations have been carried out. It was found that the presence of tetra carboxylate group in TC-PTCDA-ZnO plays very important role in electron transfer to ZnO and thus showing the higher activity compare to monocarboxylate group in MC-PTCDA-ZnO.

Chapter 5 here synthesizes the synthesis and characterization of α-Co(OH)$_2$ and β-Co(OH)$_2$. Out of this it was found that due to presence of interlayer anions in between the layers the α-Co(OH)$_2$ much more active than that of β-Co(OH)$_2$. Which led us to synthesised the perylene (PDI) modified α-Co(OH)$_2$ which led to increase in the H$_2$ evolution activity due to the continuous electrons transfer from dye to LDHs.

Chapter 6 here, another concept has been utilized that the use of optical fibers to produce hydrogen via water splitting, this approach is the novel approach and very advantageous if one is thinking to scalable the hydrogen production via water splitting since the powder catalyst and thin film-based catalyst leads to scattering and absorption and low efficiency due to reactor volume inefficiency. This optical fiber can be scalable as light passes through the fibers and one can make these fibers into numerous numbers and put inside deeper and bigger tanks and get the scalable production, in future we are planning to do scalable production of hydrogen by using optical fibers. Here we have used xCuO/TiO$_2$ as coating material over the surface of optical fibers.

7.2. Conclusion

- ✓ The use of ZnO as a semiconductor material for photocatalytic H$_2$ evolution is very useful and advantageous.
- ✓ The morphologies of ZnO can vary from nanorods, nanoflowers, hydroxides of nanorods, hexagonal micro discs and nanobat depending on the synthesis procedure.

✓ The Zn precursor and surrounding medium of reactions play an important role in forming various surface defects in ZnO, leading to various morphologies.

✓ The ZnO nanorods shows the higher activity compare to other morphologies due to its higher intrinsic structural properties and surface area.

✓ The organic-inorganic heterostructure can form a new stable system for the photocatalytic H_2 evolution.

✓ The ZnO-P shows the higher stability and activity for H_2 evolution due to its charge transfer phenomenon from PTCDA part to the ZnO in ZnO-P heterostructures.

✓ The formation of supramolecular self-assemblies of various organic-inorganic materials can form a new era for the continuous electron transfer due the presence of π-π stacking and H-bonding within the molecules.

✓ The TC-PTCDA-ZnO and MC-PTCDA-ZnO shows that the presence of tetra carboxylate group is very important for the formation of self-assemblies and forming stronger bonds with ZnO which led to higher H_2 evolution.

✓ The layered double hydroxides modified with organic dyes can also form a system for continuous electron transfer for the purpose of photocatalytic H_2 evolution.

✓ Scattering is one of the main challenges in scaling up photocatalytic water splitting using the most prevalent powder catalysts. This can be overcome by decoupling the reaction medium from light transmission, as in the case of optical fibers

✓ Optical fiber can be scalable as light passes through the fibers and one can make these fibers into numerous numbers and put inside deeper and bigger tanks and get the scalable production, in future we are planning to do scalable production of hydrogen by using optical fibers.

ABSTRACT

Name of the Student: Priyanka S Walko   **Registration No. :**10CC17A26011

Faculty of Study: Chemical Sciences   **Year of Submission:** 2023

AcSIR academic center/CSIR Lab: CSIR-NCL, Pune

Name of the Supervisor(s): Dr.R.Nandini Devi

Title of the thesis: Visible light driven photocatalytic hydrogen evolution via water splitting using novel approaches in semiconductor catalysts

----

Earth receives an incredible amount of sunlight. motivated by continuously growing global energy demands and the depletion of readily accessible fossil fuels, the search for alternative energy sources, particularly renewable solar energy, has become vital. Different types of innovative ideas have been explored. The earth absorbs a large amount of energy, and only a few of it is used by humankind annually. **Scattering is one of the main challenges in scaling up photocatalytic water splitting using the most prevalent powder catalysts.** Materials development has not translated into many large-scale photocatalytic H_2 production facilities yet. One of the main drawbacks is the necessity for huge light installations in the medium which would render them uneconomical. In addition, limitations of the catalyst forms which can be used for efficient utilization of light from an external source also contributed to the difficulty in scaling up. This thesis reports the detailed structural characterizations and photocatalytic hydrogen activities of ZnO modified with different morphologies. The construction of ZnO-P using perylene-based organic-based material has been explored along with the formation of self-assemblies of ZnO. The construction of layered double hydroxide structure α-Co(OH)$_2$-PDI is also given for photocatalytic H_2 evolution. Finally, the scattering issue in reactor design and scalability issues of powdered and this film-based systems have been addressed by using optical fibers coated with semiconductor materials given in the thesis.

List of publication

List of publications emanating from this thesis work

1. **Priyanka S Walko** and R. Nandini Devi, Scalable optical fiber photocatalytic reactor for H_2 production from water splitting: Addressing scattering issues, International Journal of Hydrogen Energy 48 (45), 17086-17096

2. **Priyanka S Walko** and R. Nandini Devi, One-pot synthesis of Zinc oxide-Perylene heterojunction for photocatalytic hydrogen evolution via oxidation of methanol to value-added products **(under the process of submission)**

3. Geeta Pandurang Kharabe, Rajith Illathvalappil, Sidharth Barik, Fayis Kanheerampockil, **Priyanka S Walko**, Suresh K Bhat, R Nandini Devi, Sreekumar Kurungot ,A cobalt–manganese modified theophrastite phase of nickel hydroxide nanoflower arrays on nickel foam as a self-standing bifunctional electrode for overall water electrolysis Sustainable Energy & Fuels 7 (10), 2428-2440

4. Ayasha Nadeema, **Priyanka S. Walko**, R. Nandini Devi and Sreekumar Kurungot, Alkaline Water Electrolysis by NiZn-Double Hydroxide-Derived Porous Nickel Selenide-Nitrogen-Doped Graphene Composite, ACS Applied Energy Materials., 1, 5500 - 5510 (2018), DOI:10.1021/acsaem.8b0108

Another list of publications from collaborative works was carried out during the Ph.D.

5. **Priyanka S Walko**, Dr. Anil Kumar Paidi, Prof. Kanamaluru Vidyasagar Syntheses and Structural Characterization of $A_3Sb_3P_2O_{14} \cdot 3H_2O$ (A=Rb, Cs, Tl and NH$_4$) Phosphates; Facile Aqueous Ion Exchange Reactions of $K_3Sb_3P_2O_{14} \cdot 3H_2O$, ChemistrySelect 2 (35), 11875-11879, https://doi.org/10.1002/slct.201702401

6. Rajith Illathvalappil, Fayis Kanheerampockil, **Priyanka S Walko**, Suresh K Bhat, R. Nandini Devi and Sreekumar Kurungot, H i e r a r c h i c a l Nanoflower Arrays of Co9S8? Ni3S2 on Nickel Foam: Highly Efficient Binder?free Electrocatalyst for Overall Water Splitting Application, Chemistry - A European Journal., 26 (35), 7900 - 7911 (2020), DOI:10.1002/chem.202000839

7. N Shilpa, A Pandikassala, P Krishnaraj, **Priyanka S Walko**, RN Devi, S Kurungot, Co– Ni Layered Double Hydroxide for the Electrocatalytic Oxidation of Organic Molecules: An Approach to Lowering the Overall Cell Voltage for the Water Splitting Process, ACS Applied Materials & Interfaces 14 (14), 16222-16232

Contributions to Symposia/Conference

1. Presented a poster at '**CATSYMP-23**' held in Bangalore, India during January 17-19, 2018

2. Presented a poster at CSIR National Chemical Laboratory on science day 2018

3. Presented a poster entitled "Supramolecular self-assembled structure of Perylene dimide and photocatalytic activity of ZnO-Perylene composite" at the conference on Energy and Environmental Challenges (CE2C)-2019 held at VNIT, Nagpur on January 18-19,2019

4. Presented a poster entitled "SUPRAMOLECULAR SELF - ASSEMBLED STRUCTURE OF PERYLENE TETRACARBOXYLIC ACID DIANHYDRIDE – ZnO AND ITS HYDROGEN EVOLUTION ACTIVITY" The Asia-Pacific Congress on Catalysis (APCAT) has been organized consecutively every three years by the Asian-Pacific Association of Catalysis Societies (APACS), for this year, Thailand is honored to host the 8th congress (APCAT-8) under the theme of "A breakthrough in Catalysis

toward efficiency and sustainable future" during August 4th-7th, 2019 at Centara Grand & Bangkok Convention Centre at Central World, Bangkok.

5. Presented a poster entitled **"Optical fibers bundles coated with xCuO/TiO₂ for hydrogen evolution by using total internal reflection phenomenon"** at CSIR National Chemical Laboratory, Pune on Science Day Celebration year 2021(**Best poster award**).

6. Presented a poster entitled **"Scalable optical fiber photocatalytic reactor for H₂ production from water splitting: Addressing scattering issues "** at TIFR, Mumbai on the conference Advances in catalysis for energy and environment (CACEE-2022) & CO2India Network 1ˢᵗ Annual Meet (held on 31ˢᵗ October to Friday, November 2022)

ROYAL SOCIETY
OF CHEMISTRY

PAPER

Check for updates

A cobalt–manganese modified theophrastite phase of nickel hydroxide nanoflower arrays on nickel foam as a self-standing bifunctional electrode for overall water electrolysis†

Geeta Pandurang Kharabe,‡[ab] Rajith Illathvalappil, [ID] ‡[ab] Sidharth Barik,[ab] Fayis Kanheerampockil, [ID] [cb] Priyanka S. Walko,[db] Suresh K. Bhat,[cb] R. Nandini Devi [ID] [db] and Sreekumar Kurungot [ID] *[ab]

Designing and developing self-supported electrodes for water electrolysis is attractive as compared to conventional catalyst-coated electrodes. Herein, a $(Co_{0.3}Mn_{0.1}Ni_{0.6})(OH)_2$/NF nanocomposite is prepared by anchoring $(Co_{0.3}Mn_{0.1}Ni_{0.6})(OH)_2$ *via* simple one-pot hydrothermal synthesis on nickel foam. The presence of Mn induces the external electronic structure of $Co(OH)_2$, and this also improves the electrochemically active surface area (ECSA). These favor better accessibility of active sites and increased intrinsic activity for the OER and HER. $(Co_{0.3}Mn_{0.1}Ni_{0.6})(OH)_2$/NF has shown promising electrochemical activity toward the OER and HER in a 1 M KOH electrolyte, with an overpotential of 270 mV for the OER and 163 mV for the HER to deliver 10 mA cm^{-2} current density. The overall water splitting was performed by employing $(Co_{0.3}Mn_{0.1}Ni_{0.6})(OH)_2$/NF as both the cathode and anode by displaying a voltage of 1.62 V at 10 mA cm^{-2}, which is comparable to that extracted from a similar system based on the state-of-the-art Pt/C@NF cathode and RuO_2@NF anode (1.60 V at 10 mA cm^{-2}) standard electrode pair. Interestingly, at high current densities, the $(Co_{0.3}Mn_{0.1}Ni_{0.6})(OH)_2$/NF//$(Co_{0.3}Mn_{0.1}Ni_{0.6})(OH)_2$/NF system displayed better overall water splitting performance (1.78 V at 100 mA cm^{-2}) compared to its Pt/C@NF//RuO_2@NF (1.89 V at 100 mA cm^{-2}) counterpart while displaying a stable output during the evolution period that lasted for 24 h. The amounts of H_2 and O_2 produced are estimated to be 701.2 and 358.6 mmol, respectively, at a time interval of 1 h; these amounts correspond to an ∼1 : 2 ratio of O_2 and H_2, respectively. This study confirms the capability for employing $(Co_{0.3}Mn_{0.1}Ni_{0.6})(OH)_2$/NF as a bi-functional and self-standing electrode for the realistic demonstrations of overall water splitting applications.

1 Introduction

The exploration of renewable sources for sustainable energy production is receiving wide interest due to the global warming issues associated with fossil fuel-based energy sources.[1–3] Replacing fossil fuels with sustainable energy sources is crucial to mitigate environmental problems. In this circumstance, hydrogen (H_2) is presented as the upcoming energy source with

zero carbon emission.[4–6] Compared to the steam reforming of natural gas for conventional H_2 production, electrochemical water splitting is a zero-greenhouse gas emission process for clean H_2 production and, hence, the process becomes attractive. Challenges are associated with H_2 production through water electrolysis due to the kinetic barriers on the respective electrodes. Electrocatalysts are essential to lower the activation energy barrier for the half-cell reactions and to further improve the overall system efficiency. The hydrogen evolution reaction (HER) is the cathodic reaction in water splitting and Pt/C is usually employed as the HER catalyst on the cathode.[7–11] The oxygen evolution reaction (OER) is a kinetically sluggish anodic reaction of water splitting.[12] Precious metal oxides like IrO_2 and RuO_2 have been employed for catalyzing the slow kinetics of the OER.[13,14] Due to the high cost and scarcity of precious metals as well as their poor durability in a corrosive environment, developing a highly stable and cost-effective bi-functional electro-catalyst for employing both as the anode and cathode of the water electrolyzer is vital.

aPhysical & Materials Chemistry Division, CSIR-National Chemical Laboratory, Pune, Maharashtra, 411008, India. E-mail: k.sreekumar@ncl.res.in

bAcademy of Scientific and Innovative Research, Postal Staff College Area, Kamla Nehru Nagar, Ghaziabad, Uttar Pradesh, 201002, India

cPolymer Science and Engineering Division, CSIR-National Chemical Laboratory, Pune, Maharashtra, 411008, India

dCatalysis and Inorganic Chemistry Division, CSIR-National Chemical Laboratory, Pune, Maharashtra, 411008, India

† Electronic supplementary information (ESI) available. See DOI: https://doi.org/10.1039/d3se00233k

‡ These authors contributed equally to this work.

Substantial research efforts have been committed by researchers to developing efficient and cost-effective OER and HER catalysts. There have been reports of effective metal single-atom electrocatalysts for the HER with low overpotentials. For example, recent work by Dang *et. al*. dealt with the quick and easy production of an Ir surface-enriched IrCo alloy catalyst and highlighted its superior performance over the commercial Pt/C catalyst for the HER in acidic environments.[15] In another report, Tiwari and co-workers reported electrocatalysts *viz*. Pt:K_2-PtC$_{14}$@NC-M and Pt-GT-FeCo/Cu, possessing substantially reduced overpotentials of 11 and 18 mV, respectively, for the HER.[16] As in the case of the HER, there are also reports on tackling the overpotential associated with the OER by developing cost-effective catalysts. Thangavel *et. al*. reported a three-dimensional (3D) OER electrode with good efficiency and low material cost by electrochemically integrating amorphous NiFeOOH on the surface of activated carbon fiber paper (CFP) (3D-a-NiFeOOH/N-CFP), which displays an OER overpotential of 170 mV in alkaline medium.[17] A recent study by Xu J. and co-workers reported an overpotential of 223 mV for the OER in 0.5 M H_2SO_4 for a catalyst composition denoted as RuIr@-CoNC.[18] However, the presence of precious metals in the system compromises its commercial viability for large-scale applications.[19]

Transition metal-based materials such as perovskites, layered double hydroxides (LDHs), carbides, nitrides, sulphides and spinel structures were also studied for water splitting applications.[20–27] Among the transition metal catalysts, hydroxides and (oxy)hydroxides of Co, Mn, and Ni are mostly considered and exhibited remarkable bifunctional activities. Mixed transitional metal hydroxides have been extensively studied because of their improved electrocatalytic activity, which is considerably higher than those of the corresponding individual metal hydroxide.[28–32] For example, Xie *et al.* reported a Ni(OH)$_2$ nanomesh synthesized by *in situ* etching of the Al component in a Ni–Al layer double hydroxide. This etching process resulted in a highly porous material, which improves the catalytic activity.[33] In a two-step method, Huang *et al.* synthesized nanosheets of Mn-doped CoOOH. The Mn doping enhances the active sites in CoOOH by significantly increasing the Fermi level of the CoOOH nanosheets.[34] The synergetic effect between the different metal centers has been attributed to this phenomenon to promote the electron transfer processes.[35] Other notable features like structural flexibility and mixed-valence states fascinate the use of mixed transition metal hydroxides for water splitting applications. Among the many transition metal-based materials, Ni and Co-based catalysts have been widely reported for OER and HER applications, especially the oxides of nickel and cobalt.[36–40] Similarly, Mn-based catalysts have also been attractive due to their multiple valencies, higher oxidation state, earth abundance, and electrochemical properties.[34,41–43]

Developing self-standing electrodes is attractive for eliminating the resistance contribution from the binders during electrode fabrication. Herein, we have prepared a self-supported ternary metal hydroxide, (Co$_{0.3}$Mn$_{0.1}$Ni$_{0.6}$)(OH)$_2$ on nickel foam (NF) through the hydrothermal process and obtained a hierarchical nanoflower morphology. Moreover, the (Co$_{0.3}$Mn$_{0.1}$Ni$_{0.6}$)(OH)$_2$ composite is directly grown on the NF surface to form an ordered structure, which could avoid the use of a binder. The binder-free synthesized electrodes expose a high surface area with improved electrical conductivity and have the ability to facilitate better mass transport in the system. The obtained (Co$_{0.3}$Mn$_{0.1}$Ni$_{0.6}$)(OH)$_2$/NF system exhibited better catalytic activities for overall water splitting. Typically, a multi-metallic system consisting of Co, Mn, and Ni, where Mn is present in multiple oxidation states, improves the bifunctional catalytic activity. Mn in the tetravalent state provides structural stability and makes the system robust.[44] The as-synthesized self-supported electrodes exhibited remarkable performance in terms of the overpotential of 270 mV for the OER and 163 mV for the HER at a current density of 10 mA cm^{-2} and excellent long-term stability. Finally, the overall water splitting was performed in a 1 M KOH electrolyte with (Co$_{0.3}$Mn$_{0.1}$Ni$_{0.6}$)(OH)$_2$/NF as the bi-functional catalyst both at the cathode and anode, which displayed prominent activity with excellent long-term stability.

2 Experimental section

2.1 Synthesis of (Co$_{0.3}$Mn$_{0.1}$Ni$_{0.6}$)(OH)$_2$/NF

For the synthesis of (Co$_{0.3}$Mn$_{0.1}$Ni$_{0.6}$)(OH)$_2$/NF, firstly, NF with the dimensions of 3.5 cm × 2.5 cm was cleaned with 1 M HCl, deionized water, and ethanol consecutively by bath sonication for 10 min, followed by drying in a vacuum oven at 60 °C for 5 h. For the synthesis of (Co$_{0.3}$Mn$_{0.1}$Ni$_{0.6}$)(OH)$_2$/NF, NF was used as a substrate, and manganese acetate tetrahydrate (Mn (CH$_3$-CO$_2$)$_2$·4H$_2$O, 1 mmol) and cobalt nitrate hexahydrate (Co(NO$_3$)$_2$·6H$_2$O, 0.5 mmol) were dispersed in deionized water (30 mL) by stirring for 15 min at room temperature. The obtained solution was transferred into a Teflon-lined autoclave with a capacity of 40 mL and the precleaned NF was kept vertically in the container. Furthermore, hydrothermal treatment was carried out at 180 °C for 12 h in an oven. After cooling down to room temperature, the material was removed from the Teflon-lined autoclave and washed three times with an ethanol–DI water mixture (1:1). The obtained material was dried in a vacuum oven for 5 h at 60 °C and the obtained material is named henceforth (Co$_{0.3}$Mn$_{0.1}$Ni$_{0.6}$)(OH)$_2$/NF. For comparison, Mn(OH)$_2$/NF and Co(OH)$_2$/NF were also synthesized under similar conditions except that only Mn(CH$_3$CO$_2$)$_2$·4H$_2$O and Co(NO$_3$)$_2$·6H$_2$O, respectively, were added to the autoclave instead of the mixture of Mn(CH$_3$CO$_2$)$_2$·4H$_2$O and Co(NO$_3$)$_2$·6H$_2$O. For comparison, two more samples were synthesized under similar conditions with different molar ratios of cobalt and manganese (Mn:Co of 0.5:0.5 and 0.5:1 mmol) and the samples are denoted correspondingly as CoMn/NF-(1:1) and CoMn/NF-(2:1). The mass loading of the active material on NF was deduced by considering the weight gain after the reaction, which was found to be nearly 3 mg cm^{-2}.

2.2 Physical characterization

The morphological and compositional information was obtained by field emission scanning electron microscopy (FESEM; Nova Nano SEM 450). A Tecnai T-20 instrument at an

accelerating voltage of 200 kV was used for transmission electron microscopy (TEM) imaging. High-resolution imaging and HAADF-STEM mapping were performed using a JEOL JEM F-200 HRTEM instrument. The samples for TEM and HRTEM were prepared by drop-wise coating the well-dispersed sample in isopropyl alcohol (a small piece of the sample dispersed in 1 mL solvent) on a carbon-coated 200 mesh copper grid. The sample-coated TEM grid was dried for 1 h under an IR lamp. The crystallinity and phase purity of the synthesized samples were investigated through X-ray diffraction (XRD) analysis on a Rigaku SmartLab X-ray diffractometer with Cu Kα radiation (λ = 1.5406 Å), at a scan rate of 10° min^{-1} in the 2θ range of 10 to 80°. X-ray photoelectron spectroscopy (XPS) was performed on a Thermo Scientific Kα+, a fully integrated, monochromatic small-spot X-ray Photoelectron Spectroscopy (XPS) system. The solid–liquid contact interface between the catalysts and water was characterized by using an optical contact angle system (KRŚS drop shape analyzer). An Xradia Versa 510 X-ray microscope (Zeiss X-ray Microscopy, Pleasanton, CA, USA) was used to record micro-computed X-ray tomography (micro-CT) images in order to get the 3D morphology.

2.3 Electrochemical analysis

Electrochemical experiments were performed using a Bio-Logic potentiostat (VMP-3) in a 1 M KOH electrolyte at room temperature. The activity and durability of the catalysts were measured by cyclic voltammetry (CV), linear sweep voltammetry (LSVs), and chronoamperometric methods using a three-electrode set-up. For this, the synthesized $(Co_{0.3}Mn_{0.1}Ni_{0.6})(OH)_2$/NF was employed as the working electrode with an active area of 1 cm^2, Hg/HgO as the reference electrode, and a graphite rod as the counter electrode. To evaluate the HER performance of the samples, LSVs were recorded from 0.20 to −0.60 V $vs.$ RHE with a scan rate of 2 mV s^{-1}. To estimate the OER activity of the samples, LSVs were recorded from 1.1 to 1.7 V $vs.$ RHE at a scan rate of 2 mV s^{-1}. Chronoamperometric performance was evaluated at a current density of 20 mA cm^{-2} for 24 h. All the potentials mentioned in the work are based on the RHE scale by calibrating Hg/HgO in a H$_2$-saturated 1 M KOH solution (details are provided in ESI, Fig. S11†).

3   Results and discussion

Scheme 1 depicts the synthesis procedure of the cobalt manganese nickel hydroxide $((Co_{0.3}Mn_{0.1}Ni_{0.6})(OH)_2)$ composite over the nickel foam (NF) through the hydrothermal process and the obtained material is named $(Co_{0.3}Mn_{0.1}Ni_{0.6})(OH)_2$/NF. To check the morphological features of the obtained material, FESEM analysis was performed and the data are presented in Fig. 1. With the combination of both cobalt and manganese ions in the hydrothermal treatment, the morphology of the obtained material is changed from
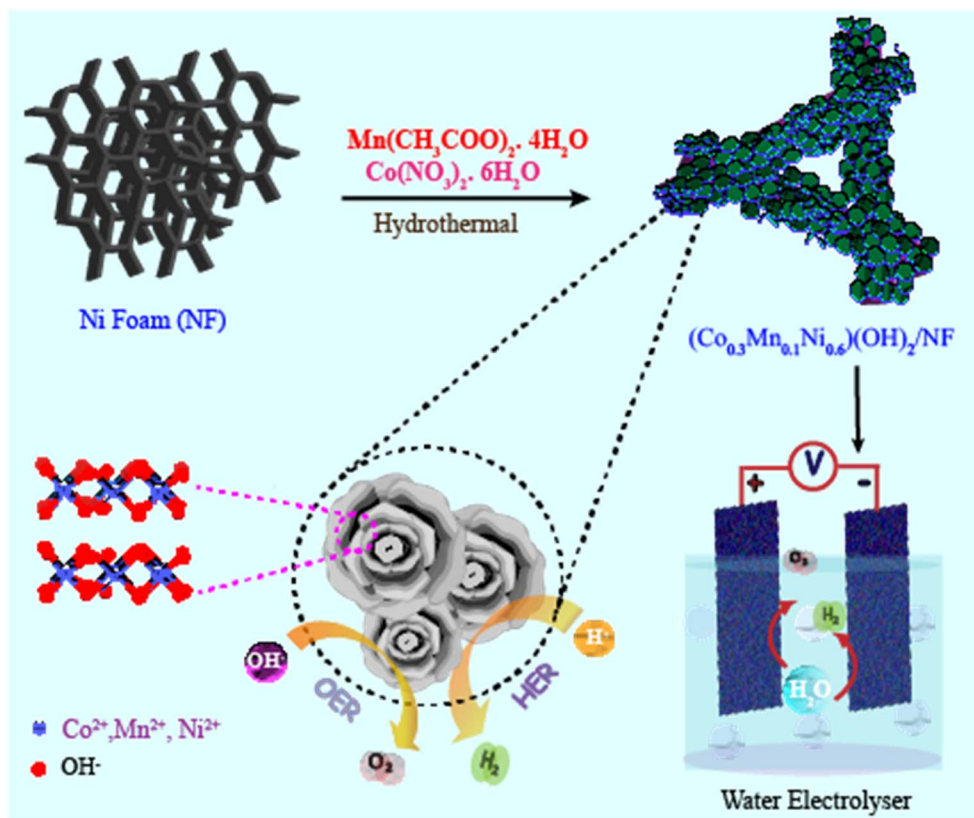
Scheme 1 Graphic representation for the synthesis of $(Co_{0.3}Mn_{0.1}Ni_{0.6})(OH)_2$/NF and its application as a self-standing bi-functional electro-catalyst in water electrolysis applications.
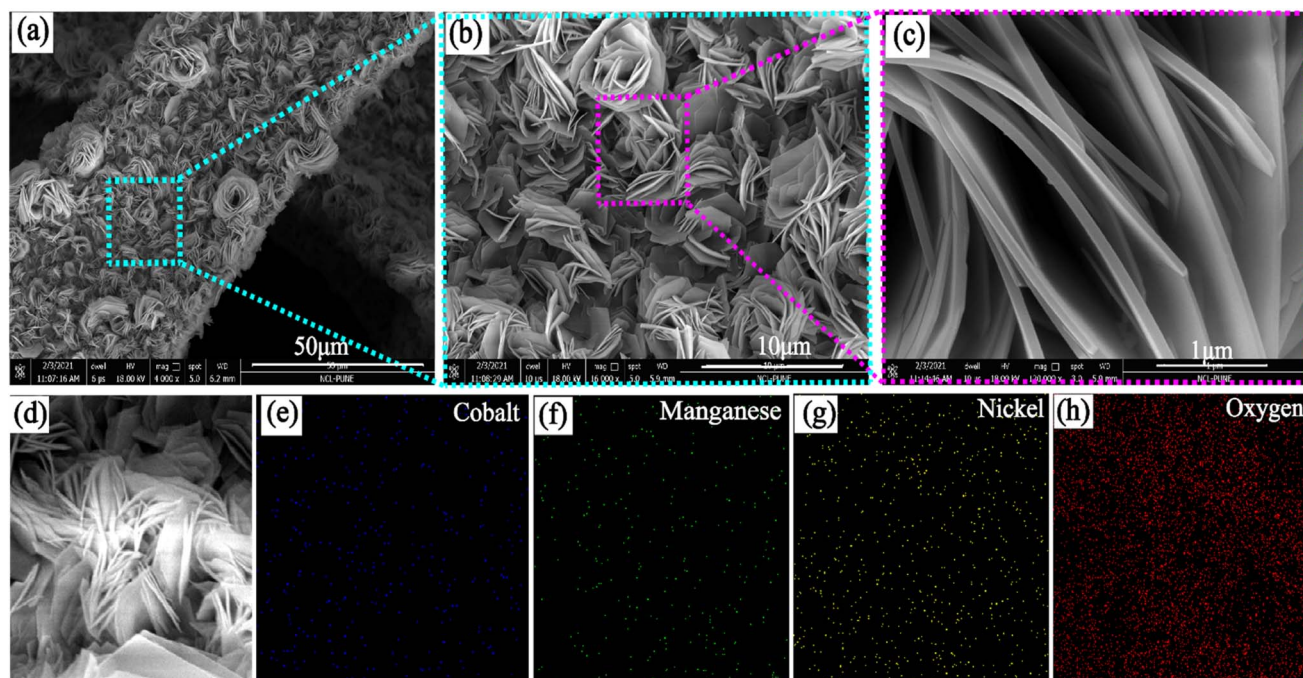
Fig. 1 FE–SEM images of $(Co_{0.3}Mn_{0.1}Ni_{0.6})(OH)_2$/NF: (a) the flower type morphology of $(Co_{0.3}Mn_{0.1}Ni_{0.6})(OH)_2$/NF, (b) the magnified image of the portion marked in the square in Fig. (a) and (c) the high magnification image of $(Co_{0.3}Mn_{0.1}Ni_{0.6})(OH)_2$/NF, (d) the image of $(Co_{0.3}Mn_{0.1}Ni_{0.6})(OH)_2$/NF and the corresponding elemental mapping showing the uniform dispersion of (e) cobalt (Co), (f) manganese (Mn), (g) nickel (Ni), and (h) oxygen (O), respectively.

nanoparticles and interconnected porous nanosheets to flower-like growth patterns. As illustrated in Fig. 1a–c, the FESEM images of $(Co_{0.3}Mn_{0.1}Ni_{0.6})(OH)_2$/NF indicated the presence of these flower-like hydroxide growth patterns over the NF surface. The flower-like morphology possesses the advantage of significantly increasing the electrochemically active surface area and would provide easy diffusion of the electrolyte and the evolved gases during water electrolysis. The high-magnification FESEM image presented in Fig. 1c displays the vertical array of the $(Co_{0.3}Mn_{0.1}Ni_{0.6})(OH)_2$ sheets (60–100 nm thick) on NF. EDX-elemental mapping was performed to confirm the presence of the elements in $(Co_{0.3}Mn_{0.1}Ni_{0.6})(OH)_2$/NF. Fig. 1d shows the image of $(Co_{0.3}Mn_{0.1}Ni_{0.6})(OH)_2$/NF and the corresponding elemental mapping (e–h) confirmed that cobalt, manganese, nickel, and oxygen are uniformly distributed in the sample. Fig. S1† represents the digital images of bare NF and $(Co_{0.3}Mn_{0.1}Ni_{0.6})(OH)_2$/NF.

The SEM images in Fig. S2a and b† show the bare NF surface. The images presented in Fig. S2c and d† illustrate the nickel hydroxide on NF $(Ni(OH)_2$/NF) showing a sheet-like morphology, which is converted into a flower type in the presence of Co and Mn. The images presented in Fig. S2e and f† illustrate the cobalt hydroxide on NF $(Co(OH)_2$/NF) showing a dense particle distribution on NF, whereas the images in Fig. S2g and h† correspond to the distribution of manganese hydroxide on NF $(Mn(OH)_2$/NF) obtained through the hydrothermal treatment.[44] $Mn(OH)_2$ exhibits an interconnected porous nanosheet-type structure. The crucial role of the 0.5 mmol Co and 1 mmol Mn $((Co_{0.3}Mn_{0.1}Ni_{0.6})(OH)_2$/NF)

precursor mixture for the formation of the flower-like morphology was further studied. Our experiments using 0.5 mmol Mn and 0.5 mmol Co (CoMn/NF-(1 : 1)) and 0.5 mmol Mn and 1 mmol Co (CoMn/NF-(2 : 1)) precursors resulted in a sheet-type morphology. The FESEM images of CoMn/NF-(1 : 1) in Fig. S3a–c† show a sheet-like morphology (26–40 nm thick) with the random array of these sheets. The FESEM images in Fig. S3d and e† show that CoMn/NF-(2 : 1) exhibits a rough surface on NF. Fig. S3f† shows the stacked type of sheet arrangement in CoMn/NF-(2 : 1). Thus, morphological analysis reveals the vital role played by the 0.5 : 1 ratio of Co to Mn precursor for acquiring the flower-type morphology in $((Co_{0.3}Mn_{0.1}Ni_{0.6})(OH)_2$/NF). In Fig. S4a,† cross-sectional FE-SEM shows that the obtained thickness of $(Co_{0.3}Mn_{0.1}Ni_{0.6})(OH)_2$ over NF is 5.3 μm, which is comparable to the average thickness determined from the 3D tomography image (Fig. S4b†). To estimate the average ratio of the elements in $(Co_{0.3}Mn_{0.1}Ni_{0.6})(OH)_2$/NF, SEM, HR-TEM EDX and ICP analyses were performed. The SEM and HR-TEM EDX comparative study shows that the average ratio of Co, Mn, and Ni is 0.3, 0.1, and 0.6 respectively, as shown in Fig. S5a and b.† Also, inductively coupled plasma (ICP) analysis was carried out to get further information in this direction. For the analysis, the sample was digested in freshly prepared aqua regia by heating at 50 °C. The corresponding content of Mn and Co is 0.63 and 1.82 wt%, respectively, in $(Co_{0.3}Mn_{0.1}Ni_{0.6})(OH)_2$/NF.

For microstructural analysis, Transmission Electron Microscopy (TEM) imaging, high-resolution imaging, and HAADF-STEM mapping were performed. The TEM images
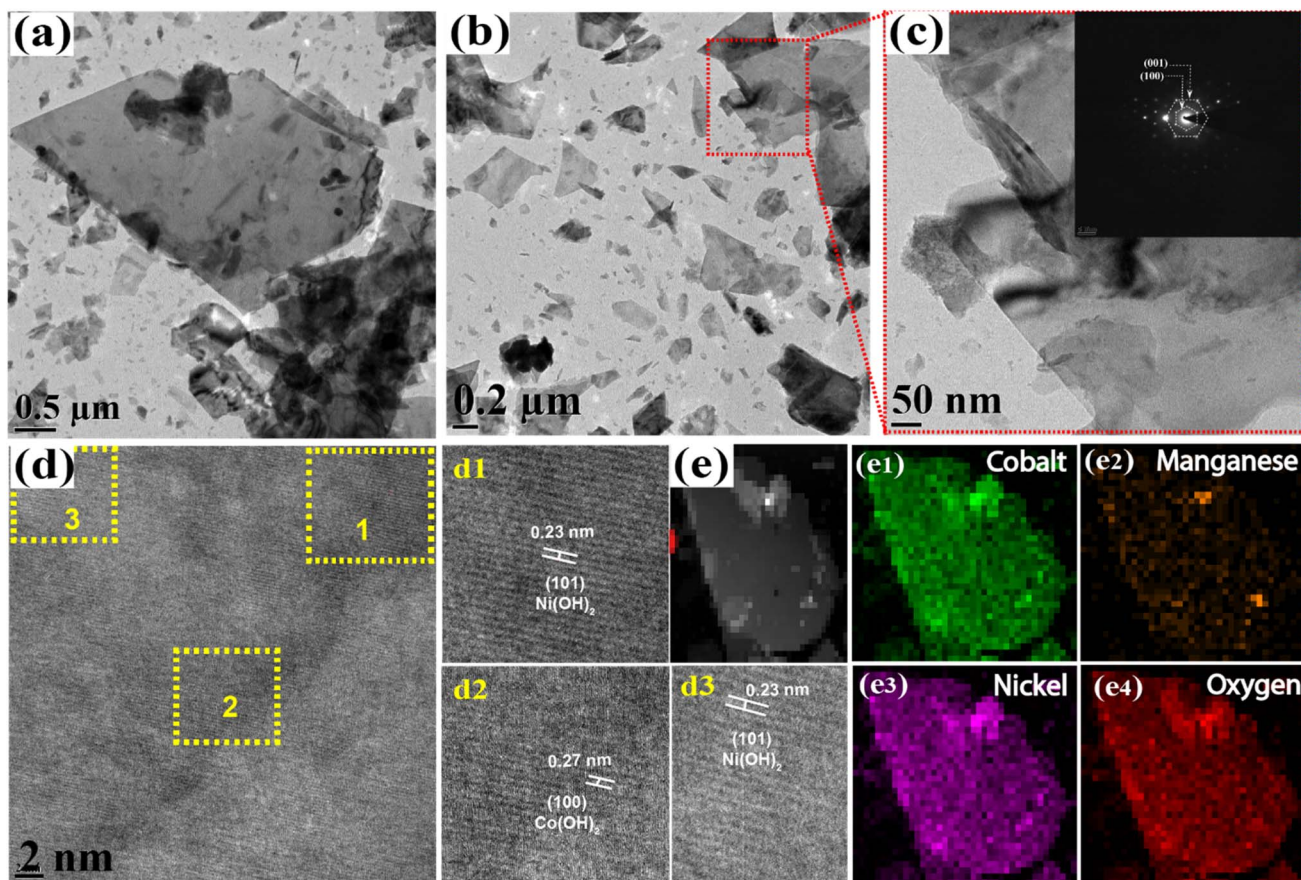
Fig. 2 (a and b) TEM images of $(Co_{0.3}Mn_{0.1}Ni_{0.6})(OH)_2$/NF at different magnifications, (c) zoomed part marked in (b) with the SAED pattern in the inset, (d) d-spacing measurements of the marked regions (represented as d1, d2 and d3), and (e) HAADF-STEM EDX elemental mapping of $(Co_{0.3}Mn_{0.1}Ni_{0.6})(OH)_2$/NF corresponding to Co (e1), Mn (e2), Ni (e3) and O (e4).

presented in Fig. 2a–c reveal that the hydrothermal treatment with the mixture of Co and Mn ions results in the formation of thin sheets of $(Co_{0.3}Mn_{0.1}Ni_{0.6})(OH)_2$/NF. The plane in the selected area electron diffraction (SAED) pattern of $(Co_{0.3}Mn_{0.1}Ni_{0.6})(OH)_2$/NF presented in the inset of Fig. 2c is readily indexed to the interplanar spacing of the hexagonal phase of the $Co(OH)_2$ structure. The d-spacing values of 0.46 and 0.28 nm are consistent with the (001) and (100) lattice planes of hexagonal $Co(OH)_2$, respectively.[44] As shown in Fig. 2d, the highlighted portions marked as d1 and d3 indicate an interplanar distance of 0.23 nm corresponding to the (101) plane of $Ni(OH)_2$ and d2 with 0.27 nm corresponds to the (100) plane of hexagonal $Co(OH)_2$.[44,45] The HAADF-STEM image and the corresponding EDX mapping in Fig. 2e reveal the uniform distribution of Co (e1), Mn (e2), Ni (e3), and O (e4) in $(Co_{0.3}Mn_{0.1}Ni_{0.6})(OH)_2$/NF. For comparison, microstructure analysis for $Co(OH)_2$/NF and $Mn(OH)_2$/NF was also performed. The TEM images presented in Fig. S6a–c† show the structure of $Co(OH)_2$/NF involving the morphology corresponding to 60–90 nm nanoparticles; Fig. S6d† represents the SAED pattern of the sample, displaying its polycrystalline nature. The images presented in Fig. S7a–c† show the interconnected sheets of $Mn(OH)_2$/NF, which helps in the formation of the flower-type morphology in

$(Co_{0.3}Mn_{0.1}Ni_{0.6})(OH)_2$/NF. The d-spacing value of 0.24 nm corresponds to the (011) lattice plane of hexagonal $Mn(OH)_2$ and is shown in Fig. S6d.†[46] The inset of Fig. S7d† corresponds to the SAED pattern of $Mn(OH)_2$/NF and indicates its crystalline nature. The d-spacing value confirms that Mn is present in the hexagonal $Mn(OH)_2$ state in $(Co_{0.3}Mn_{0.1}Ni_{0.6})(OH)_2$/NF. Fig. 3a shows the X-ray diffraction patterns of the as-synthesized materials. As observed in all the XRD patterns, the well-defined peaks located at 44.3°, 51.7°, and 76.6° correspond to the (111), (200), and (220) lattice planes of metallic nickel, respectively, which are originated from the NF substrate (JCPDS No. 04-0850).[47] The hydroxides of cobalt and nickel display similar phase structures and are difficult to differentiate from each other.[48,49] The prominent peaks located at 19.8°, 32.9°, 38.9°, 52.1°, and 59.5° correspond to the (001), (100), (101), (012), and (110) diffraction planes of the hexagonal phase of $Ni(OH)_2$ (JCPDS CARD No. 00-014-0117) and $Co(OH)_2$ (JCPDS CARD No. 01-074-1057), confirming the successful formation of $(Co_{0.3}Mn_{0.1}Ni_{0.6})(OH)_2$ over NF, in Fig. 3b.[48,50] With the addition of Mn ions in the hydrothermal process, the relative intensities of the XRD peaks in $(Co_{0.3}Mn_{0.1}Ni_{0.6})(OH)_2$/NF are increased and the peaks at 19.8° and 32.9° are slightly shifted to higher 2θ values (~0.3°) as well as the crystallinity of the material is
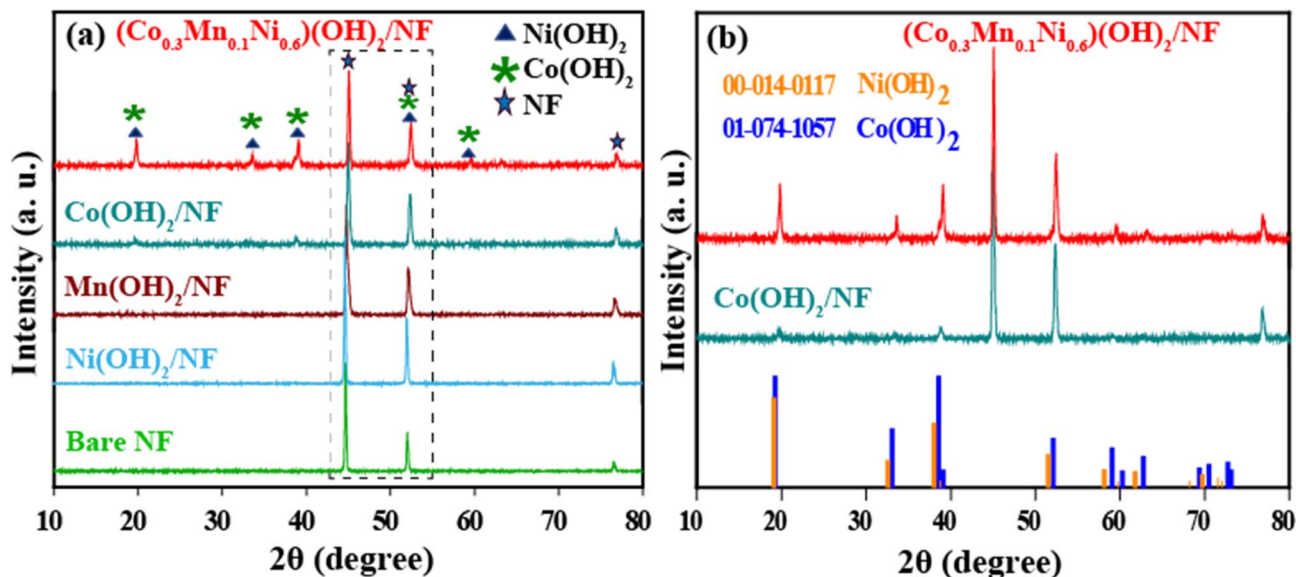
Fig. 3 (a) Comparative XRD patterns of $(Co_{0.3}Mn_{0.1}Ni_{0.6})(OH)_2/NF$, $Co(OH)_2/NF$, $Mn(OH)_2/NF$, $Ni(OH)_2/NF$, and bare NF and (b) the XRD pattern of $(Co_{0.3}Mn_{0.1}Ni_{0.6})(OH)_2/NF$ and $Co(OH)_2/NF$ with the respective JCPDS files.

increased while maintaining the same crystal structure (Fig. S8a†).[51–53] Due to the low percentage of Mn, no prominent $Mn(OH)_2$ peak is observed in the XRD spectrum of $(Co_{0.3}Mn_{0.1}Ni_{0.6})(OH)_2/NF$. However, the existence of Mn is confirmed by the d-spacing value through TEM analysis. The obtained d-spacing value of 0.24 nm is consistent with the (011) lattice plane of hexagonal $Mn(OH)_2$. From literature reports, ternary hydroxides $(M(OH)_2, M = Co, Ni, Mn)$ acquire a similar structure for different metals.[50,54] With changing the ratio of Mn and Co precursors in the hydrothermal process, the XRD pattern of CoMn/NF-(1:1) and CoMn/NF-(2:1) was recorded. The XRD spectrum shown in Fig. S8b† indicates that no phase change occurs with the different ratios of Mn and Co during the reaction. Raman analysis was done to characterize the structure of $(Co_{0.3}Mn_{0.1}Ni_{0.6})(OH)_2/NF$ and the spectrum is presented in Fig. S8c.† The peaks at 438 and 531 cm^{-1} correspond to $Co(OH)_2$ and $Ni(OH)_2$ in $(Co_{0.3}Mn_{0.1}Ni_{0.6})(OH)_2/NF$, respectively.[55]

The 3D morphology of bare NF and $(Co_{0.3}Mn_{0.1}Ni_{0.6})(OH)_2/NF$ was determined by using non-invasive 3D X-ray micro-tomography. Fig. 4a shows the tomography image of bare NF. The plane surface and porous arrangement evident from the tomography image match with the FESEM images of the bare NF. The tomography images of $(Co_{0.3}Mn_{0.1}Ni_{0.6})(OH)_2/NF$ are presented in Fig. 4b–d. The green color in the core of the structure in Fig. 4c and d indicates the Ni metal from the NF substrate and the red color shows the *in situ* covered $(Co_{0.3}Mn_{0.1}Ni_{0.6})(OH)_2$. The uniformly distributed nanoflowers of $(Co_{0.3}Mn_{0.1}Ni_{0.6})(OH)_2$ are confirmed by the tomography as it is seen as a layer on the NF. The porous macrostructure arrangement of the NF has been intact after the formation of the $(Co_{0.3}Mn_{0.1}Ni_{0.6})(OH)_2$ nanoflowers. After the morphological investigations, to understand the surface wettability and the nature of the electrode/electrolyte interface, contact angle

analysis was performed. During water electrolysis, H_2 and O_2 gas bubbles are produced continuously over the catalyst surface and hinder the active sites, which results in decreased mass transport and electron transfer. The hydrophilic nature of the catalyst surface is required to make a better electrode/electrolyte interface and to further minimize the mass-transport-related issues.[56,57] Fig. 4e and S9a–c† show that the water droplets remained over bare NF, $Co(OH)_2/NF$, $Mn(OH)_2/NF$, and $Ni(OH)_2/NF$, which indicates the highly hydrophobic nature of the surface with a contact angle of 137.1°, 117.3°, 134.0°, and 135.0°, respectively. The flower-like morphology in $(Co_{0.3}Mn_{0.1}Ni_{0.6})(OH)_2/NF$ would increase the roughness factor of the surface and improve the surface wettability of the electrode. This resulted in the fast-spreading of the water droplet in $(Co_{0.3}Mn_{0.1}Ni_{0.6})(OH)_2/NF$ during the contact angle measurement, as depicted in Fig. 4f.

To know the chemical composition of $(Co_{0.3}Mn_{0.1}Ni_{0.6})(OH)_2/NF$, XPS analysis was performed. Fig. S10a† shows the survey scan spectrum of $(Co_{0.3}Mn_{0.1}Ni_{0.6})(OH)_2/NF$ and confirms the presence of Mn, Co, Ni, and O in the sample. The Co 2p spectrum displays peaks at 780.1 and 795.1 eV due to the spin–orbit effect, which is characteristic of Co $2p_{3/2}$ and Co $2p_{1/2}$ in $Co(OH)_2$, respectively, and is shown in Fig. 5a. The Co 2p spectrum is deconvoluted into Co^{2+} at 780.0 and 795.5 eV along with two satellite peaks at 783.1 eV and 803.1 eV, respectively, for $Co(OH)_2$.[58,59] The Co 2p spectrum of $(Co_{0.3}Mn_{0.1}Ni_{0.6})(OH)_2/NF$ (Fig. 5d) shows peaks at 779.2 and 795.0 eV corresponding to the Co $2p_{3/2}$ and Co $2p_{1/2}$ peaks, respectively.[60] The core level of Co is deconvoluted into 779.1 and 795.0 eV peaks of Co^{2+}. Along with this, two satellite peaks could be seen appearing at 783.6 and 800.8 eV. In $Co(OH)_2/NF$, the difference between Co $2p_{3/2}$ and Co $2p_{1/2}$ peaks is 15.0 eV $(\Delta E = 15.0\ eV)$. However, Co $2p_{3/2}$ and Co $2p_{1/2}$ in $(Co_{0.3}Mn_{0.1}Ni_{0.6})(OH)_2/NF$ exhibit a comparatively larger spin–orbit splitting value (ΔE) of 15.8 eV with peak
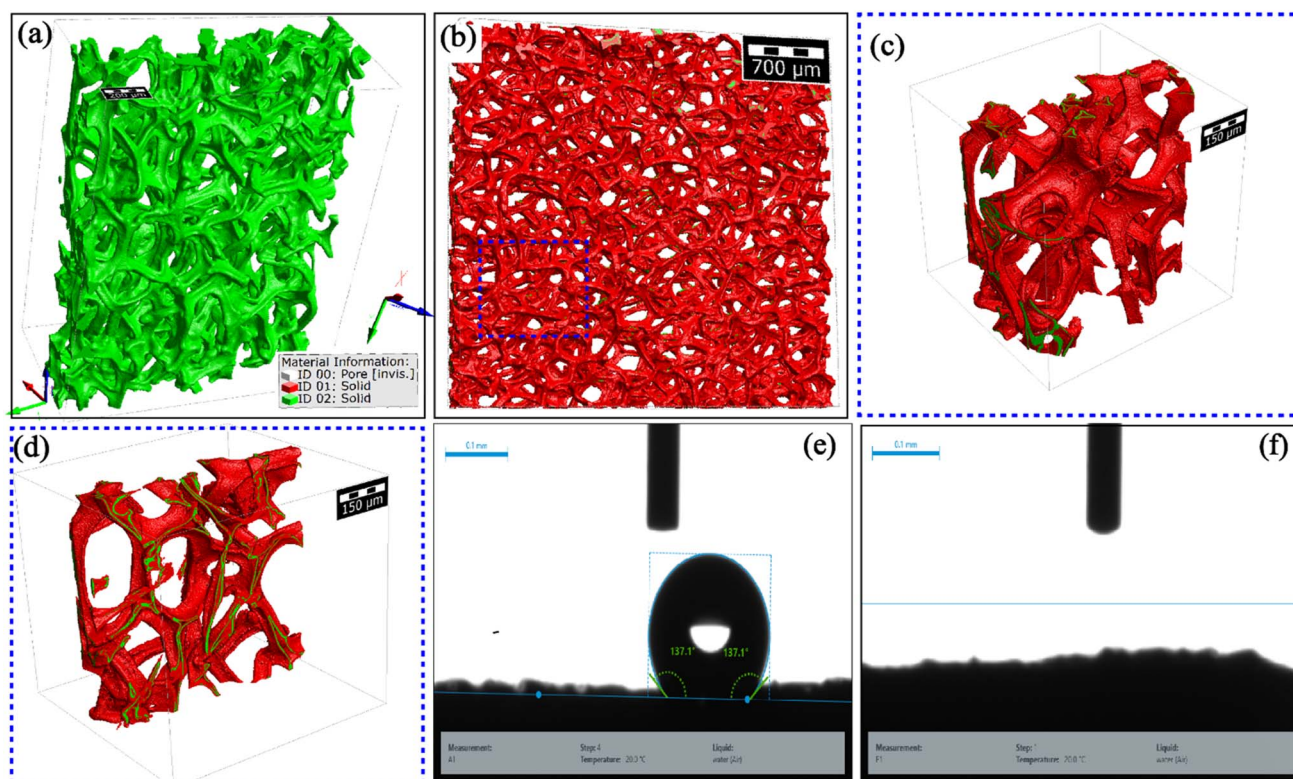
Fig. 4 Tomography images of (a) bare NF and (b–d) $(Co_{0.3}Mn_{0.1}Ni_{0.6})(OH)_2$/NF; the contact angle measurement of (e) bare NF and (f) $(Co_{0.3}Mn_{0.1}Ni_{0.6})(OH)_2$/NF.

shift towards lower binding energy (Fig. S10b†). The apparent negative shift of Co $2p_{3/2}$ and Co $2p_{1/2}$ in $(Co_{0.3}Mn_{0.1}Ni_{0.6})(OH)_2$/NF compared to $Co(OH)_2$ indicates an increased electronic density in $(Co_{0.3}Mn_{0.1}Ni_{0.6})(OH)_2$/NF after the incorporation of Mn. This is due to the difference in the electronegativity between Mn (1.55) and Co (1.88), and there could be a charge transfer from Mn to Co in $(Co_{0.3}Mn_{0.1}Ni_{0.6})(OH)_2$/NF.[44] It is also confirmed through the deconvoluted Mn core level spectrum of $Mn(OH)_2$/NF and $(Co_{0.3}Mn_{0.1}Ni_{0.6})(OH)_2$/NF. Fig. 5b shows that the Mn 2p spectra of $Mn(OH)_2$/NF are fitted into three peaks corresponding to Mn^{2+} (642.6 eV), Mn^{3+} (653.3 eV), and a satellite peak (646.9 eV), respectively.[59,61] Fig. 5e shows that the Mn 2p spectrum in $(Co_{0.3}Mn_{0.1}Ni_{0.6})(OH)_2$/NF could be deconvoluted to three peaks at 653.6, 642.8 eV, and 647.5 eV corresponding to Mn $2p_{1/2}$, Mn $2p_{3/2}$ and satellite peaks, respectively.[59] The peak at 653.6 eV is assigned to Mn^{3+} and 642.8 eV corresponds to Mn^{2+}.[52,62] Both Mn^{3+} and Mn^{2+} are shifted to higher binding energy in $(Co_{0.3}Mn_{0.1}Ni_{0.6})(OH)_2$/NF compared to $Mn(OH)_2$/NF. The positive shift in the binding energy of Mn^{2+} and Mn^{3+} in $(Co_{0.3}Mn_{0.1}Ni_{0.6})(OH)_2$/NF compared to $Mn(OH)_2$/NF indicates a decreased electronic density. This result confirmed charge transfer from Mn to Co in $(Co_{0.3}Mn_{0.1}Ni_{0.6})(OH)_2$/NF. The presence of Mn^{2+} or Mn^{3+} mixed oxidation states is also confirmed by a spin–orbit spacing value of 10.8 eV.[50,63] Fig. 5c reveals the deconvoluted spectra of Ni 2p in $(Co_{0.3}Mn_{0.1}Ni_{0.6})(OH)_2$/NF, which show two spin–orbit doublet peaks at 854.7 and 872.2 eV, corresponding to the Ni^{2+}

state. In addition to this, there are two satellite peaks at 860.3 and 877.9 eV in $(Co_{0.3}Mn_{0.1}Ni_{0.6})(OH)_2$/NF. As illustrated in Fig. 5f, the O 1s spectrum in $(Co_{0.3}Mn_{0.1}Ni_{0.6})(OH)_2$/NF has been fitted into two peaks at 528.7 and 530.0 eV corresponding to the metal–oxygen and metal–hydroxide bonds, respectively and a third peak at 531.1 eV due to the absorbed water molecules.[50,51] Based on XPS analysis, Co, Mn, and Ni show Co^{2+}, Mn^{2+}, Mn^{3+}, and Ni^{2+} oxidation states. The valence electron configuration of Ni^{2+} and Mn^{2+} in $(Co_{0.3}Mn_{0.1}Ni_{0.6})(OH)_2$/NF is t_2g^6 eg^2 and t_2g^3 eg^2, respectively. The Co^{2+} holds t_2g^5 eg^2 and Mn^{3+} possesses t_2g^3 eg^1 configuration with one unpaired electron in t_2g^5 in Co^{2+} and eg^1 in Mn^{3+}.[64–66] The charge transfer from Mn to Co further influences the adsorption of H_2O. Modulating the electronic structure further influences the adsorption of the reaction intermediates during water splitting. Also, in the multi-metallic system, where Mn is present in multiple oxidation states, it improves the bifunctional catalytic activity.

The electrochemical OER performance of the prepared sample was analyzed in N_2-saturated 1 M KOH solution at a scan rate of 2 mV s^{-1}. Fig. 6a shows the comparative linear sweep voltammetry (LSVs) plots of the as-prepared materials in comparison to the state-of-the-art RuO_2-coated NF. Fig. 6a reveals that the bare NF shows only negligible OER activity and it requires an overpotential of 400 mV to deliver a current density of 10 mA cm^{-2}. On the other hand, RuO_2@NF needs a 330 mV overpotential to reach the same current density of 10
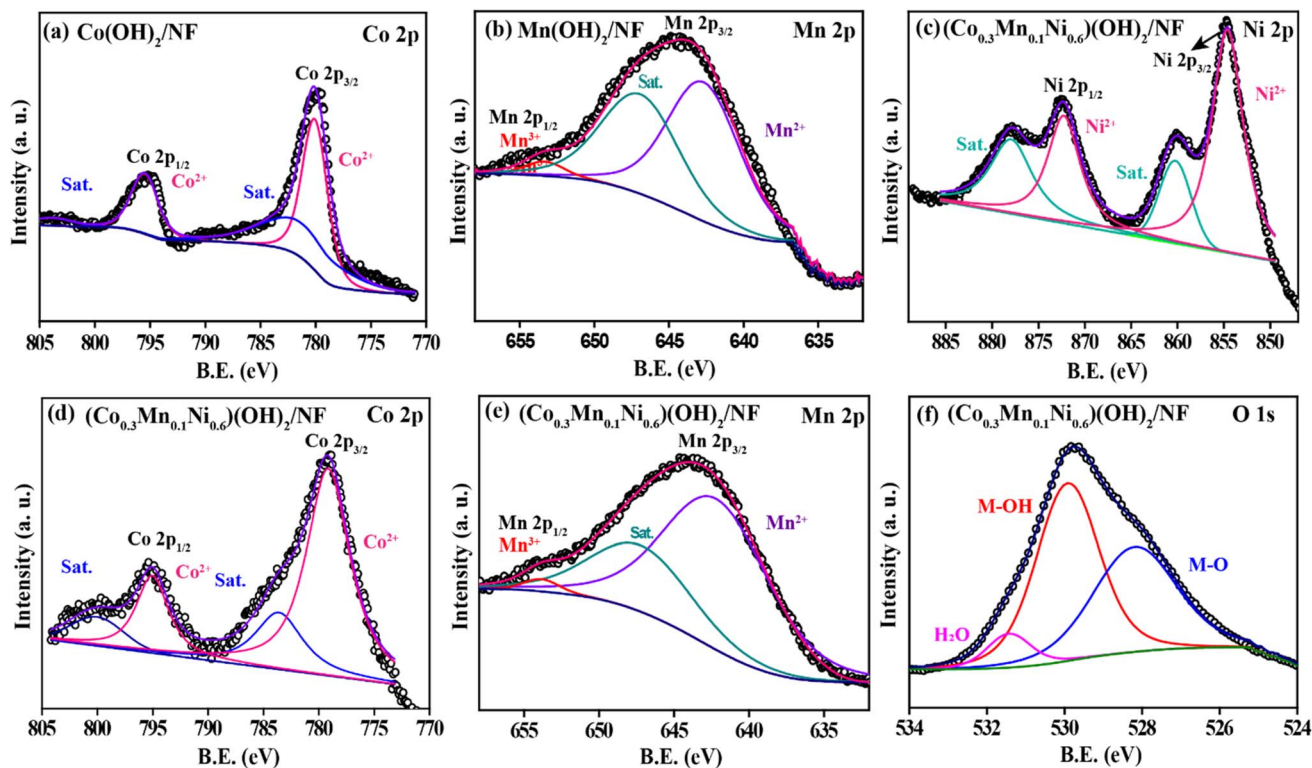
Fig. 5 XPS spectra of (a) deconvoluted Co 2p of Co(OH)$_2$/NF, (b) deconvoluted Mn 2p of Mn(OH)$_2$/NF, (c) deconvoluted Ni 2p of (Co$_{0.3}$-Mn$_{0.1}$Ni$_{0.6}$)(OH)$_2$/NF, (d) deconvoluted Co 2p of (Co$_{0.3}$Mn$_{0.1}$Ni$_{0.6}$)(OH)$_2$/NF, (e) deconvoluted Mn 2p of (Co$_{0.3}$Mn$_{0.1}$Ni$_{0.6}$)(OH)$_2$/NF, and (f) deconvoluted O 1s of (Co$_{0.3}$Mn$_{0.1}$Ni$_{0.6}$)(OH)$_2$/NF.
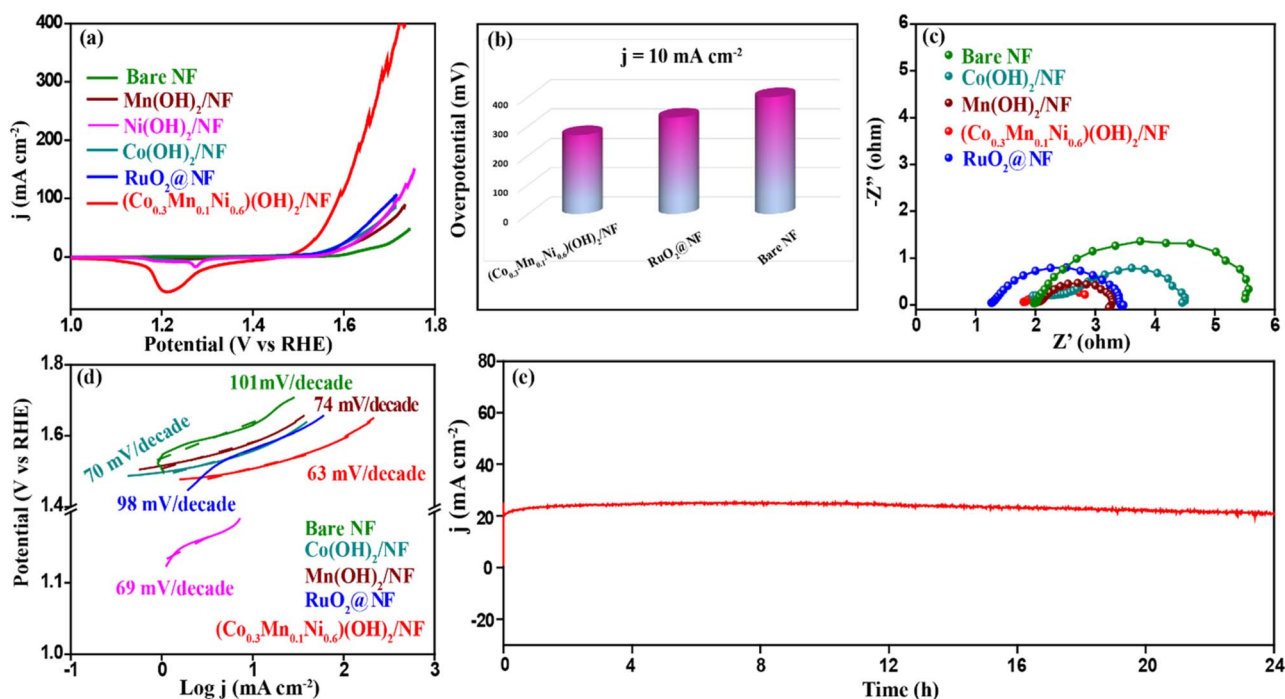
Fig. 6 (a) The OER polarisation plots of (Co$_{0.3}$Mn$_{0.1}$Ni$_{0.6}$)(OH)$_2$/NF and the control samples performed in a 1 M KOH electrolyte, (b) the OER overpotential bar diagram, (c) the electrochemical impedance data of the samples performed at 1.5 V in a 1 M KOH electrolyte, (d) the OER Tafel plot comparison of the prepared materials and (e) the OER chronoamperometric (CA) stability test performed in 1 M KOH at 20 mA cm^{-2}.

mA cm^{-2}. In comparison to these, Ni(OH)$_2$/NF shows an over-potential of 370 mV, and Co(OH)$_2$/NF and Mn(OH)$_2$/NF show an overpotential of 320 mV each at 10 mA cm^{-2}. However, the OER performance is found to be improved substantially in the case of (Co$_{0.3}$Mn$_{0.1}$Ni$_{0.6}$)(OH)$_2$/NF due to the coexistence of Mn with Co, which alters the electron pathway and stabilizes the Co and Ni structures.[67] The XPS investigation has already provided information on the possible electronic modulations incurred by the system. The overpotential exhibited by (Co$_{0.3}$Mn$_{0.1}$Ni$_{0.6}$)(OH)$_2$/NF at a current density of 10 mA cm^{-2} is 270 mV. Fig. 6b represents the bar diagram of the OER overpotentials of bare NF, (Co$_{0.3}$Mn$_{0.1}$Ni$_{0.6}$)(OH)$_2$/NF, and RuO$_2$@NF extracted at 10 mA cm^{-2} are 400, 270, and 330 mV, respectively. The over-potentials exhibited by CoMn/NF-(1:1) and CoMn/NF-(2:1) at a current density of 10 mA cm^{-2} are 310 and 320 mV, respectively, which are higher than that corresponding to (Co$_{0.3}$Mn$_{0.1}$Ni$_{0.6}$)(OH)$_2$/NF as shown in Fig. S12a;† the overpotential values are presented in Table S1.† The Nyquist plots of the materials are given in Fig. 6c. The EIS spectra validate that (Co$_{0.3}$Mn$_{0.1}$Ni$_{0.6}$)(OH)$_2$/NF possesses a charge transfer resistance (R_{CT}) value of 1.0 Ω, which is the lowest among the systems investigated and indicates faster OER kinetics in the system compared to Co(OH)$_2$/NF (2.5 Ω), Mn(OH)$_2$/NF (1.2 Ω) and NF (3.5 Ω) and RuO$_2$@NF (2.1 Ω).[34] To understand the difference in the reaction kinetics, the Tafel slope was calculated using the Tafel equation ($\eta = a + b \times \log j$, where b is the Tafel slope, η is the overpotential, and j is the current density). As represented in Fig. 6d, the reaction kinetics is found to be better on the synthesized (Co$_{0.3}$Mn$_{0.1}$Ni$_{0.6}$)(OH)$_2$/NF (63 mV per

decade) as compared to Ni(OH)$_2$/NF (69 mV per decade), Co(OH)$_2$/NF (70 mV per decade), Mn(OH)$_2$/NF (74 mV per decade), bare NF (101 mV per decade), and RuO$_2$@NF (99 mV per decade).[68,69] The Tafel values indicate that the OER kinetics gets enhanced with the incorporation of Co and Mn in (Co$_{0.3}$Mn$_{0.1}$Ni$_{0.6}$)(OH)$_2$/NF. Fig. 6e shows the stability analysis of (Co$_{0.3}$Mn$_{0.1}$Ni$_{0.6}$)(OH)$_2$/NF. Chronoamperometric analysis was performed for 24 h at 20 mA cm^{-2} and (Co$_{0.3}$Mn$_{0.1}$Ni$_{0.6}$)(OH)$_2$/NF showed a retention of 95% of the initial performance after 24 h of testing, indicating the excellent stability of the prepared catalyst under the OER conditions. We have performed LSV analysis before and after the 24 h chronoamperometry test in 1 M KOH for the OER and HER as shown in Fig. S13.† In Fig. S13a† for the OER, the activity is slightly improved after the stability analysis. The slightly improved activity could be due to the *in situ* formation of CoOOH in the materials (Co(OH)$_2$ → CoOOH) during the OER. The peak shift from 1.22 V to 1.14 V vs. RHE in the LSVs indicates the possible formation of CoOOH, leading to improved OER performance.[70]

The HER performance of the as-synthesized electrocatalysts was evaluated in N$_2$-saturated 1 M KOH solution at a scan rate of 2 mV s^{-1}. Fig. 7a depicts the comparative LSV profiles of all the materials. The overpotentials calculated from the study are bare NF (296 mV @ 10 mA cm^{-2}), Ni(OH)$_2$/NF (245 mV @ 10 mA cm^{-2}), Mn(OH)$_2$/NF (270 mV @ 10 mA cm^{-2}), CoMn/NF-(1:1) (242 mV @ 10 mA cm^{-2}), and CoMn/NF-(2:1) (286 mV @ 10 mA cm^{-2}) mV (Fig. S12b†). Co(OH)$_2$/NF holds a decent HER activity with an overpotential of 165 mV to deliver a current density of 10 mA cm^{-2}. On the other hand, (Co$_{0.3}$Mn$_{0.1}$Ni$_{0.6}$)(OH)$_2$/NF
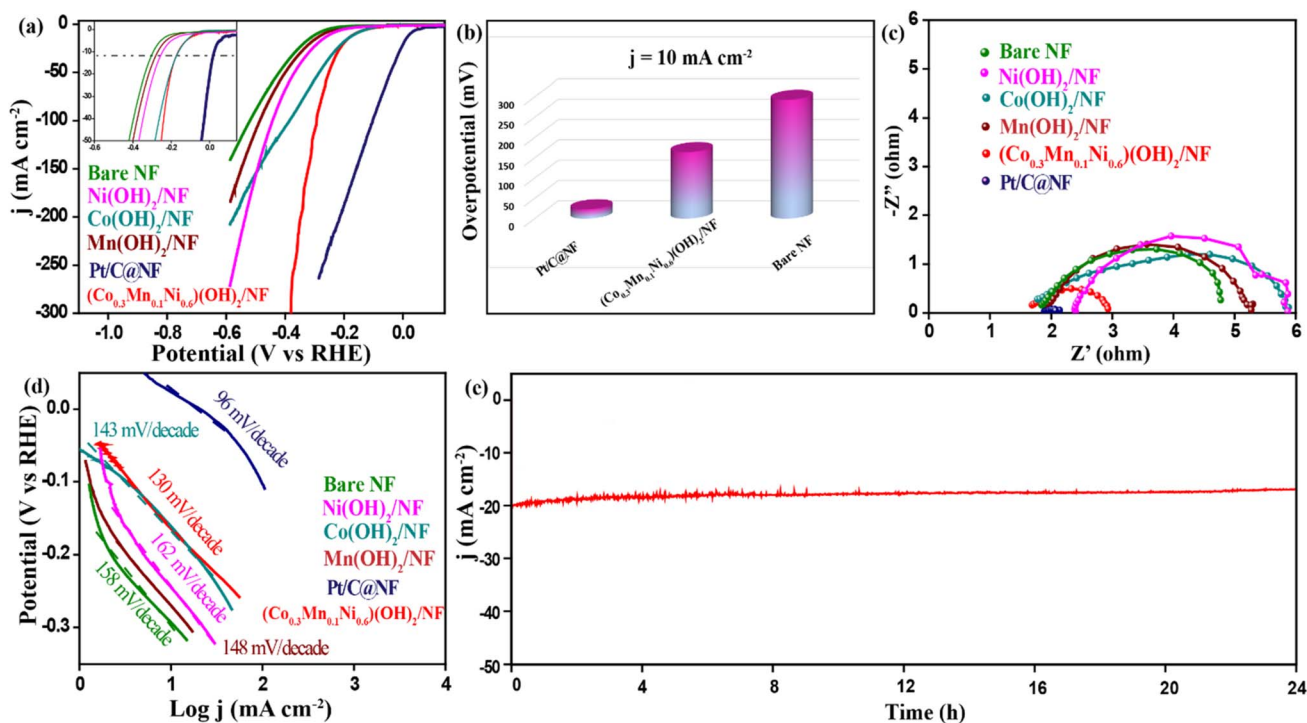
Fig. 7 (a) The HER polarisation plots of (Co$_{0.3}$Mn$_{0.1}$Ni$_{0.6}$)(OH)$_2$/NF and the control samples performed in a 1 M KOH electrolyte, (b) the HER overpotential bar diagram, (c) the electrochemical impedance analysis of the samples performed at −0.30 V in a 1 M KOH electrolyte, (d) the HER Tafel plot comparison of the prepared materials and (e) the HER chronoamperometric stability test performed in 1 M KOH at 20 mA cm^{-2}.

exhibits an overpotential of 163 mV to attain the same current density (Fig. 7a). However, in the case of $Co(OH)_2/NF$, the overpotential increases at higher current densities. Whereas, $(Co_{0.3}Mn_{0.1}Ni_{0.6})(OH)_2/NF$ shows lower ohmic drops as the current density increases. Fig. 7b shows the bar diagram corresponding to the HER overpotentials of bare NF, $(Co_{0.3}Mn_{0.1}Ni_{0.6})(OH)_2/NF$, and Pt/C@NF extracted at 10 mA cm^{-2}, which are 296, 163 and 23 mV, respectively. Fig. 7c shows the electrochemical impedance spectra of the as-synthesized materials recorded at -0.30 V $vs.$ RHE. It proves that $(Co_{0.3}Mn_{0.1}Ni_{0.6})(OH)_2/NF$ possesses the lowest charge transfer resistance (R_{CT}) (1.25 Ω), indicating fast HER kinetics from the prepared $Co(OH)_2/NF$ (4.1 Ω), $Mn(OH)_2/NF$ (3.3 Ω), $Ni(OH)_2/NF$ (3.4 Ω), and NF (2.9 Ω) materials.[70] As illustrated in Fig. 7d, $(Co_{0.3}Mn_{0.1}Ni_{0.6})(OH)_2/NF$ shows a Tafel slope of 130 mV per decade and indicates better reaction kinetics compared to the control samples. The Tafel slope values of the control samples are 143, 148, 162, 158, and 96 mV per decade for $Co(OH)_2/NF$, $Mn(OH)_2/NF$, $Ni(OH)_2/NF$, NF, and Pt/C@NF, respectively. Fig. 7e shows the chronoamperometric (CA) stability profile of $(Co_{0.3}Mn_{0.1}Ni_{0.6})(OH)_2/NF$. The test was performed for 24 h at 20 mA cm^{-2} and the system displayed a performance retention of 85% of the initial value after 24 h. After the HER stability analysis of

$(Co_{0.3}Mn_{0.1}Ni_{0.6})(OH)_2/NF$, the LSVs match the initial LSVs, which shows similar activity before and after the durability test in Fig. S13b.†

The electrochemically active surface area (ECSA) of the as-prepared samples was calculated from the double-layer capacitance (C_{dl}) under the non-faradaic area of the OER and HER, respectively. For this, CV analysis was conducted with different scan rates in the non-faradaic region of the OER (in 1 M KOH with a potential window of 0.915 to 1.015 V $vs.$ RHE) and the HER (in 1 M KOH with a potential window of 0.915 to 0.815 V $vs.$ RHE) as shown in Fig. S14 and 15.† The ECSA is proportional to the C_{dl} value and the catalytic activity is associated with the ECSA. As illustrated in Fig. S14 and Table S2,† the C_{dl} values for the OER of bare NF, $Ni(OH)_2/NF$, $Mn(OH)_2/NF$, $Co(OH)_2/NF$, and $(Co_{0.3}Mn_{0.1}Ni_{0.6})(OH)_2/NF$ are 1.9, 1.1, 0.91, 5.8, and 5.92 mF cm^{-1}, respectively. As per Fig. S15 and Table S3,† the C_{dl} values for the HER of bare NF, $Ni(OH)_2/NF$, $Mn(OH)_2/NF$, $Co(OH)_2/NF$, and $(Co_{0.3}Mn_{0.1}Ni_{0.6})(OH)_2/NF$ are 1.49, 1.23, 1.14, 5.75, and 6.03 mF cm^{-1} respectively, which validate the higher ECSA of $(Co_{0.3}Mn_{0.1}Ni_{0.6})(OH)_2/NF$ for the OER and HER. This could expose more active sites and thereby improve the catalytic activity. Our claim that the flower-like morphology increases the electrochemically active surface area is proved by the higher C_{dl}
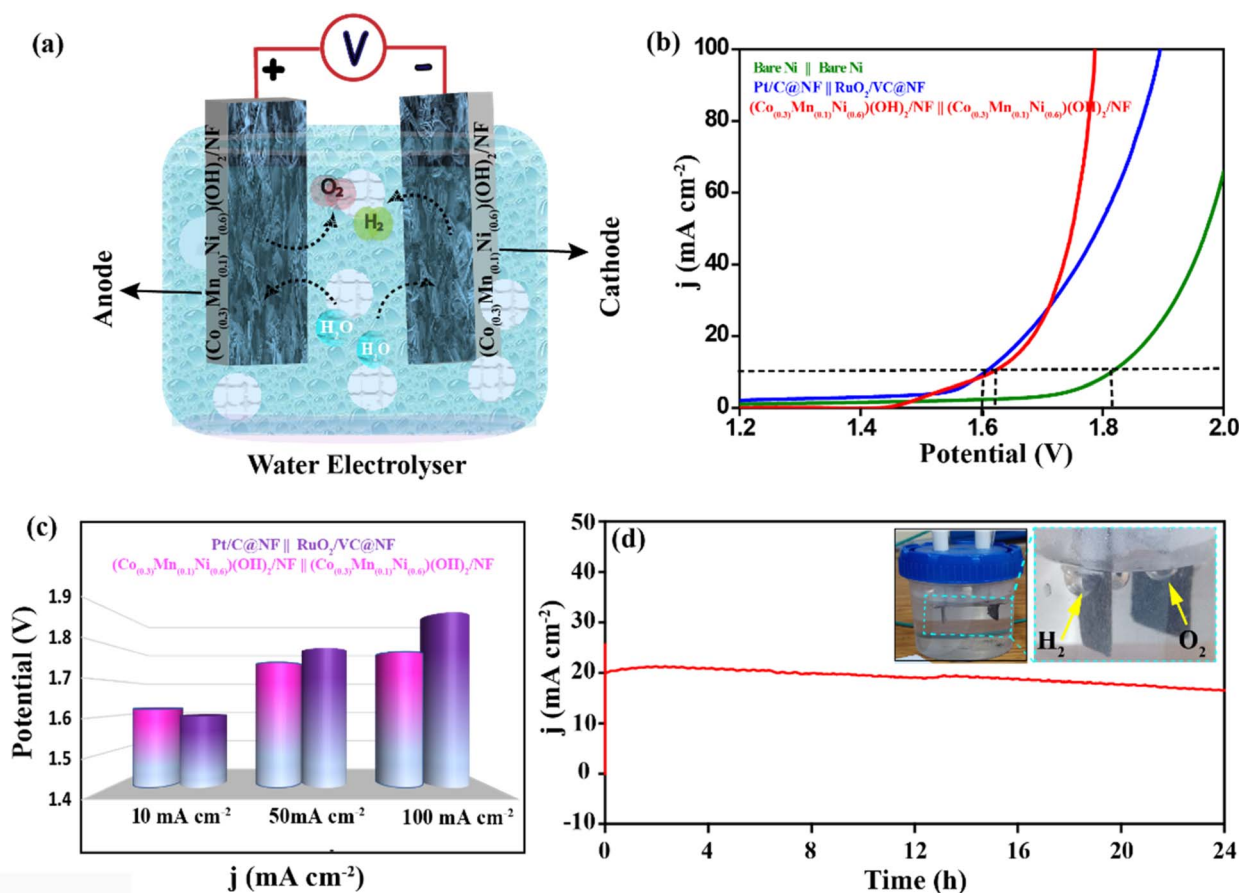
Fig. 8 (a) Schematic representation of the water electrolyzer, (b) comparative LSV plots corresponding to the overall water splitting, (c) the bar diagram representing the water electrolysis activity of $(Co_{0.3}Mn_{0.1}Ni_{0.6})(OH)_2/NF$ compared with bare NF and the state-of-the-art catalyst at different current densities, and (d) the chronoamperometric response of $(Co_{0.3}Mn_{0.1}Ni_{0.6})(OH)_2/NF$-based electrolysis in 1 M KOH for 24 h at 20 mA cm^{-2}.

value of $(Co_{0.3}Mn_{0.1}Ni_{0.6})(OH)_2$/NF. For comparison, the state-of-the-art catalysts Pt/C and RuO_2-coated NF (*i.e.,* Pt/C@NF and RuO_2@NF, respectively) were characterized similarly. The obtained C_{dl} values for Pt/C@NF and RuO_2@NF are 3.48 and 2.91 mF cm^{-2}, respectively.

Finally, overall water splitting was performed in a 1 M KOH electrolyte and the corresponding data are presented in Fig. 8. The schematic representation of the water electrolyzer is given in Fig. 8a. To investigate the water electrolysis, $(Co_{0.3}Mn_{0.1}Ni_{0.6})(OH)_2$/NF was employed as both the anode and cathode electrodes in 1 M KOH solution by maintaining an active area of 1 cm^{-2}. For comparison, bare NF//bare NF, CoMn/NF-(1:1)//CoMn/NF-(1:1), CoMn/NF-(2:1)//CoMn/NF-(2:1), and Pt/C@NF//RuO_2@NF systems were also fabricated and performance evaluation was done under similar conditions. The bare NF//bare NF system shows poor catalytic activity, which requires a potential of 1.81 V to attain a current density of 10 mA cm^{-2} (Fig. 8b). Also, CoMn/NF-(1:1)//CoMn/NF-(1:1) and CoMn/NF-(2:1)//CoMn/NF-(2:1) show a poor catalytic activity of 1.75 and 1.81 V, respectively, at 10 mA cm^{-2}(Fig. S16†). However, the $(Co_{0.3}Mn_{0.1}Ni_{0.6})(OH)_2$/NF//$(Co_{0.3}Mn_{0.1}Ni_{0.6})(OH)_2$/NF system requires 1.62 V to drive a current density of 10 mA cm^{-2} which is only 20 mV higher than that of Pt/C@NF//RuO_2@NF. With increasing the current density, $(Co_{0.3}Mn_{0.1}Ni_{0.6})(OH)_2$/NF//$(Co_{0.3}Mn_{0.1}Ni_{0.6})(OH)_2$/NF shows better performance (1.78 V @100 mA cm^{-2}) compared to Pt/C@NF//RuO_2@NF (1.89 V @100 mA cm^{-2}). This could be attributed to the improved catalytic activity along with the better mass transport of the electrolyte and evolved gases that occur in $(Co_{0.3}Mn_{0.1}Ni_{0.6})(OH)_2$/NF due to the nanoflower morphology. Furthermore, Fig. 8c shows the comparative overpotential bar diagram of Pt/C@NF//RuO_2@NF and $(Co_{0.3}Mn_{0.1}Ni_{0.6})(OH)_2$/NF//$(Co_{0.3}Mn_{0.1}Ni_{0.6})(OH)_2$/NF systems recorded at different current densities. At the current densities of 10, 50, and 100 mA cm^{-2}, the respectively measured potentials for the $(Co_{0.3}Mn_{0.1}Ni_{0.6})(OH)_2$/NF//$(Co_{0.3}Mn_{0.1}Ni_{0.6})(OH)_2$/NF system are 1.62, 1.75 and 1.78 V, whereas, for the Pt/C@NF//RuO_2@NF system, these values are respectively 1.60, 1.79, and 1.89 V. Afterward, the stability analysis of the $(Co_{0.3}Mn_{0.1}Ni_{0.6})(OH)_2$/NF//$(Co_{0.3}Mn_{0.1}Ni_{0.6})(OH)_2$/NF system was performed at 20 mA cm^{-2} for 24 h. The chronoamperometric analysis illustrated in Fig. 8d shows a stable performance for 24 h. The inset of Fig. 8d shows gas evolution during water splitting using the paired configuration of the $(Co_{0.3}Mn_{0.1}Ni_{0.6})(OH)_2$/NF bifunctional electrocatalyst. During the overall water-splitting process, the evolved gases were quantified by using gas chromatography. For this, a homemade two-compartment set-up was fabricated. $(Co_{0.3}Mn_{0.1}Ni_{0.6})(OH)_2$/NF was used as the cathode and anode electrodes. The anion exchange membrane (Fumatech FAA-3) was used as the separator between the anode and cathode chambers. The chronoamperometric analysis was performed at 1.90 V for 2 h. The produced gas was collected in the headspace of the respective chambers and was injected into the GC instrument by using a micro-syringe (500 μL). The quantification of the evolved gas with different time intervals is presented in Fig. S17.† From Fig. S17,† the amounts of H_2 and O_2 produced are estimated to be 701.2 and 358.6 mmol,

respectively, at a time interval of 1 h; these amounts correspond to an ~1:2 ratio of O_2 and H_2, respectively. This study confirms the capability of employing $(Co_{0.3}Mn_{0.1}Ni_{0.6})(OH)_2$/NF as a bi-functional and self-standing electrode for the realistic demonstrations of overall water splitting applications.

Post-characterization of the electrodes were performed after the overall water-splitting analysis. Fig. S18, ESI,† represents the FESEM images of the cathode and anode catalysts after 24 h of the operation. The images corresponding to the anode catalyst (Fig. S18a–c, ESI†) and the cathode catalyst (Fig. S18d and e, ESI†) show similar flower-like morphological features to the pristine material. The catalysts recovered from the anode and cathode were also analyzed *via* XRD for inspecting any possible phase changes under potential induced conditions. Fig. S19, ESI,† shows the comparative XRD patterns of $(Co_{0.3}Mn_{0.1}Ni_{0.6})(OH)_2$/NF before and after the 24 h CA studies (anode (blue) and cathode (green)). It can be seen that the peaks corresponding to the (001), (100), (002), (012), and (110) diffraction planes of the hexagonal phase of $Ni(OH)_2$ (JCPDS CARD No. 00-014-0117) and $Co(OH)_2$ (JCPDS CARD No. 01-074-1057) were retained even in the post-CA for 24 h. To know the chemical composition of $(Co_{0.3}Mn_{0.1}Ni_{0.6})(OH)_2$/NF after the CA, XPS analysis was performed and the corresponding data are given in Fig. S20a, ESI.† The survey scan spectrum of $(Co_{0.3}Mn_{0.1}Ni_{0.6})(OH)_2$/NF before and after the CA confirms the existence of Mn, Co, Ni, and O in the sample. In Fig. S20b, ESI,† the Co 2p spectra are found to be significantly shifted to higher binding energy values compared to the pristine material which indicates that $Co(OH)_2$ is converted into a more stable Co^{3+} (CoOOH) phase during water electrolysis under OER conditions.[71,72] The Mn 2p spectra got shifted to a lower binding energy value in the cathode compared to the pristine material, which indicates that the Mn helps with the CoOOH formation by electron transfer from Co to Mn and lowers the binding energy of Mn during water electrolysis.[73] However, the anode shows similar binding energy even after the stability analysis, which suggests that the cathodic reaction is possibly more kinetically favorable compared to the anodic reaction as shown in Fig. S20c, ESI.† Table S4† shows the comparison of the overall water-splitting performance of the present system with the various reported materials in a 1 M KOH electrolyte.

In summary, a flower-like morphology of $(Co_{0.3}Mn_{0.1}Ni_{0.6})(OH)_2$ was synthesized on nickel foam (NF) using a simple hydrothermal method. The self-supported $(Co_{0.3}Mn_{0.1}Ni_{0.6})(OH)_2$/NF having the porous flower-like morphology significantly reduces the mass-transport related issues during the overall water splitting process. The electronic and morphological modification is well understood after Mn incorporation. The $(Co_{0.3}Mn_{0.1}Ni_{0.6})(OH)_2$/NF system possesses remarkably high activity toward both the OER and the HER in a 1 M KOH solution. The overpotentials displayed by this system at 10 mA cm^{-2} are 270 mV for the OER and 163 mV for the HER. The structural stability analysis of $(Co_{0.3}Mn_{0.1}Ni_{0.6})(OH)_2$/NF during the OER and HER shows outstanding durability and structural integrity of the system. The $(Co_{0.3}Mn_{0.1}Ni_{0.6})(OH)_2$/NF bifunctional electrocatalyst was finally employed both as the cathode and anode electrodes for overall water splitting in 1 M KOH. The

system required only 1.62 V to achieve a current density of 10 mA cm^{-2} with excellent long-term stability. The value is comparable to many of the recently reported values.

Conflicts of interest

The authors declare no conflict of interest.

Acknowledgements

References

1 S. C. Paul, S. C. Dey, M. A. I. Molla, M. S. Islam, S. Debnath, M. Y. Miah, M. Ashaduzzaman and M. Sarker, *Polyhedron*, 2021, **193**, 114871.

2 B. Becker and D. Fischer, *Energy Policy*, 2013, **56**, 446–455.

3 G. P. Kharabe, N. Manna, A. Nadeema, S. K. Singh, S. Mehta, A. Nair, K. Joshi and S. Kurungot, *J. Mater. Chem. A*, 2022, **10**, 10014–10025.

4 S. Dutta, *J. Ind. Eng. Chem.*, 2014, **20**, 1148–1156.

5 N. P. Brandon and Z. Kurban, *Philos. Trans. R. Soc., A*, 2017, **375**, 20160400.

6 R. Zhang, C. Tang, R. Kong, G. Du, A. M. Asiri, L. Chen and X. Sun, *Nanoscale*, 2017, **9**, 4793–4800.

7 K. Ojha, S. Saha, P. Dagar and A. K. Ganguli, *Phys. Chem. Chem. Phys.*, 2018, **20**, 6777–6799.

8 P. Zhao, B. Zhang, X. Hao, W. Yi, J. Chen and Q. Cao, *ACS Appl. Energy Mater.*, 2022, **5**, 942–950.

9 G. Chen, T. Wang, J. Zhang, P. Liu, H. Sun, X. Zhuang, M. Chen and X. Feng, *Adv. Mater.*, 2018, **30**, 1706279.

10 J. Yin, Y. Li, F. Lv, M. Lu, K. Sun, W. Wang, L. Wang, F. Cheng, Y. Li, P. Xi and S. Guo, *Adv. Mater.*, 2017, **29**, 1704681.

11 T. Yang, M. Du, H. Zhu, M. Zhang and M. Zou, *Electrochim. Acta*, 2015, **167**, 48–54.

12 B. You and Y. Sun, *Acc. Chem. Res.*, 2018, **51**, 1571–1580.

13 T. Audichon, T. W. Napporn, C. Canaff, C. Morais, C. Comminges and K. B. Kokoh, *J. Mater. Chem. C*, 2016, **120**, 2562–2573.

14 J. Hou, Y. Wu, B. Zhang, S. Cao, Z. Li and L. Sun, *Adv. Funct. Mater.*, 2019, **29**, 1808367.

15 N. K. Dang, M. Umer, P. Thangavel, S. Sultan, J. N. Tiwari, J. H. Lee, M. G. Kim and K. S. Kim, *J. Mater. Chem. A*, 2021, **9**, 16898–16905.

16 J. N. Tiwari, S. Sultan, C. W. Myung, T. Yoon, N. Li, M. Ha, A. M. Harzandi, H. J. Park, D. Y. Kim, S. S. Chandrasekaran, W. G. Lee, V. Vij, H. Kang, T. J. Shin, H. S. Shin, G. Lee, Z. Lee and K. S. Kim, *Nat. Energy*, 2018, **3**, 773–782.

17 P. Thangavel, G. Kim and K. S. Kim, *J. Mater. Chem. A*, 2021, **9**, 14043–14051.

18 J. Xu, J. Li, Z. Lian, A. Araujo, Y. Li, B. Wei, Z. Yu, O. Bondarchuk, I. Amorim, V. Tileli, B. Li and L. Liu, *ACS Catal.*, 2021, **11**, 3402–3413.

19 C. Wang, P. Zhai, M. Xia, Y. Wu, B. Zhang, Z. Li, L. Ran, J. Gao, X. Zhang, Z. Fan, L. Sun and J. Hou, *Angew. Chem., Int. Ed.*, 2021, **60**, 27126–27134.

20 Y. Sun, T. Zhang, C. Li, K. Xu and Y. Li, *J. Mater. Chem. A*, 2020, **8**, 13415–13436.

21 J. Zhang, J. Liu, L. Xi, Y. Yu, N. Chen, S. Sun, W. Wang, K. M. Lange and B. Zhang, *J. Am. Chem. Soc.*, 2018, **140**, 3876–3879.

22 J. McAllister, N. A. G. Bandeira, J. C. McGlynn, A. Y. Ganin, Y.-F. Song, C. Bo and H. N. Miras, *Nat. Commun.*, 2019, **10**, 370.

23 Z. Pu, J. Zhao, I. S. Amiinu, W. Li, M. Wang, D. He and S. Mu, *Energy Environ. Sci.*, 2019, **12**, 952–957.

24 Y. Bi, Z. Cai, D. Zhou, Y. Tian, Q. Zhang, Q. Zhang, Y. Kuang, Y. Li, X. Sun and X. Duan, *J. Catal.*, 2018, **358**, 100–107.

25 P. Zhai, Y. Zhang, Y. Wu, J. Gao, B. Zhang, S. Cao, Y. Zhang, Z. Li, L. Sun and J. Hou, *Nat. Commun.*, 2020, **11**, 5462.

26 P. Zhai, M. Xia, Y. Wu, G. Zhang, J. Gao, B. Zhang, S. Cao, Y. Zhang, Z. Li, Z. Fan, C. Wang, X. Zhang, J. T. Miller, L. Sun and J. Hou, *Nat. Commun.*, 2021, **12**, 4587.

27 J. Hou, B. Zhang, Z. Li, S. Cao, Y. Sun, Y. Wu, Z. Gao and L. Sun, *ACS Catal.*, 2018, **8**, 4612–4621.

28 X. Huang, L. Liu, H. Gao, W. Dong, M. Yang and G. Wang, *Green Chem.*, 2017, **19**, 769–777.

29 M. Li, J. P. Cheng, F. Liu and X. B. Zhang, *Chem. Phys. Lett.*, 2015, **640**, 5–10.

30 T.-Y. Wei, C.-H. Chen, H.-C. Chien, S.-Y. Lu and C.-C. Hu, *Adv. Mater.*, 2010, **22**, 347–351.

31 X. Peng, Y. Guo, Q. Yin, J. Wu, J. Zhao, C. Wang, S. Tao, W. Chu, C. Wu and Y. Xie, *J. Am. Chem. Soc.*, 2017, **139**, 5242–5248.

32 Y. Wu, Y. Zhao, P. Zhai, C. Wang, J. Gao, L. Sun and J. Hou, *Adv. Mater.*, 2022, **34**, 2202523.

33 J. Xie, X. Zhang, H. Zhang, J. Zhang, S. Li, R. Wang, B. Pan and Y. Xie, *Adv. Mater.*, 2017, **29**, 1604765.

34 Y. Huang, X. Zhao, F. Tang, X. Zheng, W. Cheng, W. Che, F. Hu, Y. Jiang, Q. Liu and S. Wei, *J. Mater. Chem. A*, 2018, **6**, 3202–3210.

35 F. Qin, Z. Zhao, M. K. Alam, Y. Ni, F. Robles-Hernandez, L. Yu, S. Chen, Z. Ren, Z. Wang and J. Bao, *ACS Energy Lett.*, 2018, **3**, 546–554.

36 J. Masa, I. Sinev, H. Mistry, E. Ventosa, M. de la Mata, J. Arbiol, M. Muhler, B. Roldan Cuenya and W. Schuhmann, *Adv. Energy Mater.*, 2017, **7**, 1700381.

37 B. Li, M. Ai and Z. Xu, *Chem. Commun.*, 2010, **46**, 6267–6269.

38 G. S. Hutchings, Y. Zhang, J. Li, B. T. Yonemoto, X. Zhou, K. Zhu and F. Jiao, *J. Am. Chem. Soc.*, 2015, **137**, 4223–4229.

39 Y. Zhang, P. Guo, S. Li, J. Sun, W. Wang, B. Song, X. Yang, X. Wang, Z. Jiang, G. Wu and P. Xu, *J. Mater. Chem. A*, 2022, **10**, 1760–1767.

40 H. N. Nong, T. Reier, H.-S. Oh, M. Gliech, P. Paciok, T. H. T. Vu, D. Teschner, M. Heggen, V. Petkov, R. Schlögl, T. Jones and P. Strasser, *Nat. Catal.*, 2018, **1**, 841–851.

41 J. Ge, W. Zhang, J. Tu, T. Xia, S. Chen and G. Xie, *Small*, 2020, **16**, 2001856.

42 W. Wang, L. Kuai, W. Cao, M. Huttula, S. Ollikkala, T. Ahopelto, A.-P. Honkanen, S. Huotari, M. Yu and B. Geng, *Angew. Chem., Int. Ed.*, 2017, **56**, 14977–14981.

43 S. Chen, H. Huang, P. Jiang, K. Yang, J. Diao, S. Gong, S. Liu, M. Huang, H. Wang and Q. Chen, *ACS Catal.*, 2020, **10**, 1152–1160.

44 H. Zhao, J. Wang, Y. Sui, F. Wei, J. Qi, Q. Meng, Y. Ren and Y. He, *J. Mater. Sci.: Mater. Electron.*, 2021, **32**, 11145–11157.

45 L. Li, J. Xu, J. Lei, J. Zhang, F. McLarnon, Z. Wei, N. Li and F. Pan, *J. Mater. Chem. A*, 2015, **3**, 1953–1960.

46 X. Zhang, Y. Qian, Y. Zhu and K. Tang, *Nanoscale*, 2014, **6**, 1725–1731.

47 Y. Yu, C. Chen, Y. Liu, H. Yu, S. Li, Y. Xue, N. Cai, J. Wang and F. Yu, *J. Mater. Chem. C*, 2022, **126**, 5493–5501.

48 G. Xiong, P. He, L. Liu, T. Chen and T. S. Fisher, *J. Mater. Chem. A*, 2015, **3**, 22940–22948.

49 V. Gupta, S. Gupta and N. Miura, *J. of Power Sources*, 2008, **175**, 680–685.

50 S. Yang, C. Wu, J. Cai, Y. Zhu, H. Zhang, Y. Lu and K. Zhang, *J. Mater. Chem. A*, 2017, **5**, 16776–16785.

51 R. Venkatkarthick, J. Niu, A. Srikhaow, C. Sriprachuabwong, S. Vasudevan, A. Tuantranont and J. Qin, *ACS Appl. Energy Mater.*, 2021, **4**, 6520–6530.

52 H. C. Chen, Y. Qin, H. Cao, X. Song, C. Huang, H. Feng and X. S. Zhao, *Energy Storage Mater.*, 2019, **17**, 194–203.

53 M. H. Lee, Y. J. Kang, S. T. Myung and Y. K. Sun, *Electrochim. Acta*, 2004, **50**, 939–948.

54 Y. Shang, S. Ma, Y. Wei, H. Yang and Z. Xu, *Ionics*, 2020, **26**, 3609–3619.

55 L. Huang, D. Chen, Y. Ding, S. Feng, Z. L. Wang and M. Liu, *Nano Lett.*, 2013, **13**, 3135–3139.

56 N. Han, K. R. Yang, Z. Lu, Y. Li, W. Xu, T. Gao, Z. Cai, Y. Zhang, V. S. Batista, W. Liu and X. Sun, *Nat. Commun.*, 2018, **9**, 924.

57 X. Yu, Z.-Y. Yu, X.-L. Zhang, Y.-R. Zheng, Y. Duan, Q. Gao, R. Wu, B. Sun, M.-R. Gao, G. Wang and S.-H. Yu, *J. Am. Chem. Soc.*, 2019, **141**, 7537–7543.

58 B. J. Tan, K. J. Klabunde and P. M. A. Sherwood, *J. Am. Chem. Soc.*, 1991, **113**, 855–861.

59 P. Sivakumar, M. Jana, M. G. Jung, A. Gedanken and H. S. Park, *J. Mater. Chem. A*, 2019, **7**, 11362–11369.

60 X. Zhu, C. Tang, H.-F. Wang, B.-Q. Li, Q. Zhang, C. Li, C. Yang and F. Wei, *J. Mater. Chem. A*, 2016, **4**, 7245–7250.

61 T. V. Nguyen, L. T. Son, V. V. Thuy, V. D. Thao, M. Hatsukano, K. Higashimine, S. Maenosono, S.-E. Chun and T. V. Thu, *Dalton Trans.*, 2020, **49**, 6718–6729.

62 X. Wang, L. Tian, X. Long, M. Yang, X. Song, W. Xie, D. Liu, Y. Fu, J. Li, Y. Li and D. He, *Sci. China Mater.*, 2021, **64**, 1632–1641.

63 P. Sivakumar, M. Jana, M. G. Jung, A. Gedanken and H. S. Park, *J. Mater. Chem. A*, 2019, **7**, 11362–11369.

64 I. Kim, H. Lee, H.-H. Nahm and M. Choi, *Phys. Rev. Res.*, 2022, **4**, 033171.

65 Z. Sun, L. Lin, J. He, D. Ding, T. Wang, J. Li, M. Li, Y. Liu, Y. Li, M. Yuan, B. Huang, H. Li and G. Sun, *J. Am. Chem. Soc.*, 2022, **144**, 8204–8213.

66 J. Ge, W. Zhang, J. Tu, T. Xia, S. Chen and G. Xie, *Small*, 2020, **16**, 2001856.

67 S. Gupta, S. Zhao, X. X. Wang, S. Hwang, S. Karakalos, S. V. Devaguptapu, S. Mukherjee, D. Su, H. Xu and G. Wu, *ACS Catal.*, 2017, **7**, 8386–8393.

68 X. Jia, S. Gao, T. Liu, D. Li, P. Tang and Y. Feng, *Electrochim. Acta*, 2017, **245**, 59–68.

69 L. Liu, Y. Ou, D. Gao, L. Yang, H. Dong, P. Xiao and Y. Zhang, *J. of Power Sources*, 2018, **396**, 395–403.

70 T. Yoon and K. S. Kim, *Adv. Funct. Mater.*, 2016, **26**, 7386–7393.

71 S. Zhang, T. Yu, H. Wen, Z. Ni, Y. He, R. Guo, J. You and X. Liu, *Chem. Commun.*, 2020, **56**, 15387–15405.

72 C. Lee, K. Shin, C. Jung, P.-P. Choi, G. Henkelman and H. M. Lee, *ACS Catal.*, 2020, **10**, 562–569.

73 P. Nayak and M. Nookala, *Electrochem. Solid-State Lett.*, 2009, **12**, A115.
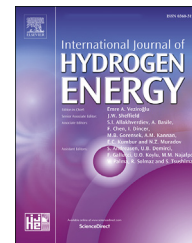
Scalable optical fiber reactor for photocatalytic H₂ production: Addressing scattering issues

Priyanka S. Walko [b], *R. Nandini Devi* [a,*]

[a] *Catalysis and Inorganic Chemistry Division, CSIR-National Chemical Laboratory, Pune, Maharashtra, 411008, India*
[b] *Academy of Scientific and Innovative Research (AcSIR), Ghaziabad, 201002, India*

HIGHLIGHTS

- 5 wt%CuO/TiO₂ coated optical fiber bundles are studied for photocatalytic hydrogen evolution via water splitting.
- Change in directionality of light reduces scattering issues observed in powder catalysts on scale up.
- H₂ production can be increased by merely increasing number of optical fibers.
- More than one order enhancement in activity in the optical fiber when compared to powder on scale up.
- Retention of ~70% activity in turbid non-potable water.

ARTICLE INFO

ABSTRACT

Scattering is one of the main challenges in scaling up photocatalytic water splitting using the most prevalent powder catalysts. This can be overcome by decoupling the reaction medium from light transmission, as in the case of optical fibers. Here we explore utilizing optical fibers coated with 5 wt% CuO supported on TiO₂ for photocatlytic H₂ production from water-methanol mixtures. CuO/TiO₂ is a well studied photo catalyst in which photoreduced Cu species are known to act as sensitizers for inducing visible light activity. Lower activity of sequentially coated systems indicates that appropriate interfaces of active Cu and TiO₂ with water are desirable. The scalability of such optical fiber-based systems along with potential in non-potable turbid water media are demonstrated. Maximum activity of 22 μmoles of H₂ in 8 h was obtained with 50 mg of catalyst coated on optical fibers, which increases linearly with increase in fiber numbers, whereas, drastic reduction in activity is observed in powder catalyst upon increasing the catalyst quantity. A one-to-one comparison of 700 mg of catalyst in powder form and coated on optical fibers indicates more than one order enhancement in activity in the optical fiber based system. In addition, ~70% retention in activity in highly turbid non-potable water was observed as compared to powdered system which shows complete reduction in the activity by 99.99%.

© 2023 Hydrogen Energy Publications LLC. Published by Elsevier Ltd. All rights reserved.

Introduction

Utilizing the abundant solar energy for fuel production is the holy grail of energy research in the current scenario of alarming pollution levels and impending fossil fuel depletion [1−9]. Photocatalytic water splitting is considered as the most benign process for producing H_2, the cleanest fuel. Huge strides are made in developing materials for photocatalytic water splitting since 1972, when Honda and Fujishima discovered photolytic cleavage of water into oxygen and hydrogen using titania and Pt electrode [10−20]. However, such a surge in materials development has not translated into many large scale photocatalytic H_2 production facilities [21−23]. One of the main drawbacks is the necessity for huge light installations in the medium which would render them uneconomical. In addition, limitations of the catalyst forms which can be used for an efficient utilisation of light from an external source also contribute to difficulty in scaling up. Most common form of the catalysts used is powder dispersion in the reactant mediums [20,24−32] which immediately brings in the disadvantage of scattering, and is all the more severe in large scale systems. An alternative reported in an allied process i.e., photocatalytic waste water treatment, is to immobilise photocatalysts on substrates like thin films and employ in a fixed bed configuration for continuous flow models [33−35]. However, these models also demand multiple high energy lamps immersed in the reaction medium ruling out utilizing sunlight directly. Hence, need of the hour is to bridge the gap between reactor design and catalyst development to achieve sustainable and economically favourable systems utilizing full solar spectrum [36,37].

In this context, optical fibres present marked advantages for a continuous flow immobilised model. In the late 70's and early 80's, Marinangeli and Ollis demonstrated photocatalyst immobilisation on optical fibres and their use in waste water treatment [38−40]. This method of photocatalysis is distinctly different from hitherto reported techniques using thin film catalysts, since photons are transmitted to the catalyst from within the light conducting medium in optical fibers. This decouples the reaction medium characteristics from photon transmission to a large extent. Optical fibres work on the phenomenon of total internal reflection where complete reflection of light takes place within the fiber material due to increase in the angle of incidence more than that of critical angle. The structure of an optical fiber consists of a core which is made up of a polymer or silica (glass) surrounded by appropriate cladding material. To attain total internal reflection, the refractive index of core should be higher than that of the cladding. The absorption at the interface is avoided by coating the fibers with non-absorbing dielectrics. It is possible to deliberately "leak" the photons from the core by various techniques; optimizing the refractive indices of core and cladding materials, addition of fluorescent materials to the cladding, creating asymmetries like cavities or air bubbles in the core and cladding geometries are some of them [41]. The leaking can also be affected by chemical, mechanical and laser stripping [42]. Marinangeli and Ollis exploited this phenomenon and used the leaked photons on the interface for

pollutant degradation. Further developments in this field have led to demonstration of dye degradation under flow using woven fiber glass cloth as light transmitting medium [43−45]. However, these developments have not been utilised for photocatalytic H_2 generation yet. Very recently, Potter et al. reported the use of microstructured optical fibre canes (MOFCs) as a novel design for the production of hydrogen from water by using the semiconductor material coated onto the surface of fused silica canes [46]. However, here also, internal reflection phenomenon is not exploited for photon impinging to catalyst.

In contrast to this work, we have employed coating of optical fiber bundles with a photocatalyst, to exploit direct delivery of light thereby reducing light losses due to scattering and absorption by reaction medium. Different coating methods of CuO/TiO_2 catalyst on silica optical fibers are adopted for optimizing the production of hydrogen by water splitting under visible light using methanol as a sacrificial reagent. Here, we have demonstrated the potential of such models for scaling up and utilisation of non-potable water for H_2 generation. Transmission of light via optical fibers opens up new gates to carry out H_2 evolution at remote environments such as deep sea and also in the turbid non-potable water where light reaching capacity is very low.

Experimental section

Synthesis of 5 wt% CuO/TiO_2

500 mg of TiO_2 (Sigma-Aldrich, P25) was taken in a beaker containing 157 mg cupric acetate monohydrate (Cu (CH$_3$COO)$_2$.H$_2$O, LOBA Chemie) dissolved in 50 mL of water. The mixture was stirred at 30 °C for 2 h at 400 rpm on magnetic stirrer. The final product was washed with water and finally with ethanol and kept for drying in oven at 80 °C for 24 h. The dried sample was calcined in a muffle furnace at a heating rate of 2 °C/min at 250 °C for 5 h to obtain 5 wt% CuO supported on TiO_2.

Coating of catalyst on optical fiber bundle

Optical fibers used in this study (Applied Optical Technologies, Thane, India) consisted of silica core, polymeric cladding and were bundled in an outer jacket made up of rubber which was adjusted according to the length of fibers required for the studies; each such bundle contained 10,000 silica fibers. The bundle of optical fibers was washed sequentially with distilled water and acetone and dried in an oven for 30 min at 80 °C. The clean fibers were then treated with 40% HF to remove cladding by dipping in HF solution for 10 s each and finally drying at 80 °C. Catalyst was coated on the etched optical fibers by a simple dip coating method. Slurry solution was prepared by dispersing ~250 mg of 5 wt% CuO/TiO_2, CuO or TiO_2 powder in 50 mL distilled water under sonication for 30 min. 7 cm of the HF treated fiber bundle was coated with the slurry by using dip coating method and dried at 80 °C for 24 h. The extent of coating was checked after weighing the remaining amount of catalyst left after the coating over the optical fibers.

Characterisation

The structure and morphology of as synthesised material and photocatalyst coated optical fibers were characterised by FEI Nova Nano SEM 450 FE-SEM instrument. EDS elemental mapping was done on Quanta 200 3D FEI with the help of TEAM EDS analysis system. Catalyst coated optical fibers were cut into small pieces and mounted on carbon tape for E-SEM analysis. TEM analysis was carried out on FEI, TECNAI G2 F20 transmission electron microscopy (TEM) instrument (conditions: accelerated voltage = S-5 200 kV, and resolution = 0.17 nm). Samples were prepared by dislodging the coating material by sonication. Material thus collected was dispersed in ethanol and drop casted on 200 mesh carbon grids for TEM analysis. Powder x-ray diffraction (XRD) of all the samples was carried out in a PANalytical X'pert Pro dual goniometer diffractometer working under 40 kV and 30 mA. The radiation used was Cu Kα (1.5418 Å) with a Ni filter, and the data collection was carried out using a flat holder in Bragg−Brentano geometry with 1° slit at the source and receiving sides. The diffuse reflectance and absorbance UV−visible spectra were recorded on a Cary series UV−vis−NIR spectrometer, in the wavelength range of 200−800 nm with BaSO$_4$ as a reference sample. Photoluminescence measurements were carried out using a Photon Technology International fluorescence QM-40 spectrophotometer at 350 nm excitation wavelength. Surface states of the samples were analysed by X-ray photoelectron spectroscopy (XPS) in a K-Apha + Thermo Fischer Scientific (UK) instrument with an Al Kα source. The catalyst was first dislodged from the optical fiber by sonication and then was drop casted on silicon wafer. XPS peaks of the compounds were fitted with Shirley type background subtraction method using XPS PEAK41 software. The data were corrected with the standardized peak for carbon at 284.8 eV. Intensity of light at particular points under various conditions is measured using a KM-LUX-100 K (Kusam Electrical Industries Ltd.) digital luxmeter.

Photocatalytic experiments

Photocatalytic H$_2$ evolution experiments were carried out in an in-house developed photoreactor as given in Fig.SI.1. It consists of a two necked 100 mL quartz cylindrical vessel, with fiber bundle inserted from the top and evolved gas injected out of the side arm. The fiber bundle is fixed at the neck using gas impermeable epoxy glue. A 450 W high pressure mercury lamp was used as the light source for the optical fibers. Here methanol was used as the sacrificial reagent. The amount of H$_2$ evolved was determined using gas chromatography (5700 Nucon gas chromatograph (Carbosphere column and Ar as carrier gas) with thermal conductivity detector. The program used in GC for all the analysis consisted of detector temperature of 100 °C and oven temperature of 50 °C at the time of injection.

Results and discussion

The strategy adopted for the maximum utilisation of photons is to avoid scattering by the reaction medium and facilitate instantaneous exposure to the reactants at the interface.

Employing optical fibres for this would entail appropriate surface modifications, specific design of the photoreactor as well as photocatalyst synthesis methods when compared to conventional powder based photoreactors.

Optical fiber etching

In our experiments, we have used optical fibres made with silica of different refractive indices as core and cladding. To be used in photocatalysis, light has to be leaked in a controlled fashion throughout the length of the fibres. This can be achieved by selectively etching the silica cladding using HF (details given in Fig.SI.2). The etching time was optimised to be 10 s, by which time, the surface becomes holey as well as rough along with drastic reduction in diameter from 42.40 μm to 28.66 μm (Fig. 1). As expected, emitted light intensity along the side of the fiber walls also increased from 100 lux to 380 lux after HF treatment (inset bar graph in Fig. 1). However, increase in etching time to 20 s decreases the transmission possibly due to severe damage to the silica cladding exposing the core fully. The irradiance spectrum of the optical fiber after etching spans a broad range from ~300 nm up to 700 nm (Fig.SI.3).
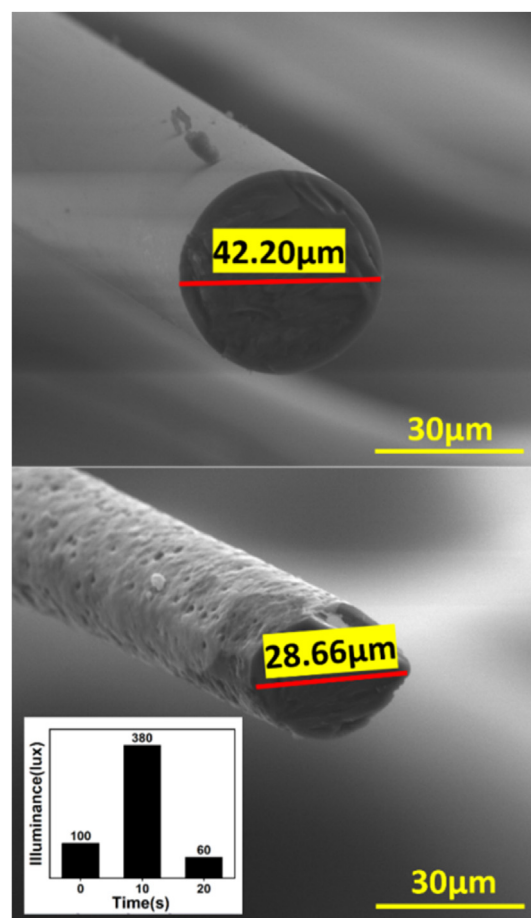
Fig. 1 − Morphology of optical fiber before HF (top) and after HF treatment for 10 s (bottom) Inset shows the extent of light leaking through the defects created by HF treatment.

Synthesis and characterisation of CuO/TiO₂ catalyst

For this study, we selected CuO deposited on TiO₂ as the photocatalyst since it is well studied and identified as one of the best H₂ evolution photocatalysts. Band gap of TiO₂ is ~3.2 eV and photoreduced CuOx is known to absorb in the visible region acting as sensitizer as well as catalytic sites for HER [35,47−61]. It is suggested that TiO₂ acts as the photocatalyst in presence of UV light and CuO gets reduced to CuOx and even further to Cu(0) [27,62−65]. These reduced CuOx species act as sensitizer and absorb visible light resulting in an electron transfer to TiO₂. For further coating, 5 wt% of CuO was deposited on TiO₂ (P25) and the as-synthesised powder catalyst (named as 5CuO/TiO₂) was characterised to ascertain formation of the desired phase as well as appropriate interface (Fig. 2). PXRD pattern indicates the presence of rutile and anatase phases of TiO₂ as expected; however, no discernible peak characteristic of CuO is seen, indicating its existence in highly dispersed form (Fig. 2a). TEM studies (Fig. 2c−h) reveal spherical particles with lattice d-spacing of 0.23 nm corresponding to the (111) plane of CuO (00-001-1117) and 0.34 nm for (101) plane of TiO₂ Anatase phase (01-071-1166) and 0.325 nm for (110) plane of rutile phase respectively, indicating intimate surface interaction between TiO₂ and CuO particles. SAED pattern also suggests highly crystalline nature of the sample and the planes of CuO (111) and (101) and (110) planes of anatase and rutile phases are visible (Fig. 2e). FFT diffractogram also indicates intimate interfaces between CuO and TiO₂ (Fig. 2 f-h). Surface interaction between CuO and TiO₂ may also be indicated by red shifted absorption edge of TiO₂ in UV−vis spectroscopy (Fig. 2b). EDAX estimates the Cu concentration to be 4 wt% in 5CuO/TiO₂ (Fig.SI.4).
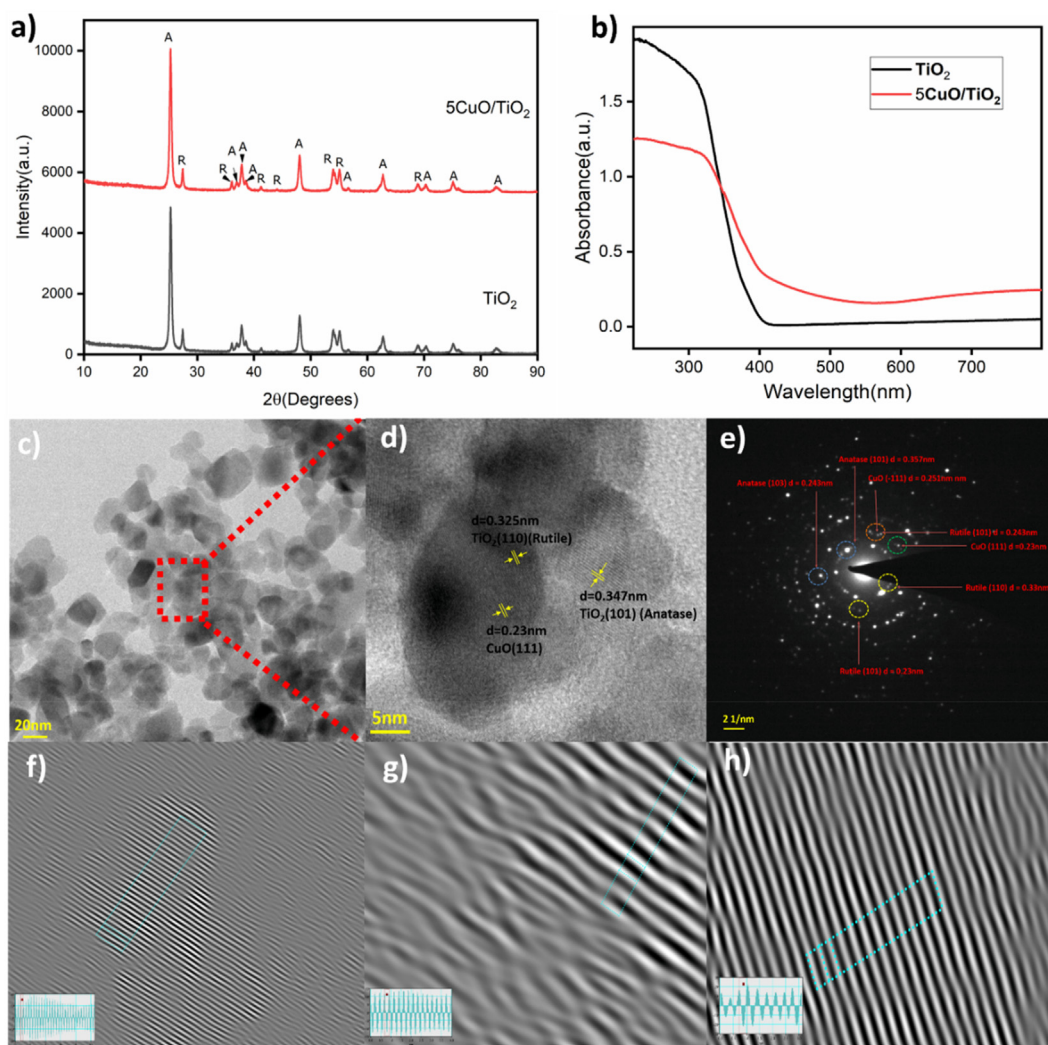
Fig. 2 − **Characterisation of powder sample of 5 wt%CuO/TiO₂ a) P-XRD pattern b) UV−Visible absorption spectra c) TEM image showing the uniform distribution of nanoparticles d) high magnification image is taken from the area in red dotted line e) SAED pattern indicating with the dotted blue (anatase phase), orange (CuO phase) and yellow (rutile phase) respectively, (f−h) Inverse Fast Fourier Transform (IFFT) diffractogram along with the d-spacing of different planes of CuO and TiO₂. (For interpretation of the references to color in this figure legend, the reader is referred to the Web version of this article.)**

Coating of catalysts over etched optical fibers and their characterisation

Deploying catalyst over the etched optical fibres also is an important step in fine tuning the exposure of catalytic sites to photons. This is mainly due to the change in directionality of light exposure; in a conventional system with dispersed powder catalyst, scattering occurs from the vessel wall, reaction medium and catalyst particles as schematically represented in Fig.SI.5 a-b. Whereas, in the optical fibre system, light comes from within the support; hence, designing the right interface with water, sensitizer and semiconductor for interaction with photons is required, but challenging.

First, the as synthesised 5 wt% CuO/TiO$_2$ catalyst was coated over the etched optical fiber bundle of diameter 0.5 cm, containing approximately 10,000 fibers (Fig.SI.6). After coating this catalyst, the surface characteristics of the optical fibers was observed by SEM which shows uniform coating over the entire length of the optical fiber as shown in Fig. 3 a. The cross section of optical fiber also shows the uniform distribution of the catalyst (Fig. 3b). Elemental mapping (Fig. 3 d-f) indicates the presence of Ti, Cu and O uniformly over the surface of optical fibers revealing the effectiveness of coating. To confirm the retention of the phase of the catalyst upon coating, TEM studies were carried out on the coated material dislodged from the fiber surface, which do not indicate any discernible alterations from the powder catalysts (Fig.SI.7).

Our understanding of the mechanism suggests that photons are absorbed by the sensitizer, ie., CuOx and an interfacial electron transfer occurs to the semiconductor, TiO$_2$ [66,67]. To understand the importance of this directionality, two more coating sequences were selected; (i) first CuO slurry deposition and then TiO$_2$ and (ii) first TiO$_2$ was coated over which CuO was deposited. SEM and elemental mapping reveal the coating of CuO and TiO$_2$ over the surface of optical fibers (Fig.SI.8 and 9 respectively for (i) and (ii)) as it is showing the presence of Ti, Cu and O over the surface of optical fibers in the alternate layers. Surface area of each sample, i.e., CuO,
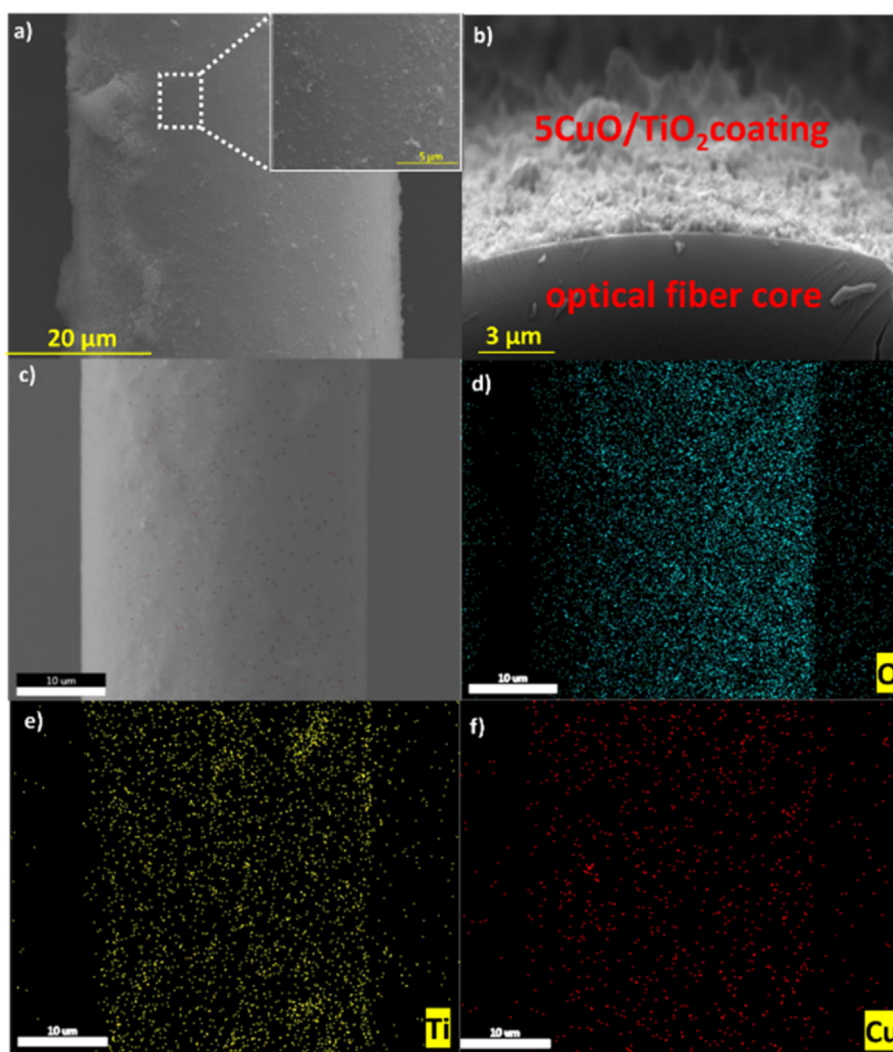
Fig. 3 – SEM images of (a) single optical fiber showing the coating over the length of fiber. Inset shows the uniformity of 5 wt %CuO/TiO$_2$ coating in a magnified view (b) Cross-sectional view of optical fiber showing the smooth core and particulate coating (c) SEM image of area selected for the elemental mapping (d−f) Elemental mapping of O, Ti and Cu over the surface of optical fiber.

TiO_2 and $5CuO/TiO_2$ was also estimated (Table SI.1) and found to be 12, 72 and 55 m^2/g respectively.

Photocatalytic studies on catalyst coated optical fibers

Photocatalytic activities of the optical fiber bundles coated with catalysts by all the three methods described above, were estimated by measuring evolved H_2 every hour up to 8 h. Amount of catalyst coated on the fiber bundle was quantified by weighing the slurry remaining after dip coating and was found to be ~50 mg. Total H_2 evolved increased with time and a maximum of 22 μmoles of H_2 was produced after 8 h in case of 5 wt%CuO/TiO_2 catalyst coated fibers (Fig. 4a). It also showed stable and repeatable H_2 evolution for 32 h under photocatalytic reaction conditions (Fig.SI.10). Apparent quantum yield AQY (%) was estimated from the expected wavelength to be 4.72%, which is comparable to reported data for thin film and powdered photocatalysts (Table SI.2). Structural stability of the catalyst after 32 h of reaction was also ascertained by Scanning Electron Microscopy and elemental analysis (SEM), which indicated no discernible variations in composition of interface structure from the fresh coated fibers (Fig.SI.11a-e). After dislodging of sample from optical fibers after 32 h of cyclic study, TEM analysis of samples was carried out which shows no changes in the structural phases in the powdered sample (Fig.SI.12 a-b). Comparatively, both the sequentially coated catalysts showed poorer activity; in case (i), ie., optical fiber bundles coated first with CuO and then with TiO_2, 12 μmol of H_2 evolution was observed after 8 h, whereas in case (ii), ie., TiO_2 coated as the first layer, only 3 μmol H_2 evolved after 8 h (Fig. 4b & Fig.SI.13). On the other hand, CuO or TiO_2 individually shows very poor H_2 evolution activity of ~2 and 1 μmol respectively (Fig. 4b). This indicates a crucial role of the interfaces between CuO and TiO_2 conducive for electron transfers dictating the activity.

Mechanistic understanding of the activity of catalyst coated optical fibers

Understanding Cu valence states gives an insight into the difference in mechansitic aspects of the three samples. This was done by comparing x-ray photoelectron spectra of the samples before and after irradiation. In case of optical fibers coated with $5CuO/TiO_2$, the freshly prepared sample (Fig. 5a) shows the existence of Cu(I) at 932.19 eV and Cu(II) at 933.46 eV with the strong satellite peaks of characteristics of Cu(II) from the range of 940−950 eV [68−70]. During reaction, the reduction of Cu(II) takes place and an increase of Cu(I) concentration is observed in the sample. In addition, intensity of the satellite peaks which are characteristic of Cu(II) also diminished (Fig. 5b). It is to be noted here that the reduced species could be Cu(0) which is not possible to be differentiated from XPS due to very close binding energy values [57,60−61]. However, such a reduction is commensurate with a notable change in colour from greenish yellow to blackish purple (Fig.SI. 14 a). In addition, plasmon resonance peak at 570 nm in the absorption spectrum (Fig.SI.14 b) of the sample after irradiation may indicate the presence of Cu(0). However, this interconversion of Cu(II) to Cu(I)/Cu(0) is not observed in the other two samples coated in a sequential manner (Fig.SI.15 a−c). It is apparent that such redox systems exist only in the as-synthesised catalyst (which is established by HRTEM in the previous section) and not in the sequentially coated fibers. On correlating this observation to the activities of the three samples, it is clear that the inherent interface between CuO and TiO_2 plays an important role in imparting the photocatalytic activity.

Flat band potentials of CuO, Cu_2O and TiO_2 are estimated using Mulliken electronegativity values and band gaps analysed [71−74]. The details of the calculations are given in the supporting information and band positions are represented with respect to the standard hydrogen electrode in Fig. 6a. It is obvious that TiO_2 is UV active and even though CuO can absorb in visible light, the band alignment is not conducive for electron transfer to TiO_2. However, the UV light present in the light emitted from the optical fiber (as presented in Fig.SI.3.) is sufficient for TiO_2 to act as the photocatalyst for CuO to CuO_x/Cu reduction, as evident from the increase in reduced Cu species in the irradiated optical fiber as well as from the visual observance of colour change. These reduced CuO_x species
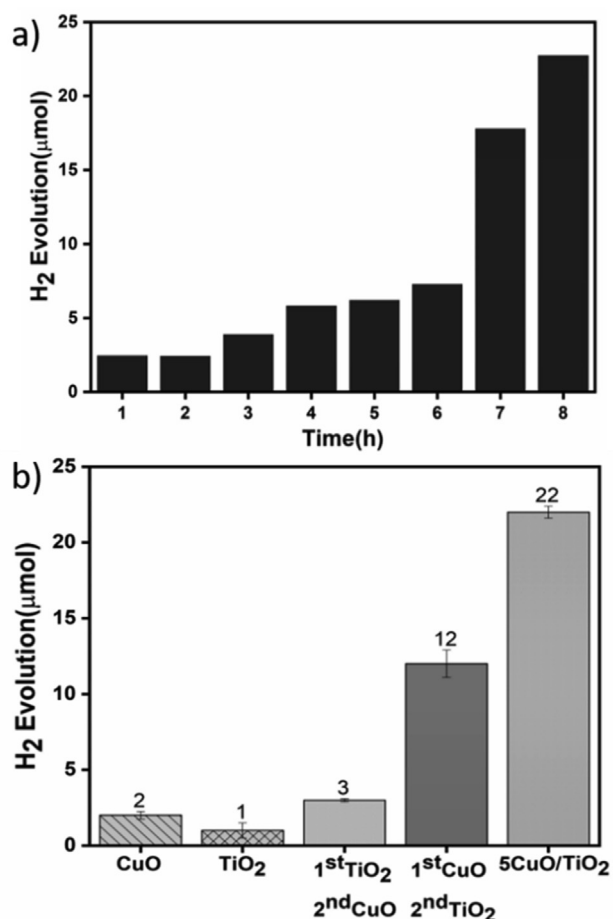
Fig. 4 − (a) H_2 evolution activity of 5 wt%CuO/TiO_2 coated optical fiber bundles in MeOH/Water system under illumination with 450 W High pressure Mercury lamp for 8 h. (b) Comparative H_2 evolution activity of 5 wt%CuO/TiO_2 coated fibers and sequentially coated fibers. All experiments were carried out in MeOH/Water system (35 vol%) under illumination of 450 W High pressure Mercury lamp for 8 h.

Fig. 5 — (a) Cu 2p spectra of 5CuO/TiO$_2$ coated optical fiber bundles of fresh sample before irradiation(b) Cu 2p spectra of 5CuO/TiO$_2$ coated optical fiber bundles of fresh sample after irradiation.

Fig. 6 — a) Valence band and Conduction band positions of CuO, TiO$_2$ and Cu$_2$O with respect to water reduction and oxidation potential b) Mechanism of H$_2$ Evolution from 5CuO/TiO$_2$ over the surface of optical fibre.
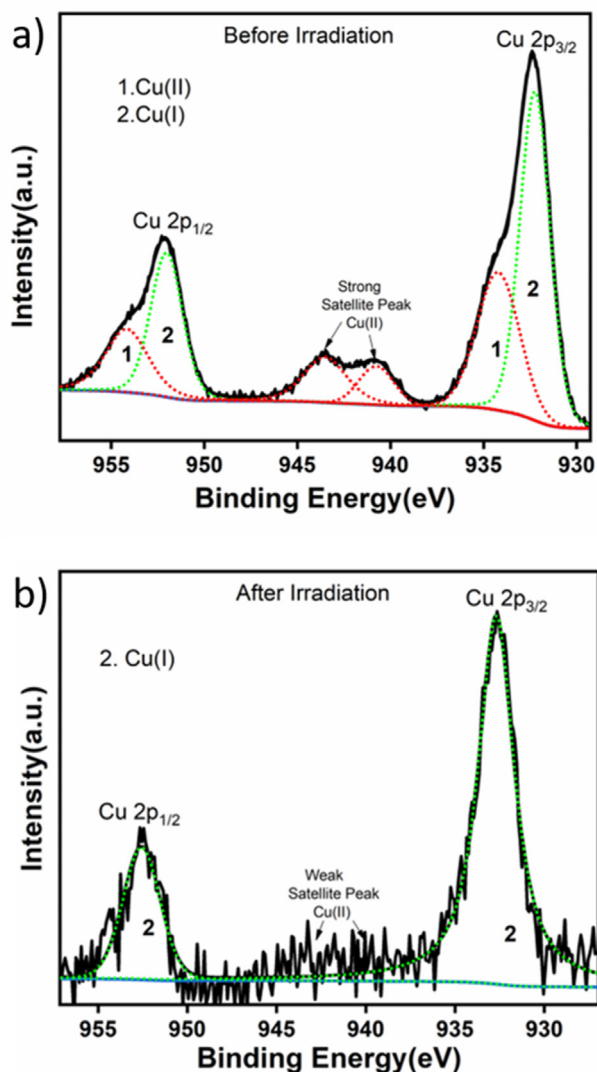
now act as visible light sensitisers with right band alignment for feasible electron transfer to TiO$_2$ which further activates the water splitting (Fig. 6b).

Advantages of catalyst coated optical fibers over dispersed powder catalyst systems

One of the perceived drawbacks of conventional dispersed powder catalysts is the difficulty in scaling up due to increase in turbidity and associated scattering on increasing the catalyst quantity. This is evidenced from Fig. 7a, where hydrogen evolution activity is estimated under high pressure 450 W Mercury lamp for varying quantities of powder 5CuO/TiO$_2$ under the same conditions. As the catalyst quantity increases from 50 mg to 1 g, the activity reduces exponentially. Thus, dispersed powder catalyst system is not conducive for scaling up. This disadvantage can be overcome by using optical fiber

bundles coated with the catalyst, since scaling up can be achieved by simply increasing the number of coated fibers. This is demonstrated by increasing the quantity of catalyst by increasing the number of optical fibers (Fig. 7b). The inset in Fig. 7b shows the amount of catalyst coated over the optical fiber. As the number of optical fibers increases from 1,000 (1 K) to 50,000 (50 K), activity also increases accordingly, from ~1 μmole to 120 μmoles, indicating a linear increase in activity with respect to catalyst amount, with a potential to overcome the scattering issue observed in the powder catalyst. Further, the quantity of catalyst coated on 50 K fiber bundle was

Fig. 8 — The normalized H_2 evolution activity (against maximum activity) of 5CuO/TiO$_2$ coated optical fiber bundles and powder samples in MeOH/Water system under 8 h of illumination of 450 W high pressure Mercury lamp using water samples of different turbidity.

active sites and interfaces. To confirm this phenomenon, hydrogen evolution activities of dispersed powder and catalyst coated optical fibers in water with varying extent of turbidity from 1 to 84 NTU were compared (Fig. SI.16). As the turbidity of water sample increases, the activity of both samples decreases (Fig. 8.); however, activity of dispersed powder in turbid water was found to be minimal with a 99.99% reduction in activity compared to clean water. Whereas, even under such severe scattering, ~70% activity was retained in the case of catalyst coated fibres. This reduction in activity in optical fiber is probably due to suspended particles in turbid water blocking the active sites rather than inability of photons to reach the active sites (Fig.SI.17). Similarly, distance of the light source and catalyst/water interface also affects the activity in conventional photoreactors due to loss of intensity by scattering from air. By bringing light directly to the medium of reaction, such losses in intensity and activity can also be addressed (Fig. SI 18).

Conclusion

In summary, a new approach of using optical fibers coated with semiconductor materials for hydrogen evolution is demonstrated. An active catalyst, 5 wt%CuO supported on TiO$_2$, was selected for coating on silica based optical fibers by a simple dip coating method. Characterisation of the loaded catalyst indicates intimate interface between CuO and TiO$_2$ possibly forming interfaces which are active electron injectors. Photocatalytic H_2 evolution of the catalyst coated optical fibers is compared with dispersed powder catalyst of the same composition. It is found that scattering of light in dispersed powder catalyst systems at higher catalyst quantities has a detrimental effect on activity which prevents scaling up in any meaningful way. However, optical fiber catalyst system can be scaled up easily by increasing the number of fibers without compromising activity due to scattering. We

Fig. 7 — (a) Effect of 5 wt%CuO/TiO$_2$ catalyst quantity in dispersed powder form (b) H_2 evolution activity of 5 wt% CuO/TiO$_2$ coated optical fiber bundles showing variation in catalyst quantity via number of optical fibers in each bundle (c) Comparative H_2 evolution activity of 5CuO/TiO$_2$ coated on optical fiber bundles (700 mg) and 5CuO/TiO$_2$ powdered catalyst (700 mg). All experiments were carried out in MeOH/Water system (35 vol%) under illumination of 450 W high pressure Mercury lamp for 8 h.

increased from 250 mg to 700 mg. Interestingly, H_2 evolution of 222 μmoles was obtained for this sample, which is more than twice that of the powder sample of same quantity (Fig. 7c).

Same phenomenon holds true for usage of powder catalysts in turbid, non-potable water, whereby scattering from the suspended particles prevents light from reaching the

have also shown that powder catalyst is completely deactivated in highly turbid media whereas optical fibers retain activity to a better extent. This is very important since this opens up the type of water sources which can be utilised for H_2 production and helps us to move away from using potable water for fuel production. The lacunae of less illuminance on the surface of the optical fibers need to be addressed by better leaking methods as well as more efficient connections to the light sources. Hence, by combining the abundant and cheap optical fibers to non-potable water usage, we envisage better scaling up opportunities in photocatalytic H_2 production.

CRediT authorship contribution statement

Priyanka S Walko has performed all the experimental parts and then discussion and conclusions has been carried out by Dr. R. Nandini Devi.

Declaration of competing interest

The authors declare that they have no known competing financial interests or personal relationships that could have appeared to influence the work reported in this paper.

Acknowledgement

Appendix A. Supplementary data

Supplementary data to this article can be found online at https://doi.org/10.1016/j.ijhydene.2023.01.148.

REFERENCES

[1] Muradov N. Low to near-zero CO_2 production of hydrogen from fossil fuels: status and perspectives. Int J Hydrogen Energy 2017;42:14058—88. https://doi.org/10.1016/j.ijhydene.2017.04.101.

[2] Chu S, Majumdar A. Opportunities and challenges for a sustainable energy future. Nature 2012;488:294—303. https://doi.org/10.1038/nature11475.

[3] Wang M. Fuel choices for fuel-cell vehicles: well-to-wheels energy and emission impacts. J Power Sources 2002;112:307—21. https://doi.org/10.1016/S0378-7753(02)00447-0.

[4] Song H, Luo S, Huang H, Deng B, Ye J. Solar-Driven hydrogen production: recent advances, challenges, and future perspectives. ACS Energy Lett 2022;7:1043—65. https://doi.org/10.1021/acsenergylett.1c02591.

[5] Sharma S, Agarwal S, Jain A. Significance of hydrogen as economic and environmentally friendly fuel. Energies 2021;14:7389. https://doi.org/10.3390/en14217389.

[6] do Sacramento EM, de Lima LC, Oliveira CJ, Veziroglu TN. A hydrogen energy system and prospects for reducing emissions of fossil fuels pollutants in the Ceará state-Brazil. Int J Hydrogen Energy 2008;33:2132—7. https://doi.org/10.1016/j.ijhydene.2008.02.018.

[7] Midilli A, Dincer I. Hydrogen as a renewable and sustainable solution in reducing global fossil fuel consumption. Int J Hydrogen Energy 2008;33:4209—22. https://doi.org/10.1016/j.ijhydene.2008.05.024.

[8] Steinberg M. Fossil fuel decarbonization technology for mitigating global warming. Int J Hydrogen Energy 1999;24:771—7. 3199(. https://doi.org/10.1016/S0360-3199(98)00128-1.

[9] Vezirolu T. Hydrogen movement and the next action: fossil fuels industry and sustainability economics. Int J Hydrogen Energy 1997;22:551—6. https://doi.org/10.1016/s0360-3199(96)00197-8.

[10] Fujishima A, Honda K. Electrochemical photolysis of water at a semiconductor electrode. Nature 1972;238:37—8. https://doi.org/10.1038/238037a0.

[11] Chen S, Takata T, Domen K. Particulate photocatalysts for overall water splitting. Nat Rev Mater 2017;2:1—17. https://doi.org/10.1038/natrevmats.2017.50.

[12] Liu R, Fang S, Dong C, Tsai K. ScienceDirect Enhancing hydrogen evolution of water splitting under solar spectra using Au/TiO_2 heterojunction photocatalysts. Int J Hydrogen Energy 2021;46:28462—73. https://doi.org/10.1016/j.ijhydene.2021.06.093.

[13] Ahmad H, Kamarudin SK, Minggu LJ, Kassim M. Hydrogen from photo-catalytic water splitting process : a review. Renew Sustain Energy Rev 2015;43:599—610. https://doi.org/10.1016/j.rser.2014.10.101.

[14] Fajrina N, Tahir M. A critical review in strategies to improve photocatalytic water splitting towards hydrogen production. Int J Hydrogen Energy 2018;44:540—77. https://doi.org/10.1016/j.ijhydene.2018.10.200.

[15] Zhu J, Zäch M. Nanostructured materials for photocatalytic hydrogen production. Curr Opin Colloid Interface Sci 2009;14:260—9. https://doi.org/10.1016/j.cocis.2009.05.003.

[16] Abouelela MM, Kawamura G, Matsuda A. A review on plasmonic nanoparticle-semiconductor photocatalysts for water splitting. J Clean Prod 2021;294:126200. https://doi.org/10.1016/j.jclepro.2021.126200.

[17] Chauhan DK, Battula VR, Jain S, Kailasam K. Photocatalytic integrated production of hydrogen and imines from aromatic amines via Ni-mesoporous carbon nitride: an acceptor less dehydrogenative pathway. J Clean Prod 2021;307:127162. https://doi.org/10.1016/j.jclepro.2021.127162.

[18] Almomani F, Shawaqfah M, Alkasrawi M. Solar-driven hydrogen production from a water-splitting cycle based on carbon-TiO2 nano-tubes. Int J Hydrogen Energy 2022;47:3294—305. https://doi.org/10.1016/j.ijhydene.2020.12.191.

[19] Li Q, Lu Q, Guo E, Wei M, Pang Y. Hierarchical Co 9 S 8/ZnIn 2 S 4 nano flower enables enhanced hydrogen evolution photocatalysis. Energy Fuels 2022;36:4541—8. https://doi.org/10.1021/acs.energyfuels.1c04322.

[20] Gupta NM. Factors affecting the efficiency of a water splitting photocatalyst : a perspective. Int J Hydrogen Energy 2017;71:585—601. https://doi.org/10.1016/j.rser.2016.12.086.

[21] Idriss H. Toward large-scale hydrogen production from water: what have we learned and what are the main research hurdles to cross for commercialization? Energy Technol 2021;9. https://doi.org/10.1002/ente.202000843.

[22] Anta JA, Calero S, Bieberle-hu A, Libisch F, Mun AB. Challenges of modeling nanostructured materials for photocatalytic water splitting. Chem Soc Rev 2022:3794—818. https://doi.org/10.1039/d1cs00648g.

[23] Narendranath SB, Yadav AK, Bhattacharyya D, Jha SN, Devi RN. Photocatalytic H2 evolution from water-methanol system by anisotropic InFeO3(ZnO)m oxides without cocatalyst in visible light. ACS Appl Mater Interfaces 2014;6:12321—7. https://doi.org/10.1021/am501976z.

[24] Baliarsingh N, Mohapatra L, Parida K. Design and development of a visible light harvesting Ni-Zn/Cr-CO 32-LDH system for hydrogen evolution. J Mater Chem 2013;1:4236—43. https://doi.org/10.1039/c2ta00933a.

[25] Ouyang W, Muñoz-Batista MJ, Kubacka A, Luque R, Fernández-García M. Enhancing photocatalytic performance of TiO2 in H2 evolution via Ru co-catalyst deposition. Appl Catal B Environ 2018;238:434—43. https://doi.org/10.1016/j.apcatb.2018.07.046.

[26] Hasan MM, Allam NK. Unbiased spontaneous solar hydrogen production using stable TiO2-CuO composite nanofiber photocatalysts. RSC Adv 2018;8:37219—28. https://doi.org/10.1039/c8ra06763e.

[27] Buraso W, Lachom V, Siriya P, Laokul P. Synthesis of TiO2 nanoparticles via a simple precipitation method and photocatalytic performance. Mater Res Express 2018;5. https://doi.org/10.1088/2053-1591/aadbf0. 0—10.

[28] Languer MP, Scheffer FR, Feil AF, Baptista DL, Migowski P, Machado GJ, et al. Photo-induced reforming of alcohols with improved hydrogen apparent quantum yield on TiO2 nanotubes loaded with ultra-small Pt nanoparticles. Int J Hydrogen Energy 2013;38:14440—50. https://doi.org/10.1016/j.ijhydene.2013.09.018.

[29] Darbandi M, Shaabani B, Schneider J, Bahnemann D, Gholami P, Khataee A, et al. TiO2 nanoparticles with superior hydrogen evolution and pollutant degradation performance. Int J Hydrogen Energy 2019;44:24162—73. https://doi.org/10.1016/j.ijhydene.2019.07.129.

[30] Pulido Melián E, Nereida Suárez M, Jardiel T, Calatayud DG, del Campo A, Doña-Rodríguez JM, et al. Highly photoactive TiO2 microspheres for photocatalytic production of hydrogen. Int J Hydrogen Energy 2019;44:24653—66. https://doi.org/10.1016/j.ijhydene.2019.07.230.

[31] Wang J, Wang Z, Qu P, Xu Q, Zheng J, Jia S, et al. A 2D/1D TiO2 nanosheet/CdS nanorods heterostructure with enhanced photocatalytic water splitting performance for H2 evolution. Int J Hydrogen Energy 2018;43:7388—96. https://doi.org/10.1016/j.ijhydene.2018.02.191.

[32] Li Q, Lu Q, Guo E, Wei M, Pang Y. Hierarchical Co 9 S 8/ZnIn 2 S 4 nano flower enables enhanced hydrogen evolution photocatalysis. Energy Fuels 2022;36:4541—8. https://doi.org/10.1021/acs.energyfuels.1c04322.

[33] Patra KK, Bharad PA, Jain V, Gopinath CS. Direct solar-to-hydrogen generation by quasi-artificial leaf approach: possibly scalable and economical device. J Mater Chem 2019;7:3179—89. https://doi.org/10.1039/C8TA11307F.

[34] Bajpai H, Patra KK, Ranjan R, Nalajala N, Reddy KP, Gopinath CS. Can half-a-monolayer of Pt simulate activity like that of bulk Pt? Solar hydrogen activity demonstration with quasi-artificial leaf device. ACS Appl Mater Interfaces 2020;12:30420—30. https://doi.org/10.1021/acsami.0c07431.

[35] de Brito JF, Tavella F, Genovese C, Ampelli C, Zanoni MVB, Centi G, et al. Role of CuO in the modification of the photocatalytic water splitting behavior of TiO2 nanotube thin films. Appl Catal B Environ 2018;224:136—45. https://doi.org/10.1016/j.apcatb.2017.09.071.

[36] Gupta A, Likozar B, Jana R, Chanu WC, Singh MK. A review of hydrogen production processes by photocatalytic water splitting — from atomistic catalysis design to optimal reactor engineering. Int J Hydrogen Energy 2022;47:33282—307. https://doi.org/10.1016/j.ijhydene.2022.07.210.

[37] Nandy S, Savant SA, Haussener S. Chemical Science Prospects and challenges in designing photocatalytic particle suspension reactors for solar fuel processing. Chem Sci 2021;12:9866—84. https://doi.org/10.1039/d1sc01504d.

[38] Marinangeli RE, Ollls DF, Fiber IS. Photoassisted heterogeneous Catalysis with optical fibers. AlChE J 1977;23:415—26. https://doi.org/10.1002/aic.690230403.

[39] Marinangeli RE, Ollis DF. Photo-assisted heterogeneous catalysis with optical fibers II. Nonisothermal single fiber and fiber bundle. AIChE J 1980;26:1000—8. https://doi.org/10.1002/aic.690260615.

[40] Du P, Carneiro JT, Moulijn JA, Mul G. A novel photocatalytic monolith reactor for multiphase heterogeneous photocatalysis. Appl Catal, A: GEN 2008;334:119—28. https://doi.org/10.1016/j.apcata.2007.09.045.

[41] Spigulis J. Side-emitting fibers brighten our world. Opt Photon News 2005;16:34—9. https://doi.org/10.1364/OPN.16.10.000034.

[42] Lee J, Dhital D, Yoon D. Investigation of cladding and coating stripping methods for specialty optical fibers. Opt Laser Eng 2011;49:324—30. https://doi.org/10.1016/j.optlaseng.2010.10.008.

[43] Marinangeli RE, Ollis DF. Photo-assisted heterogeneous catalysis with optical fibers. Part III: Photoelectrodes. AIChE J 1982;28:945—55. https://doi.org/10.1002/aic.690280609.

[44] Chen Y, Chen D, Wei Z, Chen Y. Preparation and photocatalytic properties of TiO2 immobilized on fiberglass cloth. Adv Bio Sci Res 2017;3:396—9. https://doi.org/10.2991/bep-16.2017.88.

[45] Chen YL, Kuo L-C, Tseng ML, Chen HM, Chen C-K, Huang HJ, et al. ZnO nanorod optical disk photocatalytic reactor for photodegradation of methyl orange. Opt Express 2013;21:7240. https://doi.org/10.1364/oe.21.007240.

[46] Potter ME, Stewart DJ, Oakley AE, Boardman RP, Bradley T, Sazio PJA, et al. Combining photocatalysis and optical fiber technology toward improved microreactor design for hydrogen generation with metallic nanoparticles. ACS Photonics 2020;7:714—22. https://doi.org/10.1021/acsphotonics.9b01577.

[47] Wang Y, Zhou M, He Y, Zhou Z, Sun Z. In situ loading CuO quantum dots on TiO2 nanosheets as cocatalyst for improved photocatalytic water splitting. J Alloys Compd 2020;813:152184. https://doi.org/10.1016/j.jallcom.2019.152184.

[48] Dieu T, Ung T, Liem Q, Schiller R, Weiss CK, Landfester K, et al. Synthesis and characterization of nano-CuO and CuO/TiO2 photocatalysts. Adv Nat Sci Nanosci Nanotechnol 2013;4:025002. https://doi.org/10.1088/2043-6262/4/2/025002.

[49] Reddy NL, Emin S, Kumari VD, Muthukonda Venkatakrishnan S. CuO quantum dots decorated TiO2 nanocomposite photocatalyst for stable hydrogen generation. Ind Eng Chem Res 2018;57:568—77. https://doi.org/10.1021/acs.iecr.7b03785.

[50] Li Y, Wang B, Liu S, Duan X, Hu Z. Synthesis and characterization of Cu2O/TiO2 photocatalysts for H2 evolution from aqueous solution with different scavengers. Appl Surf Sci 2015;324:736—44. https://doi.org/10.1016/j.apsusc.2014.11.027.

[51] Kum JM, Yoo SH, Ali G, Cho SO. Photocatalytic hydrogen production over CuO and TiO2 nanoparticles mixture. Int J Hydrogen Energy 2013;38:13541—6. https://doi.org/10.1016/j.ijhydene.2013.08.004.

[52] Manjunath K, Souza VS, Ramakrishnappa T, Nagaraju G, Scholten JD, Dupont J. Heterojunction CuO-TiO2 nanocomposite synthesis for significant photocatalytic hydrogen production. Mater Res Express 2016;3:115904. https://doi.org/10.1088/2053-1591/3/11/115904.

[53] Praveen Kumar D, Shankar MV, Mamatha Kumari M, Sadanandam G, Srinivas B, Durgakumari V. Nano-size effects on CuO/TiO₂ catalysts for highly efficient H₂ production under solar light irradiation. Chem Commun 2013;49:9443–5. https://doi.org/10.1039/c3cc44742a.

[54] Nuo Peh CK, Wang X-Q, Ho GW. Increased photocatalytic activity of CuO/TiO₂ through broadband solar absorption heating under natural sunlight. Procedia Eng 2017;215:171–9. https://doi.org/10.1016/j.proeng.2017.11.006.

[55] Brito JF de, Zanoni MVB. On the application of Ti/TiO₂/CuO n-p junction semiconductor: a case study of electrolyte, temperature and potential influence on CO₂ reduction. Chem Eng J 2017;318:264–71. https://doi.org/10.1016/j.cej.2016.08.033.

[56] Echeverria E. Enhancement in the performance of nanostructured CuO − ZnO solar cells by band alignment. RSC Adv 2020:7839–54. https://doi.org/10.1039/c9ra10771a.

[57] Mondal I, Pal U. Synthesis of MOF templated Cu/CuO@TiO₂ nanocomposites for synergistic hydrogen production. Phys Chem Chem Phys 2016;18:4780–8. https://doi.org/10.1039/c5cp06292f.

[58] Xu B, Dong L, Chen Y. Influence of CuO loading on dispersion and reduction behavior of CuO/TiO₂ (anatase) system. J Chem Soc Faraday Trans 1998;94:1905–9. https://doi.org/10.1039/a801603h.

[59] Zainelabdin A, Zaman S, Amin G, Nur O, Willander M. Optical and current transport properties of CuO/ZnO nanocoral p-n heterostructure hydrothermally synthesized at low temperature. Appl Phys A: Mater Sci Process 2012;108:921–8. https://doi.org/10.1007/s00339-012-6995-2.

[60] Khan MA, Nayan N, Shadiullah, Ahmad MK, Soon CF. Surface study of cuo nanopetals by advanced nanocharacterization techniques with enhanced optical and catalytic properties. Nanomaterials 2020;10:1–18. https://doi.org/10.3390/nano10071298.

[61] Bandara J, Udawatta CPK, Rajapakse CSK. Highly stable CuO incorporated TiO₂ catalyst for photocatalytic hydrogen production from H₂O. Photochem Photobiol Sci 2005;4:857–61. https://doi.org/10.1039/b507816d.

[62] Wang Z, Liu Y, Martin DJ, Wang W, Tang J, Huang W. CuOₓ-TiO₂ junction: what is the active component for photocatalytic H₂ production? Phys Chem Chem Phys 2013;15:14956–60. https://doi.org/10.1039/c3cp52496e.

[63] Bharad PA, Nikam AV, Thomas F, Gopinath CS. CuOₓ-TiO₂ composites: electronically integrated nanocomposites for solar hydrogen generation. ChemistrySelect 2018;3:12022–30. https://doi.org/10.1002/slct.201802047.

[64] Yao L, Wang W, Wang L, Liang Y, Fu J, Shi H. Chemical bath deposition synthesis of TiO₂/Cu₂O core/shell nanowire arrays with enhanced photoelectrochemical water splitting for H₂ evolution and photostability. Int J Hydrogen Energy 2018;43:15907–17. https://doi.org/10.1016/j.ijhydene.2018.06.127.

[65] Zhang J, Yang Y, Liu W. Preparation, characterization, and activity evaluation of CuO/F-TiO₂ photocatalyst. Int J Photoenergy 2012;2012:1–9. https://doi.org/10.1155/2012/139739.

[66] Tamiolakis I, Papadas IT, Spyridopoulos KC, Armatas GS. Mesoporous assembled structures of Cu₂O and TiO₂ nanoparticles for highly efficient photocatalytic hydrogen generation from water. RSC Adv 2016;6:54848–55. https://doi.org/10.1039/c6ra08546f.

[67] Lalitha K, Sadanandam G, Kumari VD, Subrahmanyam M, Sreedhar B, Hebalkar NY. Highly stabilized and finely dispersed Cu₂O/TiO₂: a promising visible sensitive photocatalyst for continuous production of hydrogen from glycerol:water mixtures. J Phys Chem C 2010;114:22181–9. https://doi.org/10.1021/jp107405u.

[68] Biesinger MC. Advanced analysis of copper X-ray photoelectron spectra. Surface Interfac 2017;49:1325–34. https://doi.org/10.1002/sia.6239.

[69] Roy K, Vinod CP, Gopinath CS. Design and performance aspects of a custom-built ambient pressure photoelectron spectrometer toward bridging the pressure gap: oxidation of Cu, Ag, and Au surfaces at 1 mbar O₂ pressure. J Phys Chem C 2013;117:4717–26. https://doi.org/10.1021/jp312706s.

[70] Janczarek M, Kowalska E. On the origin of enhanced photocatalytic activity of copper-modified titania in the oxidative reaction systems. Catalysts 2017;7:2–26. https://doi.org/10.3390/catal7110317.

[71] Swadźba-Kwaśny M, Chancelier L, Ng S, Manyar HG, Hardacre C, Nockemann P. Facile in situ synthesis of nanofluids based on ionic liquids and copper oxide clusters and nanoparticles. Dalton Trans 2012;41:219–27. https://doi.org/10.1039/c1dt11578b.

[72] Cao S, Wang CJ, Wang GQ, Chen Y, Lv XJ, Fu WF. Visible light driven photo-reduction of Cu²⁺ to Cu₂O to Cu in water for photocatalytic hydrogen production. RSC Adv 2020;10:5930–7. https://doi.org/10.1039/c9ra09590j.

[73] Subha PP, Vikas LS, Jayaraj MK. Solution-processed CuO/TiO₂ heterojunction for enhanced room temperature ethanol sensing applications. Phys Scripta 2018;93:055001. https://doi.org/10.1088/1402-4896/aaae1a.

[74] Kim Y Il, Atherton SJ, Brigham ES, Mallouk TE. Sensitized layered metal oxide semiconductor particles for photochemical hydrogen evolution from nonsacrificial electron donors. J Phys Chem 1993;97:11802–10. https://doi.org/10.1021/j100147a038.

Alkaline Water Electrolysis by NiZn-Double Hydroxide-Derived Porous Nickel Selenide-Nitrogen-Doped Graphene Composite

Ayasha Nadeema,[†,§] Priyanka S. Walko,[‡,§] R. Nandini Devi,[‡,§] and Sreekumar Kurungot*,[†,§]

[†]Physical and Materials Chemistry Division, CSIR-National Chemical Laboratory, Pune-411008, India
[‡]Catalysis Division, CSIR-National Chemical Laboratory, Pune-411008, India
[§]Academy of Scientific and Innovative Research (AcSIR), New Delhi-110001, India

Ⓢ *Supporting Information*

ABSTRACT: The large-scale application of water electrolysis for the generation of hydrogen can be made viable only by the development of inexpensive, robust, and bifunctional electrocatalysts. Here, we report a self-templating method for the design of porous, edge-site-rich hybrid nanomaterials via the selective etching of layered double hydroxide precursors that contain an amphoteric metal by alkali treatment, followed by vapor phase selenization. The obtained hexagonal nickel selenide nanoplates anchored over nitrogen-doped graphene showed highly efficient and robust oxygen evolution reaction (OER) electrocatalysis due to the inherent in situ electrochemical oxidation property of selenides demonstrating low overpotential of 311 mV to achieve the 10 mA cm^{-2} water oxidation current density in 1 M KOH. The faster reaction kinetics and long-term stability of the catalyst encouraged us to demonstrate a real alkaline water electrolyzer, which enables high-performing overall water splitting with a low overpotential of 460 mV from theoretical potential of 1.23 V to generate sufficient amounts of H$_2$ and O$_2$ by achieving a current density of 10 mA cm^{-2}. This study thus provides a valuable strategy to tailor the surface texture of the catalyst as well as its effectiveness in developing robust multifunctional electrocatalysts, promoting the efficient design of porous materials for catalytic applications.

KEYWORDS: *layered double hydroxide, nickel oxyhydroxide, selenization, Faradaic efficiency, turnover frequency*
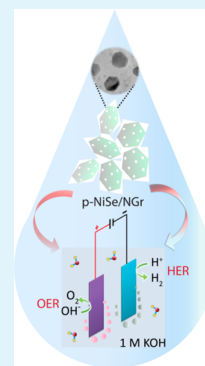
1. INTRODUCTION

Recently, fuel cells, especially hydrogen fuel cells, have come into picture as promising choices that provide green and sustainable energy using hydrogen as the fuel.[1] The sustainability, as well as ecofriendliness of the fuel cell, depends directly on the source of hydrogen.[2,3] To date, fossil fuels are the primary source of hydrogen, making the fuel cell technology non-renewable fossil fuel dependent and practically defeating its purpose.[4,5] One promising way of resolving this issue is to produce hydrogen using an environmentally inoffensive route, where water can be the best solution.[6] Interestingly, water splitting technology can benefit us in two different ways—on the one hand, it can circumvent the problems associated with the storage and transportation of hydrogen fuel in the pure form, and on the other hand, it can contribute to the viability of a hydrogen economy.[7] Hence, it is a promising technology, availing us with on-site/on-demand H$_2$ producing capability along with its feasibility of coupling with renewable energy sources to mitigate their intermittency and the localized nature. In contrast to photochemical water splitting, which solely depends on solar energy, electrochemical water splitting widens the scope for using various kinds of renewable energy sources. In this way, electrochemical water splitting technology opens up the opportunity to generate hydrogen fuel in a greener way to make the fuel cell technology fully sustainable and ecofriendly.[6]

Water electrolysis involves two half-cell reactions: the hydrogen evolution reaction (HER) and the oxygen evolution

reaction (OER).[8] The unfavorable kinetics of these two electrode reactions are considered as the bottleneck for efficient electrolysis, leading to high overpotential to facilitate the work.[7] Pt- and Ru/Ir-based catalysts have long been considered state-of-the-art electrocatalysts; however, their high cost and scarce availability have geared research at the development of inexpensive and earth-abundant material-based catalysts.[9] Development of cost-effective electrocatalysts for HER in acidic medium and for OER in alkaline medium has already achieved significant success.[10−14] However, instead of using different catalyst materials for catalyzing the two half-cell reactions, if both the electrodes employ the same material, the overall material cost can be reduced by avoiding the complicated process of designing the device to support two different catalysts.[6] However, the design of a high-performance bifunctional catalyst that works in a medium having uniform pH is quite challenging. Although sufficient progress has been made in this direction,[15−18] there is still much to be done in the design and optimization of bifunctional catalysts that make the electrolyzer more viable both in terms of cost and energy consumption.

Nickel hydroxides[19] and oxides[20,21] are among the best electrolyzer catalysts; however, replacing the oxides with

selenides introduces a number of favorable factors which can further enhance the performance of the Ni-based systems.[13,22,23] Great progress has been achieved in the past few years in developing earth-abundant metal chalcogenide-based materials for various electrochemical applications.[15,17,23] For example, Kwak et al.[24] demonstrated the excellent HER performance of $CoSe_2$ nanocrystals and good OER performance of $NiSe_2$ nanocrystals in alkaline medium. In another report, Liang et al.[16] demonstrated the improved HER performance of converted $NiSe_2$ nanosheets from the selenization of β-$Ni(OH)_2$. In a recent study, Haoyi et al.[22] demonstrated the enhancement of catalytic stability of ultrathin nickel diselenide nanowires by decorating them with amorphous nickel oxide nanoparticles for overall water electrolysis.

Hence, by screening the existing transition metal selenide-based HER and OER catalysts, one can conclude that nickel selenide can be a promising candidate as a bifunctional catalyst for alkaline water electrolysis. To further improve its performance, it is of great importance to engineering its surface configuration by considering two critical requirements; first, enrichment of the active catalytic sites and second, the stability of the active sites during an electrochemical analysis. In this context, we report a 3-step approach to design porous and edge-site-rich hybrid material via the selective etching of NiZn layered double hydroxide decorated over nitrogen-doped graphene [(Zn)Ni-LDH/NGr] precursors that contain an amphoteric metal (zinc) by alkali treatment followed by vapor-phase selenization. Additionally, the use of nitrogen-doped graphene (NGr)-supported precursor helped to reduce the aggregation of selenides over NGr resulting in open and active sites exposed catalyst system. The obtained hexagonal nickel selenide/NGr is found to contain pure monoclinic selenide phase along with a trace amount of nickel oxide and elemental selenium. Thus, the unique electronic structure of crystalline nickel selenide benefitted with the randomly oriented bonds of the amorphous NiO_x as well as elemental selenium helped for the acceleration of both HER and OER kinetics along with remarkable electrochemical stability in the strong alkaline medium. In this way, enriching the catalyst surface with abundant active sites, as well as its hybridization with electronically conducting NGr, resulted in favorable electrochemical performance toward overall alkaline water electrolysis with a low overpotential of 460 mV at 10 mA cm^{-2} for overall alkaline water electrolysis.

2. RESULTS AND DISCUSSION

2.1. Synthesis and Material Characterization.
The synthesis route for the preparation of p-NiSe/NGr is represented in Scheme 1. (Zn)Ni-LDH/NGr (designated as ZnNiNGr in all the upcoming sections) was first synthesized by following the previous report wherein we demonstrated the controlled synthesis of thin layered (Zn)Ni-LDH sheets anchored over nitrogen-doped graphene (NGr).[25] Here, we took advantage of the thin layers of the LDHs as well as the amphoteric nature of zinc to synthesize porous, hexagonal and thin β-$Ni(OH)_2$ nanoplates by selectively etching the Zn^{2+} ions from the (Zn)Ni-LDH moieties via alkali treatment. The obtained β-$Ni(OH)_2$/NGr was subsequently converted into porous NiSe/NGr (designated as p-NiSe/NGr) via reductive annealing in the presence of selenium powder under 10% H_2/ Argon atmosphere. The as-synthesized selenide system is found to contain trace amounts of nickel oxide, probably generated by the thermal treatment of selenium-vapor-inaccessible nickel hydroxide moieties. Details of the materials used for the

Scheme 1. Representation of the Steps Involved in the Synthesis of Porous-NiSe/NGr
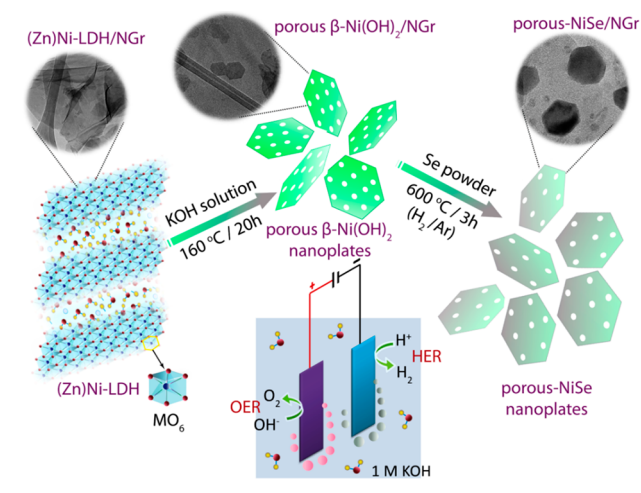
synthesis and the experimental procedures employed for all the controlled samples are provided in the experimental section of Supporting Information.

The crystallinity and phase purity of all the as-synthesized materials were investigated using X-ray diffraction (XRD) analysis. Figure 1a represents the XRD pattern of ZnNiNGr, with broad diffraction peaks corresponding to the (003), (006), (101), (012), and (110) planes of α-$Ni(OH)_2$ indicating the formation of the layered double hydroxide (LDH) of nickel and zinc (ICDD card no. 00-038-0715).[26,27] Basically, α-$Ni(OH)_2 \cdot xH_2O$ is a polymorph consisting of layers of β-$Ni(OH)_2$ with intercalated water molecules and charge balancing anions which, upon alkali treatment, loses the intercalated species and converts to β-$Ni(OH)_2$.[28] Interestingly, in the case of ZnNiNGr, along with the removal of the intercalated species, alkali treatment induces the selective etching of amphoteric Zn^{2+} ions as well, forming porous β-$Ni(OH)_2$/NGr. Figure 1b shows the diffraction peaks of the alkali-treated sample which can be assigned to the hexagonal β-$Ni(OH)_2$ phase with no additional LDH peaks[16,19] (ICDD No. 01-073-1520). The XRD pattern in Figure 1a depicts broad (003) peak that confirms the anchoring of (Zn)Ni-LDH over NGr as thin layers, which is retained in the β-$Ni(OH)_2$/NGr having broad XRD diffraction peaks, with minimum restacking of β-$Ni(OH)_2$ moieties over NGr during the KOH treatment. The vapor-phase selenization of β-$Ni(OH)_2$/NGr gives an XRD pattern that clearly identifies the presence of pure monoclinic $Ni_{1-x}Se$ (ICDD No. 00-018-0890)[17] where the phase compositions varies from $Ni_{0.83}Se$ to $Ni_{0.75}Se$ depending upon the reaction conditions and the Ni to Se ratio owing to the small electronegativity difference between Ni and Se[29,30] (Figure 1c). The XRD analysis could not recognize the presence of NiO_x moieties and elemental Se indicating their trace amount and highly amorphousness of NiO_x.

In contrast, the XRD pattern of alkali-treated α-$Ni(OH)_2$/ NGr shows diffraction planes corresponding to both the $Ni(OH)_2$ phases, confirming the incomplete $\alpha \rightarrow \beta$-phase conversion, presumably due to the absence of zinc which could aid the process (Figure S1a). Selenization of KOH treated α-$Ni(OH)_2$/NGr (β-$Ni(OH)_2Se$/NGr) was incomplete having diffraction peaks corresponding to metallic selenium (Figure S1b). The direct selenization of ZnNiNGr (designated as ZnNiSe/NGr in the upcoming sections) presented impure
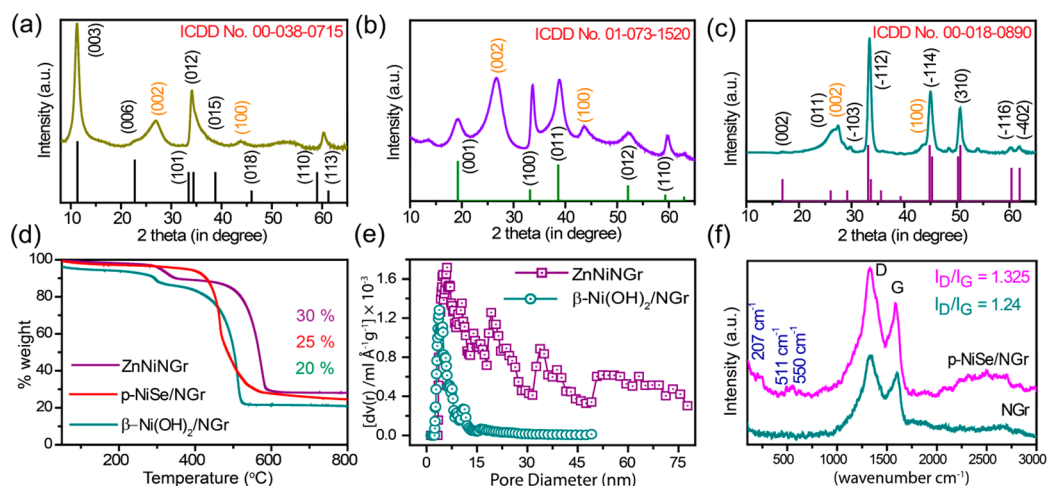
Figure 1. XRD patterns of (a) ZnNiGr, (b) β-Ni(OH)$_2$/NGr, and (c) p-NiSe/NGr. In all the three XRD spectra, orange colored (002) and (100) planes represent the NGr diffraction peaks. (d) Comparative plots of the TGA profiles, (e) comparative BET pore size distribution profiles, and (f) comparative Raman spectra.
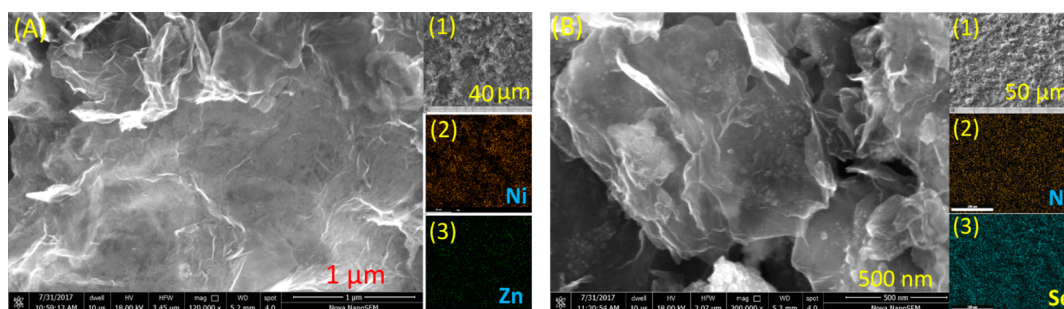
Figure 2. (A) FESEM image of ZnNiGr where the inset image A(1) represents the SEM image selected for elemental mapping and images A(2) and A(3) are the elemental distribution for Ni and Zn, respectively. (B) FESEM image of p-NiSe/NGr where the inset image B(1) represents the SEM image selected for the elemental mapping and images B(2) and B(3) are the elemental distribution for Ni and Se, respectively.

nickel selenide phase showing clear diffraction planes corresponding to zinc selenide (Figure S1c). In this way, the selenization of alkali-treated ZnNiGr over the selenization of direct ZnNiGr sample as well as the use of ZnNiGr over α-Ni(OH)$_2$/NGr helped us to synthesize desired nickel selenide. Broad diffraction peaks, characteristic of carbon (002) and (100) planes, are apparently visible in all the XRD patterns indicating the presence of substantial amounts of NGr in the catalyst system.

Subsequent to the phase identification, total loading of the selenide over NGr as well as the removal of zinc through KOH treatment was confirmed via thermogravimetric analysis (TGA) in an oxygen atmosphere (Figure 1d). The TGA graph of ZnNiGr shows an approximately 30% loading of (Zn)Ni-LDH over NGr, bearing a characteristic endothermic weight loss region of LDH which is mainly within the 250−400 °C temperature range corresponding to the removal of adsorbed water and intercalated species.[28] The removal of zinc is confirmed by comparing the TGA graph of ZnNiGr and β-Ni(OH)$_2$/NGr, where the final metal loading is decreased to 20%. TGA graph of p-NiSe/NGr showed a 5% increment in the loading after selenization with a final metal selenide loading of 25% over NGr.

Surface porosity as well as specific surface area measurements of p-NiSeNGr and other controlled samples were performed through BET analysis by multilayer N$_2$ adsorption and desorption technique with the pore sizes being deduced from

desorption branches using the DFT method. The relative pore size distribution of NGr with ZnNiGr shows the absence of pores in the size range of 2−5 nm in ZnNiGr revealing the anchoring of LDH sheets over the microporous anchoring sites of NGr (Figure S2a). Moreover, the increase in the pore size of ZnNiGr in the size range of 5−35 nm confirms the anchoring of LDH sheets over as well as in between the NGr sheets (Figure S2a).[25] However, this porosity feature of ZnNiGr vanished after the alkali treatment which induces the reorganization, aggregation as well as overlapping of the small LDH sheets into hexagonal and porous β-Ni(OH)$_2$ nanoplates having porosity in the size range of 3−12 nm (Figure 1e), which is also retained in the p-NiSe/NGr (Figure S2b). The surface areas measured for ZnNiGr, β-Ni(OH)$_2$/NGr, p-NiSe/NGr, and NGr is 68, 31, 35, and 95 m^2 g^{-1}, respectively, showing higher surface area for the sheet-like materials (NGr and ZnNiGr) which is apparent (Figure S2c). Noticeably, owing to the microporosity generated into the catalyst system as visible from Figure S2b, 13% increment in surface area is encountered after selenization. The probable reason for this microporosity is the high-temperature reductive annealing process resulting in the evaporation of amorphous impurities of KOH treatment, as well as oxygen removal from hydroxide layers creating micropores.

The defect density and the extent of graphitization of all the NGr-based controlled samples were studied through Raman spectral analysis. In the Raman spectrum, the two vibrational bands (the D band and G band) represent the disorder and
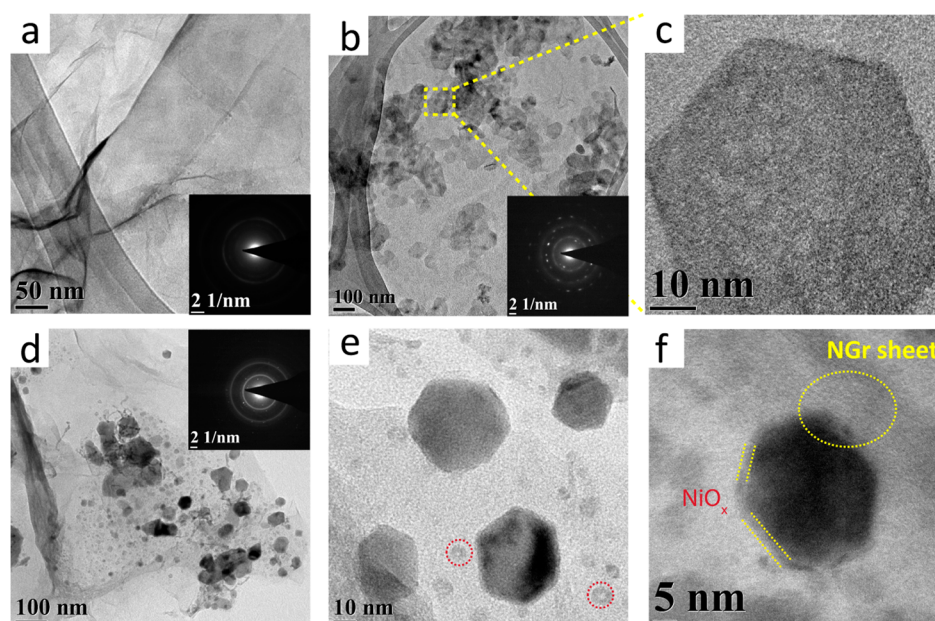
Figure 3. (a) TEM image of ZnNiNGr showing thin sheet-like structure over NGr. Panels b and c depict the TEM images of β-Ni(OH)$_2$/NGr at lower and higher magnifications, respectively, showing the hexagonal porous nanostructures embedded in the NGr matrix. Panels d−f show the TEM images of p-NiSe/NGr at different magnifications, and in image f, the yellow dotted lines represent the probable layer of NiO$_x$ over the hexagonal nickel selenide structure whereas the yellow dotted circle depicting the trapping of selenide nanostructures in the NGr sheets. Insets in the TEM images of all the three samples show their corresponding SAED patterns.

extent of graphitization of the carbonaceous material, respectively.[31] The I_D/I_G ratio for NGr is smaller (1.24) than that for ZnNiNGr (1.275), revealing the formation of the hybrid material resulting in increased disorder (Figures 1f and S2d). This ratio is increased further when Raman analysis was continued for β-Ni(OH)$_2$/NGr (1.32) and p-NiSe/NGr (1.325), confirming the increment in the defect density with the KOH treatment as well as with the thermal selenization process (Figures 1f and S2d). The 495 cm^{-1} peak of ZnNiNGr corresponds to the lattice mode of α-Ni(OH)$_2$[32] whereas the 542 cm^{-1} peak of β-Ni(OH)$_2$/NGr corresponds to the vibration of the Ni−O stretching mode of β-Ni(OH)$_2$,[23] respectively (Figure S2d). After selenization, two new Raman bands appeared at 207 and 241 cm^{-1} that can be ascribed to the stretching modes of Se−Se pairs (A$_g$ and T$_g$).[12] Another small peak visible at 511 cm^{-1} indicates the surface defects present on the NiSe (Figure 1f).[30]

The morphology of the as-synthesized samples was first examined using scanning electron microscopy (SEM). Figure 2A represents the SEM image of ZnNiNGr revealing the uniform distribution of thin patches of LDH anchored over the NGr sheets with no noticeable LDH agglomeration. These LDH patches can be distinguished from the NGr matrix by comparing the SEM image of ZnNiNGr with that of NGr (Figure S3A). Inset of Figure 2A, that is, A(1), depicts the SEM image selected for elemental mapping and the inset figures A(2), and A(3) show the elemental mapping for nickel and zinc, respectively, indicating the uniform distribution of Ni and Zn throughout the catalyst. The SEM image of β-Ni(OH)$_2$/NGr indicates the conversion of the thin LDH patches into somewhat smaller and agglomerated β-Ni(OH)$_2$ patches over the NGr due to hydrothermal KOH treatment (Figure S3B). The distribution of β-Ni(OH)$_2$ over the NGr appears uniform as evidenced by the elemental mapping for nickel and zinc with a minimum

amount of Zn remaining in the system (inset of Figure S3B(2), and B(3)).

The SEM image of p-NiSe/NGr exhibits the presence of ill-defined hexagonal nanoplates embedded in the NGr matrix with favorable dispersion characteristics (Figure 2B). Inset of the Figure 2B (B(2) and B(3)) represents the elemental mapping images for nickel and selenium revealing homogeneous and overlapping distributions of both the elements over NGr, suggesting selenide formation. To confirm the material composition, SEM energy-dispersive X-ray spectroscopy (EDS) of the samples mentioned above was performed. The EDS spectrum of ZnNiNGr depicts a molar ratio of 3:1 for Ni:Zn, equivalent to the ratio of the starting precursors (Figure S4). The EDS spectrum of β-Ni(OH)$_2$/NGr affirms the selective etching of Zn from the system with a negligible amount of Zn remaining in the system (Figure S5). The EDS pattern of p-NiSe/NGr gives a Se:Ni ratio of 1.75 indicating the presence of the Ni$_{1-x}$Se selenide phase containing selenium-rich nickel selenide component (Figure S6).

To get nanostructural insight of the as-synthesized materials, detailed characterization was performed using transmission electron microscopy (TEM) (Figure 3). Figure 3a shows the TEM image of ZnNiNGr having thin, sheet-like structure with negligible agglomeration over NGr and its amorphous nature is visible from the corresponding selected area electron diffraction (SAED) pattern having diffused diffraction rings (inset of Figure 3a). After KOH treatment, these thin LDH sheets took on the characteristic hexagonal structure of β-Ni(OH)$_2$ having porosity that results from the Zn etching and removal of the intercalated anions (β-Ni(OH)$_2$/NGr) (Figure 3b and 3c).[16,19] These porous β-Ni(OH)$_2$ structures have a size range of 50−60 nm and are found to be anchored as well as wrapped in between the NGr sheets. The inset of Figure 3b is the corresponding SAED pattern that shows the polycrystallinity of the material. Moreover, due to the porous as well as thin, plate-like nature,
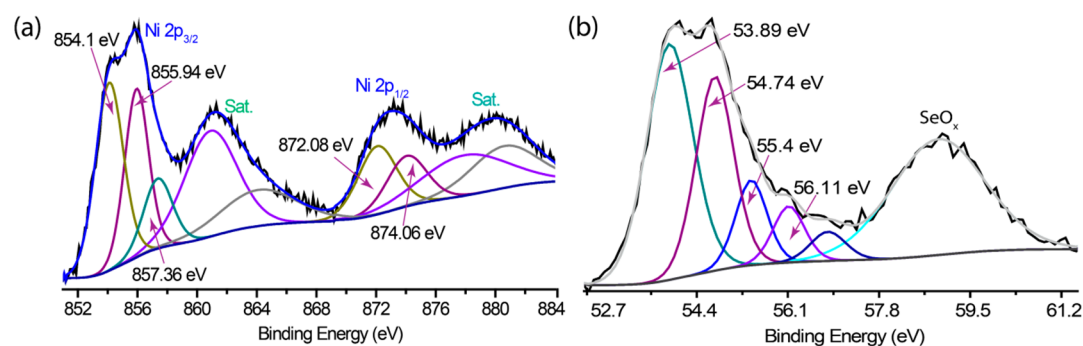
Figure 4. Deconvoluted XPS spectrum of p-NiSe/NGr: (a) Ni 2p region and (b) Se 3d region.

β-Ni(OH)$_2$ shows unclear lattice fringes with a d-spacing value of 0.23 nm corresponding to the (011) plane of β-Ni(OH)$_2$ (Figure S7a and S7b).[26] Furthermore, owing to the 20−25% selenide loading in p-NiSe/NGr, its distribution over NGr is not considered highly homogeneous; however, the hexagonal plates were found to be discrete, affirming the open and accessible structure of the thin and hexagonal NiSe nanoplates (Figure 3d and 3e). Some of these NiSe nanoplates are found to be trapped in between the NGr sheets making the d-spacing analysis difficult as visible in Figure 3f with a yellow dotted circle. Nevertheless, the high-magnification TEM image of a hexagonal nanosheet shows the lattice fringes corresponding to (001) plane of monoclinic Ni$_{1−x}$Se with a d-spacing of 0.53 nm (Figure S7c and S7d) as supported by the XRD results.[17]

Any clear indication of the NiO$_x$ or elemental selenium could not be found; however, the ill-defined hollow nanostructures (marked with maroon dotted circles), embedded into the NGr matrix, possibly could be their indications (Figure 3e). The appearance of a low-contrast outline around the hexagonal structures (Figure 3f) is found to be an indication of the NiO$_x$ moieties which is confirmed by applying FFT (Figure S8).[22]

Thus, a unique, active metal-based porous nanomaterial has been prepared using a less expensive metal like Zn, and KOH treatment played a significant role toward the successful selenization with hexagonal nickel selenide structure rather than using ZnNiNGr directly or using α-Ni(OH)$_2$/NGr in place of LDH. Since both ZnNiNGr as well as α-Ni(OH)$_2$/NGr are not found to be the suitable precursor material for successful selenization, as clear from their TEM images, that is, Figures S9 and S10, respectively. Hence, the two-step process outlined above generates open and porous nanostructures rich in edge sites, which may act as active sites used for electrocatalysis.

We further used X-ray photoelectron spectroscopy to gain an in-depth understanding of the valence and chemical states of the different elements present in p-NiSe/NGr. The XPS spectra of Ni 2p and Se 3d region are given in Figure 4, while that of C 1s and N 1s are given in Figure S11. The C 1s spectrum of p-NiSe/NGr indicates the presence of the C=C bonding and carbon−nitrogen bonding interactions, confirming the doping of nitrogen in the few-layered graphene matrix (Figure S11a).[31,33] Moreover, its N 1s spectrum reveals the presence of different types of nitrogen bonding into the graphene matrix, that is, pyridinic, pyrrolic, and graphitic nitrogens along with some pyridinic nitrogen oxides[31,34,35] (Figure S11b). These three types of nitrogen are present in the graphene matrix in different ratios, and all have remarkable catalytic activity toward different electrochemical reactions.[36,37]

The Ni 2p spectrum shows a complex spectral feature with spin−orbit doublets, that is, Ni 2p$_{3/2}$ and Ni 2p$_{1/2}$, along with

their corresponding satellites (Figure 4a). The deconvoluted Ni 2p spectrum reveals the presence of three different chemical environments for nickel. The deconvoluted doublet peaks located at 854.1 and 872.08 eV, along with their satellite peaks at 860.89 and 877.95 eV, correspond to Ni 2p$_{3/2}$ and Ni 2p$_{1/2}$ spin−orbit levels of the nickel oxide,[22,38,39] perhaps originating from the heat treatment of nickel hydroxide that was inaccessible during selenization.

Other deconvoluted doublet peaks located at 855.94 eV (Ni 2p$_{3/2}$) and 874.06 eV (Ni 2p$_{1/2}$), having their satellite peaks at 864.11 and 880.60 eV, respectively, indicate the presence of Ni^{2+} from the nickel selenide.[17,23,38] Apart from these peaks, an additional peak feature at 857.52 eV appears as a small shoulder, presumably due to the surface oxidation of the nickel selenide system.[22] The deconvoluted XPS spectrum of Se 3d also reveals the presence of three chemical environments for selenium (Figure 4b). The Se 3d deconvoluted doublet peaks positioned at 53.89 and 54.74 eV correspond to the Se 3d$_{5/2}$ and Se 3d$_{3/2}$ spin−orbit states of the nickel selenide.[12,17,23,38] The peaks at higher binding energies (55.4 and 56.11 eV) could be attributed to the Se 3d$_{5/2}$ and Se 3d$_{3/2}$ states of elemental selenium suggesting the presence of some elemental selenium on the surface, probably due to the deposition of small amounts of metalloid selenium within the carbon matrix during the selenization process.[12] The broad higher-binding-energy Se 3d peak at 58.90 eV is likely to be related to the selenium oxide, and this inference is consistent with the previous findings that the surface of metal selenides is prone to oxidation by air.[12,17,38]

In this way, our efforts at material characterization through XRD, Raman, TEM, and XPS analyses confirmed the successful selenization of nickel hydroxide along with the formation of trace amounts of amorphous NiO$_x$ and elemental Se. On the basis of these findings, it is expected that the catalyst system with nickel deficient selenide phase (monoclinic, Ni$_{1−x}$Se) having embedded NiO$_x$ and elemental selenium, developed in this study, could be a promising electrocatalyst for improving the overall performance of water electrolysis.

2.2. Electrocatalytic Performance toward OER. The oxygen evolution reaction (OER), following sequential proton-coupled four-electron transfer mechanism, is a thermodynamically, as well as kinetically sluggish reaction that forms the perpetual bottleneck for complete water electrolysis.[14] Interestingly, emerging studies uncover that the transition metal chalcogenides (TMCs) can be easily oxidized in strong alkaline media via an in situ electrochemical oxidation process, producing nanoporous transition metal oxides (TMOs), which may result into improved water oxidation activity because of their increased active surface area and more exposed electroactive sites.[40−42] These findings motivated us to study the OER

performance of our catalyst along with revealing the structural transformation of the selenide system during the OER analysis.

Figure 5a represents the LSV polarization curves for OER at 10 mV s^{-1} in 1 M KOH under N$_2$ atmosphere. The p-NiSe/NGr
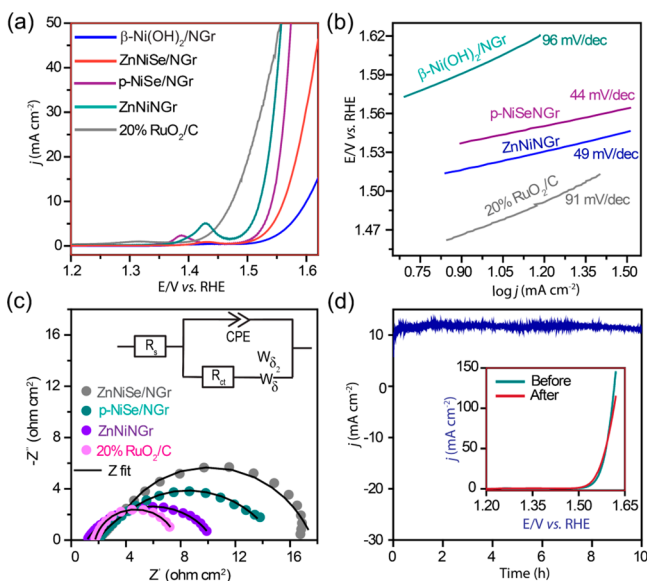

Figure 5. (a) Comparative OER polarization curves recorded at 10 mV s^{-1} in N$_2$ saturated 1 M KOH. (b) Tafel slopes corresponding to the conditions depicted in panel a. (c) Comparative fitted Faradaic impedance spectra in Nyquist form (inset shows the equivalent circuit used) and (d) chronoamperometric stability response of p-NiSe/NGr for 10 h in 1 M KOH (inset shows the LSV curves recorded before and after the chronoamperometric study).

shows good OER performance with an overpotential of only 311 mV from the thermodynamic water oxidation potential of 1.23 V (vs RHE) to drag a 10 mA cm^{-2} current density (equivalent to the 10% solar to fuel conversion efficiency under one sun illumination, η_{10}) whereas the η_{10} value obtained for ZnNiSe/NGr and β-Ni(OH)$_2$/NGr are 330 mV and 370 mV, respectively.

Although the η_{10} obtained for p-NiSe/NGr (311 mV) is little higher than that of ZnNiNGr (290 mV) and 20% RuO$_2$/C (240 mV), the Tafel analysis (eq S1) revealed the comparable reaction kinetics of p-NiSe/NGr (44 mV decade^{-1}) with ZnNiNGr (49 mV decade^{-1}) which is due to better electronic properties of selenides than hydroxides. The kinetics of 20% RuO$_2$/C (91 mV decade^{-1}) is found to be lower than the above two described samples as given in Figure 5b.

The faster Faradaic process on the catalysts is also supported by the low R_{ct} value obtained during the Faradaic impedance analysis performed at 1.55 V versus RHE (Figure 5c). The variation tendency of the R_{ct} is consistent with the overpotential obtained, which is merely 5.44 ohm cm^2 for 20% RuO$_2$/C followed by the 8.67, 11.68, and 14.75 ohm cm^2 R_{ct} values for ZnNiNGr, p-NiSeNGr, and ZnNiSe/NGr, respectively. Along with superior activity, p-NiSe/NGr catalyst also exhibited remarkable long-term stability during the continuous 10 h chronoamperometric analysis, maintaining a current density above 10 mA cm^{-2} throughout the test at an applied potential of 1.55 V vs RHE (Figure 5d). The inset of Figure 5d exhibits the LSV curves before and after the chronoamperometry test displaying a current density decay of only 30 mA cm^{-2} along with a slight improvement in the overpotential (η_{10}) by 10 mV.

This anomalous behavior probably originated from the coverage of the catalyst with active amorphous oxyhydroxide phase resulting in a small decrement in electronic conductivity but maintaining the η_{10} value. As described elsewhere, the selenides act as active substrates to facilitate and stabilize the formation of the OER-active NiOOH phase.[13] A chronoamperometric stability study was also performed for 20% RuO$_2$/C that presented a continuous activity decrement and showed only 50% activity retention after a 9 h experiment at 1.51 V vs RHE (Figure S12a). The Faradaic efficiency calculation for OER was performed using the rotating ring-disk electrode (RRDE) technique by applying sequential current steps from 1 to 10 mA cm^{-2} to the catalyst-coated GC disk in N$_2$-saturated 1 M KOH at a rotation rate of 1600 rpm (eq S2 and S3). The ring electrode was kept at a constant potential of 0.2 V vs RHE where the O$_2$ generated on the disk electrode got reduced. Figure S12b indicates a maximum Faradaic efficiency of 98.5% at 1 mA cm^{-2}, substantiating the ability of p-NiSe/NGr as an efficient OER catalyst.

The in situ electrochemical activation process on our catalyst system is studied by investigating the changes induced in the catalyst after the activity measurements. The formation of NiOOH species over selenide with increasing the CV cycles in the oxidative potential region is clearly visible from Figure S12c, which is supported by the findings of Chen et al.[40] The formation of NiOOH/α-Ni(OH)$_2$ species over selenide is confirmed through XRD, where along with the selenide diffraction planes, (00n) planes of NiOOH/α-Ni(OH)$_2$ can be differentiated (Figure S13a). Moreover, the formation of nanoporous metal oxides over selenides is also confirmed through TEM analysis of the post-OER sample as given in Figure S13b and S13c. During the in situ electrochemical oxidation process, it is claimed that the displacement of the chalcogens with the hydroxide ions results in significant crystal detachment, orientation, atomic diffusion, and recrystallization,[40] which is clearly visible from the obtained TEM images with numerous mesoporous nanosheet-like morphology with complete disappearance of the hexagonal moieties.

2.3. Electrocatalytic Performance for HER. According to few recent studies, similar to the active sites of hydrogenases, the cation sites of pyrite-type transition-metal dichalcogenides, that is, NiSe$_2$, have been suggested to be one of the most active centers toward HER. Moreover, Wang et al.[12] studied the role of elemental selenium toward HER and through controlled experiments, they revealed that the excess of selenium in the NiSe$_2$ nanosheet surface acts as a promoter, facilitating the charge transfer on the surface to achieve efficient conversion of H$^+$ into H$_2$ bubbles. In addition to this, Liang et al.[43] investigated the mechanism of the HER on nickel by surface interrogation scanning electrochemical microscopy. On the basis of the combined analysis of the Tafel slope and surface hydrogen coverage, they suggested the rate-determining step to be the adsorption of hydrogen (Volmer step), which is facilitated in the presence of the low-valence-state oxide of Ni compared to the metallic Ni. Based on these studies on selenides, as a proof of concept, we studied the HER performance of our catalyst system with monoclinic Ni$_{1-x}$Se phase along with traces of NiO$_x$ and elemental selenium.

Compared to acidic HER activity, the cathodic half-cell reaction of the electrolyzer (HER) is found to be more sluggish in alkaline media involving the reduction of hydroxide ions or neutral water molecules.[44] Hence, to compare the catalytic activity at the two pH extremes, we studied the HER

performance of our catalyst in both acidic and alkaline electrolytes via linear sweep voltammetry (LSV) recorded at a sweep rate of 10 mV s^{-1} on the reversible hydrogen electrode (RHE) scale with 1600 rpm under N$_2$ atmosphere employing the rotating disk electrode (RDE) technique. Figure 6a
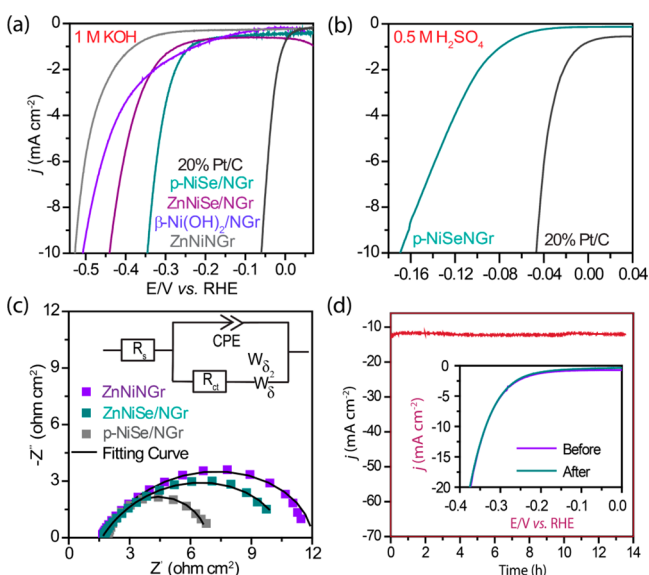

Figure 6. (a) Comparative HER polarization curves recorded at 10 mV s^{-1} in 1 M KOH. (b) Comparative HER polarization curves recorded at 10 mV s^{-1} in 0.5 M H$_2$SO$_4$. (c) Comparative fitted Faradaic impedance spectra in Nyquist form (inset shows the equivalent circuit used) and (d) chronoamperometric stability response of p-NiSe/NGr for 13 h in 1 M KOH (inset shows the LSV curves before and after chronoamperometric study) in N$_2$ saturated electrolytes at 1600 rpm.

illustrates the comparative HER polarization curves in 1 M KOH where our main catalyst, that is, p-NiSe/NGr, shows 285 mV negative potential shift to derive a current density of 10 mA cm^{-2} from the benchmark 20% Pt/C. Moreover, in 0.5 M H$_2$SO$_4$, p-NiSe/NGr showed only 122 mV negative potential shift from 20% Pt/C at 10 mA cm^{-2} (Figure 6b), thus exhibiting comparatively better HER performance in the acidic medium compared to alkaline medium. For comparison, the HER performance of the other controlled samples was also studied in alkaline medium (Figure 6a). Compared to ZnNiNGr and β-Ni(OH)$_2$/NGr, ZnNiSe/NGr shows better HER performance, indicating that the mere presence of selenium in the system without any specific selenide phase has a positive impact on the HER performance (Figure 6a). However, ZnNiSe/NGr shows an η$_{10}$ value 100 mV higher than that of p-NiSe/NGr in alkaline medium, indicating that a specific nickel selenide phase along with the open-edge structure plays a crucial role in improving the HER kinetics. The catalysts ZnNiSe/NGr, β-Ni(OH)$_2$/NGr and ZnNiNGr exhibit overpotentials of 440, 507, and 527 mV, respectively, to reach 10 mA cm^{-2} current density in the alkaline medium (Figure 6a).

After the activity measurement, HER kinetics of the catalysts was studied through Tafel analysis as represented by eq S1. Comparative Tafel plots of p-NiSe/NGr and 20% Pt/C at two extreme pH conditions are presented in Figure S14a. In alkaline medium, p-NiSe/NGr shows a Tafel slope value of 125 mV decade^{-1} which is slightly higher than the value of 90 mV decade^{-1} for 20% Pt/C; however, this value is quite lower than the previous reports on the NiSe-based HER catalysts.[23,24]

These Tafel slope values for both the aforementioned catalysts reveals that a Volmer–Heyrovsky pathway is probably controling the reaction.[45–47] In acidic medium, Pt/C shows a small Tafel slope value of 33 mV decade^{-1} indicating a facile reaction kinetics, whereas p-NiSe/NGr is found to follow the Volmer-Heyrovsky mechanism[41] with a slope of 129 mV decade^{-1}. In alkaline medium, the comparative reaction kinetics of all the controlled samples were studied through Faradaic impedance measurement and a smaller charge transfer resistance (R_{ct}) of 4.89 ohm cm^2 for p-NiSe/NGr than those of ZnNiSe/NGr (8.0 ohm cm^2) and ZnNiNGr (9.78 ohm cm^2), indicating improved electronic conductivity because of specific selenization process (Figure 6c).

The reliability of the catalyst was demonstrated through 13 h-long continuous chronoamperometric analysis at 0.38 V vs RHE in 1 M KOH. The system maintained a current density of 12 mA cm^{-2} throughout the experiment with a negligible decrement in the current density (Figure 6d). Inset of Figure 5d represents the LSV polarization curve at 10 mV s^{-1} scan rate before and after chronoamperometry that reveals the outstanding stability of our catalyst with negligible change in the η$_{10}$ and current density values. Results of the chronoamperometric stability test for 20% Pt/C at an applied potential of 0.060 V vs RHE is represented in Figure S14b displaying continual activity decay with only 50% activity retention after 10 h of the test.

In this way, our catalyst shows not only good activity but also high levels of stability which are, in fact, far better than the benchmark value for Pt/C. Hence, apart from showing good HER activity in acidic medium, p-NiSe/NGr is also a robust, nonprecious transition metal chalcogenide-based HER catalyst in alkaline media where most of the nonprecious catalysts do not perform satisfactorily.[23,24] Hence, the p-NiSe/NGr, bearing porous, thin hexagonal open structure not only provides accessible active centers but also improves the diffusion of ionic species and thus allows the efficient utilization of active sites with consistent performance during the prolonged electrochemical analysis.

The faradaic efficiency of the prepared catalyst toward hydrogen generation is calculated by comparing the theoretical amount of H$_2$ produced with the experimental value quantified using gas chromatography.[48] The product gas evolved was quantified by sampling out the product from an airtight electrochemical cell after applying a current density of 5 mA cm^{-2} for 15 min whereas the theoretical value was calculated from the total charge passed, using Faraday's law (eq S4). As illustrated in Figure S14c, the measured quantity of gas matches well with the theoretical value showing 96.36% Faradaic efficiency (eq S5).

To study the role of NiO$_x$ moieties toward the HER, post-mortem analysis of the catalyst after the HER stability test is performed through XRD and TEM analysis. Figure S15a represents the XRD of post-HER sample depicting increased amorphousness of the sample after the electrochemical stability test which is obvious due to the involvement of the catalyst in the electrolysis. Noticeably, in the post HER sample, an unpredictable diffraction peak below 10° (003), peak asymmetry in 33° (corresponding to (101) α-Ni(OH)$_2$ peak) along with prominent broad peak at 57° (110) are encountered which are due to the formation of α-Ni(OH)$_2$ from NiO$_x$ as it is ubiquitous to generate in alkaline medium. Interestingly, the emergence of few more less-intense diffractions planes of monoclinic phase can be seen at 26°, 29.2°, 35.8°, and 39.4° in this sample. The probable reason for the emergence of these
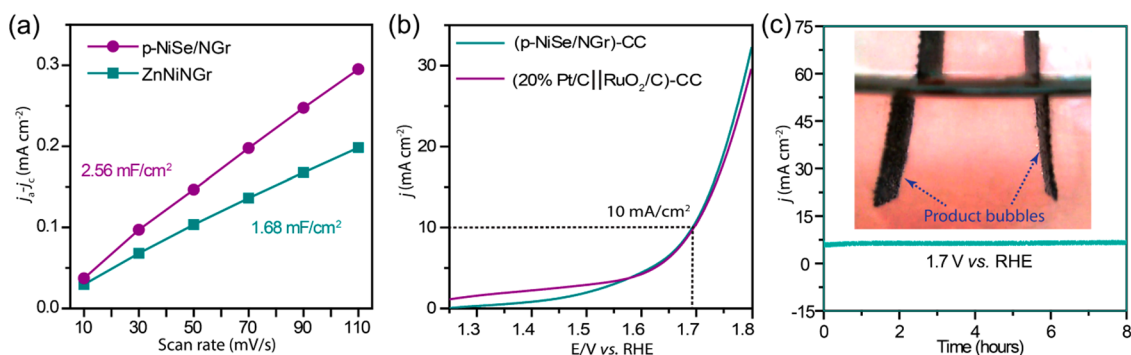
Figure 7. (a) Comparative plots of the scan rate dependent capacitive current density differences ($ja-jc$) at 0.97 V vs RHE for the electrochemically active surface area determination of the catalysts in 1 M KOH, (b) comparative polarization curves of the whole-cell water electrolysis in 1 M KOH at a scan rate of 10 mV/s, and (c) chronoamperometric stability test for the whole-cell water electrolyzer in 1 M KOH for 8 h (inset shows the picture captured during the electrolysis showing the product bubbles attached to the catalyst coated carbon cloth).

peaks could be due to the in situ electrochemical activation of the catalyst leading to the exposure of more and more active centers which were protected through the NiO_x shell in the pristine sample. However, the presence of elemental selenium still could not be detected by XRD, thereby indicating that the dominant phase is always monoclinic NiSe as the core, which during the electrochemical analysis gets covered with a thin layer of hydroxides/oxyhydroxides as shell which is visible from the TEM images (Figure S15b and S15c). In this way, another significant reason for such remarkable stability of our catalyst system compared to commercial catalyst is due to a structural synergy between selenide and NiO_x. The amorphous NiO_x coverage over NiSe, in addition to facilitating the rate-determining Volmer step, protects the active centers from harsh alkaline environment along with providing required structural flexibility to hasten the electrochemical reaction.

To study the effect of elemental selenium over HER performance, the as-synthesized p-NiSe/NGr was annealed at 250 and 350 °C under the flow of argon, which is above the melting point of Se and below the reaction temperature, to effectively control the elemental Se content into the catalyst system.[12] The phase change with increased annealing temperature is studied through XRD (Figure S16a). Comparative HER polarization curves are given in Figure S16b illustrating a slight decrement in the HER activity for the 250 °C annealed sample. However, when the annealing temperature is increased to 350 °C, there is a considerable decrement in the HER activity which can mostly be attributed to the loss of excessive elemental Se from the surface as well as due to the transition of selenide phase from monoclinic to cubic phase (Figure S16a). In this way, the intrinsic properties of the HER active sites are shown to be improved when elemental Se modifies the selenide surface, and the interface between them is thus proposed to be the efficient active site for HER in this system. Interestingly, annealing temperature did not affect the OER performance much, which infers that OER activity is independent of the Se content; however, the phase transition affected the OER performance slightly (Figure S16c). The change in selenium content after 350 °C annealing is given through the SEM-EDS analysis in Figure S17 revealing the decrement in the Se: Ni ratio from 1.75 to 1.61.

To understand the improved catalytic performance of p-NiSe/NGr in both the water electrolyzer half-cells, the comparative electrochemical active surface area (ECSA) of the solid−liquid interface was estimated by determining the double layer capacitances (C_{dl}) of ZnNiNGr and p-NiSe/NGr (eqs S6 and S7).[23] The C_{dl} was measured by using scan rate dependent

CV in the nonfaradaic potential region of 0.92−1.02 V (vs RHE) under static condition in an alkaline medium (Figure S18a and S18b). As shown in Figure 7a, the specific capacitance (C_{dl}) value is increased after selenization (2.56 mF cm^{-2}) to a value that is nearly 1.5 times higher than that of ZnNiNGr (1.68 mF cm^{-2}). Since the C_{dl} value is directly related to ECSA, the higher the C_{dl} value, the higher will be the ECSA[17] and the ECSA values obtained are 12.56 cm^2 and 8.25 cm^2 for p-NiSe/NGr and ZnNiNGr respectively, illustrating that the comparatively higher electronic conductivity of selenides in comparison to that of hydroxides, as well as the edge site-rich porous hexagonal shape of p-NiSe/NGr resulted in the increased ECSA.

The turnover frequency (TOF-rate of product molecules evolved per surface metal atom per second) calculation for each active site is also a good figure of merit for comparing the intrinsic activity of different catalytic materials.[49] The TOF determined here is the lower limit catalytic rate for the catalyst, based on the number of active sites taking part in the catalysis, although the bulk of the material is electroactive.[50,51] TOF can be determined by calculating the total number of the redox-active sites from the cyclic voltammetry data using eq S8 (Figure S19a).[49,50] The surface coverage of the redox active Ni centers on the electrode is 8.733 nmol cm^{-2} as obtained from the slope of the scan rate dependent peak current of Ni$^{(II)}$/Ni$^{(III)}$ oxidation wave using eq S9 (Figure S19b).[51] This is an upper limit to the real number of active sites; since electrocatalysis is heterogeneous occurring at the electrode−electrolyte interface.[49] With this value of the active surface coverage for p-NiSe/NGr, the TOF value for H_2 and O_2 generation based on ECSA was found to be 0.24 s^{-1} and 0.132 s^{-1} at η = 300 mV (corresponding to −5.1 mA cm^{-2} (HER) and 5.6 mA cm^{-2} (OER)), respectively. Hence, the amount of H_2 produced per second is almost double than that of O_2 molecule which is due to the similar activity of p-NiSe/NGr toward both the half-cell reaction and it is in support to the product ratio of water decomposition.

2.4. Alkaline Water Electrolysis. The ability of our newly developed bifunctional catalyst to augment overall water splitting was proved by fabricating and testing an alkaline water electrolyzer in 1 M KOH. The cathode and anode of the electrolyzer were prepared by coating the p-NiSe/NGr on carbon cloth (1 × 4 cm^2) of 1 cm^2 area with a mass loading of 1 mg cm^{-2} and is designated as (p-NiSe/NGr)-CC. For comparison, a controlled alkaline electrolyzer using the benchmark 20% Pt/C (as a cathode) and 20% RuO$_2$/C (as an anode) was also fabricated with the same loading of 1 mg cm^{-2} over CC and designated as (Pt/C)-CC||(RuO$_2$/C)-CC.

Figure 7b represents the comparative LSV polarization curves for complete water electrolysis at a scan rate of 10 mV s^{-1} in 1 M KOH. The LSV curves for (p-NiSe/NGr)-CC and (Pt/C)-CC∥(RuO$_2$/C)-CC show that voltage of 1.60 and 1.62 V, generating 5 mA cm^{-2} current density, were sufficient for complete water electrolysis using our catalyst system and the benchmark system, respectively. Moreover, (p-NiSe/NGr)-CC and (Pt/C)-CC∥(RuO$_2$/C)-CC achieved the current density of 10 mA cm^{-2} at a voltage of 1.69 and 1.70 V, respectively.

Noticeably, the whole-cell performance of the commercial catalyst-based electrolyzer ((Pt/C)-CC∥(RuO$_2$/C)-CC) is found to be lower than their respective half-cell performance, that is, the overpotential obtained for full water electrolysis is found to be higher than the overpotential sum of 20% Pt/C toward HER and 20% RuO$_2$/C toward OER (Figure S19c). Whereas, in the case of (p-NiSe/NGr)-CC, the overall water electrolysis performance is increased to a reasonable extent from their respective half-cell reaction performances which are collectively presented in Figure S19c. It was difficult to ascertain the exact reason for such an interesting finding; however, a probable reason for this anomaly can be the formation of electrocatalytically active species through the counter redox reactions occurring at the Ni centers of p-NiSe/NGr during the two-electrode reactions which mutually facilitates each other's performance. In our catalyst architecture, the H$_2$ production involves water reduction, followed by the oxidation of nickel selenide surface to OER-active γ-NiOOH phase, facilitating the counter water oxidation to evolve O$_2$, which is further followed by the reduction of γ-NiOOH to lower oxidation state Ni moieties generally Ni(OH)$_2$ promoting the hydrogen evolution reaction over selenide active centers.[52−54] In sharp contrast, the (Pt/C)-CC∥(RuO$_2$/C)-CC electrolyzer system is a hybrid system where the two electrode catalysts show poor performance toward their counter electrode reaction, and hence have no such synergy that can improve the overall electrolyzer performance.

The stability test for (p-NiSe/NGr)-CC-based electrolyzer was performed through chronoamperometry for 8 h at 1.7 V showing that a current density above 5 mA cm^{-2} was maintained throughout the analysis (Figure 6c). Although our catalyst is not among the best ones for overall water splitting, its performance is comparable and even better than that of many selenides- and other transition metal-based bifunctional catalysts as mentioned in the Table S3.[16,23,55,56] After the electrolyzer stability study, the XRD pattern of p-NiSe/NGr confirmed the presence of nickel in various chemical environments such as the OER active NiOOH phase that is generated during the water reduction reaction and the exposure of metallic Se, indispensable in facilitating the charge transfer during HER (Figure S20a).[12] Interestingly, the post stability TEM images show agglomeration, distortion as well as connection between the nearby hexagonal selenide nanoplates (Figure S20b and S20c). The TEM images also give clear evidence of the formation of amorphous layers over the selenides, which are probably α-Ni(OH)$_2$/NiOOH moieties (Figure S20d and S20e).

3. CONCLUSION

In this study, we synthesized nickel selenide-nitrogen-doped graphene nanocomposite using (Zn)Ni-LDH/NGr as a precursor resulting in the formation of porous hexagonal nickel selenide nanoplates. These unique structural features that contain crystalline monoclinic nickel selenide phase along with amorphous NiO$_x$ and metallic selenium embedded in the NGr matrix endows our catalyst system with short charge transport distances, abundant exposed active centers, improved mass transfer properties and high structural stability against agglomeration, resulting in good activity as well as stability toward whole-cell water electrolysis in alkaline medium. The results indicate that nickel selenide designed with an open and porous structure holds significant promise for the rational design of nonprecious bifunctional electrocatalysts for overall water splitting.

■ ASSOCIATED CONTENT

Ⓢ Supporting Information

The Supporting Information is available free of charge on the ACS Publications website at DOI: 10.1021/acsaem.8b01081.

Materials and synthesis procedures, structural characterization techniques, additional material characterizations, electrochemical procedures employed, calculation methods, additional electrochemical studies, and comparison tables (PDF)

Practical demonstration of H$_2$ and O$_2$ evolution during the whole-cell water electrolysis analysis of (p-NiSe/NGr)-CC-based electrolyzer through LSV in the potential window of 1.2−1.8 V (AVI)

■ AUTHOR INFORMATION

Corresponding Author

*E-mail: k.sreekumar@ncl.res.in. Fax: +91 20-25902636. Tel: +91 20-25902566.

ORCID Ⓘ

R. Nandini Devi: 0000-0002-6219-8089
Sreekumar Kurungot: 0000-0001-5446-7923

Author Contributions

The manuscript was written through contributions of all authors. All authors have given approval to the final version of the manuscript.

Notes

The authors declare no competing financial interest.

■ ACKNOWLEDGMENTS

■ REFERENCES

(1) Koper, M. T. M. A Basic Solution. *Nat. Chem.* **2013**, 5, 255−256.

(2) Obama, B. The Irreversible Momentum of Clean Energy. *Science* **2017**, 355, 126−129.

(3) Seh, Z. W.; Kibsgaard, J.; Dickens, C. F.; Chorkendorff, I.; Nørskov, J. K.; Jaramillo, T. F. Combining Theory and Experiment in Electrocatalysis: Insights into Materials Design. *Science* **2017**, 355, No. eaad4998, DOI: 10.1126/science.aad4998.

(4) Dhavale, V. M.; Singh, S. K.; Nadeema, A.; Gaikwad, S. S.; Kurungot, S. Nanocrystalline Fe-Fe$_2$O$_3$ Particle-Deposited N-Doped Graphene as an Activity-Modulated Pt-Free Electrocatalyst for Oxygen Reduction Reaction. *Nanoscale* **2015**, 7, 20117−20125.

(5) Unni, S. M.; Bhange, S. N.; Anothumakkool, B.; Kurungot, S. Redox-Mediated Synthesis of Functionalised Graphene: A Strategy

towards 2D Multifunctional Electrocatalysts for Energy Conversion Applications. *ChemPlusChem* **2013**, *78*, 1296−1303.

(6) Ng, J. W. D.; Gorlin, Y.; Hatsukade, T.; Jaramillo, T. F. A Precious-Metal-Free Regenerative Fuel Cell for Storing Renewable Electricity. *Adv. Energy Mater.* **2013**, *3*, 1545−1550.

(7) Li, X.; Hao, X.; Abudula, A.; Guan, G. Nanostructured Catalysts for Electrochemical Water Splitting: Current State and Prospects. *J. Mater. Chem. A* **2016**, *4*, 11973−12000.

(8) Blakemore, J. D.; Crabtree, R. H.; Brudvig, G. W. Molecular Catalysts for Water Oxidation. *Chem. Rev.* **2015**, *115*, 12974−13005.

(9) Ng, J. W. D.; Hellstern, T. R.; Kibsgaard, J.; Hinckley, A. C.; Benck, J. D.; Jaramillo, T. F. Polymer Electrolyte Membrane Electrolyzers Utilizing Non-Precious Mo-Based Hydrogen Evolution Catalysts. *ChemSusChem* **2015**, *8*, 3512−3519.

(10) Cheng, N.; Stambula, S.; Wang, D.; Banis, M. N.; Liu, J.; Riese, A.; Xiao, B.; Li, R.; Sham, T.-K.; Liu, L.-M.; Botton, G. A.; Sun, X. Platinum Single-Atom and Cluster Catalysis of the Hydrogen Evolution Reaction. *Nat. Commun.* **2016**, *7*, 13638−13646.

(11) Swesi, A. T.; Masud, J.; Nath, M. Nickel Selenide as a High-Efficiency Catalyst for Oxygen Evolution Reaction. *Energy Environ. Sci.* **2016**, *9*, 1771−1782.

(12) Wang, F.; Li, Y.; Shifa, T. A.; Liu, K.; Wang, F.; Wang, Z.; Xu, P.; Wang, Q.; He, J. Selenium-Enriched Nickel Selenide Nanosheets as a Robust Electrocatalyst for Hydrogen Generation. *Angew. Chem., Int. Ed.* **2016**, *55*, 6919−6924.

(13) Li, X.; Han, G.-Q.; Liu, Y.-R.; Dong, B.; Hu, W.-H.; Shang, X.; Chai, Y.-M.; Liu, C.-G. NiSe@NiOOH Core−Shell Hyacinth-like Nanostructures on Nickel Foam Synthesized by in Situ Electrochemical Oxidation as an Efficient Electrocatalyst for the Oxygen Evolution Reaction. *ACS Appl. Mater. Interfaces* **2016**, *8*, 20057−20066.

(14) Suen, N.-T.; Hung, S.-F.; Quan, Q.; Zhang, N.; Xu, Y.-J.; Chen, H. M. Electrocatalysis for the Oxygen Evolution Reaction: Recent Development and Future Perspectives. *Chem. Soc. Rev.* **2017**, *46*, 337−365.

(15) Liu, D.; Lu, Q.; Luo, Y.; Sun, X.; Asiri, A. M. NiCo$_2$S$_4$ Nanowires Array as an Efficient Bifunctional Electrocatalyst for Full Water Splitting with Superior Activity. *Nanoscale* **2015**, *7*, 15122−15126.

(16) Liang, H.; Li, L.; Meng, F.; Dang, L.; Zhuo, J.; Forticaux, A.; Wang, Z.; Jin, S. Porous Two-Dimensional Nanosheets Converted from Layered Double Hydroxides and Their Applications in Electrocatalytic Water Splitting. *Chem. Mater.* **2015**, *27*, 5702−5711.

(17) Ming, F.; Liang, H.; Shi, H.; Xu, X.; Mei, G.; Wang, Z. MOF-Derived Co-Doped Nickel Selenide/C Electrocatalysts Supported on Ni Foam for Overall Water Splitting. *J. Mater. Chem. A* **2016**, *4*, 15148−15155.

(18) You, B.; Jiang, N.; Sheng, M.; Gul, S.; Yano, J.; Sun, Y. High-Performance Overall Water Splitting Electrocatalysts Derived from Cobalt-Based Metal−Organic Frameworks. *Chem. Mater.* **2015**, *27*, 7636−7642.

(19) Gao, M.; Sheng, W.; Zhuang, Z.; Fang, Q.; Gu, S.; Jiang, J.; Yan, Y. Efficient Water Oxidation Using Nanostructured α-Nickel-Hydroxide as an Electrocatalyst. *J. Am. Chem. Soc.* **2014**, *136*, 7077−7084.

(20) Ren, J.; Antonietti, M.; Fellinger, T.-P. Efficient Water Splitting Using a Simple Ni/N/C Paper Electrocatalyst. *Adv. Energy Mater.* **2015**, *5*, 1401660.

(21) Yang, Y.; Fei, H.; Ruan, G.; Xiang, C.; Tour, J. M. Efficient Electrocatalytic Oxygen Evolution on Amorphous Nickel-Cobalt Binary Oxide Nanoporous Layers. *ACS Nano* **2014**, *8*, 9518−9523.

(22) Li, H.; Chen, S.; Lin, H.; Xu, X.; Yang, H.; Song, L.; Wang, X. Nickel Diselenide Ultrathin Nanowires Decorated with Amorphous Nickel Oxide Nanoparticles for Enhanced Water Splitting Electrocatalysis. *Small* **2017**, *13*, 1701487.

(23) Li, X.; Zhang, L.; Huang, M.; Wang, S.; Li, X.; Zhu, H. Cobalt and Nickel Selenide Nanowalls Anchored on Graphene as Bifunctional Electrocatalysts for Overall Water Splitting. *J. Mater. Chem. A* **2016**, *4*, 14789−14795.

(24) Kwak, I. H.; Im, H. S.; Jang, D. M.; Kim, Y. W.; Park, K.; Lim, Y. R.; Cha, E. H.; Park, J. CoSe$_2$ and NiSe$_2$ Nanocrystals as Superior

Bifunctional Catalysts for Electrochemical and Photoelectrochemical Water Splitting. *ACS Appl. Mater. Interfaces* **2016**, *8*, 5327−5334.

(25) Nadeema, A.; Dhavale, V. M.; Kurungot, S. NiZn Double Hydroxide Nanosheet-Anchored Nitrogen-Doped Graphene Enriched with Υ-NiOOH Phase as an Activity Modulated Water Oxidation Electrocatalyst. *Nanoscale* **2017**, *9*, 12590−12600.

(26) Hu, B.; Chen, S.-F.; Liu, S.-J.; Wu, Q.-S.; Yao, W.-T.; Yu, S.-H. Controllable Synthesis of Zinc-Substituted α- and β-Nickel Hydroxide Nanostructures and Their Collective Intrinsic Properties. *Chem. - Eur. J.* **2008**, *14*, 8928−8938.

(27) Wang, X.; Hu, J.; Liu, W.; Wang, G.; An, J.; Lian, J. Ni-Zn Binary System Hydroxide, Oxide and Sulfide Materials: Synthesis and High Supercapacitor Performance. *J. Mater. Chem. A* **2015**, *3*, 23333−23344.

(28) Hall, D. S.; Lockwood, D. J.; Bock, C.; MacDougall, B. R. Nickel Hydroxides and Related Materials: A Review of Their Structures, Synthesis and Properties. *Proc. R. Soc. London, Ser. A* **2015**, *471*, No. 20140792.

(29) Subbarao, U.; Marakatti, V. S.; Amshumali, M. K.; Loukya, B.; Singh, D. K.; Datta, R.; Peter, S. C. Size and Morphology Controlled NiSe Nanoparticles as Efficient Catalyst for the Reduction Reactions. *J. Solid State Chem.* **2016**, *244*, 84−92.

(30) Kukunuri, S.; Krishnan, M. R.; Sampath, S. The Effect of Structural Dimensionality on the Electrocatalytic Properties of the Nickel Selenide Phase. *Phys. Chem. Chem. Phys.* **2015**, *17*, 23448−23459.

(31) Zafar, Z.; Ni, Z. H.; Wu, X.; Shi, Z. X.; Nan, H. Y.; Bai, J.; Sun, L. T. Evolution of Raman Spectra in Nitrogen Doped Graphene. *Carbon* **2013**, *61*, 57−62.

(32) Hall, D. S.; Lockwood, D. J.; Poirier, S.; Bock, C.; MacDougall, B. R. Raman and Infrared Spectroscopy of α and β Phases of Thin Nickel Hydroxide Films Electrochemically Formed on Nickel. *J. Phys. Chem. A* **2012**, *116*, 6771−6784.

(33) Niedziałkowski, P.; Ossowski, T.; Zięba, P.; Cirocka, A.; Rochowski, P.; Pogorzelski, S. J.; Ryl, J.; Sobaszek, M.; Bogdanowicz, R. Poly-L-Lysine-Modified Boron-Doped Diamond Electrodes for the Amperometric Detection of Nucleic Acid Bases. *J. Electroanal. Chem.* **2015**, *756*, 84−93.

(34) Xing, Z.; Ju, Z.; Zhao, Y.; Wan, J.; Zhu, Y.; Qiang, Y.; Qian, Y. One-Pot Hydrothermal Synthesis of Nitrogen-Doped Graphene as High-Performance Anode Materials for Lithium Ion Batteries. *Sci. Rep.* **2016**, *6*, 26146.

(35) Wang, H.; Maiyalagan, T.; Wang, X. Review on Recent Progress in Nitrogen-Doped Graphene: Synthesis, Characterization, and Its Potential Applications. *ACS Catal.* **2012**, *2*, 781−794.

(36) Zhou, W.; Zhou, J.; Zhou, Y.; Lu, J.; Zhou, K.; Yang, L.; Tang, Z.; Li, L.; Chen, S. N-Doped Carbon-Wrapped Cobalt Nanoparticles on N-Doped Graphene Nanosheets for High-Efficiency Hydrogen Production. *Chem. Mater.* **2015**, *27*, 2026−2032.

(37) Zhao, Y.; Nakamura, R.; Kamiya, K.; Nakanishi, S.; Hashimoto, K. Nitrogen-Doped Carbon Nanomaterials as Non-Metal Electro-catalysts for Water Oxidation. *Nat. Commun.* **2013**, *4*, 2390.

(38) Xu, X.; Song, F.; Hu, X. A nickel Iron Diselenide-Derived Efficient Oxygen-Evolution Catalyst. *Nat. Commun.* **2016**, *7*, 12324.

(39) Liu, W.; Lu, C.; Wang, X.; Liang, K.; Tay, B. K. In situ Fabrication of Three-Dimensional, Ultrathin Graphite/Carbon Nanotube/NiO Composite as Binder-Free Electrode for High-Performance Energy Storage. *J. Mater. Chem. A* **2015**, *3*, 624−633.

(40) Chen, W.; Liu, Y.; Li, Y.; Sun, J.; Qiu, Y.; Liu, C.; Zhou, G.; Cui, Y. In Situ Electrochemically Derived Nanoporous Oxides from Transition Metal Dichalcogenides for Active Oxygen Evolution Catalysts. *Nano Lett.* **2016**, *16*, 7588−7596.

(41) Tang, C.; Cheng, N.; Pu, Z.; Xing, W.; Sun, X. NiSe Nanowire Film Supported on Nickel Foam: An Efficient and Stable 3D Bifunctional Electrode for Full Water Splitting. *Angew. Chem., Int. Ed.* **2015**, *54*, 9351−9355.

(42) Bose, R.; Jothi, V. R.; Velusamy, D. B.; Arunkumar, P.; Yi, S. C. A Highly Effective, Stable Oxygen Evolution Catalyst Derived from Transition Metal Selenides and Phosphides. *Part. Part. Syst. Charact.* **2018**, *35*, No. 1800135.

(43) Liang, Z.; Ahn, H. S.; Bard, A. J. A Study of the Mechanism of the Hydrogen Evolution Reaction on Nickel by Surface Interrogation Scanning Electrochemical Microscopy. *J. Am. Chem. Soc.* **2017**, *139*, 4854−4858.

(44) Durst, J.; Siebel, A.; Simon, C.; Hasche, F.; Herranz, J.; Gasteiger, H. A. New Insights into the Electrochemical Hydrogen Oxidation and Evolution Reaction Mechanism. *Energy Environ. Sci.* **2014**, *7*, 2255−2260.

(45) Zeng, M.; Li, Y. Recent Advances in Heterogeneous Electrocatalysts for the Hydrogen Evolution Reaction. *J. Mater. Chem. A* **2015**, *3*, 14942−14962.

(46) Gong, M.; Zhou, W.; Tsai, M.-C.; Zhou, J.; Guan, M.; Lin, M.-C.; Zhang, B.; Hu, Y.; Wang, D.-Y.; Yang, J.; Pennycook, S. J.; Hwang, B.-J.; Dai, H. Nanoscale Nickel Oxide/Nickel Heterostructures for Active Hydrogen Evolution Electrocatalysis. *Nat. Commun.* **2014**, *5*, 4695.

(47) Jin, H.; Wang, J.; Su, D.; Wei, Z.; Pang, Z.; Wang, Y. In situ Cobalt-Cobalt Oxide/N-Doped Carbon Hybrids as Superior Bifunctional Electrocatalysts for Hydrogen and Oxygen Evolution. *J. Am. Chem. Soc.* **2015**, *137*, 2688−2694.

(48) McCrory, C. C. L.; Jung, S.; Ferrer, I. M.; Chatman, S. M.; Peters, J. C.; Jaramillo, T. F. Benchmarking Hydrogen Evolving Reaction and Oxygen Evolving Reaction Electrocatalysts for Solar Water Splitting Devices. *J. Am. Chem. Soc.* **2015**, *137*, 4347−4357.

(49) Pintado, S.; Goberna-Ferrón, S.; Escudero-Adán, E. C.; Galán-Mascarós, J. R. Fast and Persistent Electrocatalytic Water Oxidation by Co-Fe Prussian Blue Coordination Polymers. *J. Am. Chem. Soc.* **2013**, *135*, 13270−13273.

(50) Aiyappa, H. B.; Thote, J.; Shinde, D. B.; Banerjee, R.; Kurungot, S. Cobalt-Modified Covalent Organic Framework as a Robust Water Oxidation Electrocatalyst. *Chem. Mater.* **2016**, *28*, 4375−4379.

(51) Manna, P.; Debgupta, J.; Bose, S.; Das, S. K. A Mononuclear CoII Coordination Complex Locked in a Confined Space and Acting as an Electrochemical Water-Oxidation Catalyst: A "Ship-in-a-Bottle" Approach. *Angew. Chem., Int. Ed.* **2016**, *55*, 2425−2430.

(52) Chen, L.; Dong, X.; Wang, Y.; Xia, Y. Separating Hydrogen and Oxygen Evolution in Alkaline Water Electrolysis using Nickel Hydroxide. *Nat. Commun.* **2016**, *7*, 11741.

(53) Danilovic, N.; Subbaraman, R.; Strmcnik, D.; Chang, K.-C.; Paulikas, A. P.; Stamenkovic, V. R.; Markovic, N. M. Enhancing the Alkaline Hydrogen Evolution Reaction Activity through the Bifunctionality of $Ni(OH)_2$/Metal Catalysts. *Angew. Chem., Int. Ed.* **2012**, *51*, 12495−12498.

(54) Trotochaud, L.; Young, S. L.; Ranney, J. K.; Boettcher, S. W. Nickel−Iron Oxyhydroxide Oxygen-Evolution Electrocatalysts: The Role of Intentional and Incidental Iron Incorporation. *J. Am. Chem. Soc.* **2014**, *136*, 6744−6753.

(55) Guo, Y.; Yao, Z.; Shang, C.; Wang, E. Amorphous Co_2B Grown on $CoSe_2$ Nanosheets as a Hybrid Catalyst for Efficient Overall Water Splitting in Alkaline Medium. *ACS Appl. Mater. Interfaces* **2017**, *9*, 39312−39317.

(56) Yan, X.; Tian, L.; Atkins, S.; Liu, Y.; Murowchick, J.; Chen, X. Converting $CoMoO_4$ into CoO/MoO_x for Overall Water Splitting by Hydrogenation. *ACS Sustainable Chem. Eng.* **2016**, *4*, 3743−3749.

Appendix 2a

Physicochemical Characterizations

Various physicochemical techniques can be used for the characterizations of semiconductor-based materials as in this thesis work, we have used ZnO, PTCDA, layered double hydroxides (α-Co (OH)$_2$)-PDI, optical fibers coated with xCuO/TiO$_2$. The principle and handling of the techniques such as powder X-ray diffraction(P-XRD), FESEM, EDAX, TEM-HRTEM, XPS spectroscopy, NMR, UV-Vis spectroscopy, Photoluminescence spectroscopy, Lifetime measurements, and Gas chromatography are explained here.

1. Powder Diffraction

Understanding and predicting the properties of scientific and technologically important materials require knowing their structure. The structure of an idealized crystal lattice consists of periodic arrangement atoms and single crystal analysis is the most suitable technique to understand it. However, because of the unavailability of suitable single crystals in many cases and to extract information on the bulk material, an alternative technique, powder diffraction is routinely used. Moreover, it can be used to determine microstructural properties, disorders in materials, studies of macroscopic stresses in components, and the texture of polycrystalline samples. X-rays are electromagnetic waves having wavelengths of the order of 1Å, which is comparable with the spacing between lattice planes in crystals. X-ray diffraction, based on the wide-angle elastic scattering of X-rays, is the most important and common tool to determine the structure of the materials characterized by long-range ordering. X-ray diffraction involves the measurement of the intensity of X-rays scattered from electrons or neutrons bound to atoms. Waves scattered at atoms at different positions arrive at the detector with a relative phase shift. Therefore, the measured intensities yield information about the relative atomic positions. The

diffraction patterns give information about structure formation, phase purity, degree of crystallinity, and unit cell parameters of the materials. The formation of a structural phase can be confirmed by comparing the powder diffraction patterns with pure reference phases distributed by the International Centre for Diffraction Data (ICDD). Bragg's equation is the easiest way to get to the structural information in powder diffraction, the derivation of which considers X-ray diffraction as a reflection of X-rays by sets of lattice planes. As the X-rays penetrate deeply, additional reflections occur at thousands of consecutive parallel planes. The overlap of the scattered X-rays occurs since all are reflected in the same direction.

The Braggs equation is $n\lambda = 2d\sin\theta$, where d is the interplanar spacing of parallel lattice planes and 2θ is the diffraction angle, the angle between the incoming and outgoing X-ray beams. Sharp intensities emerge from the sample only at the special angles where Bragg's equation holds. For crystalline materials, the destructive interference results in a complete destruction of intensity in all the other directions. The divergent incident beam can reflect from the sample in the modern flat-plate powder X-ray diffractometer, used mostly in industrial and academic laboratories. It converges at a fixed radius from the sample position. This configuration is commonly referred to as "Bragg– Brentano" geometry (shown in Figure 1). The spinning of the sample about an axis normal to the flat plate results in a good powder average.
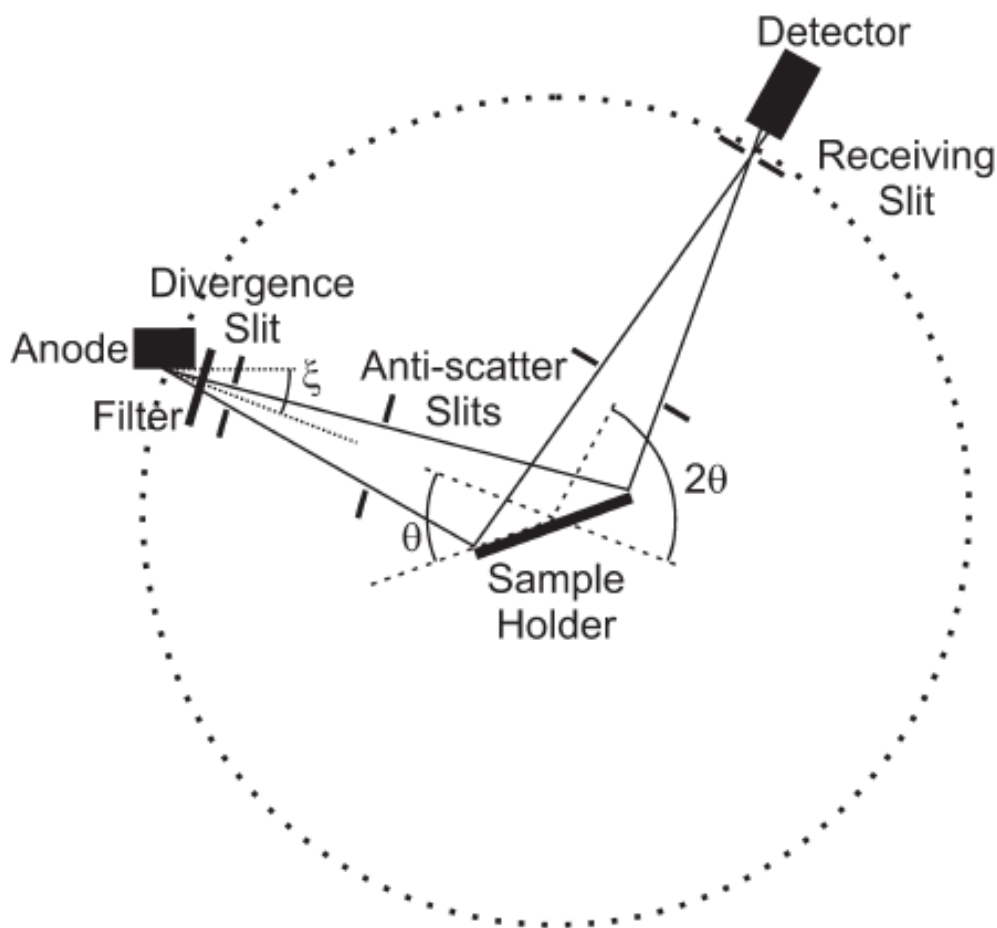
Figure 1. Schematic representation of Bragg–Brentano geometry.

Powder diffraction experiments exploit X-rays from a laboratory generator, high-energy storage ring (synchrotron radiation), or neutrons produced in a reactor or spallation source. A typical wavelength used lies in the range of 0.1-5 Å, comparable with the spacings between lattice planes in crystals. Data can be collected in transmission or reflection modes, depending on the absorption of radiation by the sample. Here is a brief description of the different sources used for the powder diffraction experiments.

1.1. Laboratory Xray Sources

In a standard laboratory instrument, the X-rays are produced in a sealed-tube source where electrons, accelerated by a potential difference of up to 60 kV, bombard ametal anode inside a

vacuum tube. This results in the formation of a characteristic radiation spectrum composed of discrete peaks arising from the filling of vacant level in the inner shell (created from the ejection of electron by the incoming electron) by a higher atomic level electron. The emission of an X-ray photon is characterised by the difference in energy between the two levels. A higher resolution copper X-ray spectrum consists of components labeled as K⬚1 (1.54056Å) and K⬚2(1.54439Å). The most commonly used target element is Cu but Mo, Cr, Fe, Co, Ag and W are also used for specialist applications . Cu tube is the most common choice for routine analysis, which gives X-rays of shortest wavelength above 1A˚. Also relatively high power can be applied to the target because of the good thermal conductivity of copper.

Table 1. Approximate principle emission lines for various anode targets.

Anode	Cu	Mo	Cr	Fe	Co	Ag	W
$\Lambda(K_\alpha)$Å	1.54	0.71	2.29	1.94	1.79	0.56	0.21

2. Transmission Electron Microscopy (TEM)

A TEM works much like a slide projector. A projector shines a beam of light through (transmits) the slide , as light passes through it is affected by structures and objects on the slide. These effects result in only certain parts of light beam being transmitted through certain parts of the slide. This transmitted beam is then projected onto the viewing screen forming an image of the slide. TEM works same way except that they shine beam of electrons (like light) through the specimen (slide). Whatever part is transmitted is projected into a phosphor screen. A "light source" at the top of the microscope emits electrons that travel through vacuum in the column of the microscope. The TEM uses electromagnetic lenses to focus electrons into a very thin beam. The electron beam then travel through the specimen .Depending on the density of the material, some of the electrons are scattered and disappear from the beam. At the bottom of the

microscope the unscattered electrons hit a fluorescent screen ,which gives rise to a shadow image of the specimen with its different parts displayed in varied darkness according to their density. The image can be studied directly by operator or photographed with a camera. The darker area of the image represent those area of the sample that fewer electrons were transmitted through (they are thicker or denser).The lighter of image represent those area of the sample that more electrons were transmitted through (they are thinner or less dense).
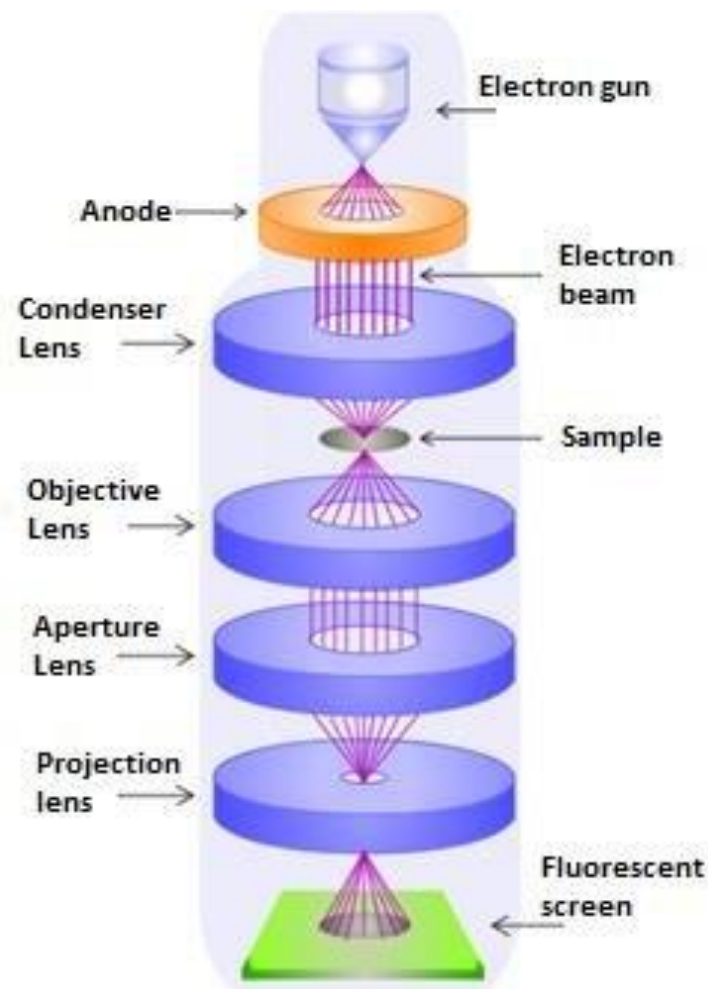

Figure 2. Principle of TEM

3.NMR Spectroscopy

All the NMR measurements were carried out on a Bruker AV400 MHz NMR spectrometer equipped with a 9.4 Tesla superconducting magnet. The resonance frequency for 1H at this magnetic field is 400 MHz and for 13C, it is 100 MHz. The proton NMR spectra were taken with a standard one pulse experiment using a 30 degree flip angle and 1 sec relaxation delay. 32 to 64 scans and 32K data points were used for data collection. The raw data obtained are Fourier Transformed to get the frequency domain spectrum without the application of any window function. 13C spectra were obtained with a standard pulse sequence with continuous proton decoupling. A flip angle of ~ 30 degree, relaxation delay of 2 sec and 32K data points were used for data collection. The proton decoupling was achieved by a standard ZGPG30 pulse technique. A standard DEPT pulse sequence with a sorting pulse of 135 degree (DEPT135) was employed for the 13C spectral editing so that the CH2 peaks appear as negative and CH and CH3 as positive. The number of scans for the 13C spectral data collection varied from a few hundred to a couple of thousand depending on the concentration. Prior to Fourier Transformation, the raw 13C data (FID's) were multiplied by an exponential window function with a line broadening (LB) of 2Hz for sensitivity enhancement. The chemical shifts for the solvent peak is found at 2.5ppm (1H, DMSO-d6) and 39.9 ppm (13C, DMSO-d6).

4. IR SPECTROSCOPY (Infra-red Spectroscopy)

In IR Spectroscopy, IR radiation is passed through a sample. Some of the infra radiation is absorbed by the sample and the other is transmitted. The resulting spectrum represents the molecular absorption and transmission, creating a molecular fingerprint of the sample. It represents the fingerprint of the absorption peaks which corresponds to frequencies of the vibrations between the bonds of atoms making up the material .Because each different material

is a unique combination of atoms, no two compounds produce the exact same infrared spectrum. Therefore, infrared spectroscopy can result in a positive identification (qualitative) of every different kind of material. In addition the size of peaks in the spectrum is a direct indication of the amount of material present. FT-IR spectrometers are often called as FT-IRs. FT-IR is a method of obtaining infrared spectra by collecting an Interferogram of a sample signal using an interferometer and thenperforming a Fourier transform on the Interferogram to obtain the spectrum. An FT-IR spectrometer collects and digitalizes the Interferogram, performs FT function and displays the spectrum. The technique works on the fact that bonds and groups of the bonds vibrate at characteristic frequencies. A molecule that is exposed to infrared rays absorbs infrared energy at frequencies which are characteristic to that molecule. During FT-IR analysis, a spot on the specimen is subjected to a modulated IR beam. The specimen's transmittance and reflectance of infrared rays at different frequencies is translated into an IR absorption plot consisting of reverse peaks. The resulting FT-IR spectral pattern is then analyzed and matched with known signatures of identified materials in the FT-IR library. FT-IR spectroscopy bases its functionality on the principle that almost all molecules absorb infrared light. Molecules only absorb at those frequencies where its infrared light affects the dipolar moment of the molecule. Molecule with dipolar moment allows infrared photons to interact with the molecule causing excitation to higher vibrational states. As mentioned earlier almost all molecules absorb infrared light and each molecule absorbs IR light at certain frequencies. This property provides unique characteristic for each molecule. It provides a way to identify the molecular type (qualitative analysis) and the amount or quantity of the molecule in the sample (quantitative analysis). Since each type of molecules only absorbs at certain frequencies it provides the unique absorption spectral pattern or finger print through the entire IR spectrum. As a conventional infrared spectroscopy, FT-IR is used to detect the vibrational transitions of a molecule. The advantage of FT-IR compared to conventional infrared

spectroscopy is that all wave numbers are measured at once with the help of Michelson interferometer.
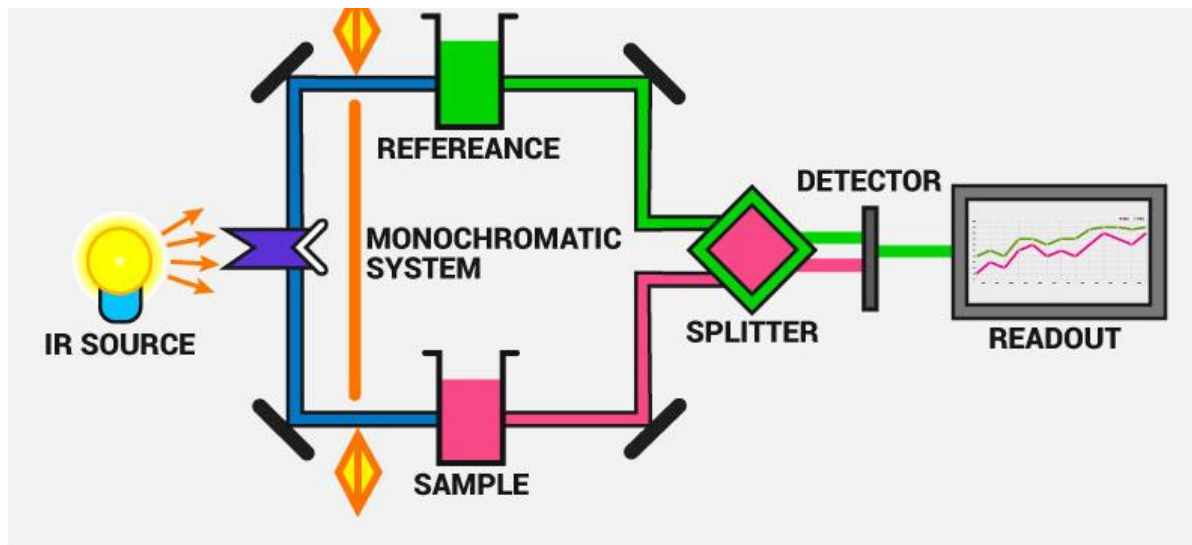

Figure 3. Schematic diagram of Infrared Spectroscopy

4. Scanning Electron Microscopy

Scanning electron microscopy (SEM) is one of the most widely used techniques for characterization of nanomaterials and nanostructures. The resolution of the SEM approaches a few nanometres, and the instruments can operate at A magnifications that are easily adjusted from ~10 to over 300,000. This technique provides not only topographical information like optical microscopes do, but also information of chemical composition near the surface. A scanning electron microscope can generate an electron beam scanning back and forth over a solid sample. The interaction between the beam and the sample produces different types of signals providing detailed information about the surface structure and morphology of the sample. When an electron from the beam encounters a nucleus in the sample, the resultant columbic attraction leads to a deflection in the electron's path, known as Rutherford elastic scattering. A fraction of these electronswill be completely backscattered, remerging from the incident surface of the sample. Since the scattering angle depends on the atomic number of the

nucleus, the primary electrons arriving at a given detector position can be used to produce images containing topological and compositional information. The high-energy incident electrons can also interact with the loosely bound conduction band electrons in the sample. However, the amount of energy given to these secondary electrons as a result of the interactions is small, and so they have a very limited range in the sample. Hence, only those secondary electrons that areproduced within a very short distance from the surface are able to escape from the sample. As a result, high-resolution topographical images can be obtained in this detection mode.
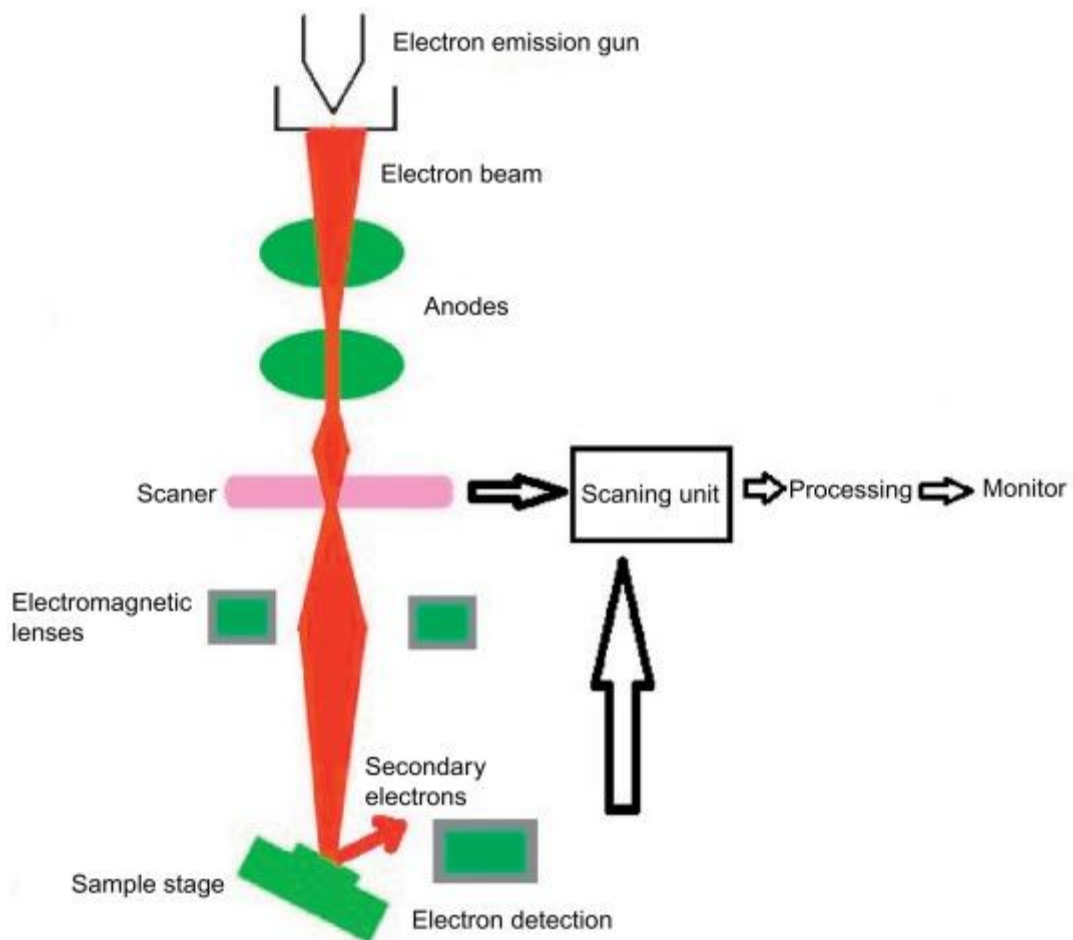

Figure.4. Principle of SEM

5. UVvisible Spectroscopy

Absorption spectroscopy in the visible region has long been an important tool to the analyst [11]. Appearance of colour arises from the property of the colored material to absorb selectively and reflect its complementary colour which falls within the visible region of the electromagnetic spectrum. Absorption of energy leads to a transition of electron from ground state to an excited state which is governed by the following equation $\Delta E = h\nu = hc/\lambda$ (2.11) where h represents Planck's constant, ν is the frequency of radiation, c is the velocity of light and λ is the radiation wavelength. Thus from the equation it seems that the UV-energy is quantized and hence a single discrete line should be obtained from a single electronic spectrum. However, this is not the case of reality as excitation of electronic energy levels would also involve excitation of the embedded vibrational and rotational energy levels of an atom, thus giving rise to a broad absorption band [12]. The intensity of the absorption band depends on three factors namely (a) transition probability, (b)population of states and (c) concentration or path length. Almost all relationships between intensities of incident and transmitted radiation and the concentration and path-length is governed by Beer-Lambert's law which is written as

$I = I_0 \exp(-\kappa cl)$

$\log(I_0/I) = A = \kappa cl$ (2.12)

where I = Intensity of the emitted radiation, I_0 = Intensity of the incident radiation, κ = constant, c = concentration and l = path length. A is known as the absorbance or the optical density and κ, the constant generally represented as ε, known as the molar absorption coefficient. In a dual beam spectrophotometer, light from either the visible or ultraviolet source enters the grating monochromator before it reaches the filter. Broad band filters contained in a filter wheel are automatically indexed into position at the required wavelengths to reduce the amount of stray light and unwanted orders from the diffraction grating. The light from the source is alternatively split into one of the two beams by a rotating mirror called a chopper; one beam is passed

through the sample and the other through the reference. The detector alternately sees the beam from the sample and then the reference. Its output which ideally would be an oscillating square-wave gives the ratio of I to Io directly i.e. the reference correction is made automatically. Array-detector spectrophotometers allow rapid recording of absorption spectra. Dispersing the source light after it passes through a sample allows the use of an array detector to simultaneously record the transmitted light power at multiple wavelengths. These spectrometers use photodiode arrays as the detector. The light source is a continuum source such as a tungsten lamp. All wavelengths pass through the sample. The light is dispersed by a diffraction grating after the sample and the separated wavelengths fall on different pixels of the array detector. The resolution depends on the grating, spectrometer design, and pixel size, and is usually fixed for a given instrument. Diffuse reflectance UV-Vis measurements were performed on a spectrophotometer with Teflon pellet as the reference material.

6. Electrochemical Impedance Spectroscopy

Electrochemical impedance spectroscopy (EIS) is a very versatile electrochemical tool to characterize intrinsic electrical properties of any material and its interface. This is a steady state method measuring the current response to the application of an ac voltage as a function of the frequency. The basis of impedance spectroscopy is the analysis of the impedance (resistance of alternating current) of the observed system with respect to the applied frequency and applied signal. An important advantage of EIS over other techniques is the possibility of using tiny ac voltage amplitudes exerting a very small perturbation on the system. EIS provides quantitative information about the conductance, dielectric coefficient and some interfacial properties. Also this has been widely employed to study the kinetics of electrochemical and

photoelectrochemical processes including the elucidation of salient electronic and ionic processes occurring in the DSC. EIS data for electrochemical cells are most often represented in Nyquist and Bode plots. Bode plots refer to representation of the impedance magnitude (or the real or imaginary components of the impedance) and phase angle as a function of frequency. Because both the impedance and the frequency often span orders of magnitude, they are frequently plotted on a logarithmic scale. Bode plots explicitly show the frequency-dependence of the impedance of the device under test. A complex plane or Nyquist plot depicts the imaginary impedance, which is indicative of the capacitive and inductive character of the cell, versus the real impedance of the cell. Nyquist plots have the advantage that activation-controlled processes with distinct time-constants show up as unique impedance arcs and the shape of the curve provides insight into possible mechanism or governing phenomena. The flat band potential can be calculated using a circuit which fits for the Nyquist plot. From which the capacitance (C) at various voltages can be measured. 1/C vs voltage gives rise to Mott-Schottkey plot. Using this plot flat band potential can be measured.

7. Xray photoelectron spectroscopy

X-ray Photoelectron Spectroscopy (XPS) or Electron Spectroscopy for Chemical Analysis (ESCA) is based on the principle that when X-rays hi atoms, electrons are ejected. It is a typical surface-sensitive technique as only electrons that are generated in the top few atomic layers (mean free path ~1.5 nm) are detected, even though the absorption length of the X-rays is about 100 - 1000 nm. The technique provides quantitative information about the elemental composition of the surface of all kinds of solid material like insulators, conductors, polymers etc. The sample material is irradiated with monoenergetic soft x-rays causing electrons to be

ejected. The measurement of kinetic energies of these ejected photoelectrons helps in the identification of the elements in the sample as each element produces a characteristic set of XPS peaks at characteristic binding energy values. All elements except H and He can be detected. Moreover the relative concentrations of elements can be determined from the photoelectron intensities. The most important advantage of XPS is its ability to obtain information on chemical states from the variations in binding energies, or chemical shifts, of the photoelectron lines. Most modern instruments have detection limits for most of the elements in the parts per thousand ranges. Detection limits of parts per million (ppm) are possible under special conditions such as concentration at top surface or very long collection time. In XPS, soft X-rays with energies range from 200-2000 eV are used. The development of synchrotron radiation sources has enabled high resolution studies with much wider and more complete energy range (5 - 5000 eV). A sample placed in ultra-high vacuum is irradiated with photons of energy, hv. Electrons of the atoms on the surface absorb the photons and leave the atom by using some of its energy to overcome the coulomb attraction of the nucleus, reducing its KE by its initial state BE. The kinetic energy of the ejected electron is related to the energy of the X-ray photon as

$$KE = h\nu - BE - \Phi$$

where BE represents the binding energy of the atomic orbital from which the electron ejected and Φ is the spectrometer work function which is an adjustable instrumental correction factor that accounts for the few eV of KE loss of the photoelectron as it becomes absorbed by the instrument's detector. An electron energy analyzer measures the kinetic energy distribution of the emitted photoelectrons and a photoelectron spectrum can thus be recorded. The number of detected electrons is a measure for the elemental concentration. Atomic concentrations can be obtained by dividing the peak areas by standard sensitivity factors and normalizing to 100%. For bulk materials the surface concentraions can be determined with a 20% inaccuracy.

However, in most cases, the surface composition varies as a function of depth, where the signal of an element in a lower layer will be attenuated more strongly than that in the top layer. In such cases either angle-resolved measurements or model calculations are performed to extract quantitative information. The basic requirements for a XPS experiment are:

1. A fixed-energy radiation source. The most commonly employed X-ray sources are those giving rise to Mg Kα radiation (hν = 1253.6 eV) and Al Kα radiation (hν = 1486.6 eV).

2. An electron energy analyser. This separates the emitted electrons according to their KE, and measures the flux of emitted electrons of a particular energy. The most preferred design is a concentric hemispherical analyser (CHA) where an electric field is applied between two hemispherical surfaces to disperse the electrons according to their KE

3. A high vacuum environment which enables the emitted photoelectrons to be analysed without interference from gas phase collisions. XPS detectors must be operated under ultra-high vacuum (UHV, P < 10−9 millibar) conditions in order to count the number of electrons with a minimum of error, as they are kept one meter away from the sample.

8. Photoluminescence Spectroscopy

Photoluminescence is a term used to designate a number of effects, including fluorescence, phosphorescence, and Raman scattering. Photoluminescence spectroscopy is a contactless, nondestructive method of probing the electronic structure of materials. Light is directed onto a sample, where it is absorbed and imparts excess energy into the material in a process called photo-excitation. One way this excess energy can be dissipated by the sample is through the emission of light, or luminescence. In the case of photo-excitation, this luminescence is called photoluminescence. Photo-excitation causes electrons within a material to move into permissible excited states. When these electrons return to their equilibrium states, the excess energy is released and may include the emission of light (a radiative process) or may not (a

nonradiative process). The energy of the emitted light (photoluminescence) relates to the difference in energy levels between the two electron states involved in the transition between the excited state and the equilibrium state. The quantity of the emitted light is related to the relative contribution of the radiative process. Fluorescence is the result of a three-stage process that occurs in certain molecules called fluorophores or fluorescent dyes. A fluorescent probe is a fluorophore designed to localize within a specific region of a biological specimen or to respond to a specific stimulus. The process responsible for the fluorescence of fluorescent probes and other fluorophores is illustrated by a Jablonski diagram. Stage 1: Excitation. A photon is supplied by an external source such as an incandescent lamp or a laser and absorbed by the fluorophore, creatingan excited electronic singlet state (S1'). This process distinguishes fluorescence from chemiluminescence, in which the excited state is populated by a chemical reaction. Stage 2: Excited-State Lifetime. The excited state exists for a finite time (typically 1–10nanoseconds). During this time, the fluorophore undergoes conformational changes and is also subject to a multitude of possible interactions with its molecular environment. These processes have two important consequences. First, the energy of S1' is partially dissipated, yielding a relaxed singlet excited state (S1) from which fluorescence emission originates. Second, not all the molecules initially excited by absorption (Stage 1) return to the ground state (S0) by fluorescence emission. Other processes such as collisional quenching, fluorescence resonance energy transfer (FRET) and intersystem crossing (see below) may also depopulate S1. The fluorescence quantum yield is the ratio of the number of fluorescence photons emitted (Stage 3) to the number of photons absorbed (Stage 1). Stage 3: Fluorescence Emission. A photon of energy is emitted, returning the fluorophore to its ground state S0. Due to energy dissipation during the excited-state lifetime, the energy of this photon is lower, and therefore of longer wavelength, than the excitation photon. The difference in energy or wavelength represented by the absorbed and emitted photon is called the Stokes shift. The Stokes shift is

fundamental to the sensitivity of fluorescence techniques because it allows emission photons to be detected against a low background, isolated from excitation photons. In contrast, absorption spectrophotometry requires measurement of transmitted light relative to high incident light levels at the same wavelength.
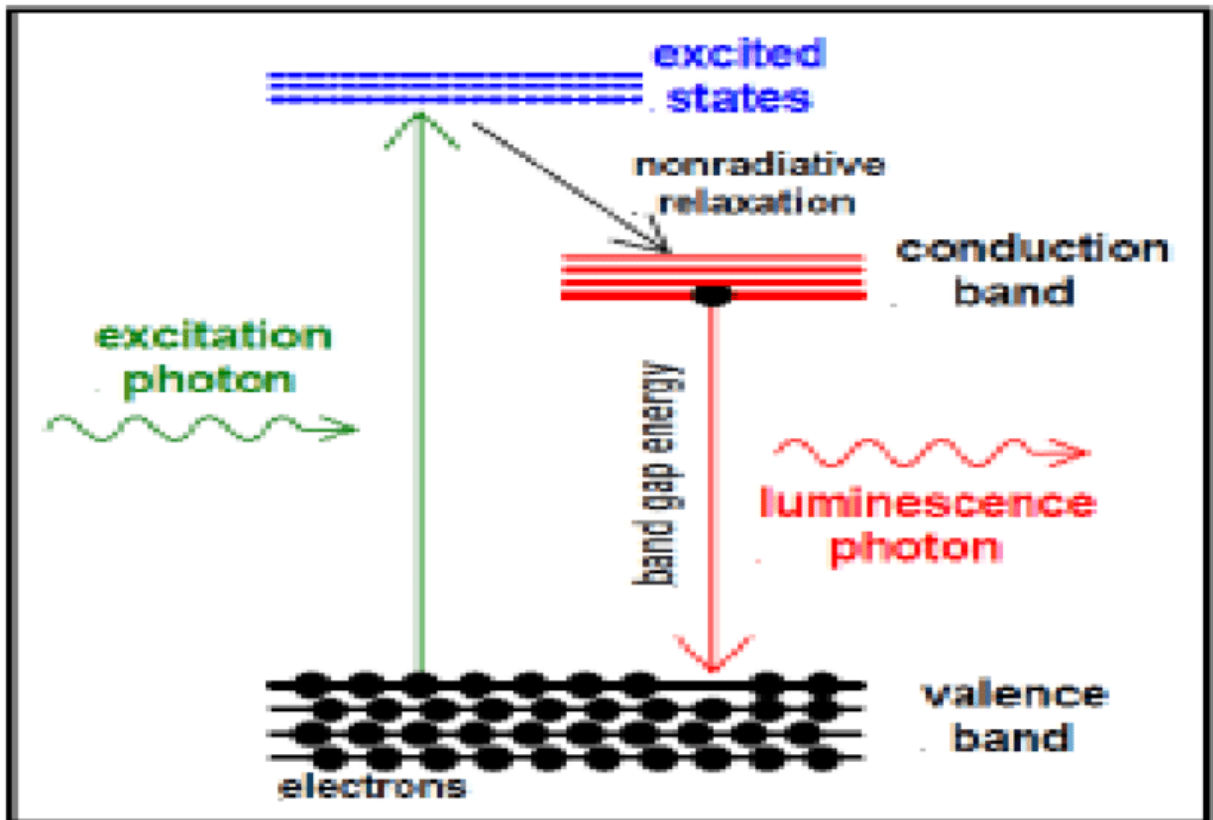

Figure.5. Jablonski Diagram

9. Gas Chromatography

A Gas Chromatograph is used to detect the components based on the selective affinity of components towards the adsorbent materials. The sample is introduced in the liquid/gas form with the help of GC syringe into the injection port, it gets vaporized at injection port then passes through column with the help of continuously flowing carrier stream (mobile phase), mainly H2 (for TCD), and gets separated/detected at the detection port with suitable temperature programming. We visualize this on computer in the form of peaks Carrier medium can be liquid

(e.g. HPLC) or gas (e.g. GC) for the ease of separation/detection, if it is gas then called gas chromatography otherwise called liquid chromatography. Different chemical constituents of the sample travel through the column at different rates depending upon,

1. Physical properties

2. Chemical properties, and

3. Interaction with a specific column filling (stationary phase).

As the chemicals exit the end of the column, they are detected and identified electronically. The function of the stationary phase in the column is to separate different components, causing each one to exit the column at a different time (retention time). Other parameters that can be used to alter the order or time of retention are the carrier gas flow rate, and the temperature. Physical Components involve inlet port, Adsorption column, detector port, flow controller (to control the flow of carrier gas), etc. Packed columns are 1.5 - 10 m in length and have an internal diameter of 2 - 4 mm. The tubing is usually made of stainless steel or glass and contains a packing of finely divided, inert, solid support material (eg. diatomaceous earth) that is coated with a liquid or solid stationary phase. The nature of the coating material determines what type of materials will be most strongly adsorbed. Capillary columns have a very small internal diameter, on the order of a few tenths of millimeters, and lengths between 25-60 meters are common. The inner column walls are coated with the active materials (WCOT columns). Some columns are quasi solid filled with many parallel micro pores (PLOT columns). Most capillary columns are made of fused silica with a polyimide outer coating. These columns are flexible, so a very long column can be wound into a small coil. Temperature dependence of molecular adsorption and of the rate of progression along the column necessitates a careful control of the column temperature to within a few tenths of a degree for precise work. Reducing the temperature produces the greatest level of separation, but can result in very long elution times. The choice of carrier gas (mobile phase) is important, with hydrogen being the most efficient

and providing the best separation. However, helium has a larger range of flow rates that are comparable to hydrogen in efficiency, with the added advantage that helium is non-flammable, and works with a greater number of detectors. Therefore, helium is the most common carrier gas used.

Detectors:

A number of detectors are used in gas chromatography. The most common are the Flame ionization detector (FID) and the thermal conductivity detector (TCD). While TCDs are essentially universal and can be used to detect any component other than the carrier gas (as long as their thermal conductivities are different than that of the carrier gas, at detector temperature), FIDs are sensitive primarily to hydrocarbons, and are more sensitive to them than TCD. Both detectors are also quite robust. Since TCD is non-destructive, it can be operating in-series before an FID (destructive), thus providing complementary detection of the same eluents.
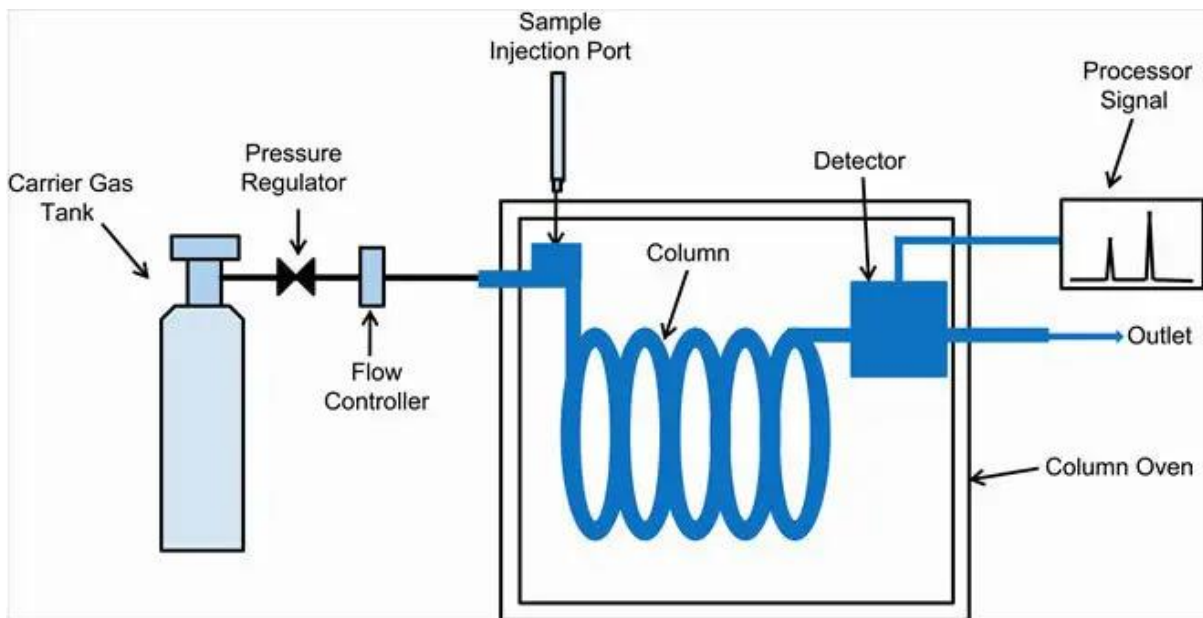

Figure.6.Gas Chromatography

Appendix 4a

Flat band potential was calculated using the equation, $V_{fb} = EA - E_{ref} + 1/2 E_g$

Where V_{fb} is the flat band potential, EA is the electron affinity of the individual atom, E_{ref} is the energy of free electrons on the hydrogen scale, $E_{ref} = 4.5$ eV and E_g is the band gap of the material

For ZnO

$EA = ((X_{Zn}) * (X_O)*)^{1/2}$

Where X_{Zn}, and X_o are the electronegativities in Mulliken scale of Titanium and Oxygen respectively.

The detailed calculation is given below

$X_{Zn} = 4.45$eV

$X_o = 7.53$ eV

Band gap of ZnO is 3.2 eV

$EA = (4.45 \times (7.53))^{1/2}$

$\quad = 5.788$eV

$V_{fb} = 5.788 - 4.5 + (½ \times 3.2)$

$V_{fb} = +2.89$eV

Now,

$VB + CB = E_g$

$2.89 + CB = 3.2$

$CB = -0.31$eV

Appendix 4b

The energy levels of the highest occupied molecular orbital (HOMO) of the self-assembled supramolecular were determined by oxidative half-cyclic voltammetry in THF Ferrocene/ferrocenium (Fc/Fc+) was used as an internal reference and 0.1 M tetra-n-butylammonium hexafluorophosphate (TBAPF6) as a supporting electrolyte. The HOMO levels of TC-PTCDA and MC-PTCDA were at 1.53V and 0.89 V vs. NHE, respectively. The relationship between

$$-E_{V \; vs. \; vacuum} = E^{onset} - E_{V \; vs. \; Fc/Fc+} + 4.8 \; eV \qquad (4.2)$$

$$E_{V \; vs. \; NHE} = -(E_{V \; vs. \; vacuum} + 4.5 \; eV) \qquad (4.3)$$

The LUMO levels were calculated from the equation of

$$E_{LUMO} + E_{HOMO} = E_g \qquad (4.4)$$

TC-PTCDA
HOMO= (1.84-0.61+4.8)+4.5eV
= 1.53V

LUMO= $E_{HOMO} - E_g$
= 1.53-2.41
= -0.88

MC-PTCDA
HOMO= (1.20 - 0.61+4.8)+4.5eV
= 0.89

LUMO = $E_{HOMO} - E_g$
= 0.89-1.9
= -1.01

The data were found to be that for TC-PTCDA, the LUMO is -0.88V, and MC-PTCDA is -1. 01V.This data shows that the redox potentials of respective TC-PTCDA and MC-PTCDA are higher than that of redox potential of hydrogen evolution and thus this will make sure to get enough driving force for water reduction and to get H_2 evolution.
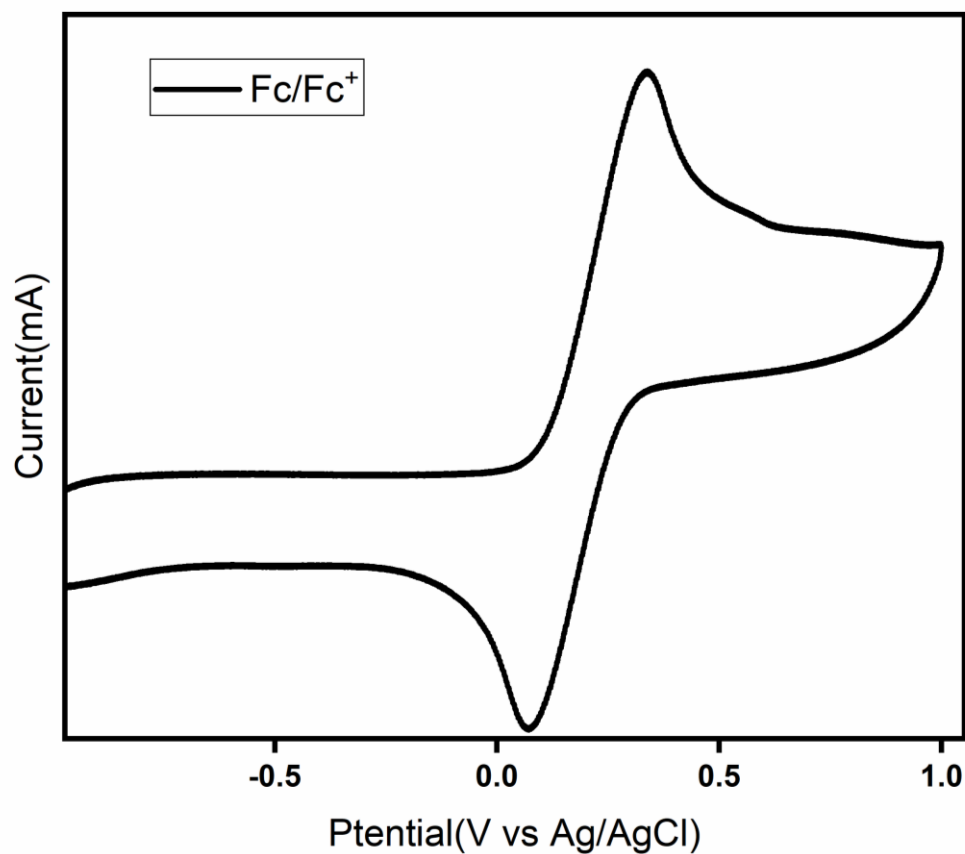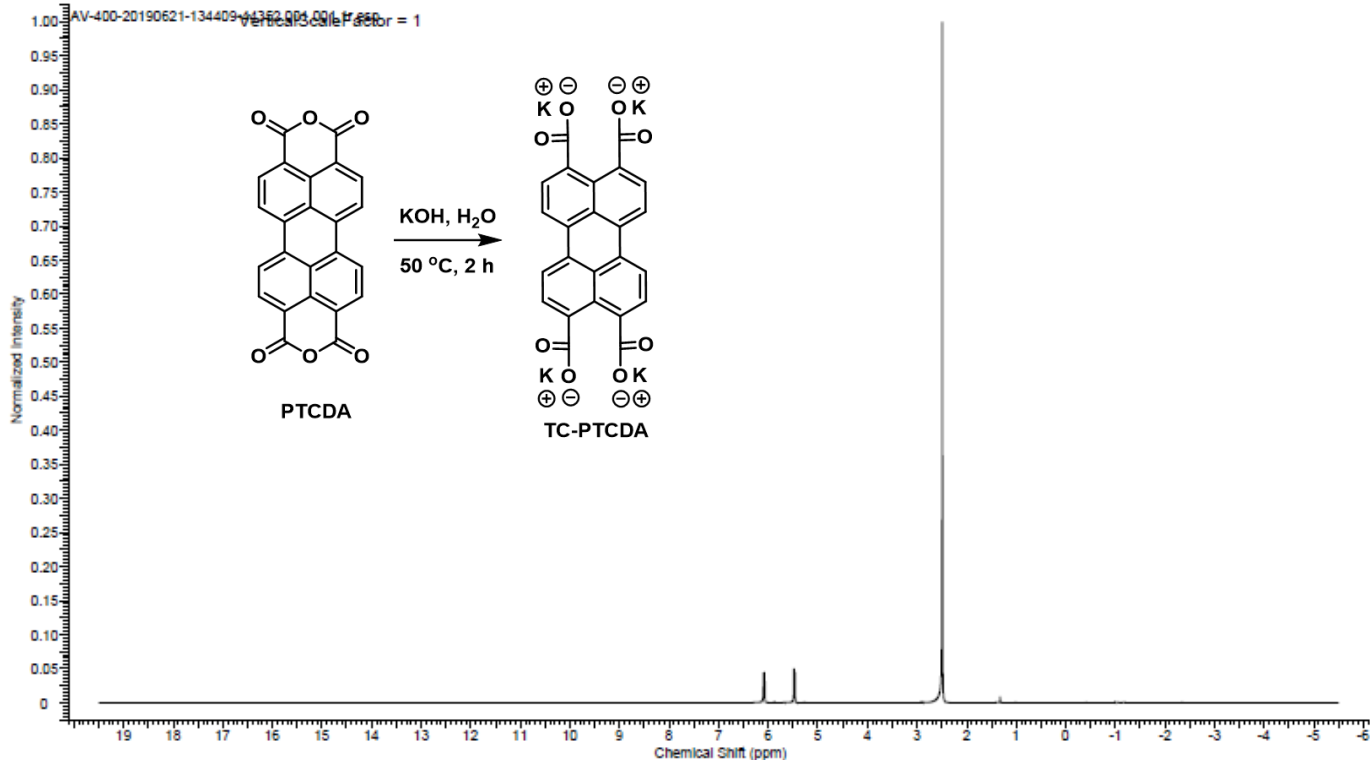

Fig.4b.1. Cyclic voltammograms curves of Ferrocene/Ferrocenium (Fc/Fc$^+$) redox couple
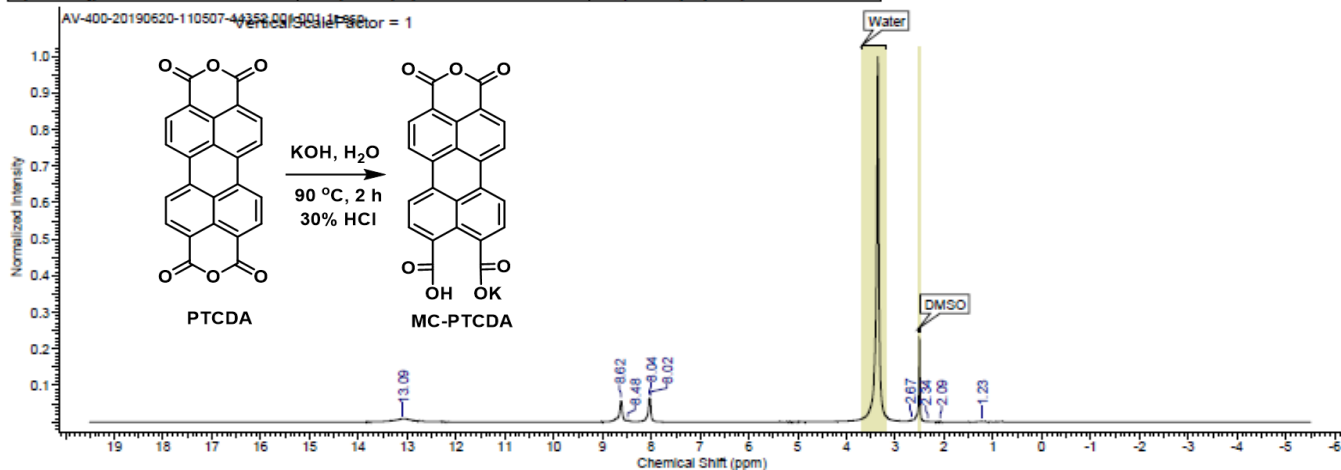
NMR –TC-PTCDA

Acquisition Time (sec)	1.6384	Comment	Priyanka W 1H	Date	24 Jun 2019 10:33:44		
Date Stamp	24 Jun 2019 10:33:44			File Name	\\172.16.2.7\nmr_data\AV400\June_19_400\AV-400-20190621-134409-44352\1\pdata\1\1r		
Frequency (MHz)	400.13	Nucleus	1H	Number of Transients	28	Origin	spect
Original Points Count	16384	Owner	root	Points Count	16384	Pulse Sequence	zg30
Receiver Gain	228.00	SW(cyclical) (Hz)	10000.00	Solvent	DMSO-d6	Spectrum Offset (Hz)	2800.9102
Spectrum Type	STANDARD	Sweep Width (Hz)	9999.39	Temperature (degree C)	21.800		

NMR –MC-PTCDA

Acquisition Time (sec)	1.6384	Comment	Priyanka 1H	Date	21 Jun 2019 12:41:44		
Date Stamp	21 Jun 2019 12:41:44						
File Name	C:\Users\priyanka walko\Desktop\THesis chapter wise\ptcdk\NMR Data\NMR OF PTCDK FROM one side\AV-400-20190620-110507-44352\1\pdata\1\1r						
Frequency (MHz)	400.13	Nucleus	1H	Number of Transients	56	Origin	spect
Original Points Count	16384	Owner	root	Points Count	16384	Pulse Sequence	zg30
Receiver Gain	322.00	SW(cyclical) (Hz)	10000.00	Solvent	DMSO-d6	Spectrum Offset (Hz)	2800.9102
Spectrum Type	STANDARD	Sweep Width (Hz)	9999.39	Temperature (degree C)	22.900		

No.	(ppm)	Annotation	Layer No.	Created By	Created At	Modified By	Modified At
1	[2.49 .. 2.53]	DMSO	1	plya	Fri 21-06-2019 15:00:07		
2	[3.20 .. 3.68]	Water	1	plya	Fri 21-06-2019 15:00:07		

Appendix 5a

^{1}H-NMR

N,N'-Bis(P-Carboxyl-Phenylene)
perylene-3,4,9,10-Peryelene bisimide
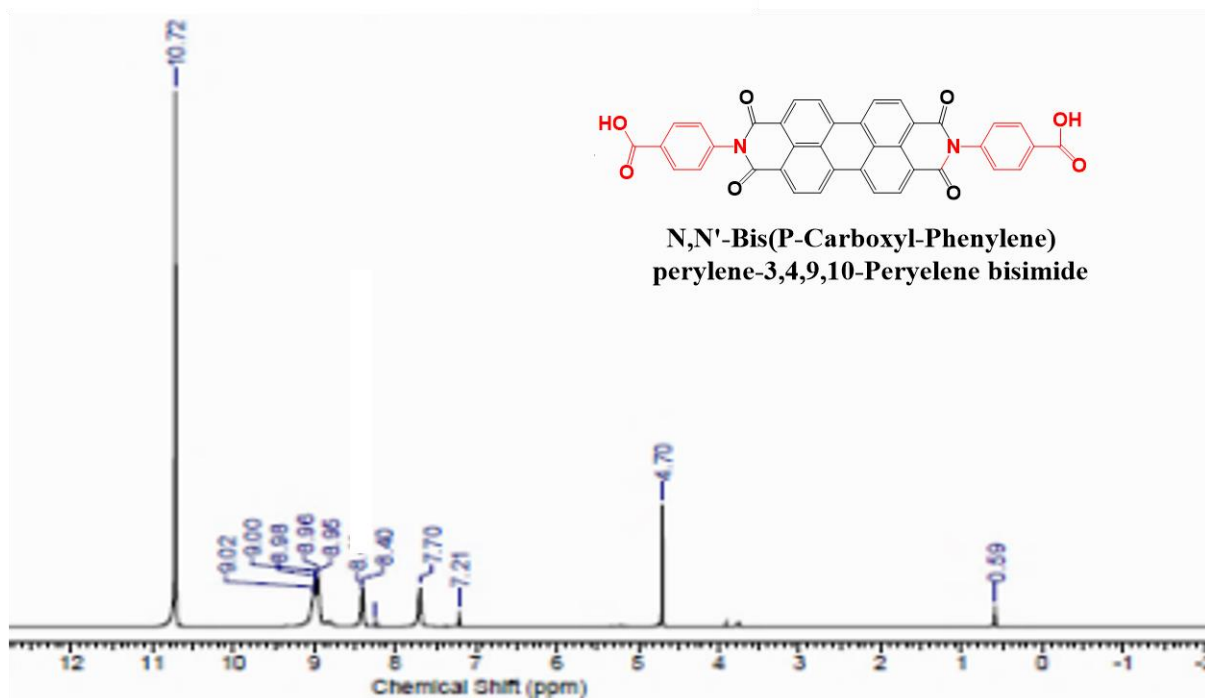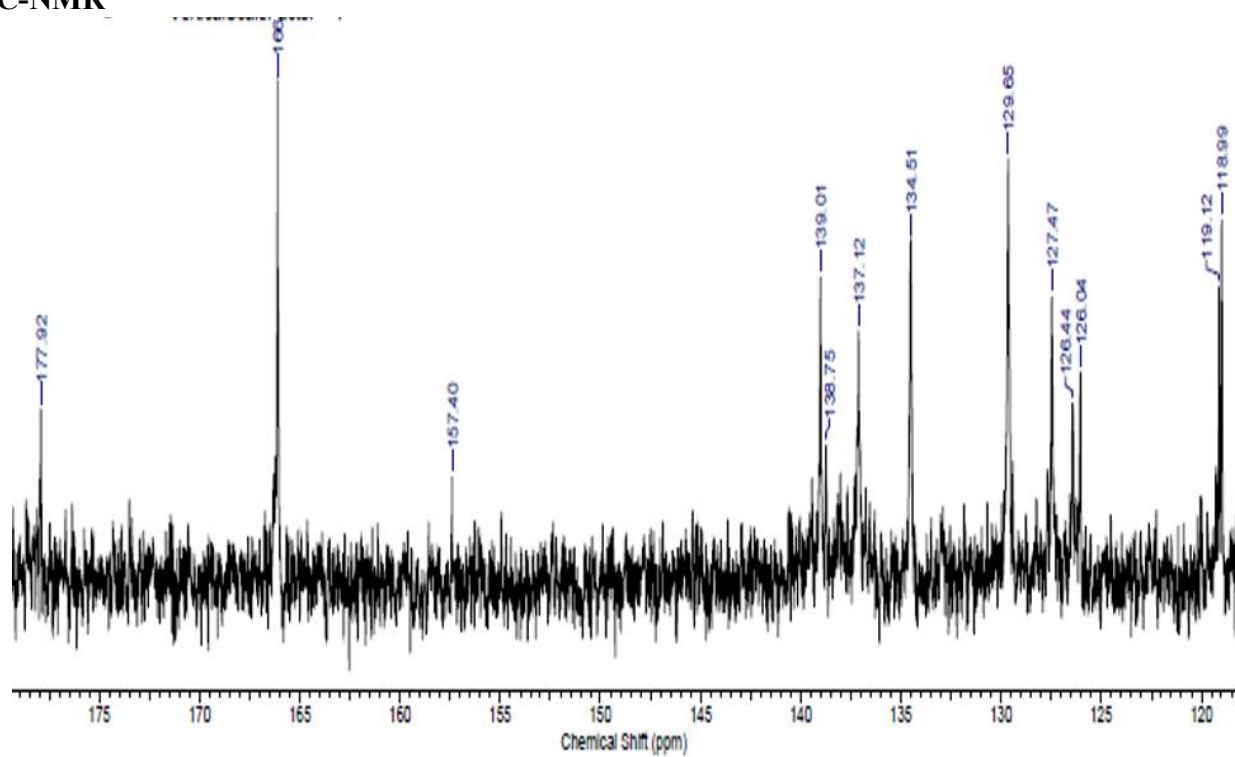
^{13}C-NMR

DEPT

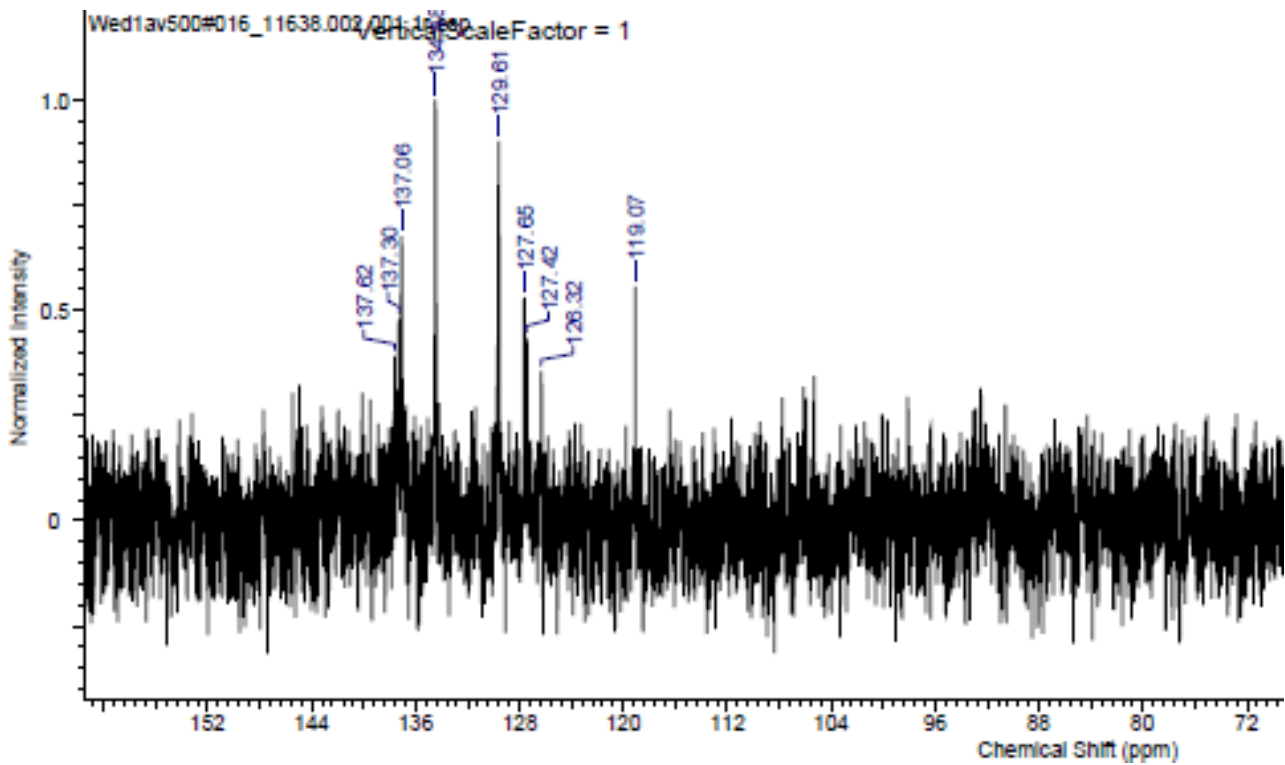**Fig.5a.1.^{1}H-NMR,13C-NMR and DEPT of N,N-Bis(P-Carboxyl-Perylene) perylene-3,4,9,10-Peryelene bisimide**

Flat band potential was calculated using the equation, Vfb=EA-Eref+1/2Eg

Where Vfb is the flat band potential, EA is the electron affinity of the individual atom, Eref is the energy of free electrons on the hydrogen scale, Eref= 4.5 eV and Eg is the band gap of the material

For Co(OH)$_2$

$EA=((X_{Co})* (X_O)*)^{1/2}$

Where X_{Co} and X_o are the electronegativities in the Mulliken scale of Titanium and Oxygen respectively.

The detailed calculation is given below

$X_{Co} = 6.21$ eV

$X_o = 7.53$ eV

Band gap of **Co(OH)₂** is 1.76 eV

$EA = (6.21 \times (7.53)^2)^{1/3}$

$= 7.06$ eV

$Vfb = 7.06 - 4.5 + (½ \times 1.76)$

Vfb= +2.38eV

Now,

VB+CB=Eg

2.38+CB=1.76

CB= -0.62Ev

For PDI

The energy levels of the highest occupied molecular orbital (HOMO) of the self-assembled supramolecular were determined by oxidative half-cyclic voltammetry in THF Ferrocene/ferrocenium (Fc/Fc+) was used as an internal reference and 0.1 M tetra-n-butylammonium hexafluorophosphate (TBAPF6) as a supporting electrolyte. The HOMO levels of TC-PTCDA and MC-PTCDA were at 1.53V and 0.89 V vs. NHE, respectively.

The relationship between

$$-E_{V\ vs.\ vacuum} = E^{onset} - E_{V\ vs.\ Fc/Fc+} + 4.8\ eV \qquad (5.2)$$

$$E_{V\ vs.\ NHE} = -(E_{V\ vs.\ vacuum} + 4.5\ eV) \qquad (5.3)$$

The LUMO levels were calculated from the equation of
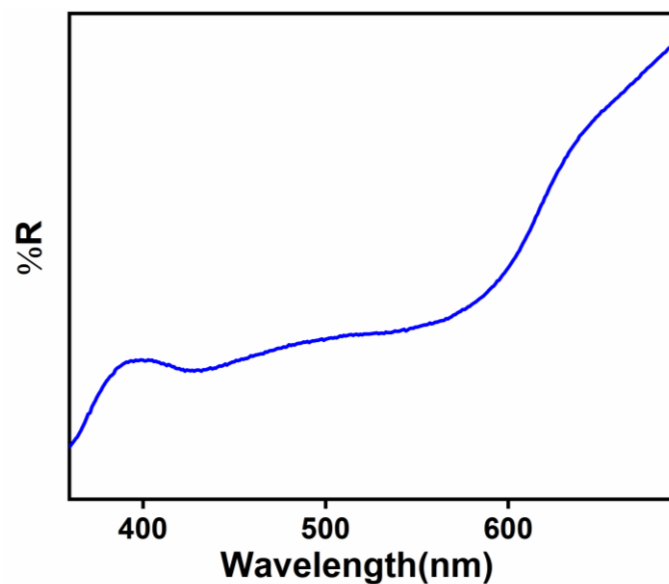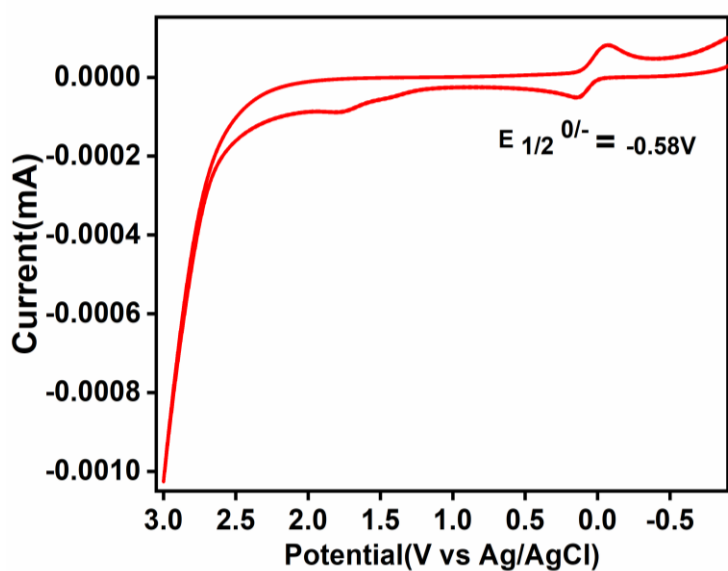
$$E_{LUMO}+E_{HOMO}=Eg \qquad (5.4)$$

HOMO=(1.79-0.58+4.8)-4.5

=+1.51

LUMO= $E_{HOMO} - E_g$

= 1.51-2.30

= -0.79

Apparent quantum yield:

The apparent quantum yield calculations by using the formula

$$AQY\ (\%) = \frac{2 \times \text{Number of evolved } H_2 \text{ molecules}}{\text{Number of incident photons}} \times 100\%$$

C=No. of Hydrogen molecules in umol per hour

NA = Avagadros number (6.02×10^{23} mol^{-1})

S= Irradiation area (127.17 cm^2)

t = time of reaction

h= Plancks constant (6.626×10^{-34} J)

C = 3×10^8 m/s

P= light intensity detected by lux meter (for 500 lux for optical fibers=7.3206×10^{-5} W/Cm^2)

λ= 350-700nm

Reaction conditions: 40ml solution (30ml water, 10ml methanol), bunch of optical fibers coated with 50mg of catalyst (5CuO/TiO$_2$)

430nm

AQY(%)=1.34%

500nm

AQY(%)= 1.1%

630nm

AQY%=8.96%

750nm

AQY%=7.5%

Average AQY(%)=4.72%

Flat band potential

The band gap calculations has been done by using Mullikens electronegativity scale

Flat band potential was calculated using the equation, $V_{fb}=EA-E_{ref}+1/2E_g$

Where V_{fb} is the flat band potential, EA is the electron affinity of the individual atom, E_{ref} is the energy of free electrons on the hydrogen scale, E_{ref}= 4.5 eV and E_g is the band gap of the material

For TiO_2

$EA=((X_{Ti})* (X_O)^2*)^{1/3}$

Where $X_{Ti,}$ and X_o are the electronegativities in Mulliken scale of Titanium and Oxygen respectively.

The detailed calculation is given below

$X_{Ti} = 3.45eV$

$X_o = 7.53$ eV

$X_{Cu} = 4.48eV$

Band gap of TiO_2 is 3.2 eV

$EA = (3.45 \text{ x } (7.53)^2)^{1/3}$

$\quad = 5.80eV$

$V_{fb} = 5.80 - 4.5 + (\frac{1}{2} \text{ x } 3.2)$

$\quad$ **$V_{fb}= +2.9eV$**

Now,

VB+CB=Eg

2.9+CB=3.2

CB= -0.3eV

Band gap for CuO is 1.9eV

EA= $(4.48 \times 7.53)^{1/2}$

    =5.80

Vfb= 5.80-4.5 +(1/2x1.9)

    = 2.25eV

CB=1.9-2.25=+0.35eV

CB=+0.35eV

Band gap for Cu_2O is 2.38eV

EA= $(4.48^2 \times 7.53)1/3$

    = 5.32eV

Vfb= 5.32-4.5 +(1/2x2.38)

    = 2.01eV

CB=2.38-2.01=-0.37eV